ANALYSIS OF THE DEFORMATION BEHAVIOR OF THE HEXAGONAL CLOSE-PACKED ALPHA PHASE IN TITANIUM AND TITANIUM ALLOYS

By

Hongmei Li

A DISSERTATION

Submitted to
Michigan State University
in partial fulfillment of the requirements
for the degree of

Materials Science and Engineering - Doctor of Philosophy

2013

ABSTRACT

ANALYSIS OF THE DEFORMATION BEHAVIOR OF THE HEXAGONAL CLOSE-PACKED ALPHA PHASE IN TITANIUM AND TITANIUM ALLOYS

By

Hongmei Li

Due to their high specific strength, good corrosion resistance, and the ability to withstand high temperature, titanium (Ti) alloys are often employed in structural applications, such as the aerospace industry. The intrinsic deformation mechanisms of Ti alloys activated within the broad service conditions for targeted structural components have not been as well documented as those for cubic metals. A greater knowledge of the distribution of the active deformation mechanisms in Ti alloys would be useful for developing a robust crystal plasticity finite element (CPFE) model to simulate the damage nucleation process of polycrystalline Ti alloys, thereby advancing efforts to establish Ti alloys with enhanced mechanical performance.

In this dissertation, a systematic investigation of the deformation behavior was conducted on commercially pure (CP) Ti, and the Ti-5Al-2.5Sn (wt.%), Ti-3Al-2.5V (wt.%), and Ti-6Al-4V (wt.%) alloys. Experiments were performed in tension and tensile-creep at 296K-763K using an *in-situ* scanning electron microscopy (SEM) testing method, which allows for the observation of the surface deformation evolution. A technique combining backscattered electron (BSE) and secondary electron (SE) imaging and electron backscattered diffraction (EBSD) was used to identify the distribution of the active deformation systems observed under various testing conditions.

The main findings of this work were that the distribution of the deformation modes varied as a function of the material composition, texture, and the testing condition (i.e. temperature and stress). For the lower Al-containing materials, prismatic slip dominated the tensile deformation.

However, the basal slip activity increased with increased Al content in the alloys. For example for the Ti-5Al-2.5Sn and Ti-6Al-4V alloys, basal slip was almost as equally active as prismatic slip. In fact, for some testing conditions of these alloys, such as the 728K tension tests of Ti-6Al-4V, basal slip was more active than prismatic slip. Basal slip activity was also enhanced by increasing temperature. The twinning behavior was also dependent on the Al content of the materials; less twinning occurred for the alloys containing more than 3wt.% Al. Moreover, increasing temperature usually resulted in a decreased twinning activity. Texture also influenced the distribution of the deformation modes by affecting the Schmid factors, which played an important role in the deformation behavior. Compared to the higher-stress tensile experiments, slip was observed to a significantly lesser extent during creep. Instead, grain boundary sliding (GBS) was dominant. In some cases, GBS eventually evolved into grain boundary cracks. For Ti-5Al-2.5Sn, the formation of grain boundary cracks was associated with grains which displayed hard orientations, where the c-axis was nearly perpendicular to the tensile direction.

A novel methodology for calculating the CRSS ratios of the different deformation modes was developed. The calculated CRSS ratios indicated that the CRSS ratios of α-phase Ti changed as a function of alloy composition and test temperature. The methodology developed provides a flexible manner to assess the CRSS ratios for a variety of deformation systems in polycrystalline microstructures, and it has the potential to be applied to a wide range of materials and crystal systems.

This work has established a thorough understanding of the deformation mechanisms of Ti and Ti alloys as a function of alloy composition and test temperature. The insights gained from these data have a broad impact on understanding the heterogeneous deformation processes in Ti and Ti alloys and also on development of CPFE modeling.

ACKNOWLEDGEMENTS

First, I would like to thank my advisor Dr. Carl Boehlert for his patience and invaluable guidance throughout my PhD work. He taught me how to use *in-situ* test equipment and was always available to help me solve the problems that arose during the tests. He also provided me with many opportunities to present my work at technical conferences held in both China and United States. Moreover, he showed great understanding and care for students' everyday life and set an example of being a nice advisor.

I would also like to thank my co-advisor Dr. Thomas Bieler. He taught me a lot of crystallography and also taught me how to incorporate the crystallographic information into Matlab^{TM} programming to calculate useful values and draw meaningful figures. This knowledge was an important steppingstone for my PhD work. Furthermore, his enthusiasm and passion for exploring new areas in science and research inspired me through this work and will continue inspiring me in my future work.

I would also like to thank my co-advisor Dr. Martin Crimp. He provided me with his tremendous help of polishing my writing. I would like to thank him for the hard questions and insightful discussions during the group meeting. These experiences were invaluable treasures when I presented my work in technical conferences.

I would also like to thank Dr. Darren Mason. Dr. Mason provided insightful statistical analysis of my experiment data, which elevated my PhD work to a new height. I would also like to thank him for driving from Albion to East Lansing to participate in the discussions. I would also want to express my thankfulness to my committee member, Dr. Dahsin Liu, for his constructive suggestions in completion of this work.

I would also like to thank the current and former members in the group of Professors Boehlert, Bieler, and Crimp, who have directly and indirectly helped me during the past four years, including Dr. Leyun Wang, Dr. Yiyi Yang, Dr. Zhe Chen, Mr. James Seal, Ms. Sara Longanbach, Mr. Chen Zhang, Mr. Ajith Chakkedath, and Mr. Di Kang. I would also like to thank Dr. Per Askeland for his assistance with using the SEMs. I would also like to thank those who sacrificed their time to help me in any respect during the completion of my degree.

I would like to acknowledge that the funding for this research was supported by the US Department of Energy, Office of Basic Energy Science through grant No. DE-FG02-09ER46637. I would also like to thank Mr. Thomas Van Daam of Pratt & Whitney, Rocketdyne for providing the Ti–5Al–2.5Sn and Ti-3Al-2.5V alloys used in this study and Dr. Christopher Cowen, previously at National Energy Technology Laboratory, Albany, Oregon and currently at United States Mint, West Point, NY, who provided the CP Ti and the Ti-6Al-4V alloy used in this study.

Finally, my deepest gratitude goes to my family and Bite for their understanding, support, and encouragement.

TABLE OF CONTENTS

LIST OF TABLES

LIST OF FIGURES

KEY TO SYMBOLS AND ABBREVIATIONS

2D	Two-dimensional
3D	Three-dimensional
α_p	Primary α
α_s	Secondary α
AFM	Atomic force microscopy
Al	Aluminum
ANOVA	One-way analysis of variance
APS	Advanced photon source
Approx.	Approximate
ASTM	American society for testing and materials
$\boldsymbol{b}$	Dislocation slip direction
BCC	Body center cubic
BSE	Backscattered electron
CP	Commercially pure
CPFE	Crystal plasticity finite element
Cr	Chromium
CRSS	Critical resolved shear stress
EBSD	Electron backscattered diffraction
EDM	Electrodischarge machined
ε_f	Elongation-to-failure

ε_{GBS}	GBS strain
ε_{tot}	Total strain
Fe	Iron
GBS	Grain boundary sliding
HCP	Hexagonal closed-packed
ICP-MS	Inductively coupled plasma mass spectroscopy
IPF	Inverse pole figure
m	Schmid factor
Mg	Magnesium
Mo	Molybdenum
Ms	Start of the martensite transformation
$\boldsymbol{n}$	Dislocation slip/twin plane normal
N	Nitrogen
Ni	Nickel
O	Oxygen
pct.	Percent
$\boldsymbol{\sigma}$	Applied stress
SE	Secondary electron
SEM	Scanning electron microscopy
SiC	Silicon carbide
RT	Ambient temperature
TEM	Transmission electron microscopy
Ti	Titanium

Tin	Sn
V	Vanadium
VPSC	Viscoplastic self-consistent
wt.%	Weight percent
XRD	X-ray diffraction
YS	Yield strength
Zr	Zirconium

CHAPTER 1

INTRODUCTION

1.1 Rationale and research objective

Compared with other structural metallic metals based on iron (Fe), nickel (Ni), aluminum (Al), and magnesium (Mg), titanium (Ti) stands out with the advantages of high specific strength (high strength and low density), extraordinary corrosion resistance, and the ability to withstand extreme temperatures [Leyens et al. 2003]. As shown in Table 1.1, Ti exhibits a density of ~4.5g/cm^3. Although Mg exhibits a density of ~1.8g/cm^3, the disadvantages of low corrosion resistance, low melting point (650 ℃, 923K), and relatively low yield strength (YS) make it less competitive than Ti for many structural applications. Al (~2.7g/cm^3) also exhibits the drawbacks of a low melting temperature (660 ℃, 933K) and a low YS. Fe and Ni can overcome these disadvantages but the densities are twice that of Ti.

Ti and Ti alloys are often employed in a variety of applications, including armor (high specific strength), portable electronic devices (high specific strength), biomedical devices (corrosion resistance and high specific strength), automobiles (high specific strength and the ability to withstand high temperatures), and aerospace components (high specific strength and the ability to withstand extreme temperatures) [Leyens et al. 2003]. The aerospace industry is the primary consumer of Ti and Ti alloys. Nowadays, two-thirds of all the Ti produced is used in the aerospace industry [Leyens et al. 2003]. Figure 1.1 and Figure 1.2 show examples of an aero engine and an aero gas turbine component made of Ti alloys.

The percentage of Ti and Ti alloys use in the aircraft has increased steadily in the past several decades. Since 1948, when DuPont first produced Ti commercially, there has been a

steady growth of Ti usage in the aerospace industry, specifically for aircraft engines and airframes. Figure 1.3 shows the increase of Ti usage in Boeing commercial aircrafts from the 1960s to the 2000s [Peters et al. 2003]. The weight percentage of Ti in an aircraft increased from less than 1% in the early Boeing 707 to approximately 9% in the Boeing 777. Similar percentages are also found for Airbus aircraft. The use of Ti alloys is even higher (35 to 50%) in military fighter aircraft. For the SR-71 "Blackbird", the percentage can be as high as 95% [Peters et al. 2003].

Table 1.1 Important characteristics of Ti and Ti based alloys as compared to other structural metallic materials based on Fe, Ni, Al, and Mg [Lütjering et al. 2003]

	Ti	Fe	Ni	Al	Mg
Melting Temperature (°C)	1670	1538	1455	660	650
Room Temperature Yong's Modulus E (GPa)	115	215	200	72	45
Yield Stress (MPa)	1000	1000	1000	500	130
Density (g/cm^3)	4.5	7.9	8.9	2.7	1.8
Comparative Corrosion Resistance	Very High	Low	Medium	High	Low
Comparative Price of Metal	Very High	Low	High	Medium	Medium

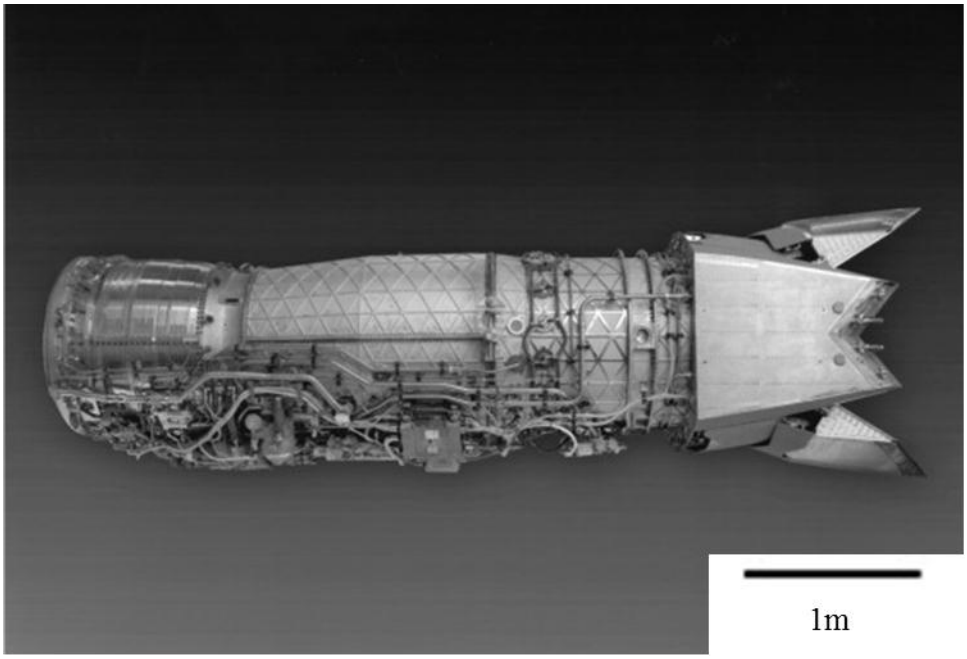

Figure 1.1 F119 engine by Pratt & Whitney powering the F22 Raptor aircraft [Donachie 1988].

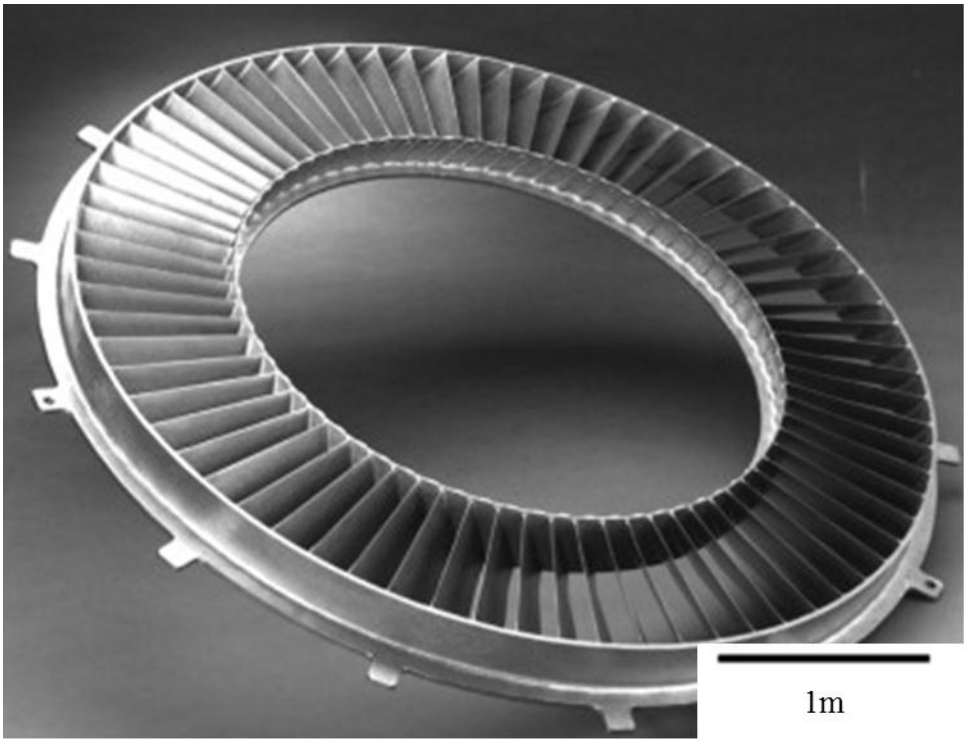

Figure 1.2 Typical Ti alloy casting for aircraft gas turbine use [Donachie 1988].

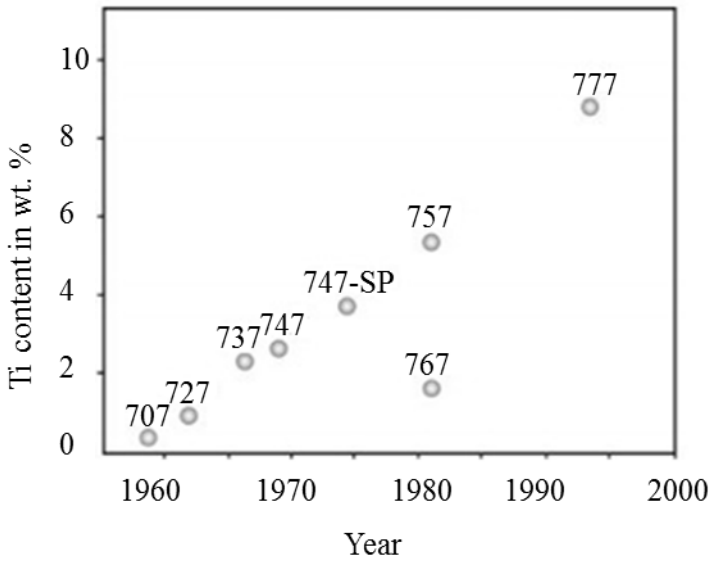

Figure 1.3 Increase in usage of Ti alloys in commercial Boeing aircraft [Peters et al. 2003].

To tailor Ti alloys to achieve a desirable combination of strength, toughness, elongation-to-failure (ε_f), and fatigue and creep resistance, various Ti alloys with different chemical compositions have been developed. Based on the composition and the resultant ambient temperature (RT) equilibrium constituent phase(s), Ti alloys are divided into four types, namely fully-α Ti, near-α Ti alloys, α+β two-phase Ti alloys, and β Ti alloys [Donachie 1988, Boyer 1996]. Each of these alloy types is used for manufacturing certain aerospace components, depending on the mechanical performance requirement. The YS of fully-α commercially-pure (CP) Ti at RT varies from 170MPa to 480MPa, depending on various interstitial and impurity levels [Donachie 1988]. This YS of CP Ti is the lowest among all of the four Ti alloy types. Thus, CP Ti is often chosen for its excellent corrosion resistance when high strength is not required. The near-α Ti alloys are categorized by their creep resistance, cold weldability, and relatively high strength as compared with CP Ti [Donachie 1988, Boyer, 1996]. The near-α Ti alloys do not exhibit a ductile-to-brittle transition, and therefore they can remain ductile at

cryogenic temperatures. The near-α alloy, Ti-5Al-2.5Sn (wt.%)[1], is often used for cryogenic temperature applications. Another common near-α alloy, Ti-3Al-2.5V, exhibits excellent cold formability and is often used for hydraulic tubing in modern aircraft [Boyer 1996]. β alloys are characterized by high hardenability and excellent forgeability, but sometimes they exhibit the disadvantage of low creep strength. In general, β alloys are often fabricated for components used for moderate-temperature applications. Two-phase α+β Ti alloys exhibit a good balance of mechanical properties, such as a high strength and stability at moderate temperature (up to 673K), good corrosion resistance, and fatigue resistance. The two-phase α+β alloy, Ti-6Al-4V, is the most used commercial Ti alloy and can be used for blades, discs, and wheels of turbine engines as well as cargo-handling and torque tubes for rakes in airframe applications [Boyer 1994].

Because Ti and Ti alloys are often used in safety critical applications, it is imperative to understand their deformation mechanisms. Furthermore, a thorough understanding of the deformation mechanisms is also required for the development of new Ti alloys with higher strengths and better damage tolerance. However, the deformation of Ti is highly heterogeneous, making the study of the deformation mechanisms of Ti more difficult than for cubic materials. The ability to characterize such heterogeneous deformation will lead to a better overall mechanistic understanding of the deformation behavior, will provide experimental results that are beneficial for modeling/simulation work, and will lead to better prediction of the material performance in polycrystalline Ti alloys.

The deformation mechanisms of hexagonal α CP Ti and hexagonal α Ti alloys have been studied over the past few decades [Bridier et al. 2005, Williams et al. 2005, Wang et al. 2010, Gong et al. 2009 and 2011]. Generally, there are three slip systems with a $<\bar{2}110>$ Burgers

[1] Henceforth, all alloy compositions are given in weight percent.

vector (*a*-type), which have been observed to slip on basal $\{0001\}$, prismatic $\{10\bar{1}0\}$, and pyramidal $\{10\bar{1}1\}$ planes. According to the von Mises criterion [Von Mises 1928], five independent slip systems are required to accommodate any arbitrary shape change during plastic deformation. Thus, in addition to the three a-type slip systems, some additional non a-type deformation mechanisms must be activated during polycrystalline deformation. Pyramidal <c+a> slip as well as four twinning systems (i.e. $\{10\bar{1}2\}\langle\bar{1}011\rangle$ T1 tensile twinning, $\{11\bar{2}1\}\langle\bar{1}\bar{1}26\rangle$ T2 tensile twinning, $\{11\bar{2}2\}\langle 11\bar{2}\bar{3}\rangle$ C1 compressive twinning, and $\{10\bar{1}1\}\langle 10\bar{1}2\rangle$ C2 compressive twinning) in α-phase Ti [Christian 1995] are additional deformation systems allow Ti to meet this requirement. Of these, pyramidal <c+a> and $\{10\bar{1}2\}\langle\bar{1}011\rangle$ T1 tensile twinning are the most commonly reported for RT deformation of CP Ti.

The ease of slip or twinning on a particular system is quantified by the critical resolved shear stress (CRSS). Researchers have investigated the CRSS or the CRSS ratios of Ti and Ti alloys under various conditions, both experimentally and computationally. However, there is no consensus on the CRSS values or ratios, as they change as a function of alloy content and testing condition. Table 1.2 shows a number of reported values for the CRSS and/or CRSS ratios for the different slip systems at RT and elevated temperatures for Ti and Ti alloys. There are significant CRSS variations even for the same nominal alloys under the same deformation temperature and testing condition [Salem et al. 2005, Wu et al. 2007, Gong et al. 2009, and Poty et al. 2011]. Much of the uncertainty in the CRSS and CRSS ratios can be attributed to the difficulty in directly measuring these parameters in non-cubic metals.

The overarching goal of this research is to understand the deformation behavior of various Ti and Ti alloys and develop a methodology of determining the CRSS ratios of the

different deformation systems under different testing conditions. A thorough knowledge of the deformation mechanisms would benefit crystal plasticity finite element (CPFE) modeling, which can help us understand and predict the damage nucleation events and subsequent deformation evolution processes, and aid in the development of Ti alloys with enhanced mechanical performance. In this dissertation, the deformation behavior of various Ti and Ti alloys were compared under various testing conditions.

Table 1.2 List of the CRSS (in MPa) and CRSS ratios (relative values) of slip systems in single-crystal and polycrystalline Ti and Ti alloys. E: experimental, S: simulated.

Materials/ testing method	Basal	Prism	Pyram <a>	Pyram <c+a>	Ref.
Single Crystal Ti [E]	209MPa	181MPa		474MPa	Gong et al. 2009
Single Crystal Ti [E]	1	0.8		2.1	Paton et al. 1973
Polycrystal CP Ti [E]		1		13 (upper bond)	Zaefferer 2003
Polycrystal CP Ti (RT) [S]	150MPa	30MPa		120MPa	Wu et al. 2007
Polycrystal CP Ti (RT) [S]	3.1MPa	4.2MPa		12MPa	Poty et al. 2005
Polycrystal CP Ti (RT) [S]	49MPa	37MPa		197MPa	Salem et al. 2005
Polycrystal Ti (1023K) [S]	1	1	1	10	Balasubramanian et al. 2002
Single Crystal Ti64(RT) [E]					Jones et al. 1981
Tension	444MPa	376MPa		441MPa	
Compression		392MPa	404MPa	631MPa	
Polycrystal Ti64 (RT) [E]					Perilla et al.1995
Tension	494MPa	395MPa	395MPa	494MPa	
Compression	513MPa			612MPa	
Polycrystal Ti64(RT) [E]	373MPa	388MPa			Bridier et al. 2005
Polycrystal Ti64(RT) [E]	<1	1			Zaefferer 2003
Polycrystal Ti64(RT) [S]	400MPa	380MPa		640MPa	Dick et al. 2006
Polycrystal Ti64 (RT) [S]	3-6	1	3-6	4-10	Fundenberger et al. 1997
Polycrystal Ti64 (RT) [S]	1	0.67	2	0.67	Dunst et al. 1996
Polycrystal Ti64 (RT) [S]	1	1	8		Lebensohn et al. 2002
Polycrystal Ti64 (1088-1228K) [E]	1	0.7		3	Bieler et al. 2002
Polycrystal Ti6246 (RT) [S]	380MPa			615MPa	Feaugas et al. 1997
Single Crystal Ti-6.6Al (RT) [E]	~1	~1			Williams et al. 2002
Polycrystal Ti8Al1Mo1V (RT) [E]	275.8MPa	206.9MPa	248.2MPa		Chan, 2004

1.2 Work performed

In this dissertation work, the deformation behavior of four different Ti and Ti alloys were studied; namely fully-α CP Ti, the near-α Ti-5Al-2.5Sn and Ti-3Al-2.5V alloys, and the two-phase α+β Ti-6Al-4V alloy. The materials were supplied by Mr. Thomas Van Daam of Pratt & Whitney Rocketdyne and Dr. Christopher Cowen (Michigan State University Chemical Engineering and Materials Science PhD graduate), previously at National Energy Technology Laboratory in Albany, Oregon, and now at the US Treasury and Mint, West point, New York.

In Chapter 2, a background on Ti is provided, including the fundamental crystal structure, alloy classification, and available deformation mechanisms. A review on the current understanding of the relative activity of the different deformation systems and the available methodologies for measuring the relative activity (i.e. relative CRSS values) is also provided.

In Chapter 3, the materials and experimental procedures used in this dissertation work are described. The bulk alloy composition and the thermomechanical processing history are provided for each material. The details of the *in-situ* specimen preparation and the *in-situ* experimental procedures are also presented. The methods used for slip/twin trace analysis and Schmid factor calculation are also provided.

In Chapter 4, the results from the microstructure and texture characterization, the *in-situ* tensile experiments, and the *in-situ* tensile-creep experiments for each of the four materials are presented. For each material, the grain size was measured using the line-intercept method based on the secondary electron (SE) or backscattered electron (BSE) images [ASTM 2004]. The Texture was characterized for each specimen using electron backscattered diffraction (EBSD). Bulk X-ray diffraction (XRD) was performed to investigate the texture of Ti-5Al-2.5Sn and Ti-3Al-2.5V. *In-situ* tensile tests were performed at 296K and 728K for each alloy. The surface

deformation evolution was captured by the *in-situ* collected SE and/or BSE images. EBSD was performed both before and after the deformation. The active deformation systems for each testing condition of each material were determined by trace analysis. *In-situ* tensile-creep tests were performed at 728K for all of the four materials, with constant creep stresses equivalent to ~75% YS at 728K. For Ti-5Al-2.5Sn, tensile-creep tests were also performed with stresses between 200-300MPa at 728-763K.

In Chapter 5, a discussion of the deformation behavior of the four materials is presented. The microstructure and texture differences among the four materials are discussed. How these differences affect the strength for each material at 296K and 728K is presented. Furthermore, the relative activity of the different deformation systems at different testing conditions for each material is compared and discussed. The relationship between the crystallographic orientations and the cracking observed during the creep of Ti-5Al-2.5Sn and Ti-6Al-4V is also discussed.

In Chapter 6, a novel methodology of estimating the CRSS ratios of the different deformation modes for Ti and Ti alloys is presented. Using this methodology, the mean CRSS ratios and the associated confidence intervals for the CRSS values of prismatic, pyramidal <a>, and pyramidal <c+a> slip and T1 twin compared to basal slip were determined.

In Chapter 7, the conclusions of this dissertation are presented and potential future work is suggested.

CHAPTER 2

BACKGROUND AND LITERATURE REVIEW

2.1 Fundamental of Ti and Ti alloys

2.1.1 Crystal structure

Ti is allotropic and therefore can be processed to exhibit more than one crystal structure. At low temperature, CP Ti exhibits a hexagonal closed-packed (HCP, α phase) crystal structure with lattice parameters of *a*=0.295nm and *c*=0.468 [Lütjering et al. 2003, Leyens et al. 2003]. This results in a smaller *c/a* ratio (1.587) than the ideal *c/a* ratio of 1.633 for the HCP structure [Lütjering et al. 2003, Leyens et al. 2003]. Upon increasing temperature to 1155±2K (β-transus temperature), the HCP α phase transforms to a body center cubic (BCC) β phase (*a*=0.332nm), following the Burger's relationship $\{0001\}_\alpha \| \{110\}_\beta$, $<11\bar{2}0>_\alpha \| <111>_\beta$ [Lütjering et al. 2003, Leyens et al. 2006, Burgers 1934]. For each of the 6 {110} planes in a β grain, there are two <111> closed packed directions. Therefore, according to the Burger's relationship, there are 12 possible orientation variants between a BCC β grain and the transformed HCP α grain. The BCC structure is in equilibrium only at temperatures above the β-transus temperature for the CP Ti. With alloying, the BCC structure can be equilibrated at lower temperatures than the β-transus temperature for the CP Ti.

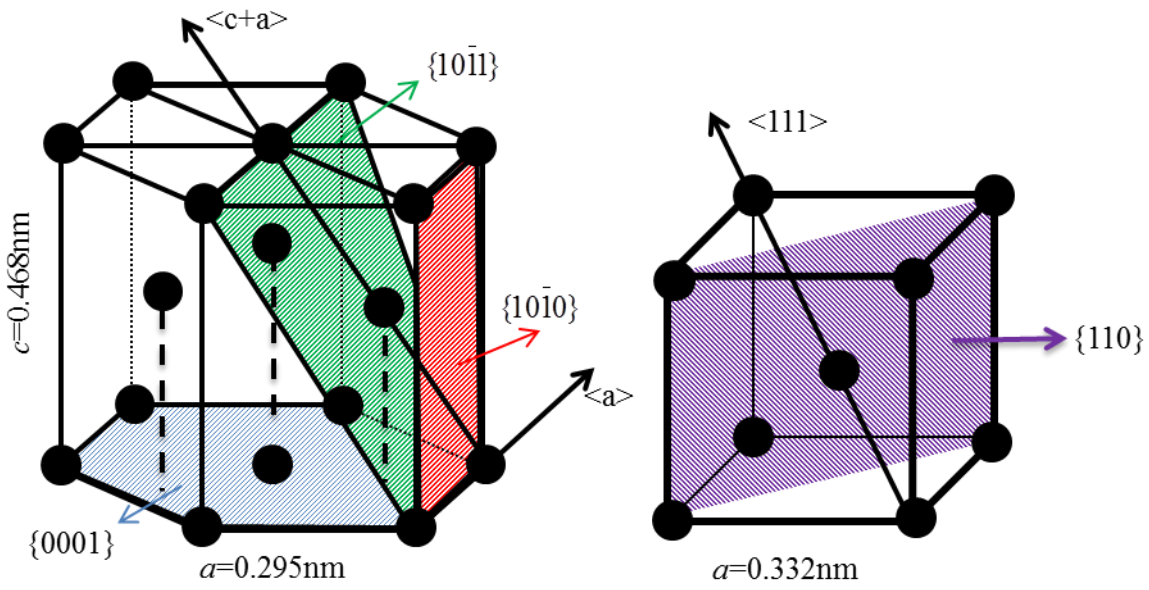

Figure 2.1 (a) Unit cell of the α phase with the lattice parameters. Selected crystallographic planes are highlighted by colors: basal plane {0001} in blue, prismatic plane {10-10} in red, and pyramidal plane {10-11} in green. (b) Unit cell of the β phase with the lattice parameter and {110} plane. For interpretation of the references to color in this and all other figures, the reader is referred to the electronic version of this dissertation.

2.1.2 Alloy classification

By adding alloying elements, the microstructure of thermomechanical processed Ti and Ti alloys can be classified as fully-α, near-α, two-phase α+β, and fully-β phase (including metastable β) [Donachie 1988, Boyer 1996]. Depending on the influence of the alloying elements on the final phase constitution, the alloying elements of Ti are classified as α-phase stabilizers, β-phase stabilizers, and/or neutral elements. Al, Oxygen (O), and Nitrogen (N) are the common α-phase stabilizers, which increase the stability of the α-phase by raising the β-transus temperature and also increase the α-phase volume fraction in the microstructure. Molybdenum (Mo), Fe, V, Chromium (Cr), and Mg are the common β-phase stabilizers as these elements decrease the β-transus temperature and increase the β phase volume fraction in the

microstructure. Tin (Sn) and Zirconium (Zr) are neutral elements and do not affect the phase stability [Donachie 1988, Boyer 1996].

The influence of the α-phase stabilizers and the β-phase stabilizers on the phase constitutions is schematically shown in the three-dimensional (3D) phase diagram in Figure 2.2 [Leyens et al. 2003]. As shown in Figure 2.2, for the fully-α phase Ti and Ti alloys, only α-phase stabilizers and/or neutral elements are added. Adding a small amount of β-phase stabilizers (1 to 2 wt.%) to the fully-α alloys results in the formation of near-α microstructures, which contain primary α phase and a small fraction of retained β phase (<5%) [Joshi 2006]. The two-phase α+β Ti alloys usually contain 4-6 wt.% β-phase stabilizers, resulting in a β volume fraction between 5-40% [Joshi 2006]. With further increases in the β-phase stabilizer level, metastable/near-β alloys (10-15 wt.% β-phase stabilizers) and single-phase β alloys (>20 wt.% β-phase stabilizers) are achieved [Joshi 2006].

Different Ti alloy groups have different mechanical properties. The α alloys usually exhibit good stability, while not being easily amenable to heat treatment for property modification. The near-α alloys have improved strength compared with unalloyed CP Ti and they also exhibit good workability. Moreover, the absence of a ductile-to-brittle transition of these near-α alloys ensures adequate ε_f at low temperatures. Therefore, near-α alloys are often used for cryogenic applications. The most popular near-α alloy is Ti-5Al-2.5Sn, which is used in numerous aerospace applications. Other near-α alloys include Ti-3Al-2.5V, Ti-2.25Al-11Sn-5Zr-1Mo-0.2Si, and Ti-8Al-1Mo-1V.

The α+β alloys are the most widely used alloy group and can be heat-treated to develop a variety of microstructures and mechanical properties. The α+β alloys usually contain both α-

phase stabilizers and β-phase stabilizers. The most commonly researched and commercially used α+β alloys are Ti-6Al-4V and Ti-6Al-2Sn-4Zr-6Mo.

The mestastable β and β alloys generally exhibit high toughness, excellent hardenability, and good forgeability. However, these alloys exhibit a ductile-to-brittle transformation and therefore are not suitable for low temperature applications. Some commercial metstable β alloys include Ti-15Mo-5Zr, Ti-15Mo-5Zr-3Al, and Ti-11Mo-6Zr-4.5Sn.

Figure 2.4 summarizes the general understanding of the characteristics of the different Ti groups [Donachie 1988]. As shown in Figure 2.4, the α alloys tend to exhibit higher β-transus temperatures, higher flow stresses, better weldability, and higher elevated-temperature strength than the near-β and β alloys. On the other hand, with increased β-phase stabilizers, the near-β and β alloys tend to exhibit better formability, higher strain-rate sensitivity, better heat treatment capacity, and higher RT strengths than the α alloys but suffer from the lack of good creep strength. Nevertheless, the two-phase α+β Ti-6Al-4V alloy exhibits a good balance of properties and is the most widely used Ti alloy.

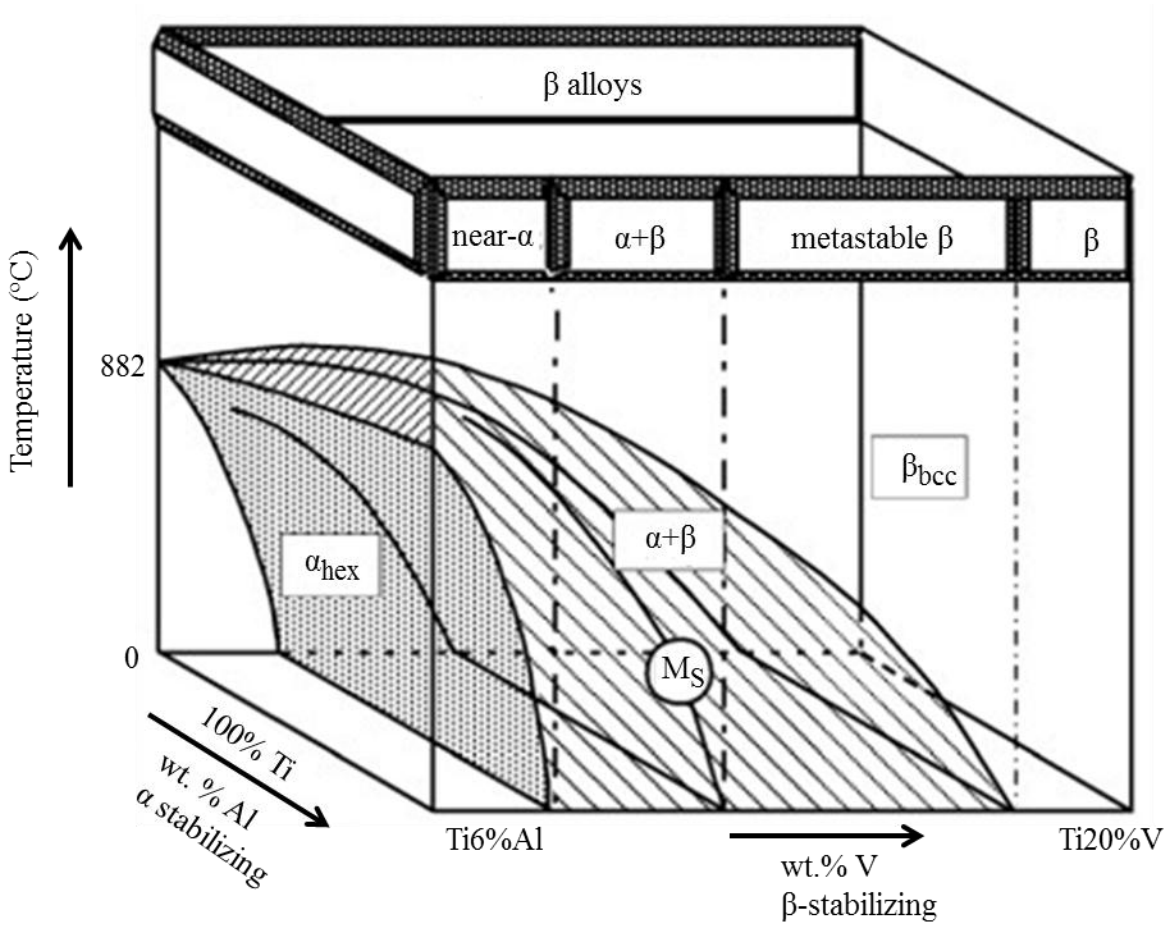

Figure 2.2 3D phase diagram used to classify Ti alloys (schematically). M_S refers to the start of the martensite transformation [Leyens et al. 2003].

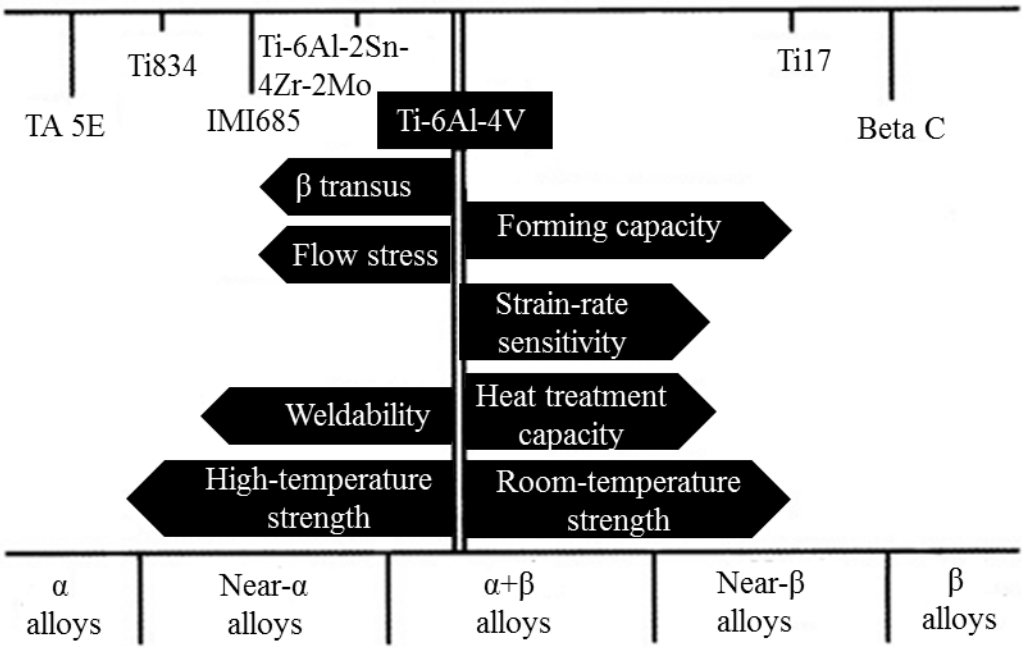

Figure 2.3 Characteristics of different Ti alloy groups [Donachie 1988].

In the next section, some substitutional and interstitial elements related to the Ti and Ti alloys studied in this dissertation work will be introduced.

(a) Al additions

Al is a substitutional α-phase stabilizer and is the most widely used alloying element in Ti alloys. The addition of Al can raise the β-transus temperature and strengthen the α phase by substitutional solid-solution strengthening. Al also has a large solubility in Ti. To avoid precipitation of the Ti_3Al intermetallic phase at RT, the Al content in Ti alloys is usually restricted to 7 wt.% [Joshi 2006]. Figure 2.4 shows the Ti-Al binary phase diagram [Massalski et al. 1990]. With increased Al content, different intermetallic compounds can be formed, including Ti_3Al, TiAl, and $TiAl_3$. The Ti_3Al phase has a DO_{19} ordered hexagonal crystal structure. The TiAl phase has a $L1_0$ ordered tetragonal crystal structure. The $TiAl_3$ phase has a

$D0_{22}$ body-centered tetragonal crystal structure. The alloys investigated in this dissertation work had a maximum of 6 wt. % Al, inhibiting the intermetallic-phase formation.

Adding Al content results in an increase of the *c/a* ratio and leads to a more closed packed basal plane. The atomic radius of Al (0.125nm) is smaller than Ti (0.176nm) [Clementi et al. 1963], which leads to a compression of the HCP unit cell when Ti is substituted with Al atoms. Studies [Teer et al. 1977, Buckley et al. 1966] have shown that Al addition results in an increase of the *c/a* ratio, see Figure 2.5. The *c/a* ratio of CP Ti is 1.587, which increases to approximately 1.595 with 5 wt.% Al [Teer et al. 1977]. As the *c/a* ratio increases with increasing Al content, the basal plane becomes more closely packed and thus more favorable for slip, while the prismatic plane becomes less close-packed and less favorable for slip.

Increases in Al content also result in a decrease in the stacking fault energy on the basal planes. Guo et al. [2006] found that the stacking fault energy decreases from 0.31 J/m^2 for CP Ti to 0.082J/m^2 for Ti-5.3Al (wt.%). Zaefferer [2003] found that the increase in Al content results in a decrease in the stacking fault energy on the basal planes, and as a consequence, dislocation movement is increasingly restricted to the basal planes when increased Al contents are presented.

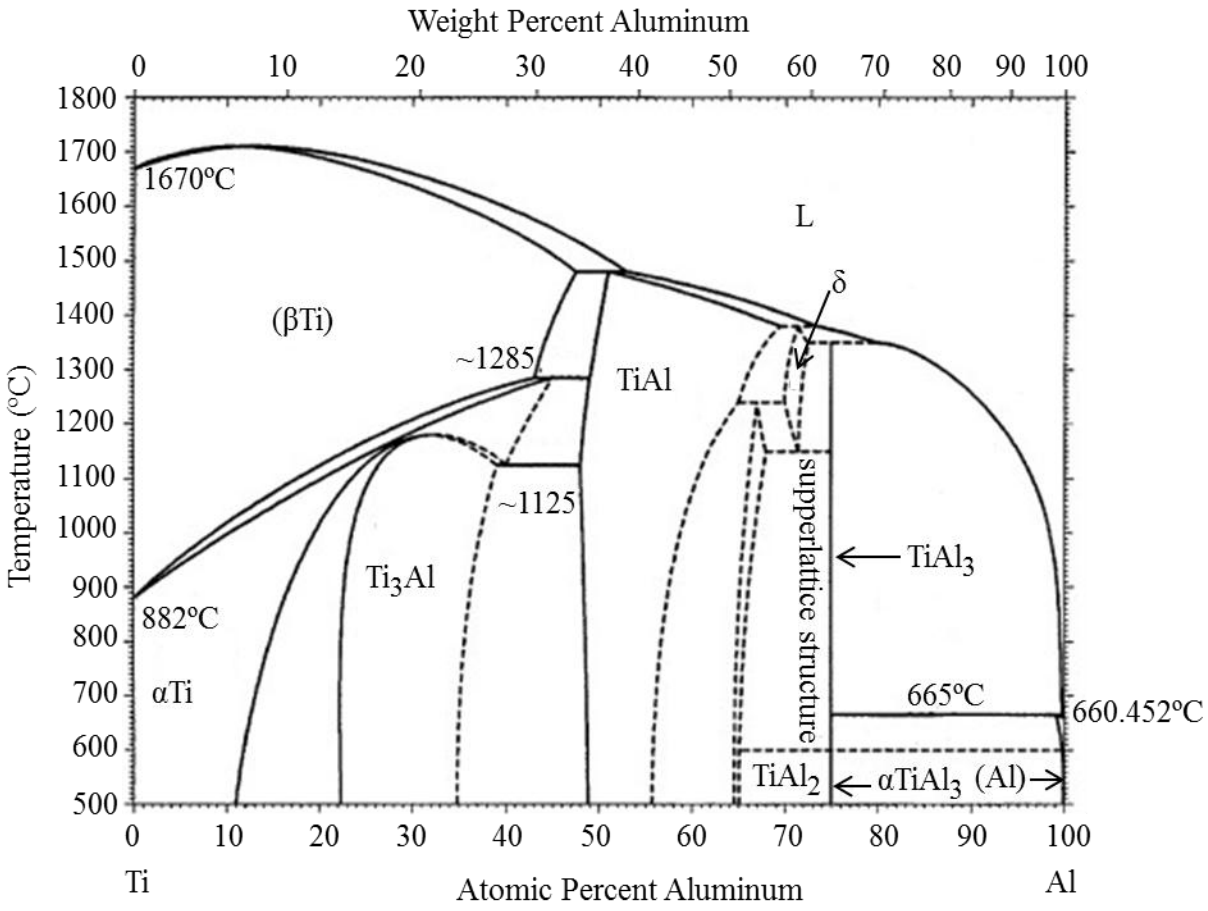

Figure 2.4 Ti-Al phase diagram [Massalski et al. 1990].

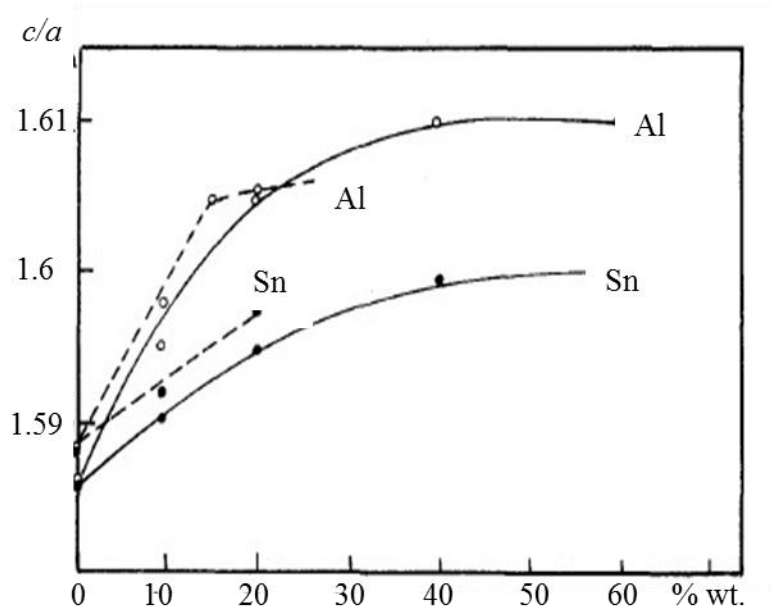

Figure 2.5 The effect of Al on the c/a ratio of Ti alloys [Teer et al. 1977, Buckley et al. 1966].

(b) V additions

V is an important substitutional β-phase stabilizer for Ti alloys. V decreases the β-transus temperature, increases the strength, and plays an important role in controlling the microstructure and properties of Ti alloys [Donachie 1988]. V has a similar atomic radius (0.171nm) to that of Ti (0.176nm) [Clementi et al. 1963]. The effect of V content on the *c/a* ratio has not been reported yet. Because the atomic radius difference between Ti and V (Δradii=0.005nm) is 10 times smaller than the same difference between Ti and Al (Δradii=0.051), the effect of V content on the *c/a* ratio is not expected to be as significant as the effect of Al content. Unlike the Ti-Al system, there is no intermetallic compound formation between Ti and V, see Figure 2.6.

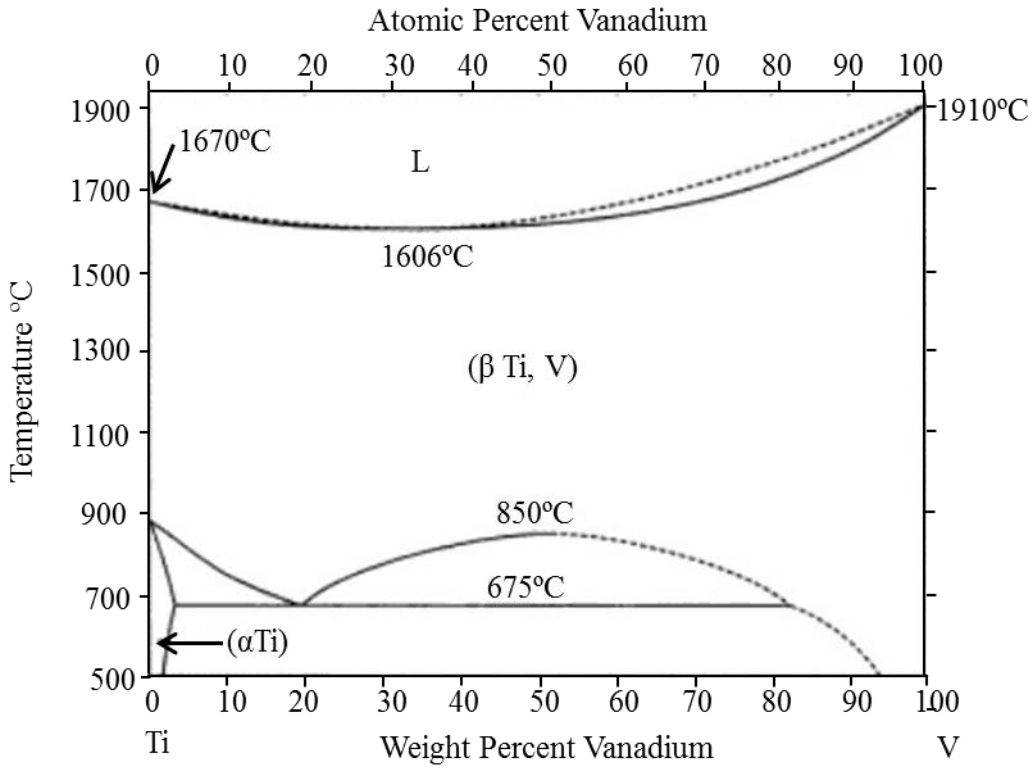

Figure 2.6 Ti-V phase diagram [Okamoto, 2000].

(c) Sn additions

Sn is a substitutional neutral element for Ti alloys. Sn does not stabilize either the α or the β phase, but it can strengthen Ti alloys by providing solid-solution strengthening. Sn has an atomic radius of 0.145nm, which is smaller than Ti (0.176nm). When Ti is substituted by Sn atoms, the HCP unit cell shrinks. As shown in Figure 2.5, Sn addition results in an increased *c/a* ratio [Teer et al. 1977, Buckley et al. 1966]. For the same weight percent of Al and Sn additions in Ti alloys, the increase of the *c/a* ratio due to Sn is not as dramatic as that when Al is added to Ti. Sn has a large solubility in Ti. Figure 2.7 shows the Sn-Ti binary phase diagram [Murray 1987]. There is no new phase formed in Ti until 15 wt.% of Sn is added. For all the alloys investigated in this dissertation work, the maximum weight percent of Sn was 2.5%. Therefore,

the complex intermetallic compounds formed between Ti and Sn, such as $SnTi_3$ and $SnTi_2$, were avoided.

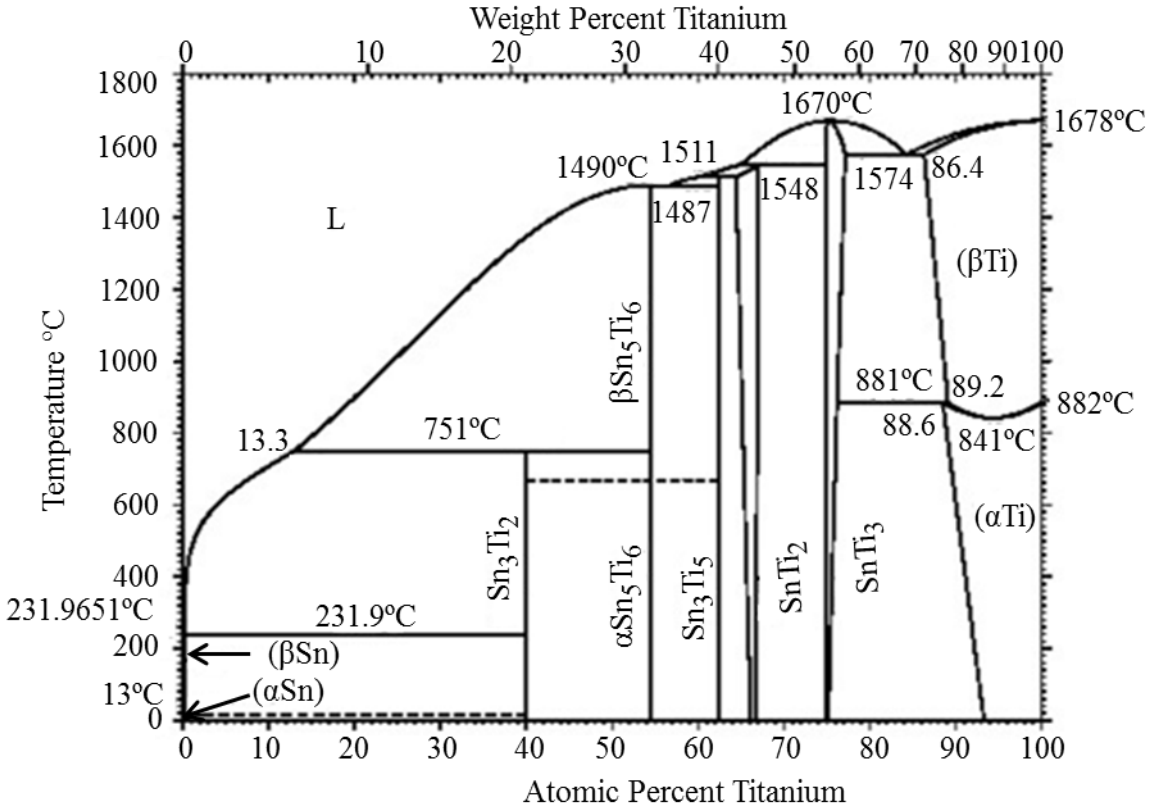

Figure 2.7 Sn-Ti phase diagram [Murray 1987].

(d) O additions

O is one of the most important interstitial α-phase stabilizers. O can improve the strength of Ti and Ti alloys. Table 2.1 lists four grades of unalloyed Ti with the corresponding chemical compositions and mechanical properties [Lütjering et al. 2003]. The YS increases from 170MPa for grade 1 CP Ti to 480MPa for grade 4 CP Ti [Lütjering et al. 2003]. Although Fe and N also vary between the different CP Ti grades, the principal difference is the oxygen concentration, which increases from 0.18wt.% for grade 1 to 0.40wt.% for grade 4 [Lütjering et al. 2003].

O also has high solubility in Ti. The maximum O solubility in Ti is about 1.7 wt.% without forming any short range ordering [Wasz et al. 1996]. For low O concentrations in CP Ti, the interstitial O is randomly distributed in the octahedral positions in the HCP Ti lattice [Churchman 1954]. Some studies have reported that O interstitials increase the lattice parameters as well as the *c/a* ratio for HCP Ti [Murry et al. 1987, Ottaviani et al. 1987]. Nevertheless, the extent of such increase in the lattice parameters and the *c/a* ratio due to O content is not clear yet.

Low O additions can also affect the deformation mechanism. Low oxygen is known to enhance twinning [Zaefferer 2003]. Zaefferer [2003] reported that Ti with 1000ppm (0.1 wt.%) oxygen exhibits larger twinning activity than Ti with 2000ppm (0.2 wt.%) oxygen. Churchman [1954] stated that the interstitial O atoms are more likely to interfere with dislocation motion in the basal and prismatic planes rather than the pyramidal planes. Therefore, increasing O concentrations can decrease the relative CRSS values for pyramidal slip compared with prismatic and basal slip. Welsch et al. [1982] found that planar pyramidal slip occurs in Ti-6Al-4V with 0.19 wt.% O while 0.07 wt.% O in the same alloy was not sufficient to promote pyramidal slip.

Table 2.1 Tensile strengths and impurity limits for different American Society for Testing and Materials (ASTM) CP Ti grades [Boyer et al. 1994].

ASTM grade	Maximum impurity limits, wt.% O	Fe	H	N	C	Minimum Tensile Strength (MPa)	YS (MPa)
Grade 1	0.18	0.20	0.015	0.03	0.10	240	170-310
Grade 2	0.25	0.30	0.015	0.03	0.10	354	275-450
Grade 3	0.35	0.30	0.015	0.05	0.10	440	380-550
Grade 4	0.40	0.50	0.015	0.03	0.10	550	480-655

2.2 Deformation mechanisms

2.2.1 Dislocation slip

Generally, there are three slip systems with a $<\bar{2}110>$ Burgers vector (*a*-type), which have been observed to slip on basal $\{0001\}$, prismatic $\{10\bar{1}0\}$ and first-order pyramidal $\{10\bar{1}1\}$ planes. According to the von Mises criterion [Von Mises 1913], five independent slip systems are required to accommodate any arbitrary shape change during plastic deformation. Thus, in addition to the three *a*-type slip systems, additional non *a*-type deformation mechanisms must be activated in order to allow arbitrary shape changes. Therefore, pyramidal <c+a> slip systems need to be activated to meet the von Mises criterion. Basal, prismatic, pyramidal <a>, and pyramidal <c+a> slip systems are the most common slip systems in HCP Ti, as shown in Figure 2.8.

The ease of slip on a particular system is quantified by the CRSS. Researchers have investigated the CRSS or the CRSS ratios of Ti and Ti alloys under various conditions, both experimentally and computationally. However, there is no consensus on these values or ratios, particularly as they change as a function of alloy content and testing conditions.

As shown before in Table 1.2, the reported values for the CRSS and/or CRSS ratios for the different slip systems at RT and elevated temperatures for Ti and Ti alloys vary significantly, even for the same nominal alloys under the same deformation temperatures and testing conditions. For CP Ti, although the CRSS values measured at RT vary significantly, there is general agreement that prismatic slip is easier to activate than other deformation modes, and that basal slip is more easily activated than pyramidal <c+a> slip [Yoo et al. 1981, Gong et al. 2009, Conrad 1981, Akhtar et al. 1975, Zaefferer 2003, Williams et al. 2002]. Conrad [1981] and Akhtar [Akhtar et al. 1975] both found that this trend continued up to 1100K. Table 2.2 also

indicates that compared with CP Ti, alloys with Al additions have increased CRSS values for both basal and prismatic slip systems. For CP Ti, the CRSS of basal and prismatic slip were measured to be 209 MPa and 181 MPa [Gong et al. 2009], respectively, but increased to 373 MPa and 388 MPa for Ti-6Al-4V [Bridier et al. 2005] and 276 MPa and 207 MPa for Ti-8Al-1Mo-1V [Chan 2004].

The relative activity of basal and prismatic slip changes with alloying. Although prismatic slip remains the most easily activated slip system in CP Ti, basal slip tends to be more easily activated in the near-α and α+β alloys [Zaefferer 2003, Bridier et al. 2005, Williams et al. 2002]. Studies have shown that both Al and Sn additions result in an increase of the *c/a* ratio [Teer et al. 1977, Buckley et al. 1966], i.e. towards the ideal *c/a* ratio of 1.633 [Lütjering et al. 2003] (see Figure 2.5). Thus, a more close-packed basal plane is expected in the alloys containing Al and Sn compared to CP Ti. This can help account for more favorable basal slip with increasing Al and Sn.

Although it is known that basal slip is more favored in alloys compared with CP Ti, the relative CRSS values of basal slip and prismatic slip remain elusive. Conflicting results have been reported on how the CRSS values of prismatic and basal slip systems are affected by alloying. This is illustrated for Ti-6Al-4V, where in some cases, the CRSS of basal slip is reported to be lower than prismatic slip [Zaefferer 2003, Bridier et al. 2005]. However, others have reported that basal slip exhibits a higher CRSS than prismatic slip in Ti-6Al-4V at both RT [Jones et al. 1981, Perilla et al. 1995, Fundenberger et al. 1997, Dick et al. 2006] and between 1088K-1288K [Bieler et al. 2002].

Temperature also plays an important role in the relative activation of basal and prismatic slip systems. Williams et al. [2002] showed that increasing temperature leads to a decrease in

the CRSS of both basal and prismatic slip for single crystal α Ti-Al alloys with compositions ranging from Ti-1.4Al to Ti-6.6Al, but this decrease was more dramatic for the basal slip. Therefore, the CRSS of the basal slip decreases more rapidly with increasing temperature than that for prismatic slip.

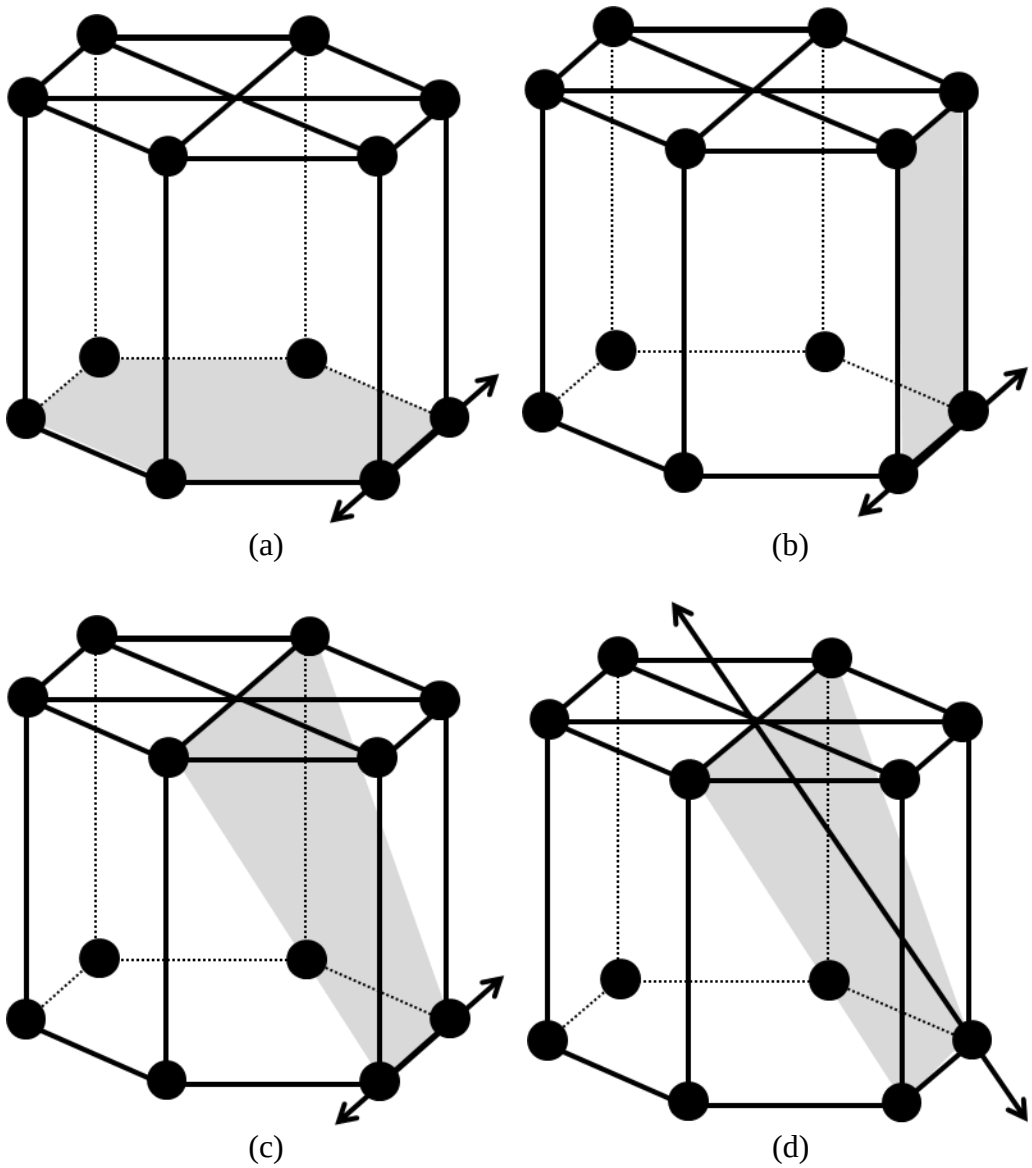

Figure 2.8 (a) $\{0001\}<\bar{2}110>$ basal, (b) $\{10\bar{1}0\}<\bar{2}110>$ prismatic, (c) $\{10\bar{1}1\}<\bar{2}110>$ pyramidal <a>, and (d) $\{10\bar{1}1\}<1\bar{2}13>$ pyramidal <c+a> slip systems in HCP Ti. The arrows only indicate the slip directions, not the magnitudes of the dislocation slip.

2.2.2 Twinning

In addition to dislocation slip, twinning contributes to the deformation. In tension, $\{10\bar{1}2\}\langle\bar{1}011\rangle$ T1 twinning and $\{11\bar{2}1\}\langle\bar{1}\bar{1}26\rangle$ T2 twinning may be activated [Christian et al. 1995]. Compression loading may lead to $\{11\bar{2}2\}\langle 11\bar{2}\bar{3}\rangle$ C1 twinning and $\{10\bar{1}1\}\langle 10\bar{1}2\rangle$ C2 twinning formation [Christian et al. 1995]. These four twinning modes are illustrated in Figure 2.9. When the maximum principal stress direction is oriented close to the crystal c-axis, either pyramidal <c+a> slip and/or twinning systems will have high Schmid factors, i.e. high resolved shear stress than basal and prismatic slip systems, which allows easier twinning and/or pyramidal <c+a> slip activation. Each type of twinning mode has a unique misorientation angle and rotation axis with respect to the parent orientation, as summarized in Table 2.2 [Christian et al. 1995]. In Table 2.3, the twinning shear is the shear that is required to restore the lattice in a new orientation [Bevis et al. 1968]. The lower the value, it is easier for the twin to form. Of the four types of twinning modes listed in Table 2.3, the most commonly observed twinning system at RT for CP Ti is T1 tensile twinning, due to its relatively low magnitude of shear (0.171). T1 tensile twinning is also the most frequently observed twinning mode in other HCP metals, such as Mg and Zr [Song et al. 1995, Bringert et al. 2002, Stanford et al. 2008, and Boehlert et al. 2012].

The Schmid factor influences twin activation, but it is not the only factor that influences twin activation. Generally, twinning is often observed in grains that exhibit high Schmid factors for twinning systems [Yang et al. 2011, Li et al. 2013]. Recently, Beyerlein et al. investigated the mechanical twinning in Mg, where they observed 8550 twins in 2000 grains [Beyerlein et al. 2010]. They found that about ~20% of the activated twins exhibited Schmid factors below 0.2, and these twins were the twins with the highest Schmid factors. Combining the twin nucleation observations and simulation studies, slip transfer is probably a key factor in twin nucleation at

grain boundaries, as slip transfer was associated with almost half of the observed twin nucleation events in CP Ti [Wang et al. 2010, and 2012, Bieler et al. in press 2013]. However, identification of subsurface twin and slip observations is difficult, particularly in a non-destructive manner, which make verification of the fraction of twins arising from slip transfer challenging. Recently, using 3D tomographic XRD, Bieler et al. [2013] observed that of three twins studied, two could have been formed as a result of slip transfer. The effect of slip transfer on twin nucleation at grain boundaries may be as influential as the Schmid factor.

Several other factors, including temperature and alloying additions, have also been reported to affect the twinning activation. Low O content also promotes twinning activity [Zaefferer 2003], as stated in section 2.1.2. Extensive twin activity was found during RT four-point bending of polycrystalline CP Ti [Yang et al. 2011, Wang et al. 2010] and 728K tensile tests of polycrystalline CP Ti [Li et al. 2013], even at the onset of the plastic deformation. Twinning has also been observed at 1088K in polycrystalline CP Ti [McHargure et al. 1953]. It is generally agreed that the twinning activity decreases with increasing temperature as well as decreases with increasing Al content [Williams et al. 2002]. A lack of twinning has been reported for Ti-Al alloy single crystals with more than 5 wt.% Al content [Williams et al. 2002]. Paton et al. [1976] stated that Ti alloyed with 6 wt.% Al does not twin, even at temperatures at low as 100K. Therefore, it appears that twinning in Ti alloys containing more than 5 wt.% Al, such as Ti-6Al-4V, is much more difficult than in CP Ti. However, for Ti-6Al-4V, twinning has been reported during deformation under very high strain rates of 1000 s^{-1} [Johnson et al. 2003] and 1 s^{-1} [Yapici et al. 2006] as well as for a low strain rate of 10^{-6} s^{-1}[Prakash et al. 2010]. Twinning has also been reported for monotonic tensile deformation of Ti-6Al-4V at 20K (no

strain rate value was given) [Di Iorio et al. 2004 and 2007]. Thus, the factors influencing twinning activity in Ti-6Al-4V are not completely understood yet.

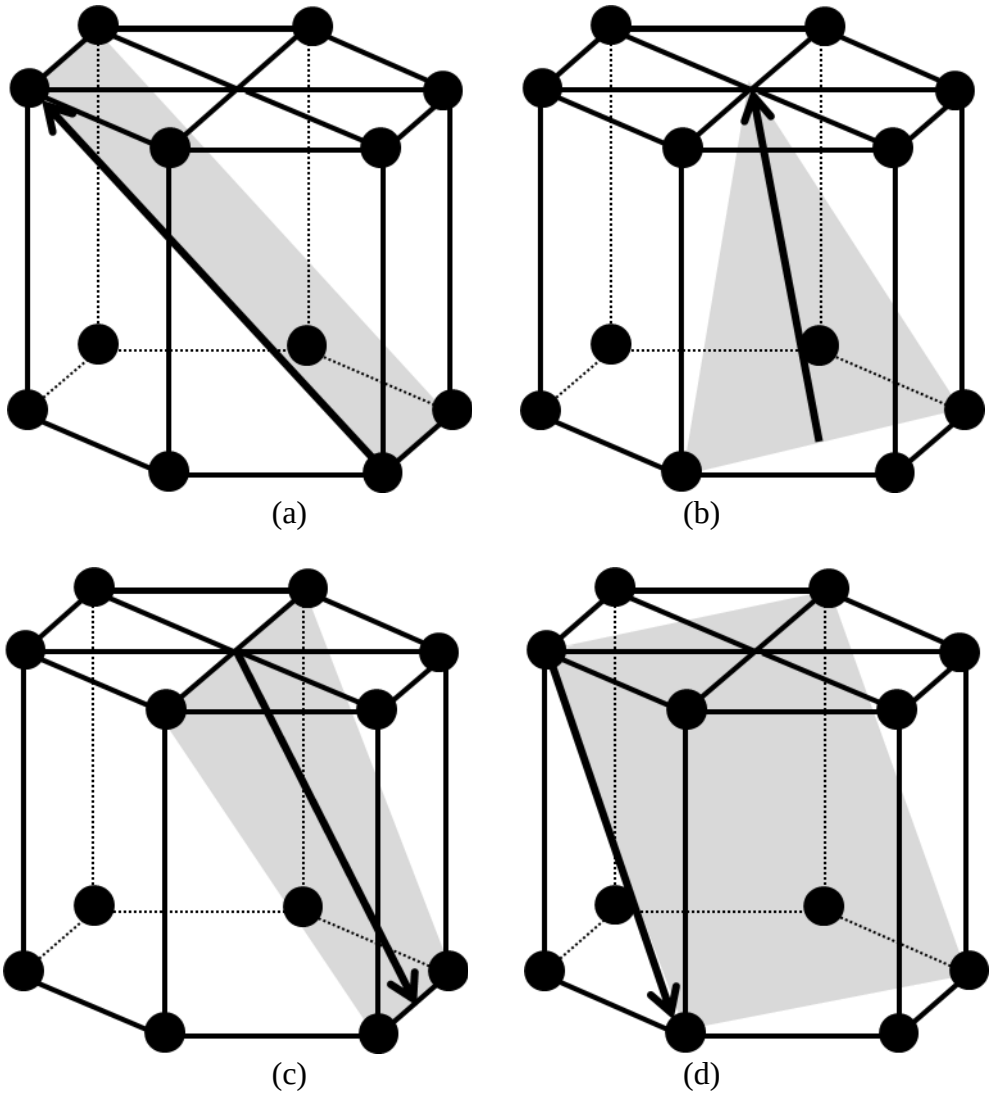

Figure 2.9 (a) $\{10\bar{1}2\}\langle\bar{1}011\rangle$ T1 twinning, (b) $\{11\bar{2}1\}\langle\bar{1}\bar{1}26\rangle$ T2 twinning, (c) $\{11\bar{2}2\}\langle 11\bar{2}\bar{3}\rangle$ C1 twinning, (d) $\{10\bar{1}1\}\langle 10\bar{1}2\rangle$ C2 twinning systems in HCP Ti. The arrows only indicate the twinning directions, not the magnitudes of the twinning.

Table 2.2 Deformation twinning modes in HCP Ti [Christian et al. 1995].

Mode	Twinning system	Misorientation	Twin shear
T1	$\{10\bar{1}2\}\ \langle\bar{1}011\rangle$	$85^{\circ}\langle 1\bar{2}10\rangle$	0.171
T2	$\{11\bar{2}1\}\ \langle\bar{1}\bar{1}26\rangle$	$35^{\circ}\langle\bar{1}100\rangle$	0.629
C1	$\{11\bar{2}2\}\langle 11\bar{2}\bar{3}\rangle$	$65^{\circ}\langle\bar{1}100\rangle$	0.221
C2	$\{10\bar{1}0\}\langle 10\bar{1}2\rangle$	$54^{\circ}\langle\bar{1}2\bar{1}0\rangle$	0.101

2.2.3 Grain boundary sliding

Grain boundary sliding (GBS) is a shear process where grains in polycrystalline microstructures move relative to each other along the grain boundary interface [Dieter 1986]. GBS is a deformation mode distinct from dislocation slip and twinning and it is especially important at elevated temperatures [Gifkins 1976]. GBS must be accommodated by diffusion- or dislocation-controlled deformation mechanisms. Based the accommodation mechanism, there are two distinct types of GBS, diffusion-controlled Lifshitz sliding and dislocation-controlled Rachinger sliding [Langdon 2006].

Lifshitz sliding is prevalent during Nabarro-Herring and Coble diffusional creep and refers to the boundary movements that develop as a consequence of stress-directed vacancies diffusion [Lifshitzi 1963, Langdon 2006]. The shapes of grains are elongated after Lifshitz sliding.

Rachinger sliding occurs by dislocation glide or dislocation climb [Rachinger 1952, Ishiday et al 1967, Langdon 2006]. The components of the Burgers vectors parallel to the grain boundary contribute to shear parallel to the boundary. Both grain boundary dislocations and lattice dislocations can be involved in this GBS process. In Rachinger sliding, adjacent grains become visibly displayed with respect to each other and the original grain shape is retained during the deformation [Rachinger 1952].

Although the Lifshitz sliding and the Rachinger sliding are intrinsically different, they exhibit similar offsets at grain boundaries [Langdon 2006]. By comparing the grain shapes before and after the deformation, these two GBS can be distinguished. The grain shape remains the same for the Rachinger sliding, while the Lifshitz sliding leads to grain elongation in the loading direction [Langdon 2006]. Nevertheless, it is reasonable to believe that experimentally-observed GBS is a result of a combination of these two mechanisms [Cannon et al. 1973].

There are a number of approaches to measure the amount of GBS on a sample's surface. Using a polished surface scribed with fiducial marker lines, the amount of GBS can be determined by measuring the relative offsets in the fiducial marker lines [Dieter 1986]. The magnitude of GBS can also be determined using two-beam interferometry to measure the sliding offsets perpendicular to the specimen surface [Ayensu et al. 1996]. If the grain boundary vertical offsets are smaller than several micrometers (±2.5μm), the offsets can be measured using atomic force microscopy (AFM) [Clarisse et al. 1999]. When offsets become large and are beyond the maximum vertical range of AFM, the vertical offsets can be determined by focusing on the grains on each side of a grain boundary to measure the change of working distance using a digital microscope with a fine-focus knob [Gifkins 1994]. By measuring the amount of sliding for a number of grain boundaries using the techniques above, the mean amount of sliding, with a standard error, can be obtained.

GBS strain (i.e. strain accommodated by GBS, ε_{GBS}) can be estimated using equation:

$$\varepsilon_{GBS}=s/d \tag{2.1}$$

where s is the average step height of GBS in sample surface normal direction and d is the average grain size [Barnett et al. 2009]. The contribution of GBS to the total deformation can be

estimated by taking the ratio $\varepsilon_{GBS}/\varepsilon_{tot}$ (the contribution of GBS to the deformation), where ε_{tot} is the total axial strain of the deformed microstructural patch [Gifkins 1994]. In this manner, the relative amount of GBS for various materials under different testing conditions can be compared.

The GBS activity can be affected by several factors. A decrease in grain size results in an increase in the magnitude of GBS [Zelin et al. 1992, Koike et al. 2003]. This is simply due to the fact that a smaller grain size leads to a larger total number of grain boundaries, which allows more chances for slip or diffusion to occur along the grain boundaries and therefore enhances the extent of GBS. Ashby and Crossman found that GBS became more extensive with decreasing stress at constant temperature [1975]. A similar conclusion was made by Lütthy et al. [1979].

2.3 Current methods and difficulties of measuring the CRSSs

As stated in section 2.2.1, there are conflicting results about the CRSS ratios of Ti and Ti alloys and much of the uncertainty in the CRSS and CRSS ratios in these Ti alloys can be attributed to the difficulty in directly measuring these parameters in non-cubic metals using traditional single-crystal approaches. To date, CRSS values and ratios have been measured using single crystals for CP Ti [Gong et al. 2009, Paton et al. 1973], Ti–1.4Al [Williams et al. 2002], Ti–2.9Al [Williams et al. 2002], Ti–5Al [Williams et al. 2002], Ti-6Al-4V [Jones et al. 1981], and Ti-6.6Al [Williams et al. 2002] at temperatures ranging from 295K to 1000K. However, depending on the relative CRSS values, it is not always possible to determine these values for all slip systems using conventional uni-axial tests. This is because even with high Schmid factors it can be difficult or impossible to initiate slip on some systems if the CRSS is much lower on other systems. Furthermore, many commercial structural metals are polycrystalline and/or multiphase

materials and are often not available in single crystal form, making traditional approaches difficult.

A number of alternative approaches have been taken to determine CRSS values. Nano-indentation of grains within a polycrystal, combined with CPFE simulations, has been used to quantitatively determine the CRSS for different slip systems for CP Ti [Zambaldia et al. 2012, Yang 2011]. By optimizing the simulations of the nano-indentation behavior in different grains with different orientations, CRSS values have been determined using an optimization procedure by constraining the CRSS values to account for the topographic results measured experimentally.

Although the activation of deformation systems in polycrystals is complicated by the constraints associated with neighboring grains, studying polycrystalline deformation may provide a means for understanding deformation systems that are difficult to activate. A viscoplastic self-consistent (VPSC) model has also been used to study the deformation of Ti alloys and determine the CRSS values [Dunst et al. 1996, Lebensohn et al. 1997]. However, even for a simplified model, simulations require a vast number of computations, limiting the technique. Using a global stress state tensor, Zaefferer [2003] calculated the relative resolved shear stresses for the different deformation systems for CP Ti without simulations. The same author also estimated the upper bound of the CRSS ratios of different slip systems by calculating the ratios of the Schmid factors of activated and non-activated slip systems [Zaefferer 2003]. The relative CRSSs were determined for individual grains with visible slip bands, based on the Schmid factors of the activated slip system and each inactivated slip system. Different CRSS ratios were obtained from different grains with different orientations, showing significant variations in the relative CRSS values.

In the present study, instead of calculating the CRSS ratios for individual grains, an optimization methodology was developed to compute the CRSS ratios. This technique minimizes the difference between the observed and expected number of observations (accounting for texture) of activated deformation systems in all of the grains from a given microstructure patch. This calculation provides one set of CRSS ratios for a given testing condition and given microstructural patch, and with statistical analysis, the confidence of this set of computed CRSS values is assessed. The confidence in this method depends on the assumption that a large number of slip observations is sufficient to represent the average behavior of material, and thereby overcome the fact that the local stress tensor in some grains (or parts of grains) can differ significantly from a global uniaxial stress tensor.

CHAPTER 3

EXPERIMENTAL PROCEDURES

3.1 Material

The bulk chemical compositions of CP Ti, Ti-3Al-2.5V, and Ti-6Al-4V were measured using optical emission spectroscopy by NSL Analytical (Cleveland, OH). The bulk chemical composition of Ti-5Al-2.5Sn was measured by inductively coupled plasma mass spectroscopy (ICP-MS) in Spain. Table 3.1 lists the chemical composition of the four materials.

3.1.1 CP Ti

The CP Ti was provided by the National Energy Technology Laboratory in Albany, Oregon, and was made using the Armstrong process to produce the original sponge that was compacted into an electrode and melted. The resulting 150mm diameter ingot had been triple vacuum arc remelted, and then upset forged, forge flattened, and squared before rolling. The forging steps were performed above the β transus temperature, while the rolling passes were performed at temperatures below the β transus. The measured bulk chemical composition of the CP Ti was (in weight percent) 0.25% O, <0.09% V, <0.025% Fe, 0.01% C, <0.01% Al, 0.0069% N, 0.0008% H, with the balance being Ti. The chemical composition suggested that the CP Ti was grade 2.

3.1.2 Ti-5Al-2.5Sn

The Ti-5Al-2.5Sn alloy was provided by Pratt & Whitney, Rocketdyne and had been forged in the upper half of the α+β phase field. The forged material had been given a 1227K

recrystallization anneal for 1 hour followed by air cooling, and a subsequent vacuum anneal at 1033K for 4 hours which was used to reduce the hydrogen content. The measured bulk composition of the alloy was (in weight percent) 4.7% Al, 2.7% Sn, 0.2% Fe, 0.1% Zn, with the balance being Ti.

3.1.3 Ti-3Al-2.5V

The Ti-3Al-2.5V alloy examined in this study was provided by Pratt & Whitney, Rocketdyne. Two plates with significantly different textures were examined in this work. The measured bulk chemical composition of plate 1 was (in weight percent) 2.86% Al, 2.63% V, 0.18% Fe, 0.085% O, 0.015% C, 0.0033% N, 0.0017% H, with the balance being Ti. The measured bulk chemical composition of plate 2 was (in weight percent) 2.89% Al, 2.49% V, 0.18% Fe, 0.092% O, 0.0097% C, 0.0040% N, 0.0024% H, with the balance being Ti.

3.1.4 Ti-6Al-4V

The Ti-6Al-4V was provided by the National Energy Technology Laboratory in Albany, Oregon. The measured bulk chemical composition of the as-received Ti-6Al-4V alloy was (in weight percent) 5.90% Al, 4.06% V, 0.24% O, 0.031% Fe, 0.019% C, 0.0078% N, 0.0019% H, with the balance being Ti.

Table 3.1 Chemical composition of the raw materials (wt.%, in descending order).

(a) CP Ti

O	C	V	Fe	Al	N	H	Ti
0.25	0.01	<0.09	<0.025	<0.01	0.0069	0.0008	Balance

(b) Ti-5Al-2.5Sn

Al	Sn	Fe	Zn	Ti
4.7	2.7	0.2	0.1	Balance

(c) Ti-3Al-2.5V

	Al	V	Fe	O	C	N	H	Ti
Plate 1	2.86	2.63	0.18	0.085	0.0115	0.0033	0.0017	Balance
Plate 2	2.89	2.49	0.18	0.092	0.0097	0.0040	0.0024	Balance

(d) Ti-6Al-4V

Al	V	O	Fe	C	N	H	Ti
5.90	4.06	0.24	0.031	0.019	0.0078	0.0019	Balance

3.2 Microstructural characterization

3.2.1 Metallography preparation

Prior to deformation, specimens were mechanically polished. The specimens were first polished using silicon carbide (SiC) grinding papers through 400, 600, 1200, 2400, and 4000 grits sequentially. Each polishing step took 5 to 10 minutes. Water was used to rinse the specimens before moving to the next grinding step. A solution of five parts colloidal silica with 0.06μm particle size and one part 30% hydrogen peroxide was used as the finish polish. This usually required more than 1 hour of polishing time. The polishing cloth used in this step was purchased from Buehler with catalog No. M500-12PS. After polishing, water was used to rinse away the colloidal silica. Finally, the specimens were ultrasonically cleaned in acetone and methanol, respectively, to remove the residual colloidal silica.

3.2.2 Scanning electron microscopy

The microstructures of the different alloys investigated in this study were characterized using scanning electron microscopy (SEM). The SEMs used in this dissertation work included a field emission gun Camscan 44FE SEM, a Carl Zeiss Variable Pressure EVO LS25 SEM, and a field emission gun Tescan Mira3 SEM. The Camscan 44FE SEM is located in room 3507A of the engineering building at Michigan State University. The latter two SEMs are located in room 1130 of the engineering building at Michigan State University.

Phase volume fractions and grain sizes were determined using BSE images. The different phases could be readily distinguished using BSE imaging. Phases containing larger average atomic numbers appear brighter in BSE images than phases containing lower average atomic numbers [Flegler et al. 1993]. The α phase of the Ti alloys evaluated in this study appeared dark or grey due to its low average atomic number (Al is the most common α-phase stabilizer and it has an atomic number of 13) while the β-phase appeared brighter because it is enriched V (V is the most common β stabilizer and it has an atomic number of 23) [Boyer et al. 1994]. Phase volume fractions were measured based on the BSE images using the functions "Area Fraction" and "Threshold" in ImageJ analysis software. These functions allowed determination of the fraction of a chosen phase to the entire BSE image. The equiaxed grain sizes of the CP Ti, Ti-5Al-2.5Sn, and Ti-3Al-2.5V were measured using the line-intercept method on BSE images [ASTM 2004]. For the complex α+β bimodal microstructure of the Ti-6Al-4V alloy, the average grain size was calculated using the appropriate functions provided in the EDAX-TSL (Mahwah, NJ) EBSD software (version 6.1).

3.2.3 EBSD and X-ray texture analysis

EBSD orientation maps were acquired from the gage section of the *in-situ* test specimens before and after the deformation. Prior to deformation, the specimens were polished using the procedures described in section 3.2.1. Grain orientation maps were obtained using a field emission Camscan 44FE SEM and a field emission Tescan Mira3 SEM, equipped with EDAX-TSL (Mahwah, NJ, USA) EBSD systems. The specimens were tilted 70 degrees from the horizontal surface. For the Camscan 44FE SEM, EBSD was performed using a 25KV electron beam and a 33mm working distance. For the Tescan Mira3, the same voltage was used and the working distance was approximately 20mm. For the CP Ti and the Ti-5Al-2.5Sn, which exhibited relatively large average grain sizes, a 2μm step was used for the undeformed microstructures and 0.5μm-2μm step sizes were used for the deformed microstructures. For both the Ti-3Al-2.5V and the Ti-6Al-4V alloys, which exhibited smaller average grain sizes, a 0.75μm step size was used for both undeformed and deformed microstructures. A 0.08μm step size was used to acquire the lenticular grain boundary β grain orientations of the Ti-3Al-2.5V deformed microstructures. A 2×2 binning setting was used for all the EBSD scans. An acquisition speed of about 17 points per second was obtained by the Canscan SEM/EBSD system. An acquisition speed of about 25-30 points per second was obtained by the Mira3 SEM/EBSD system.

After acquiring the EBSD data, post-processing "clean-up" was performed to remove erroneous data points coming from un-indexed or inappropriately indexed patterns. "Neighbor CI Correlation" and "Grain Dilation" were the two clean-up procedures used in this study. "Neighbor CI Correlation" was accomplished by replacing the orientation of the erroneous data point with the orientation of the neighboring point that had the highest confidence index. An

erroneous data point was defined as a point with a confidence index below a user defined threshold, usually between 0.05-0.1. A minimum grain size (in terms of pixels, usually 5-10 pixels) was used to perform the "Grain Dilation". Using "Grain Dilation", any grouping of less than 5-10 pixels with misorientation greater than 5 degrees was considered to be insufficient to be defined as a single grain in this procedure. The orientations of these points were re-assigned to match the adjacent grain orientation.

XRD was performed on the Ti-5Al-2.5Sn and the Ti-3Al-2.5V bulk materials to investigate the global texture of the materials. An X'Pert Pro MRD XRD system, (Philips, Eindhoven, Netherlands) located at IMDEA Materials Institute, Madrid, Spain, was used.

3.3 *In-situ* Mechanical testing

3.3.1 Sample configuration

Flat dog-bone mechanical test samples with a 3mm gage width and 10mm length were electrodischarge machined (EDM) for *in-situ* testing. Figure 3.1 shows a photograph of an EDM cut specimen. The specimens were then polished using the method described in section 3.2.1. Table 3.2 lists the testing conditions of the specimens investigated in this study.

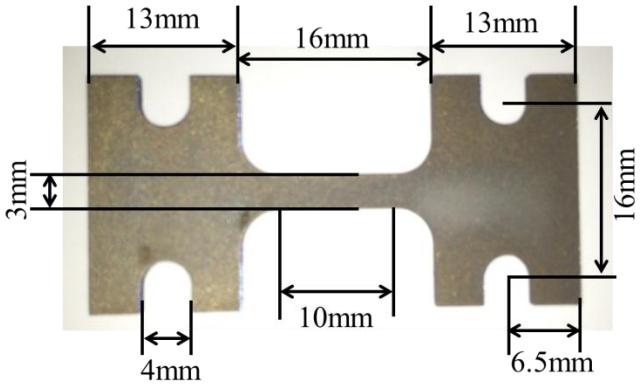

Figure 3.1 A photo of an *in-situ* test specimen representative of those used in the tensile and tensile-creep experiments. The sample dimensions are provided.

Table 3.2 Testing conditions of the investigated specimens.

Material	Test Mode	Temperature	Number of tests performed
CP Ti	Tension	296K	2
CP Ti	Tension	728K	2
CP Ti	45MPa Creep (0.73 yield stress)	728K	1
Ti-5Al-2.5Sn	Tension	296K	1
Ti-5Al-2.5Sn	Tension	728K	1
Ti-5Al-2.5Sn	250MPa Creep (0.76 yield stress)	728K	1
Ti-5Al-2.5Sn	300MPa Creep (0.91 yield stress)	728K	1
Ti-5Al-2.5Sn	200MPa Creep	763K	1
Ti-5Al-2.5Sn	250MPa Creep	763K	1
Ti-3Al-2.5V	Tension	296K	2
Ti-3Al-2.5V	Tension	728K	2
Ti-3Al-2.5V	180MPa Creep (0.72 yield stress)	728K	1
Ti-6Al-4V	Tension	296K	2
Ti-6Al-4V	Tension	728K	2
Ti-6Al-4V	310MPa Creep (0.74 yield stress)	728K	1

3.3.2 *In-situ* tensile testing

The *in-situ* SEM testing methodology allows the capture of the deformation evolution on the specimen surface during the tensile and tensile-creep experiments. A screw-driven tensile stage built by Ernest F. Fullam, Incorporated (originally located in Lantham, NY and later acquired by MTI Instruments, Albany, NY) was placed inside either the Carl Zeiss Variable Pressure EVO LS25 SEM or the Tescan Mira3 SEM. A photograph of the testing stage placed inside the Tescan Mira3 SEM is shown in Figure 3.2.

In-situ tensile tests were performed on the CP Ti and the Ti-5Al-2.5Sn, Ti-3Al-2.5V, and Ti-6Al-4V alloys at 296K and 728K with a constant displacement rate of 0.004 mm/s (i.e. an approximate strain rate of 10^{-3} s^{-1}) (see Table 3.1). The displacement, time, and load data were recorded during the tests using the MTESTW version F 8.8e data acquisition and control software (Admet, Inc., Norwood, MA, USA). BSE and/or SE SEM images were acquired during the 296K tensile experiments. The test was paused for 5-10 minutes while the images were

acquired. During this pause, some stress relaxation of the specimens occurred. After imaging, deformation continued at the same displacement rate. For the 728K tensile experiments, a 6mm diameter tungsten-based heating unit, powered by a constant voltage power supply, was used to heat the samples to the desired temperature, which was maintained for a minimum of 30 minutes before loading. The temperature was monitored using a thermocouple spot-welded to the side of the gage section. The vacuum was maintained below 2×10^{-6} Torr throughout the experiments. SE SEM images were acquired during the 728K experiments. It is noted that the displacement data collected by the MTESTW software included the deformation in the gage section as well as the grip sections. Thus, the total strains calculated based on the specimen gage length did not actually represent the actual strains of the *in-situ* imaged areas. The displacement divided by the gage length tended to overestimate the strain achieved by the gage section alone. Local strains were determined by measuring relative displacements of obvious features, such as triple points and polishing defects, on *in-situ* collected SEM images acquired before, during, and after deformation. Therefore, the strains reported are local strains unless otherwise specified. None of the samples were taken to failure.

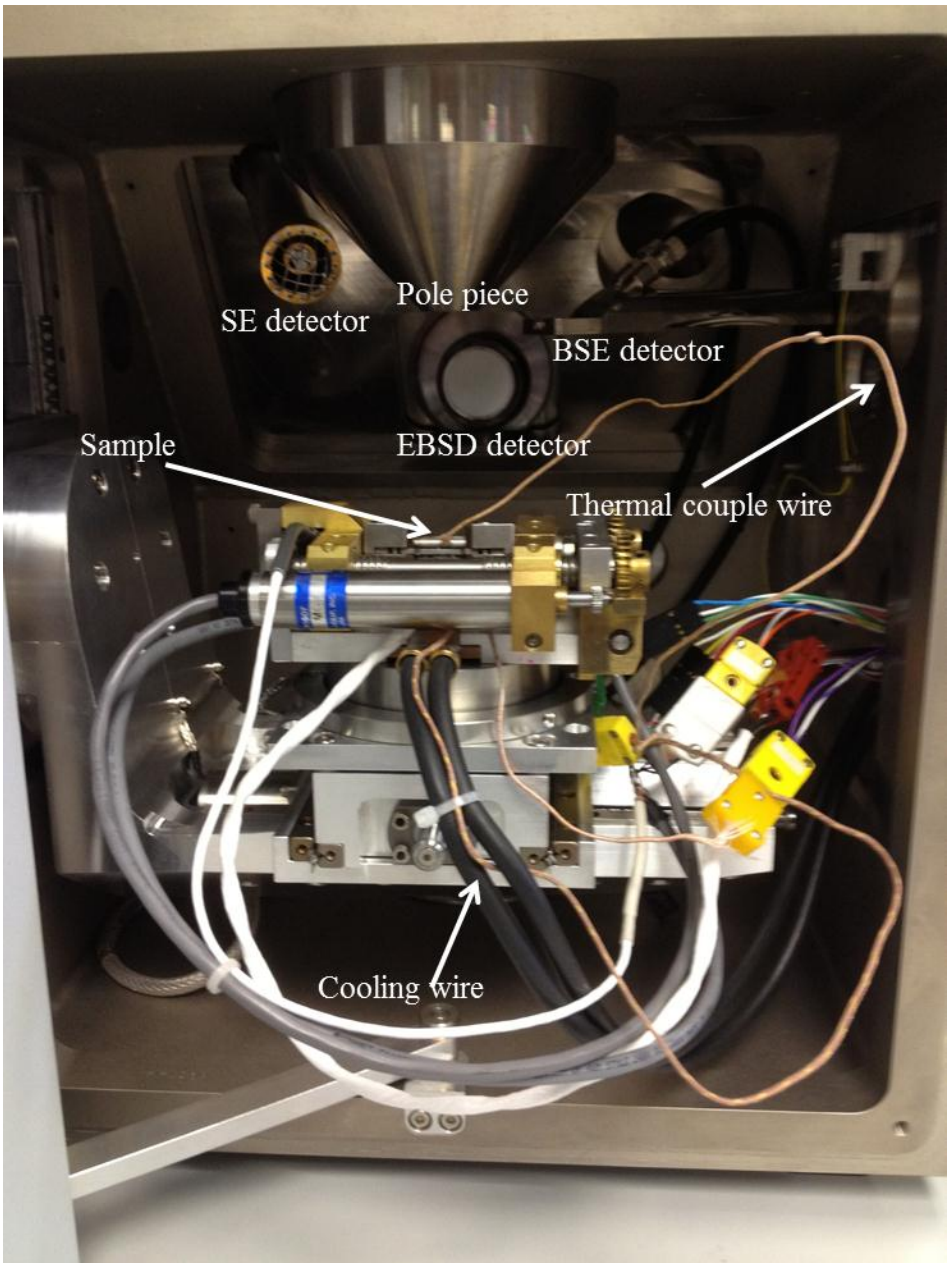

Figure 3.2 A photo showing the *in-situ* testing setup in the Tescan Mira3 SEM chamber.

3.3.3 *In-situ* tensile-creep testing

For the *in-situ* tensile-creep experiments, the specimens were heated and monitored using the same configuration and conditions described in the previous section. The creep testing conditions of the CP Ti and the Ti-5Al-2.5Sn, Ti-3Al-2.5V, and Ti-6Al-4V alloys are listed in Table 3.1. The creep stresses were chosen based on the YSs of the different materials. Typically the applied creep stress ranged between 0.72~0.91 of the YS. The temperature was controlled within ±10K of the target temperature for the duration of the experiments. SE SEM images were acquired without pausing the experiments. EBSD orientation maps were acquired before starting the experiments. The EBSD mapped regions were then imaged *in-situ* during the experiments. None of the samples were taken to failure.

3.4 Slip/twin trace analysis and Schmid factor calculation

A slip/twin trace analysis was used to identify the active deformation systems. The crystallographic orientation of each individual grains with respect to the sample/lab coordinate system was given by the EBSD data in the form of three Euler angles (φ1, Φ, φ2). The rotation matrix (*g*) between the crystal coordinate system and the sample/lab coordinate system was calculated by:

$$g = \begin{bmatrix} \cos\varphi 2 & \sin\varphi 2 & 0 \\ -\sin\varphi 2 & \cos\varphi 2 & 0 \\ 0 & 0 & 1 \end{bmatrix} \begin{bmatrix} 1 & 0 & 0 \\ 0 & \cos\Phi & \sin\Phi \\ 0 & -\sin\Phi & \cos\Phi \end{bmatrix} \begin{bmatrix} \cos\varphi 1 & \sin\varphi 1 & 0 \\ -\sin\varphi 1 & \cos\varphi 1 & 0 \\ 0 & 0 & 1 \end{bmatrix} \quad (3.1)$$

For a given slip/twin system, the slip plane and the slip direction can be expressed as (h k l) [u v w] in the crystal coordinate system using Miller indices. The transformation of the slip

plane and the slip direction from the crystal coordinate system to the sample/lab coordinate system can be achieved by:

$$n = g^T \bullet \begin{bmatrix} h \\ k \\ l \end{bmatrix} \tag{3.2}$$

$$b = g^T \bullet \begin{bmatrix} u \\ v \\ w \end{bmatrix} \tag{3.3}$$

where *n* and *b* are the corresponding slip plane normal and slip direction of a given slip system presented in the sample/lab coordinate system. The plane trace was then calculated by the cross product of the slip/twin plane normal (*n*), expressed in the sample/lab coordinate, and the sample normal direction ([001]). The reason for using the cross product of the slip/twin plane normal and the sample normal to calculate the plane trace is that if slip/twin occurred, the intersection line between the slip/twin plane of a given deformation system and the sample surface should be parallel to the experimentally-observed slip/twin bands. A Matlab^{TM} code was generated to calculate all the possible plane traces of the deformation systems for a given grain orientation (see Appendix). The experimentally-observed deformation systems in a given grain were identified by comparing the calculated plane traces with the slip/twin plane traces observed in the BSE/SE images.

Assuming a uniaxial tension stress state, represented as σ, the global Schmid factor (*m*) of each slip/twin system in an individual grain could be calculated by resolving the stress in the slip direction (Burgers vector direction) of a particular slip plane, expressed as:

$$m = n \bullet \sigma \bullet b^T \tag{3.4}$$

Because there are three different slip directions on the basal (three <a>) and pyramidal (one <a> and two <c+a>) planes, the slip direction cannot be unambiguously determined by slip trace analysis, so the slip system with the highest Schmid factor was assumed to be the active slip system when basal or pyramidal plane trace were observed. When the deformation systems exhibited similar plane traces and did not come from the same plane, the deformation system with the highest Schmid factor was chosen. It is noteworthy that all the Schmid factor values in this dissertation were calculated based on a uniaxial global stress state. Therefore, the Schmid factor values presented in this dissertation refer to the global Schmid factors.

Table 3.3 lists the slip systems available in Ti for trace analysis. There are 3 basal, 3 prismatic, 6 pyramidal <a>, and 12 pyramidal <c+a> slip systems. These 4 types of slip systems are numbered from 1-3, 4-6, 7-12, 13-24, respectively, in the Matlab code of the Appendix.

Figure 3.3 illustrates an example of the slip-trace analysis methodology used in this dissertation. Figure 3.3 (a) shows a Ti-5Al-2.5Sn 296K tensile deformed microstructural patch with ~3.5% strain. In Figure 3.3 (b), the grain of interest is highlighted by the HCP unit cell showing the crystallographic orientation in the inverse pole figure (IPF) EBSD map in tensile direction. Inputting the orientation angles acquired by EBSD (on the deformed microstructure) into the Matlab code in the Appendix, the slip traces of all of the 24 possible slip systems were calculated and are provided in Figure 3.3 (d). Comparing the calculated the slip traces with the experimentally-observed slip bands, it is clear that the calculated basal slip traces (number 1, 2, and 3) matched the observed slip band direction. Figure 3.3 (e) lists the Schmid factors of the three basal slip systems. Slip system number 3 ($(0001)\,[\bar{1}\bar{1}20]$) was chosen to be the active slip system for this particular grain as it had the highest Schmid factor (0.47) among all the three basal slip systems. Figure 3.3 (f) shows the HCP unit cell of the grain of interest with the

calculated slip trace for slip system number 3 indicated by the red line, the Burgers vector indicated by the light blue line starting from the solid circle, and the slip plane shaded in gray.

Both slip and twinning events were identified using this trace analysis approach. Please see Figure 4.6 in Chapter 4 for the trace analysis of twining using the same methodology as for slip. As shown in Figure 4.6, twins were also confirmed by comparing the twin orientations with their parent orientations using EBSD, as each type of twin has a unique misorientation angle and rotation axis with respect to the parent orientation.

It is important to note that if a given grain displays the activation of two prismatic slip systems and one pyramidal <c+a> slip system, this will result in three entries/counts in the total number of activated deformation systems. It is also important to note that if a given grain exhibits a set of parallel slip lines, such as the slip lines of grain "A" in Figure 3.3, this will be considered as one activated deformation system.

The observed slip traces were a result of dislocation motion. There are several reasons why some grains may not develop observable slip lines. This could happen when the Burgers vectors were parallel to the sample surface. This could also occur if the slip was diffuse and not constrained to well-defined slip bands. This could also occur if the magnitude of slip was small and the slip bands were not well developed. Therefore, the activation of some of the deformation systems may not have been detected.

Table 3.3 List of slip systems in Ti for slip trace analysis.

Deformation mode	Slip system	Number of variant	Slip system number
Basal <a>	$\{0001\}<2\bar{1}\bar{1}0>$	3	1-3
Prismatic <a>	$\{01\bar{1}0\}<2\bar{1}\bar{1}0>$	3	4-6
Pyramidal <a>	$\{01\bar{1}1\}<\bar{2}\bar{1}\bar{1}0>$	6	7-12
Pyramidal <c+a>	$\{10\bar{1}1\}<2\bar{1}\bar{1}3>$	12	13-24

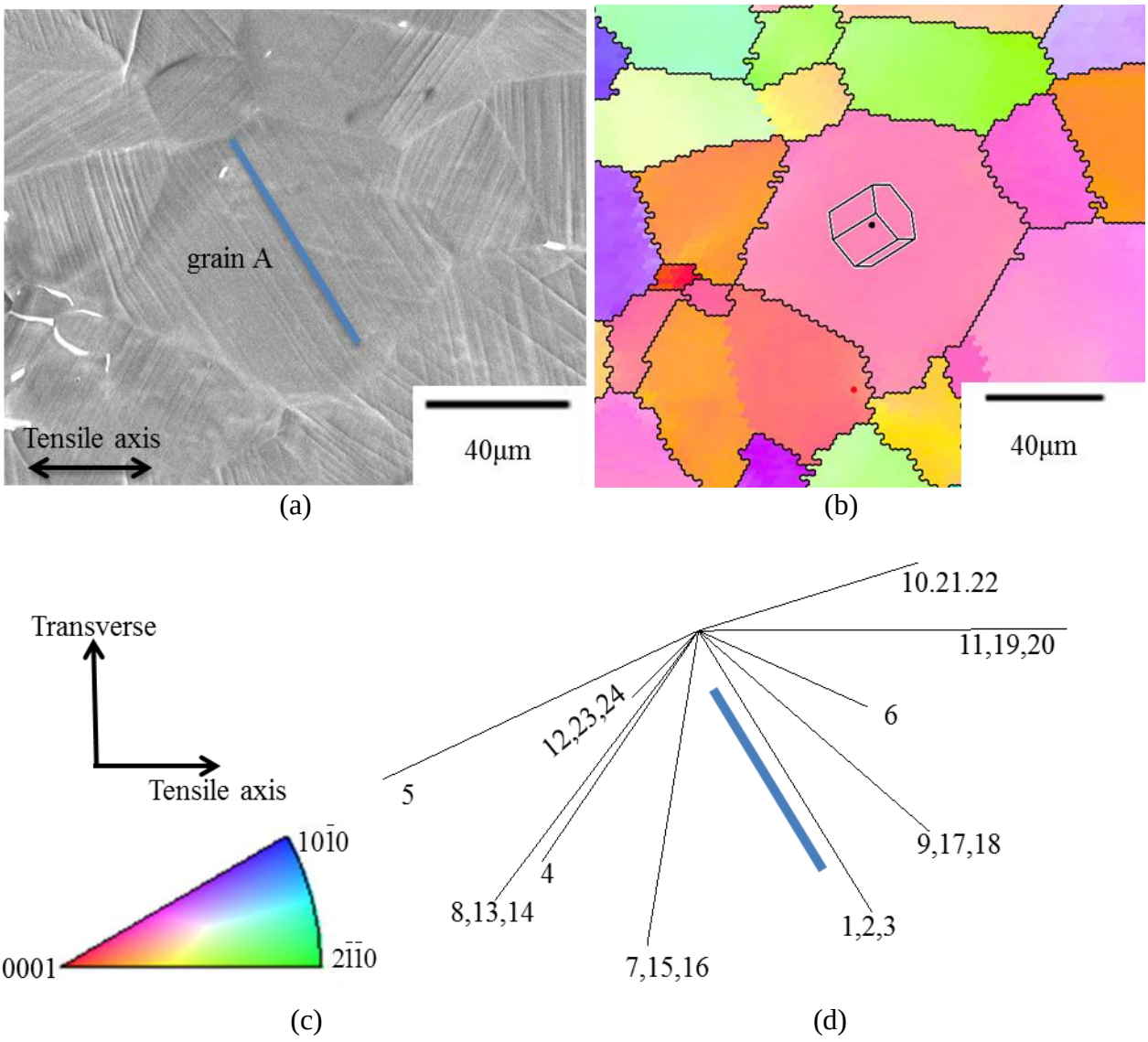

Figure 3.3 Example of slip trace analysis performed on grain A in (a), taken for a 296K tensile deformed Ti-5Al-2.5Sn microstructure with ~3.5% strain. The blue line in (a) indicated the experimentally-observed slip band direction. (b) The EBSD IPF map in the tensile direction with the HCP unit cell showing the grain orientation for grain A. (c) The EBSD color code map and the loading direction. (d) The calculated slip trace directions for all of the possible 24 slip systems and only basal slip systems 1, 2, and 3 matched the experimentally-observed slip band direction. The experimentally-observed slip band direction was indicated by the dark blue line. (e) Tabulated slip system chart showing the Schmid factors for all of the 24 slip systems and basal slip system number 3 (0001) $[\bar{1}\bar{1}20]$ (bold highlighted in (e)) was determined to be the active slip system with a Schmid factor of 0.47. (f) The HCP unit cell drawing with the calculated slip trace indicated by the red line, the Burgers vector indicated by the light blue line starting from the solid circle, and the slip plane shaded using a gray color.

Figure 3.3 (cont'd)

Slip system number	Slip system type	Slip system	Schmid factor
1	Basal	(0001) $[2\bar{1}\bar{1}0]$	0.09
2	Basal	(0001) $[\bar{1}2\bar{1}0]$	0.37
3	**Basal**	**(0001)** $[11\bar{2}0]$	**0.47**
4	Prism	$(01\bar{1}0)$ $[2\bar{1}\bar{1}0]$	0.08
5	Prism	$(10\bar{1}0)$ $[\bar{1}2\bar{1}0]$	0.20
6	Prism	$(\bar{1}100)$ $[\bar{1}\bar{1}20]$	0.13
7	Pyramidal <a>	$(01\bar{1}1)$ $[2\bar{1}\bar{1}0]$	0.11
8	Pyramidal <a>	$(10\bar{1}1)$ $[\bar{1}2\bar{1}0]$	0.36
9	Pyramidal <a>	$(\bar{1}101)$ $[\bar{1}\bar{1}20]$	0.33
10	Pyramidal <a>	$(0\bar{1}11)$ $[2\bar{1}\bar{1}0]$	0.02
11	Pyramidal <a>	$(\bar{1}011)$ $[\bar{1}2\bar{1}0]$	0
12	Pyramidal <a>	$(1\bar{1}01)$ $[\bar{1}\bar{1}20]$	0.11
13	Pyramidal <c+a>	$(10\bar{1}1)$ $[2\bar{1}\bar{1}3]$	0.43
14	Pyramidal <c+a>	$(10\bar{1}1)$ $[11\bar{2}\bar{3}]$	0.24
15	Pyramidal <c+a>	$(01\bar{1}1)$ $[11\bar{2}\bar{3}]$	0.30
16	Pyramidal <c+a>	$(01\bar{1}1)$ $[\bar{1}2\bar{1}3]$	0.36
17	Pyramidal <c+a>	$(\bar{1}101)$ $[\bar{1}2\bar{1}3]$	0.22
18	Pyramidal <c+a>	$(\bar{1}101)$ $[\bar{2}11\bar{3}]$	0.39
19	Pyramidal <c+a>	$(\bar{1}011)$ $[\bar{2}11\bar{3}]$	0
20	Pyramidal <c+a>	$(\bar{1}011)$ $[\bar{1}\bar{1}2\bar{3}]$	0
21	Pyramidal <c+a>	$(0\bar{1}11)$ $[\bar{1}\bar{1}2\bar{3}]$	0.18
22	Pyramidal <c+a>	$(0\bar{1}11)$ $[\bar{1}2\bar{1}3]$	0.17
23	Pyramidal <c+a>	$(1\bar{1}01)$ $[\bar{1}2\bar{1}3]$	0.17
24	Pyramidal <c+a>	$(1\bar{1}01)$ $[2\bar{1}\bar{1}3]$	0.11

(e)

Figure 3.3 (cont'd)

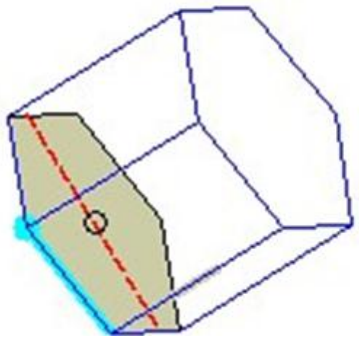

(f)

3.5 3D XRD

Synchrotron XRD experiments were performed on beamline 34-ID-E at the Advanced Photon Source (APS) at Argonne National Laboratory (Chicago, Illinoi). These experiments were intended to provide supplemental information about the dislocation arrangement, grain boundary inclination, and the subgrain boundary distribution beneath the specimen surface. It is noted that such experiments were not the main focus of this dissertation. The experimental set-up is illustrated in Figure 3.4. The sample surface was inclined 45 degrees towards the incident white beam, which had a beam size of 0.5μm×0.5μm. The line scan was set to be in either the H or X directions. The scanning step size was set to be either 1μm or 2μm. Laue patterns were generated from the sample surface to regions several hundreds of microns beneath the surface along the incident white beam direction, and these patterns were recorded by the area detector. Using the differential aperture and post imaging processing procedures by a computer cluster, the Laue pattern from each $1\mu m^3$ volume element (voxel) along the incident white beam direction was reconstructed. Knowing the crystal structure and lattice parameters, the Laue pattern was auto-indexed [Larson et al. 2002, Liu et al. 2004]. In addition to the auto indexing, the Laue

pattern from a given voxel element can also be manually indexed using IGOR software with the plugin analysis software package developed by Oak Ridge National Lab and APS [Sector 34-ID-E].

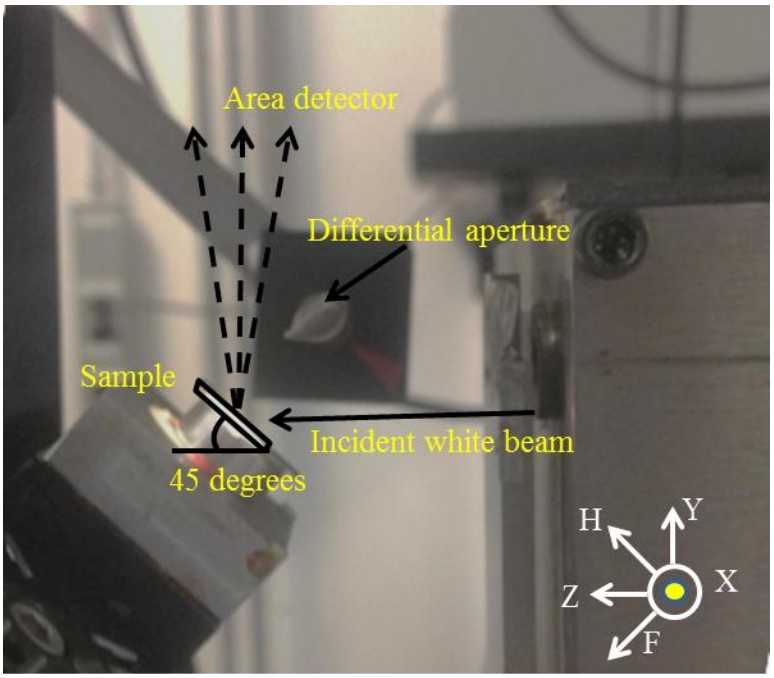

Figure 3.4 A photo showing the experimental setup of 3D XRD. The sample was inclined 45 degrees towards the incident white beam. H, F, Y, and Z lie in the same plane. X points out of the paper.

3.6 Grain boundary ledge measurement

The vertical step height of a grain boundary ledge between two grains was measured using a digital optical microscope VHX-600 (Keyence Corp., Osaka, Japan) located at room 3136 of engineering building at Michigan State University. The resolution of this microscope in z-direction is 0.05μm. The vertical step height between two grains was estimated by measuring the change of the working distances, which were determined by focusing on grains at each side of a particular grain boundary.

CHAPTER 4

RESULTS

This chapter presents the experimental results obtained from the CP Ti and the Ti-5Al-2.5Sn, Ti-3Al-2.5V, and Ti-6Al-4V alloys. This chapter is divided into four sections, pertaining to each of the above mentioned materials. Subsections provided within each of the four sections, present the results of the microstructure and texture characterization, the *in-situ* tensile experiments, and the *in-situ* tensile-creep experiments. The *in-situ* tensile and tensile-creep experiments allow for the observation of the deformation evolution of the surface microstructure in real time. The EBSD and slip-trace analysis was performed to identify the active deformation systems for each material studied at the different testing conditions (see Table 3.1). The simplest material was investigated first, a single-phase α microstructure for CP Ti. Then a near-α microstructures containing only a small fraction of the β phase, Ti-5Al-2.5Sn (β-phase volume fraction <1%) and Ti-3Al-2.5V (β-phase volume fraction 6.1 ±1.1%) was examined. Then a two-phase α+β microstructure containing 18.2 ±3.2% β phase was examined. Simpler microstructures were examined first, leading to a more complex microstructures. In this manner, the deformation of the α phase was the initial focus, and the influence of the β phase was thus systematically examined. From the single-phase α and the near-α phase microstructures, the effect of the alloy composition and temperature on the deformation behavior, including the YS values and relative activity of the different deformation systems, was evaluated. For the two-phase α+β microstructure, the deformation behavior was more complicated. A discussion and comparison of the results among the four materials will be presented in Chapter 5.

4.1 CP Ti

4.1.1 Microstructure

Figure 4.1 shows representative SE SEM images of the as-received CP Ti microstructure at low- and high-magnification. The average HCP α grain size was 140.4±25.7μm as measured by the line-intercept method [ASTM 2004].

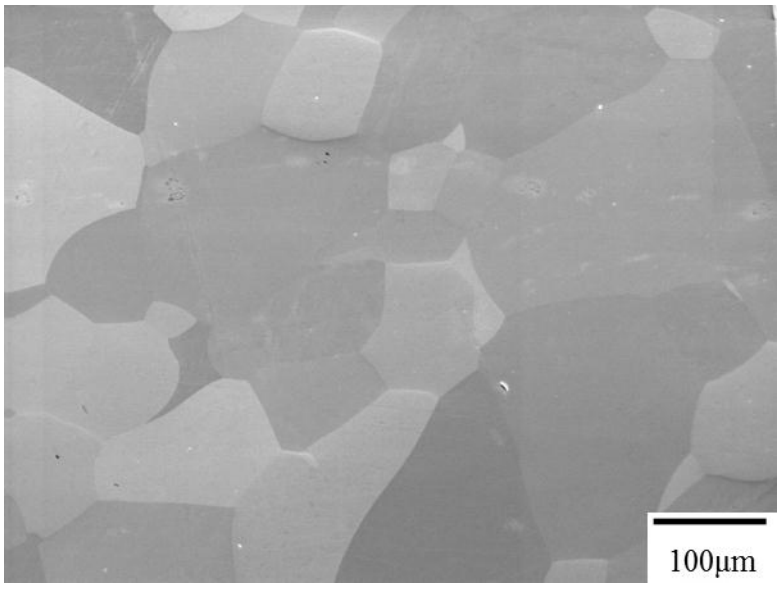

Figure 4.1 SE SEM images showing the microstructure of CP Ti at (a) high- and (b) low-magnifications. The intentional scratch in the middle of (b) was used as a fiducial marker for the *in-situ* SEM experiments.

4.1.2 *In-situ* tension

As stated in section 3.3, *in-situ* tensile tests were performed on CP Ti at 296K and 728K. Two tests were performed for each temperature, resulting in a total of four tests. Of the four tests, two tests (one at 296K and one at 728K) were performed to acquire the stress versus displacement curves at 296K and 728K. EBSD data was not acquired for these two experiments. The other two tests were performed to study the deformation behavior at 296K and 728K. EBSD data was acquired for these two experiments.

The engineering stress versus displacement curves for the CP Ti 296K and 728K tensile tests are illustrated in Figure 4.2. The load drops indicate that stress relaxation occurred when the tests were paused for imaging. The magnitude of the load drop increased with increased plastic deformation. None of the specimens were taken to failure and a minimum local strain of ~8.4% was achieved. As shown in Figure 4.2, the YS of CP Ti decreased dramatically (from ~440MPa to ~62MPa) with increasing temperature from 296K to 728K. In Table 4.1, the YS and maximum stress (the ultimate tensile stress was not achieved) obtained from the MTESTW data acquisition software are comparable with the YS and the ultimate tensile stress (UTS) found in the Ti handbook by Boyer et al. [1994]. Any differences in the YS and UTS between the values obtained in the current study and the values found in literature could have been due to small compositional differences, heat treatment differences, texture differences, etc.

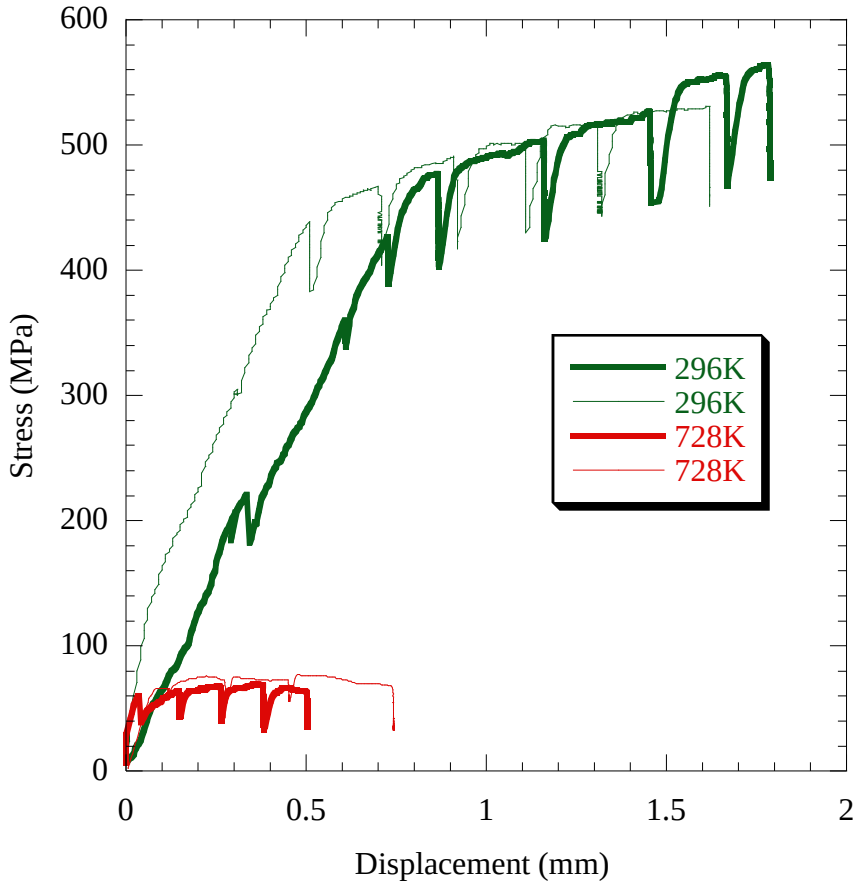

Figure 4.2 Stress vs. displacement plots for CP Ti samples tensile tested at 296K and 728K. The load drops indicate that stress relaxation occurred when the tests were interrupted for imaging. The displacement values included displacements in both the gage section and the grip regions. The curve with thick blue line corresponded to the specimen in section 4.2.1.1 and the curve with thick red line corresponded to the specimen in section 4.2.1.2.

Table 4.1 CP Ti tensile property comparison between the experiments in the current work and the Ti handbook by Boyer et al. [1994]. It is noted that tensile properties for CP Ti were only found for temperatures up to 573K.

Test temperature	YS (MPa)	Max Stress (MPa)	YS (MPa) in Boyer et al.	UTS (MPa) in Boyer et al.	Comment
296K	~440	~564	165-520	240-617	Various CP Ti grades
728K	~62	70	<100	<150	Only found for temperature below 573K

4.1.2.1 296K tension

Figure 4.3 shows an EBSD IPF map in the tensile direction and the corresponding {0001} and $\{10\bar{1}0\}$ pole figures from the gage section of a 296K tensile-tested CP Ti specimen. In Figure 4.3 (a), the red grains indicated that the c-axes were almost parallel to the tensile axis. In such orientations, both basal and prismatic slip exhibited low Schmid factors while twinning and pyramidal <c+a> slip exhibited larger Schmid factors and were highly stressed for activation. The red grains were therefore considered to exhibit "hard" orientations. In contrast, the blue and green grains are considered to exhibit "soft" orientations. As shown in Figure 4.3 (a), the EBSD map exhibited a variety of colors for the approximately 520 α grains, with no prevalent color observed, indicating that the CP Ti was not strongly textured. In Figure 4.3 (b), the {0001} peak locations were aligned almost perpendicular to the transverse direction and a relatively weak fiber texture (an approximately 4 times random) was observed.

Macrozones, formed by a cluster of α grains having relatively close orientations, are commonly observed in Ti alloys such as Ti-6Al-4V (Le Biavant et al. 2002, Prakash et al. 2013), IM834 (German et al. 2005, Gey et al. 2012), and Ti-6Al-2Sn-4Zr-6Mo (Szczepanski et al. 2008). However, macrozones were not observed in all of the CP Ti specimens examined in this study.

Figure 4.4 shows the sequential SE SEM images taken from the same area of the 296K tensile-test specimen. Both slip and twinning were observed at a stress level of 426MPa, which was just below the global YS, ~440MPa. Most of the slip traces were for prismatic slip systems (highlighted by red lines in Figure 4.4 (b)) and their global Schmid factors ranged from 0.25 to 0.48. Twins (highlighted by black lines in Figure 4.4 (b) were activated with high Schmid factors, ranging from 0.48-0.50. More twins and slip traces were observed at higher strain levels

(see in Figure 4.4 (c)). T1 twins were the only type of twins observed. This is consistent with previous findings stating that T1 twins were the easiest to activate for RT deformed CP Ti [Christian et al., 1995]. After ~8.4% strain, ~80% of grains in Figure 4.4 (f) exhibited identifiable slip traces. Some grain boundary ledges developed during the deformation (see Figure 4.4 (f)).

Figure 4.5 shows the EBSD IPF maps in the tensile direction for the same area portrayed in Figure 4.4 before and after deformation (~8.4% strain). Before deformation (see Figure 4.5 (a)), the color within individual grains was relatively uniform, indicating that no significant pre-strain gradient existed. The majority of the grain orientation spread before the deformation was within 1 degree (see Figure 4.5 (c)). However, a significant grain orientation gradient developed (up to ~5 degrees) after the deformation, see Figure 4.5 (c). In general, the red or reddish grains ("hard" orientations) developed less orientation gradients than the green and blue grains ("soft" orientations). It is noted that the pink pixels in the grains labeled as "B" in Figure 4.4 were due to the improper indexing and the confidence indices of those pink pixels were below 0.1. No twining was observed in this grain.

Four twins were observed in the grain highlighted by the red box in Figure 4.4 (f). Figure 4.5 (a) shows the SE SEM image of the parent grain with the plane traces for each identified twin. Figure 4.5 (b)-(d) show the EBSD IPF map in the transverse direction, tensile direction, and specimen normal direction of the same area in Figure 4.5 (a) with HCP unit cells overlaid. Table 4.1 lists the active twinning systems and the corresponding Schmid factors. Each of the four twins was identified as T1 type and exhibited a ~85° misorientation around the $<2\bar{1}\bar{1}0>$ direction with respect to the parent grain orientation. The Schmid factors of all the identified

twins were 0.50 assuming a uniaxial global tensile state, suggesting twinning was highly favored for activation in this grain.

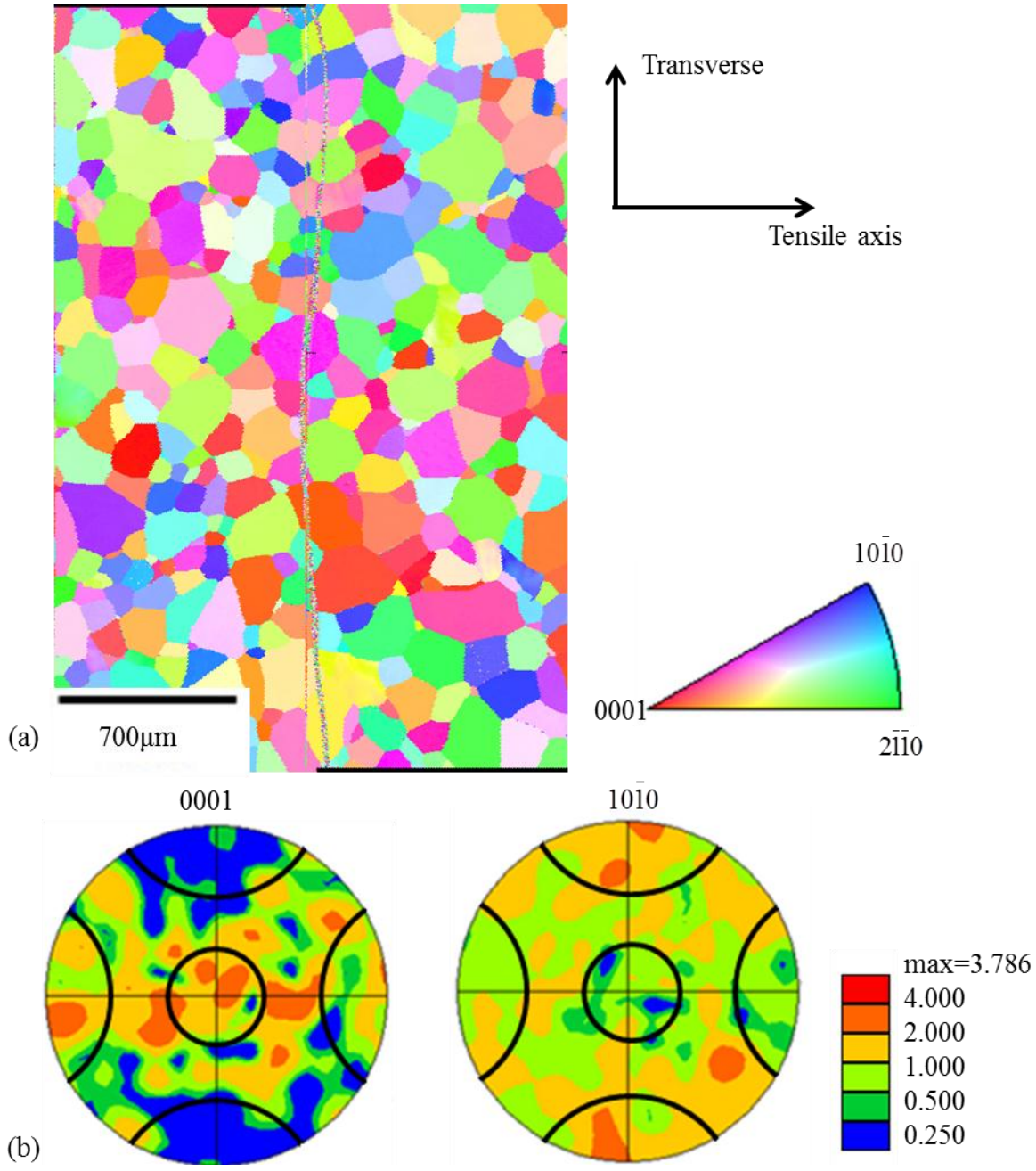

Figure 4.3 EBSD data of the CP Ti 296K tensile-tested specimen: (a) EBSD IPF map in the tensile direction of the α-phase Ti containing approximately 520 α grains, (b) the {0001} and the $\{10\bar{1}0\}$ pole figures with 30° cones along the major axes. The intentional scratch on the middle of the EBSD map was used as a fiducial marker. The loading direction was horizontal.

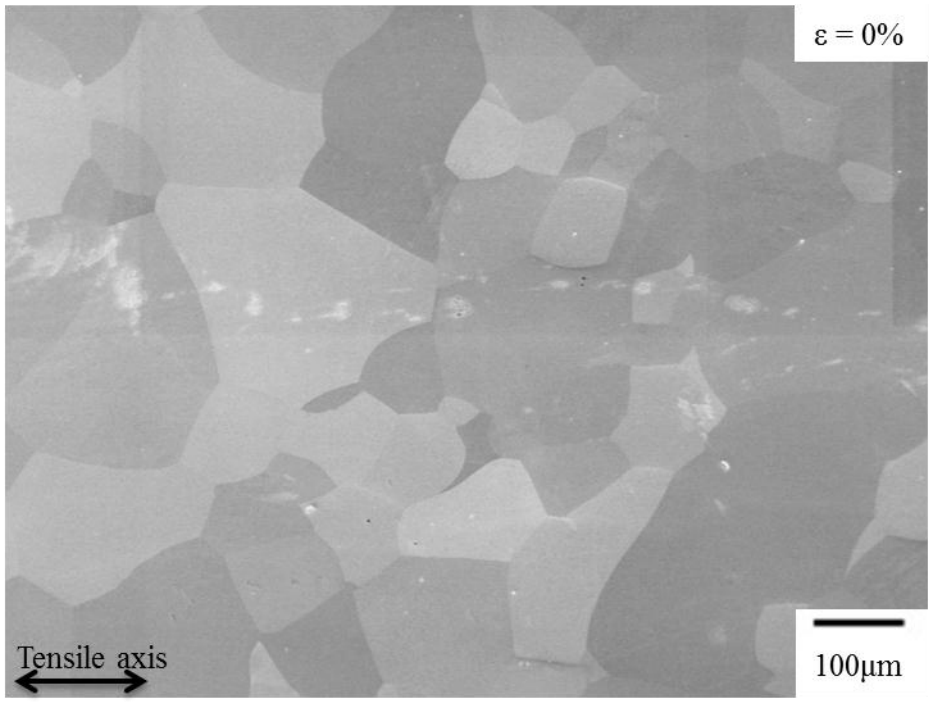

(a)

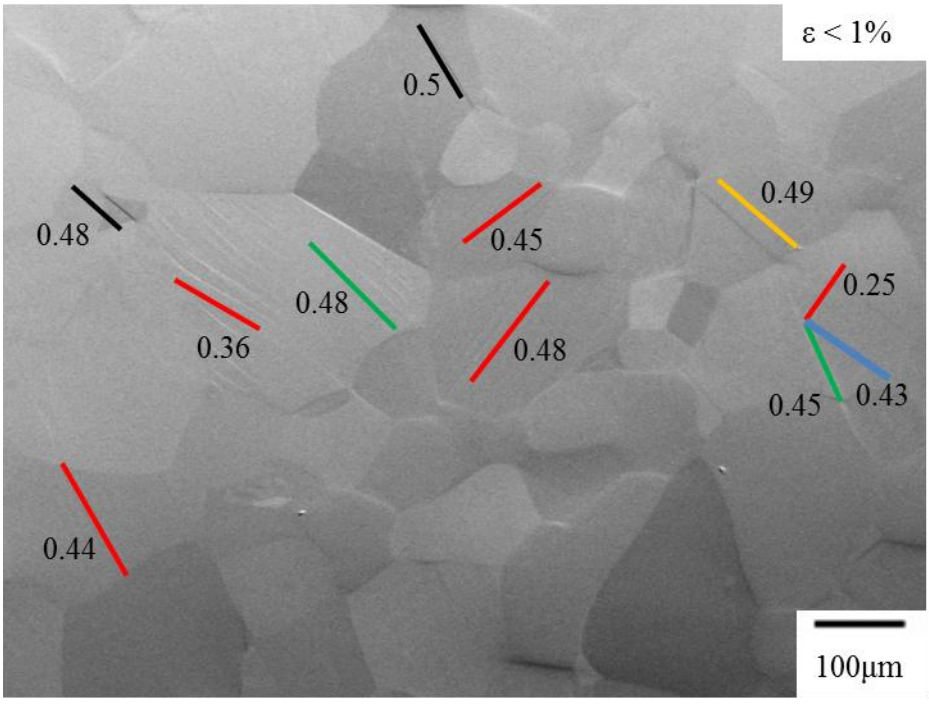

(b)

Figure 4.4 Sequential SE SEM images for the CP Ti 296K tensile-tested specimen: (a) undeformed, (b) 426MPa (when slip bands were first observed), (c) 477MPa (~1.5% strain), (d) 504MPa (~4% strain), (e) 522MPa (~5.9% strain), and (f) 564MPa (~8.4% strain). In (b) and (c), planes traces are color coded for prismatic slip (red), basal slip (blue), pyramidal <a> (green), pyramidal <c+a> (orange), and twin (black). The loading direction was horizontal. Multiple twinning systems were observed in area highlighted in red box.

Figure 4.4 (cont'd)

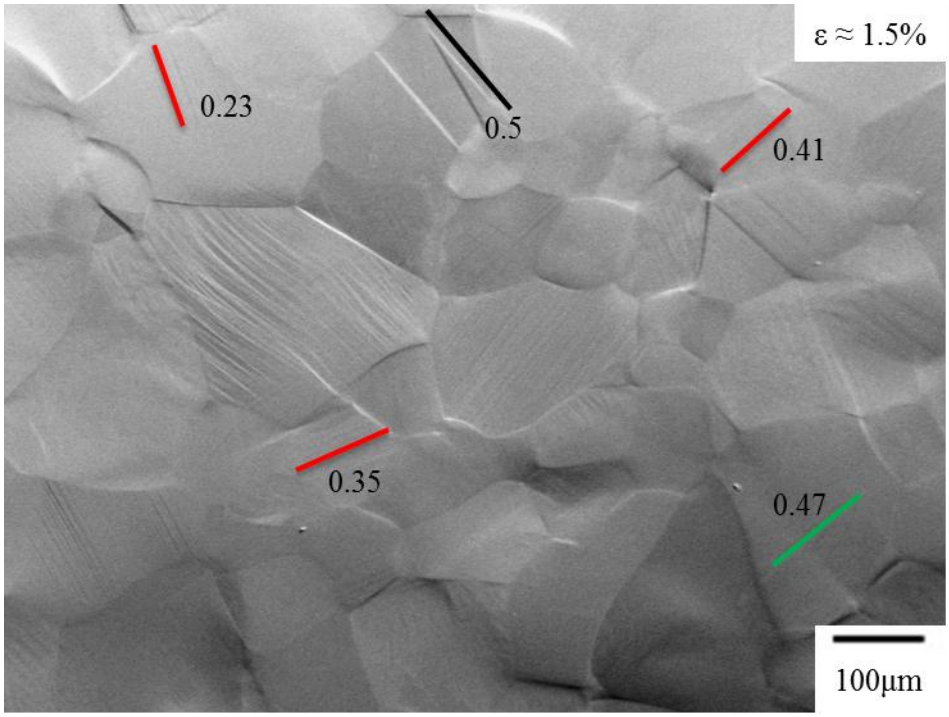

(c)

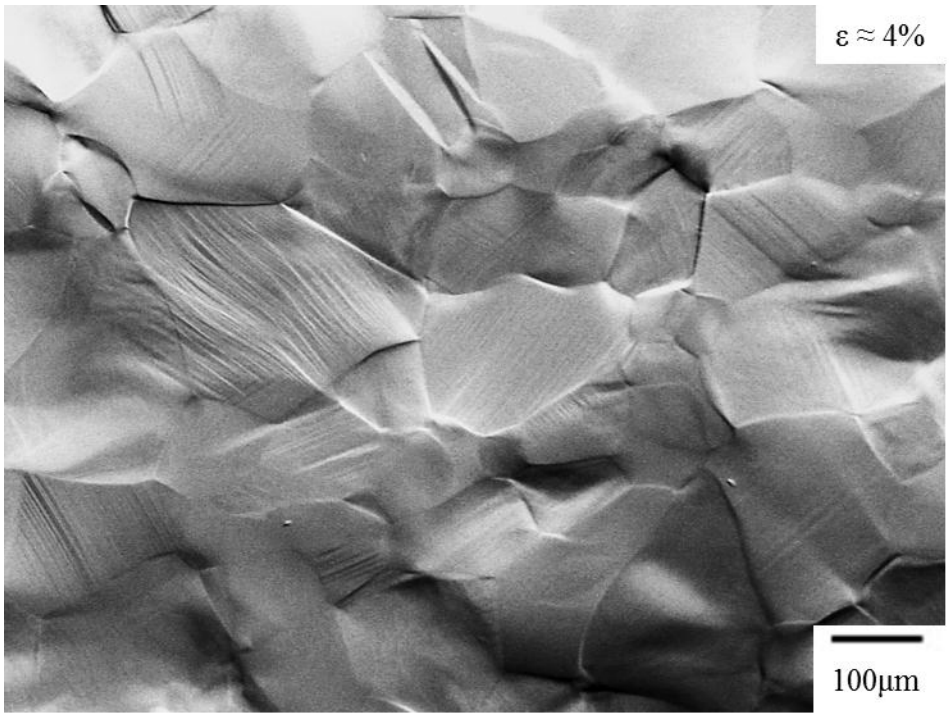

(d)

Figure 4.4 (cont'd)

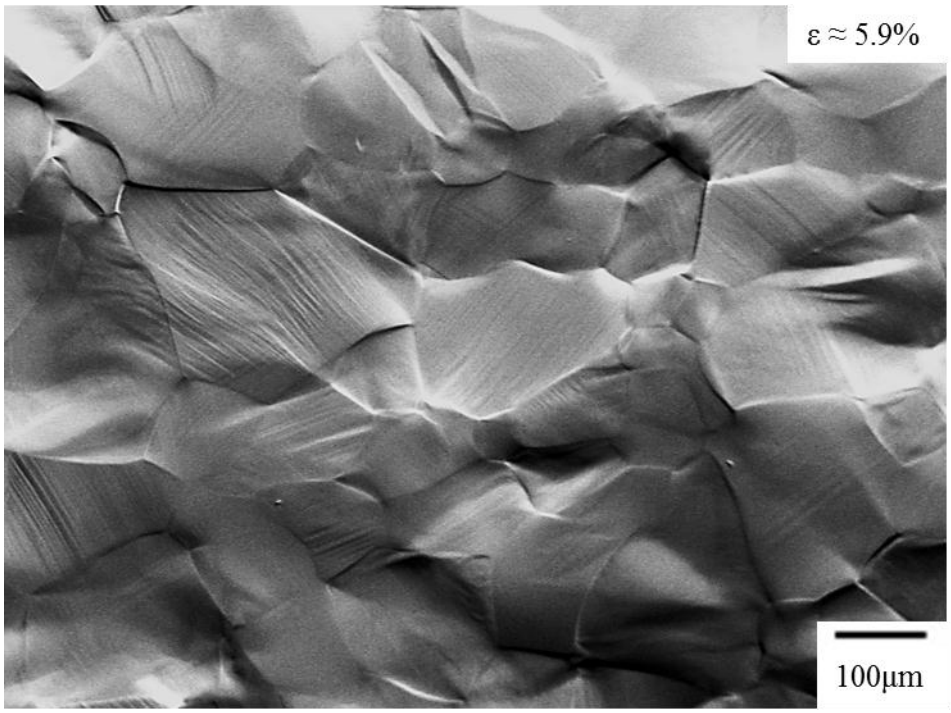

(e)

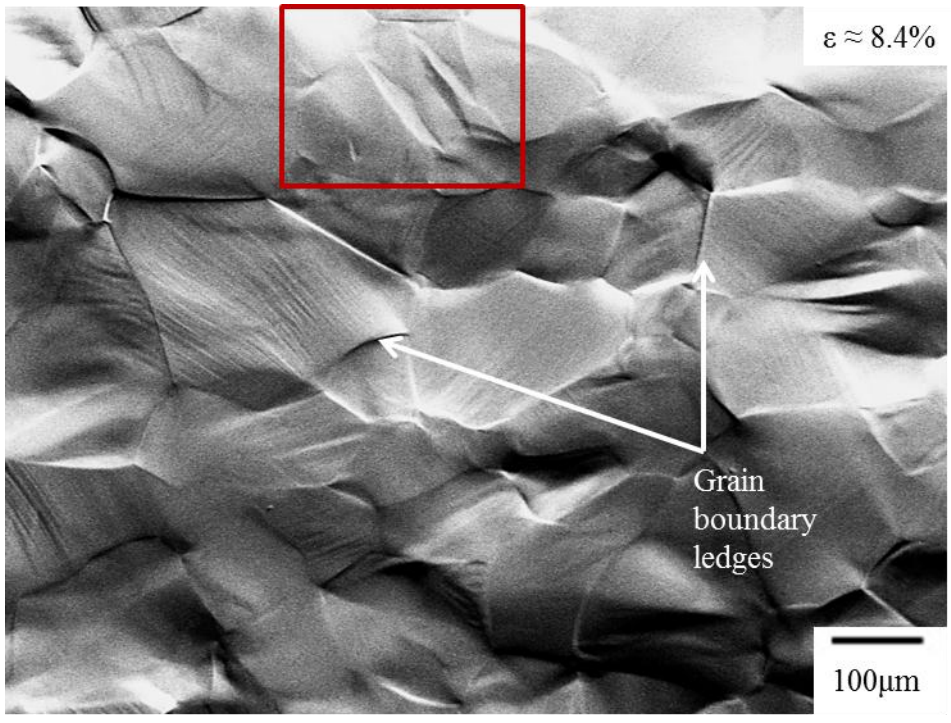

(f)

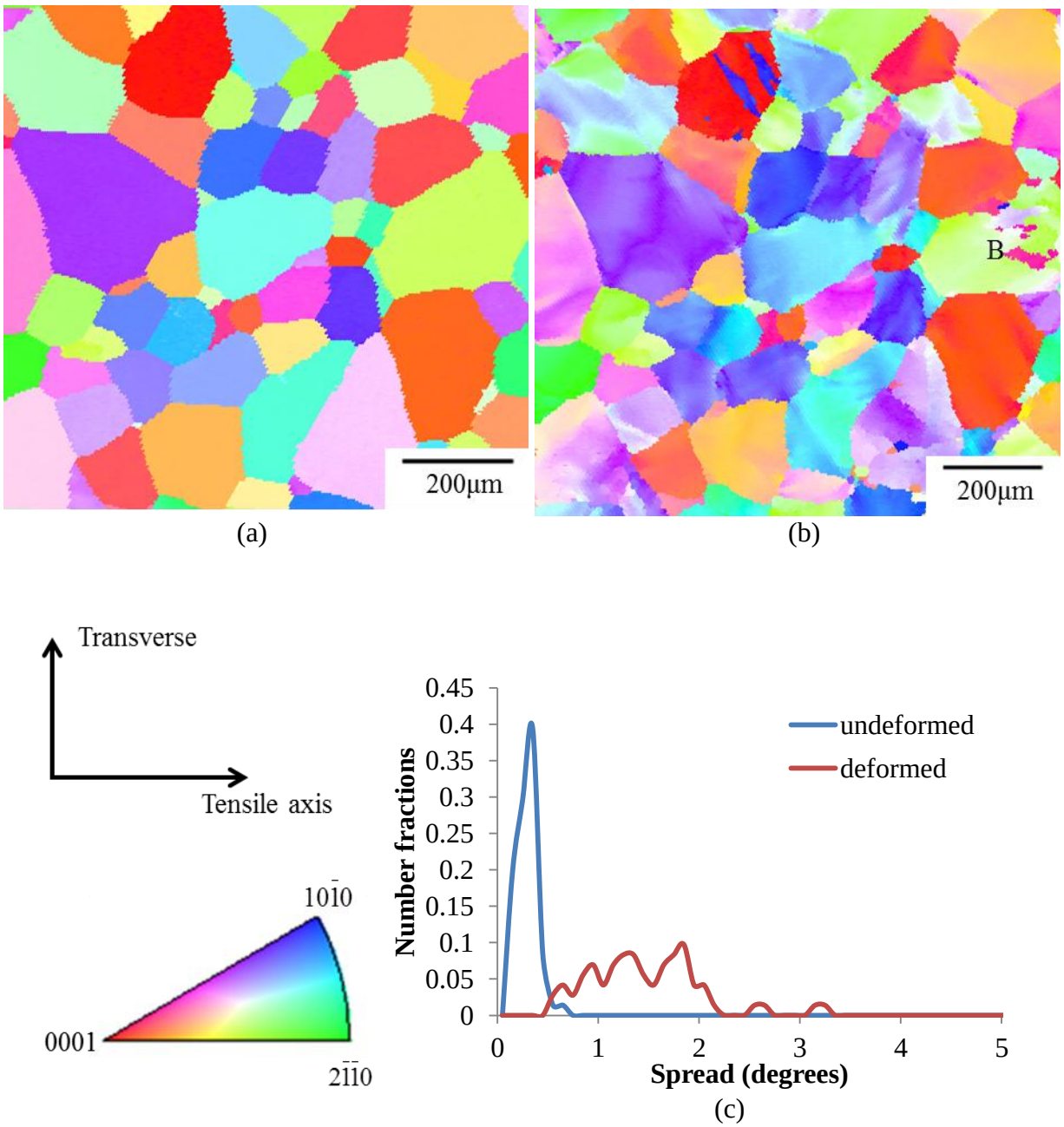

Figure 4.5 EBSD IPF maps in the tensile direction for the same area in the tensile-tested sample for the CP Ti at 296K (a) before and (c) after 8.4% tensile strain. It is noted that grain labeled as "B" is not a twined grain. The grain orientation spread of the grains shown in (a) and (b) was plotted in (c).

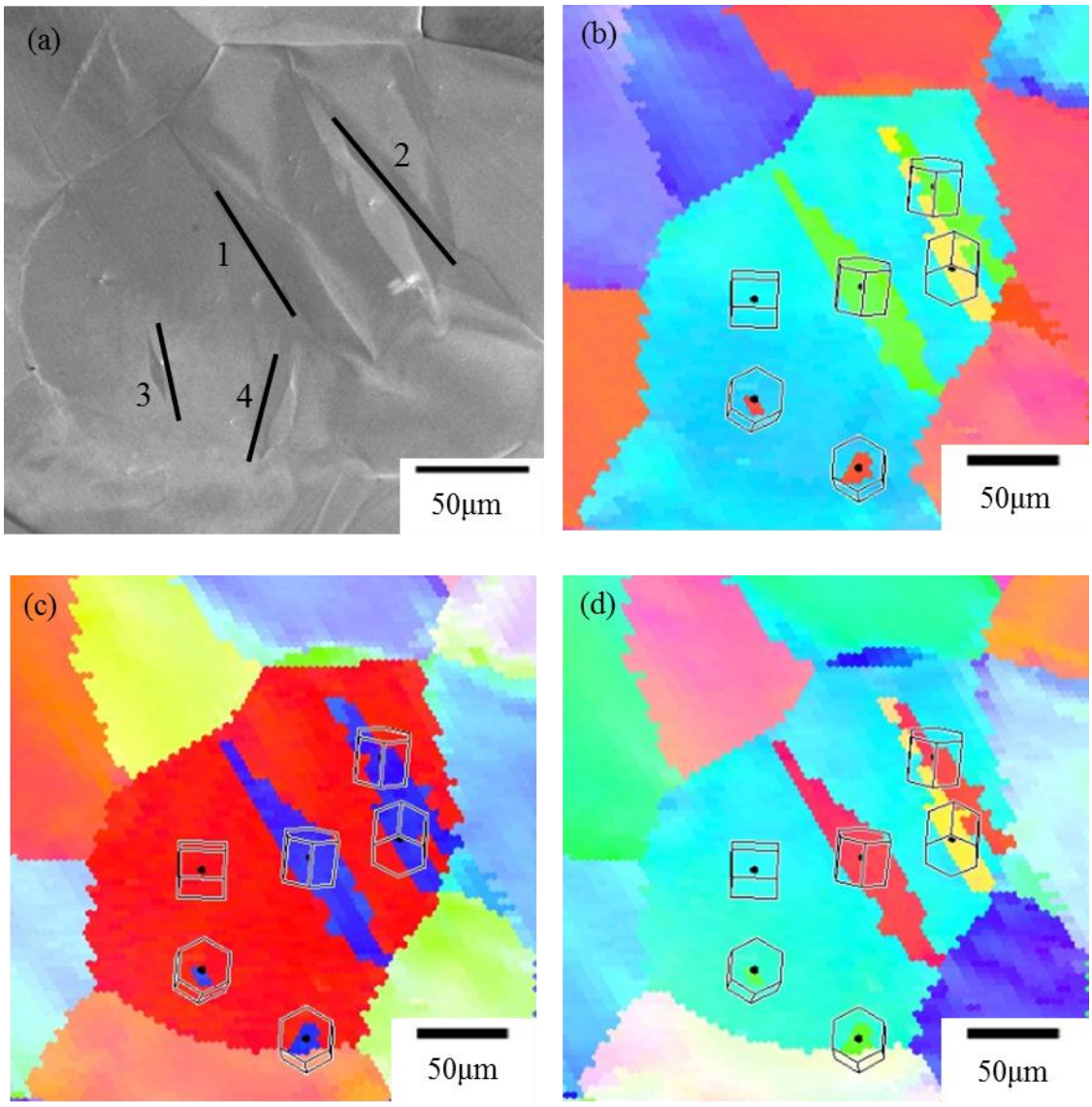

Figure 4.6 (a) SE SEM image showing multiple twin activation within a single grain of the CP Ti 296K tensile deformed to ~8.4% strain. Four twinning systems were identified, labeled 1-4. EBSD IPF maps (HCP unit cell overlaid) showing the parent and the twin orientations in the (b) transverse direction, (c) tensile direction, and (d) specimen normal direction.

Table 4.1 Twinning systems observed in Figure 4.6

Twin number	Misorientation between parent grain and twinning grain orientation	Twinning system	Schmid factor
1	85.1 °@ $[11\bar{2}0]$	$(\bar{1}102)[\bar{1}101]$	0.50
2	86.8 °@ $[\bar{2}110]$	$(\bar{1}012)[10\bar{1}1]$	0.50
3	84.7 °@ $[2\bar{1}\bar{1}0]$	$(0\bar{1}12)[01\bar{1}1]$	0.50
4	88.6 °@ $[\bar{1}2\bar{1}0]$	$(01\bar{1}2)[0\bar{1}11]$	0.50

Trace analysis was performed on 77 grains and a total of 104 active deformation systems were identified. As noted previously in section 3.3.3, if a given grain displays the activation of two prismatic slip systems and one pyramidal <c+a> slip system, this will result in three entries/counts in the total number of activated deformation systems. Figure 4.7 plots the number of observations of a particular deformation mode versus the global Schmid factor range. In Figure 4.7, more than 85% of the activated deformation systems in these 77 grains exhibited global Schmid factors greater than 0.3. 11 basal (11/104≈11%), 64 prismatic (64/104≈62%), 5 pyramidal <a> (5/104≈5%), and 14 pyramidal <c+a> (14/104≈13%) slip systems were identified, along with 10 twinning systems (10/104≈10%). The majority of the active deformation systems were prismatic slip, which was activated over almost the entire global Schmid factor range. Thus, prismatic slip was the dominant deformation mode at the 296K. Basal, pyramidal <a>, and pyramidal <c+a> slip systems and twinning comprised only a small fraction of the observed deformation modes, and most of those were associated with global Schmid factors greater than 0.4. Figure 4.8 shows stereographic triangles with the grain orientations plotted for basal, prismatic, pyramidal <a>, pyramidal <c+a>, and twinning deformation modes with Schmid factor contours overlaid. Generally, basal, pyramidal <a>, and pyramidal <c+a> slip and T1 twin were confined to grains with high Schmid factors for these deformation modes. In contrast, grains with prismatic slip were almost evenly distributed in the unit triangles. Some grains exhibited prismatic slip with Schmid factors lower than 0.2.

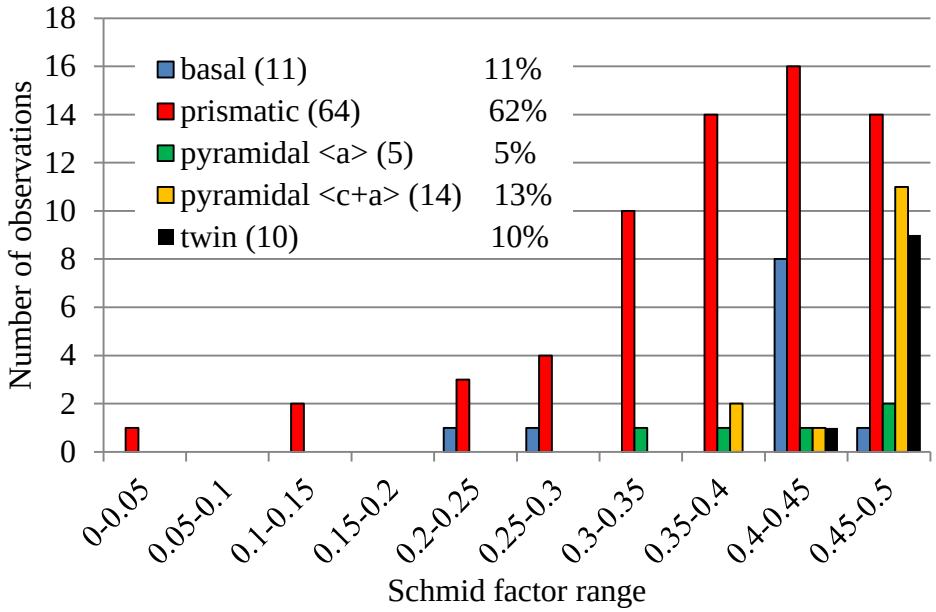

Figure 4.7 A histogram of the Schmid factor distribution of basal, prismatic, pyramidal <a>, and pyramidal <c+a> slip systems and T1 twinning systems for the CP Ti 296K tension experiment after ~8.4% strain.

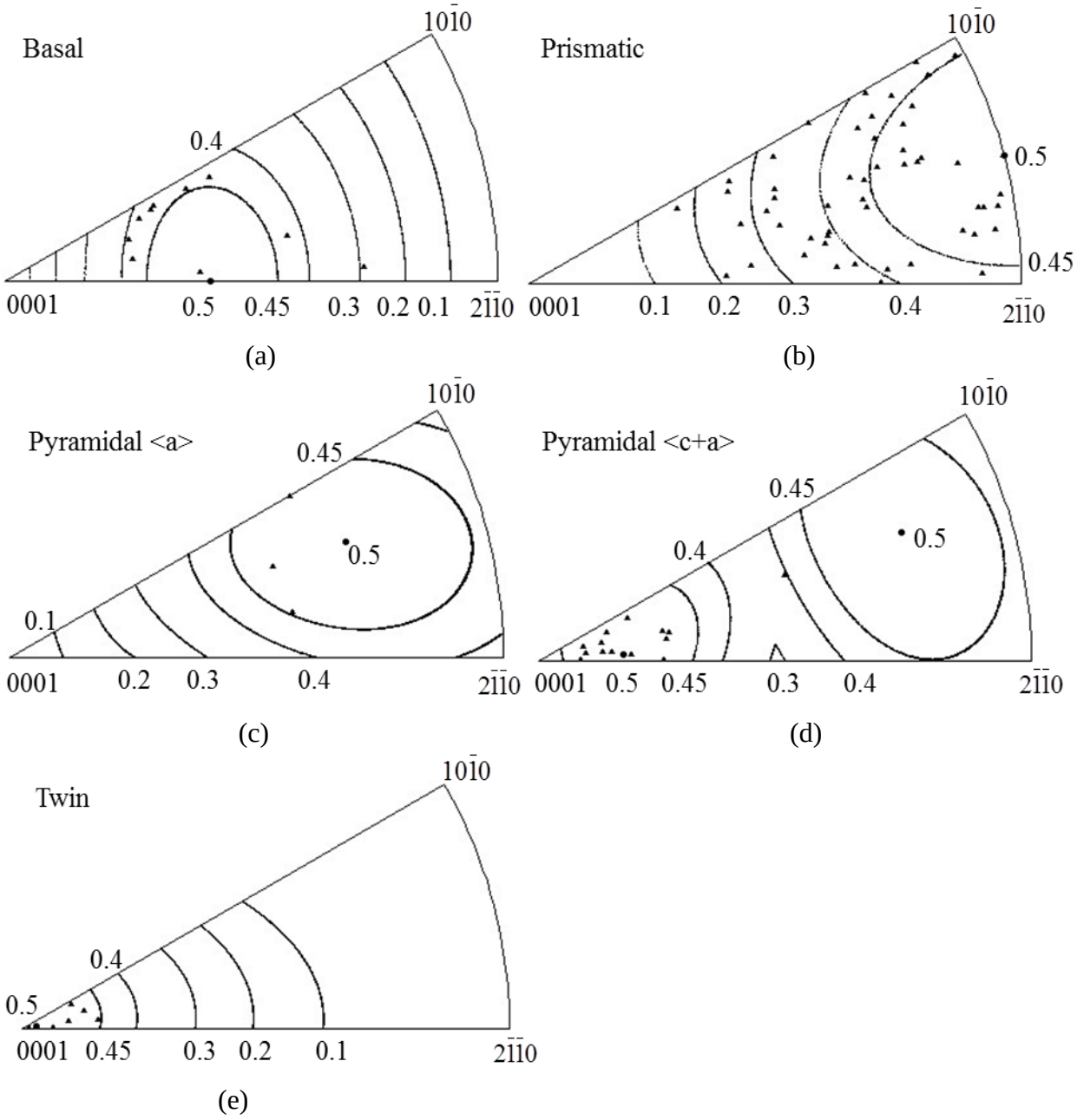

Figure 4.8 Unit triangle plots of grains which exhibited (a) basal, (b) prismatic, (c) pyramidal <a>, and (d) pyramidal <c+a> slip and (e) T1 twin for the CP Ti 296K tension test deformed to ~8.4% strain with Schmid factor contours overlaid.

4.1.2.2 728K tension

Figure 4.9 shows an EBSD IPF map in the tensile direction and the corresponding {0001} and $\{10\bar{1}0\}$ pole figures from the gage section of a 728K tensile-tested specimen for CP Ti. There were approximately 540 α grains in Figure 4.9 and no prevalent color was observed, indicating that the CP Ti was not strongly textured. Similar to the texture of the 296K tensile-tested specimen represented in Figure 4.3 (b), the {0001} peak locations in Figure 4.9 (b) were aligned almost perpendicular to the transverse direction and a weak fiber texture (approximately 5 times random) was observed.

Figure 4.10 shows the sequential SE SEM images taken from the same area of the gage section of the 728K tensile-test specimen. Both slip and twinning were observed at a stress level of 64MPa (~2.4%, see in Figure 4.10 (b)), which was just above the global YS (~62MPa). Most of the slip traces were identified to be prismatic slip systems (highlighted by red lines) and their global Schmid factors ranged from 0.26 to 0.43. Much less basal (highlighted by blue lines), pyramidal <c+a> (highlighted by yellow lines), and twinning (highlighted by black lines) traces were observed. Pyramidal <a> slip was not observed in this microstructural patch. More twins and slip traces were observed at higher strain levels. T1 twins were the only type of twins observed. This is similar to that observed for the CP Ti 296K tension tests. At ~8% strain, ~84% of grains in Figure 4.10 (c) exhibited slip/twinning. This fraction increased to ~90% at 11.2% strain and some grains exhibited more than one active deformation system. Some grain boundaries developed ledges, which become evident at ~4.3% strain.

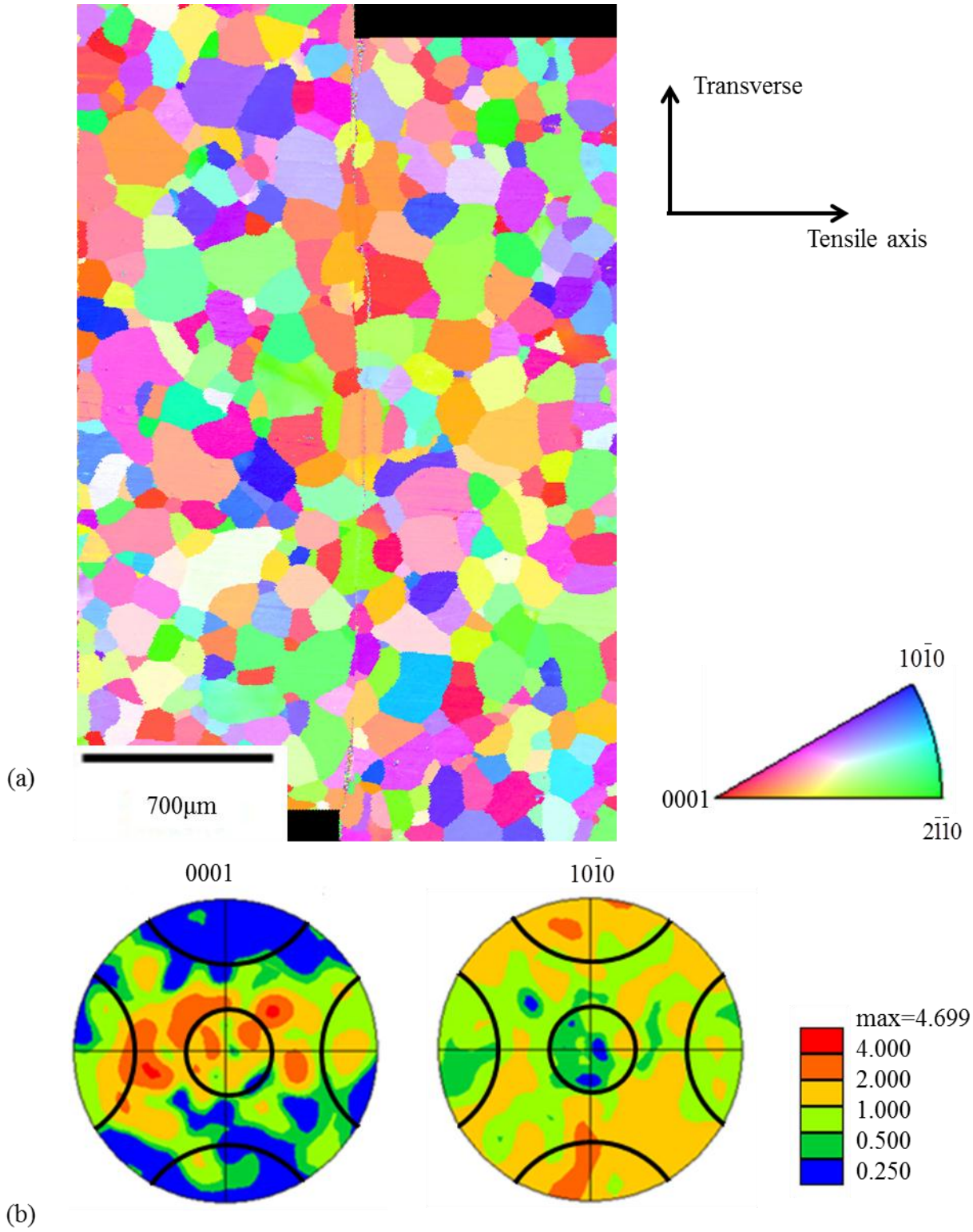

Figure 4.9 EBSD data of the CP Ti 728K tensile-tested specimen: (a) the EBSD IPF map in the tensile direction of the α phase Ti containing approximately 540 α grains, (b) the {0001} and the $\{10\bar{1}0\}$ pole figures with 30° cones along the major axes. The intentional scratch on the middle of the EBSD map was used as a fiducial marker. The loading direction was horizontal.

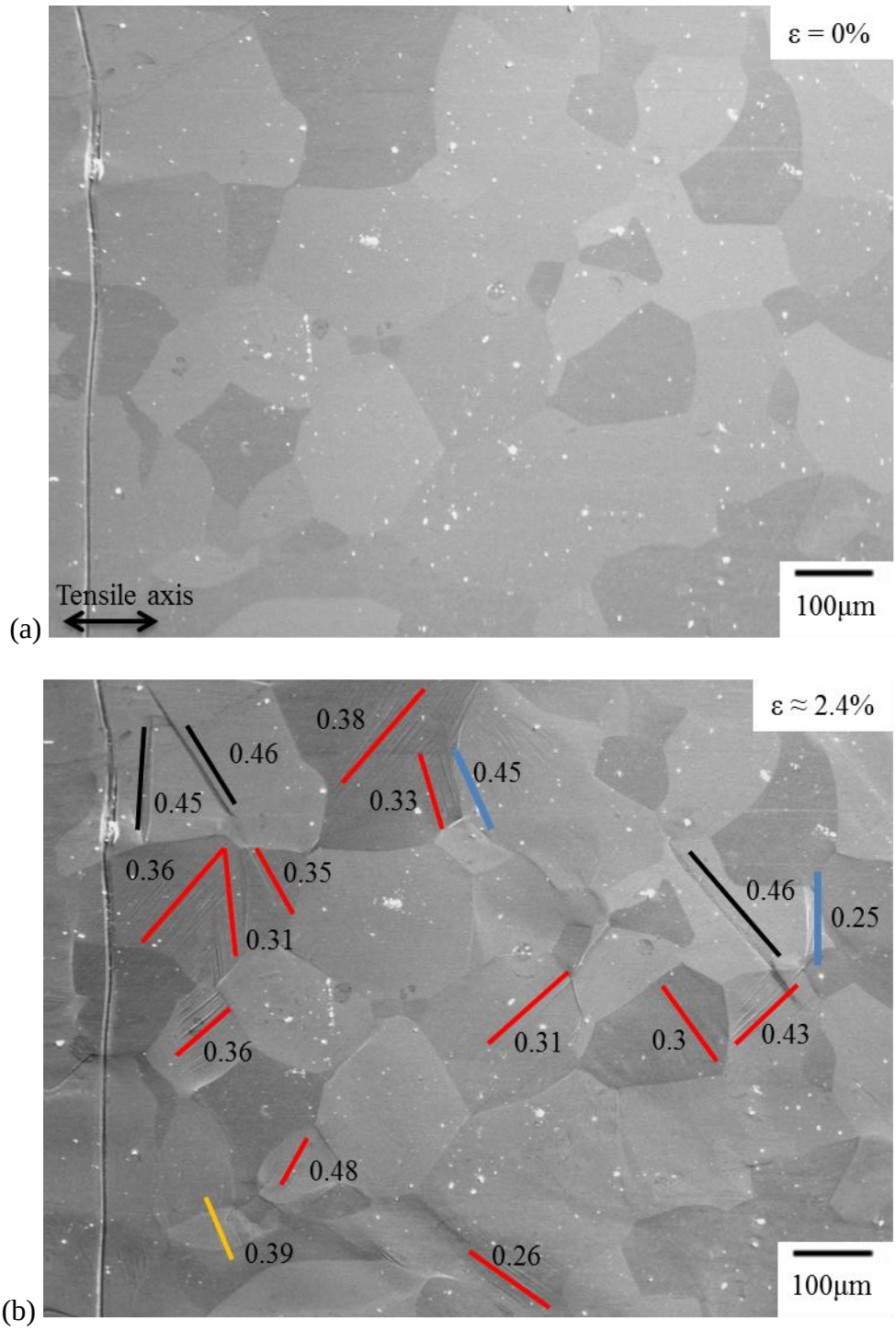

Figure 4.10 Sequential SE SEM images for CP Ti tensile-tested at 728K: (a) undeformed, (b) 64MPa (~2.4% strain) (when slip bands were first observed), (c) 70MPa (~9% strain), and (d) 66MPa (~11.2% strain). In (b), planes traces are color coded for prismatic slip (red), basal slip (blue), pyramidal <a> (green), pyramidal <c+a> (orange), and twin (black). The loading direction was horizontal.

Figure 4.10 (cont'd)

(c)

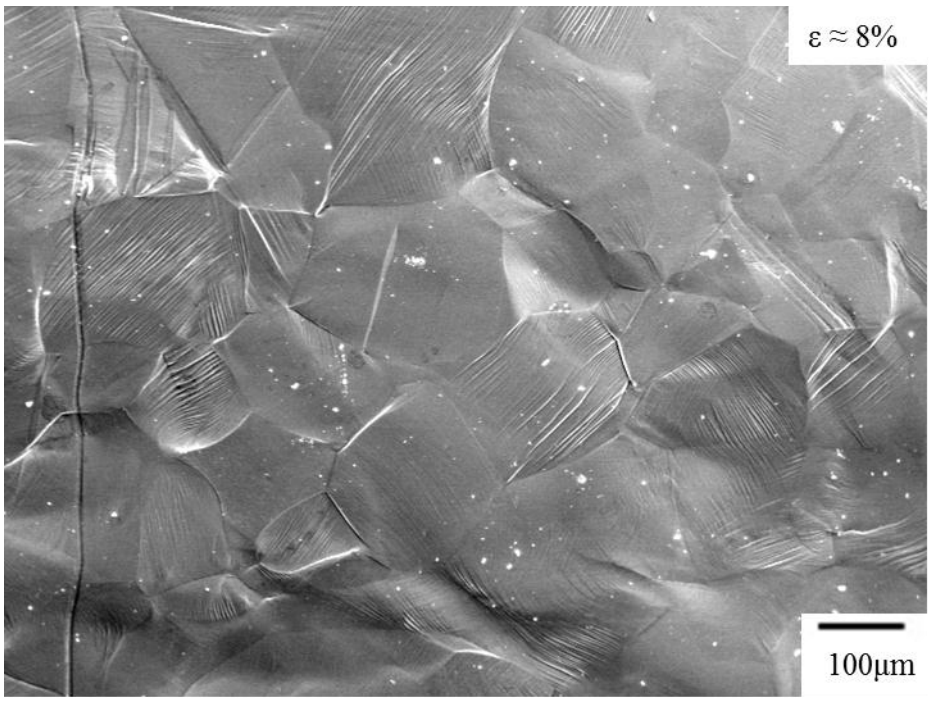

(d)

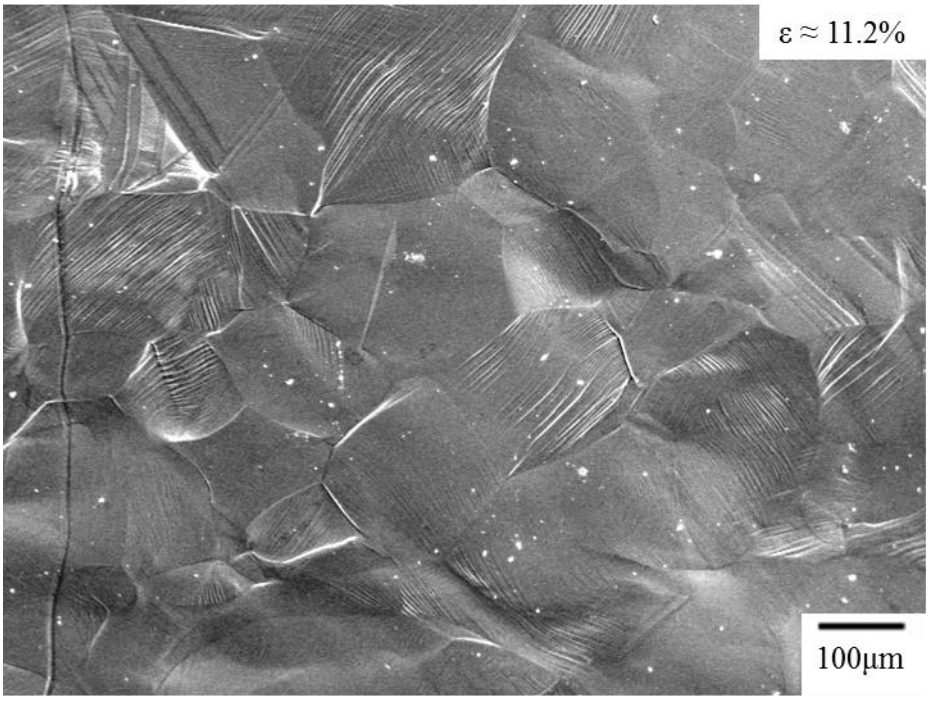

Slip trace analysis was performed for 86 grains and 120 deformation systems were identified in those grains. The histogram of the deformation modes with respect to the global Schmid factor is provided in Figure 4.11. 11 basal (11/120≈9%), 73 prismatic (73/120≈61%), 7 pyramidal <a> (7/120≈6%), and 16 pyramidal <c+a> (16/120≈13%) slip were identified, along with 13 twinning systems (13/120≈10%). About 79% of observed deformation systems were activated with global Schmid factors greater than 0.3. The majority of the deformation systems were prismatic slip and a few prismatic slip systems were activated with low global Schmid factors (smaller than 0.1), which was similar to that observed for the 296K CP Ti specimen in Figure 4.7. The activation of the other slip systems occurred over a global Schmid factor range of 0.2 to 0.5. Figure 4.12 shows stereographic triangles with the grain orientations plotted for basal, prismatic, pyramidal <a>, pyramidal <c+a>, and twinning deformation modes with Schmid factor contours overlaid. Similar to the 296K tension test results portrayed in Figure 4.8, grains with prismatic slip were distributed over the entire triangle and some grains exhibited prismatic slip with Schmid factors as low as 0.2. Basal, pyramidal <a>, pyramidal <c+a>, and twinning were confined to the high Schmid factor regions. Overall, it did not appear that temperature had a significant effect on the relative activation distribution of the different deformation systems. This will be further discussed in Chapter 5. The relative CRSS values for the different deformation systems at 296K and 728K will also be calculated and presented in Chapter 6.

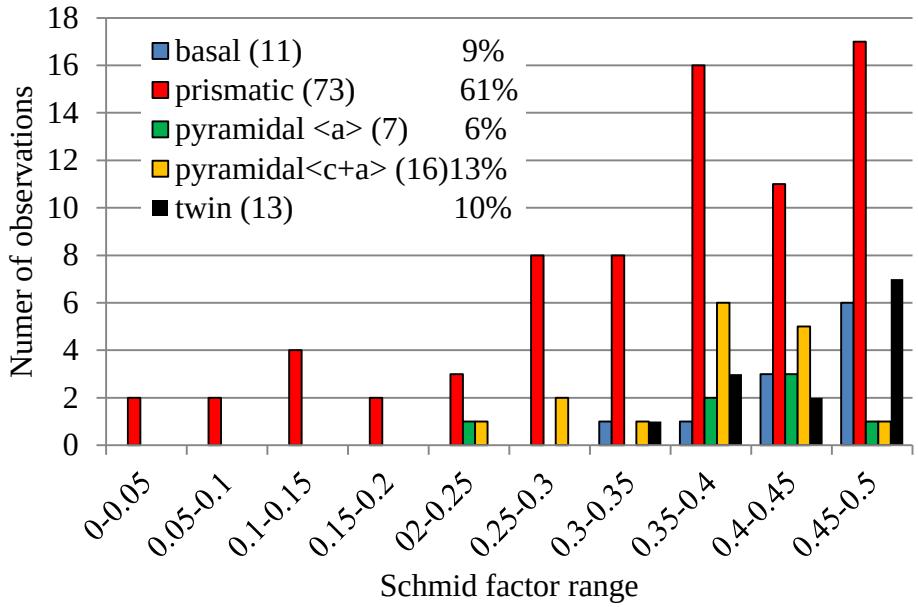

Figure 4.11 A histogram of the Schmid factor distribution of basal, prismatic, pyramidal <a>, and pyramidal <c+a> slip systems and T1 twinning systems for the CP Ti 728K tension experiment after ~11.2% strain.

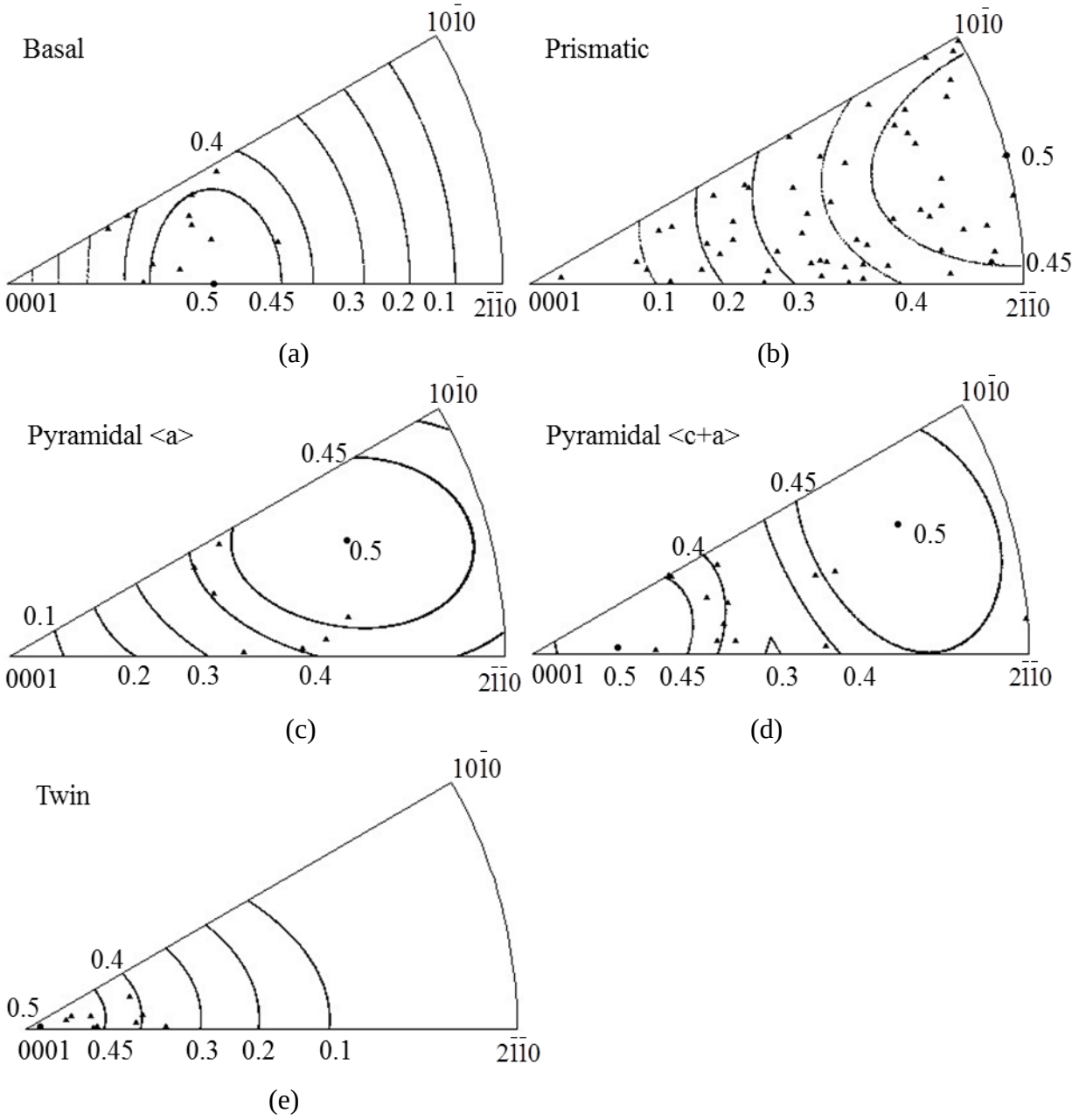

Figure 4.12 Unit triangle plots of grains which exhibited (a) basal, (b) prismatic, (c) pyramidal <a>, and (d) pyramidal <c+a> slip and (e) T1 twin for the CP Ti 728K tension test deformed to ~11.2% strain with Schmid factor contours overlaid.

4.1.3 *In-situ* 728K-45MPa creep

One *in-situ* creep test was performed on CP Ti at 728K with a constant stress of 45MPa, which was equivalent to 73% of the YS at 728K. Figure 4.13 shows an EBSD IPF map in the tensile direction and the corresponding {0001} and $\{10\bar{1}0\}$ pole figures from the gage section of the 728K-45MPa creep tested specimen. There were approximately 450 α grains in Figure 4.13 and no prevalent color was observed, indicating that the CP Ti was not strongly textured. Similar to the texture of the tensile-tested specimens in Figure 4.3 (b) and Figure 4.9 (b), the {0001} peak locations in Figure 4.13 (b) were aligned almost perpendicular to the transverse direction and a weak fiber texture (approximately four times random) was observed.

Figure 4.14 shows the sequential SE SEM images taken from the same area of the specimen during the 728K-45MPa tensile-creep test for the CP Ti specimen. Grain boundary ledges were first observed at ~1.4% strain (see Figure 4.14 (b), prior to any noticeable surface slip-trace formation. At larger strain levels (see Figure 4.14 (c)-(f)), almost all the grains developed identifiable traces and some grains exhibited more than one active deformation system. At ~6% strain, ~86% of grains in Figure 4.14 (c) exhibited slip/twin traces. This percentage was close to that (~80%) for the 296K tension test at ~8.4% strain and that (~84%) for the 728K tension test at ~8% strain. At ~23.2% strain in Figure 4.14 (f), this percentage increased to ~97%. Grain boundary ledges became more evident at larger strain levels.

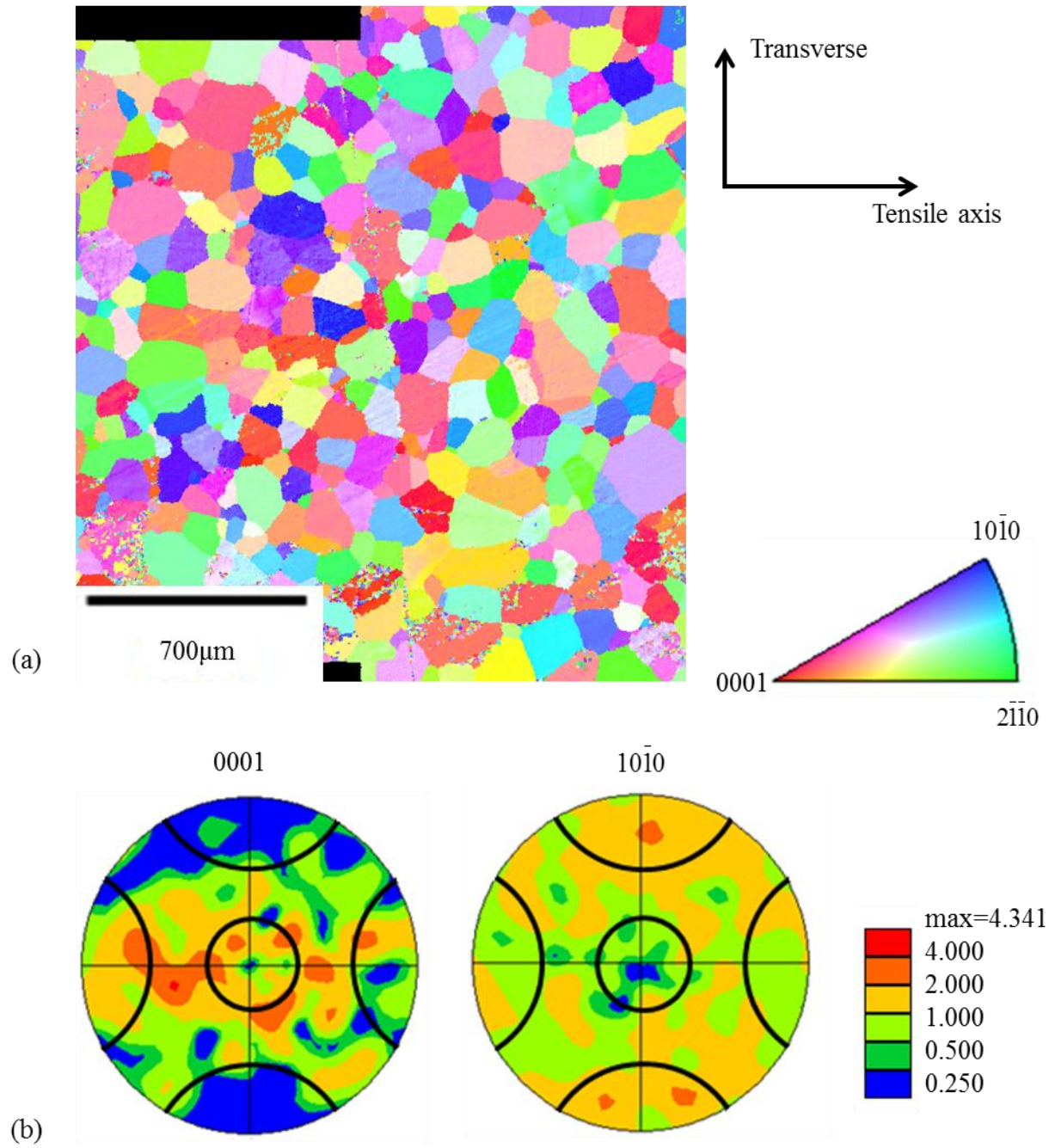

Figure 4.13 EBSD data of the CP Ti 728K-45MPa tensile-creep tested specimen: (a) EBSD IPF map in the tensile direction of the α-phase Ti containing approximately 450 α grains, (b) the $\{0001\}$ and the $\{10\bar{1}0\}$ pole figures with 30 ° cones along the major axes. The intentional scratch on the middle of the EBSD map was used as a fiducial marker. The loading direction was horizontal.

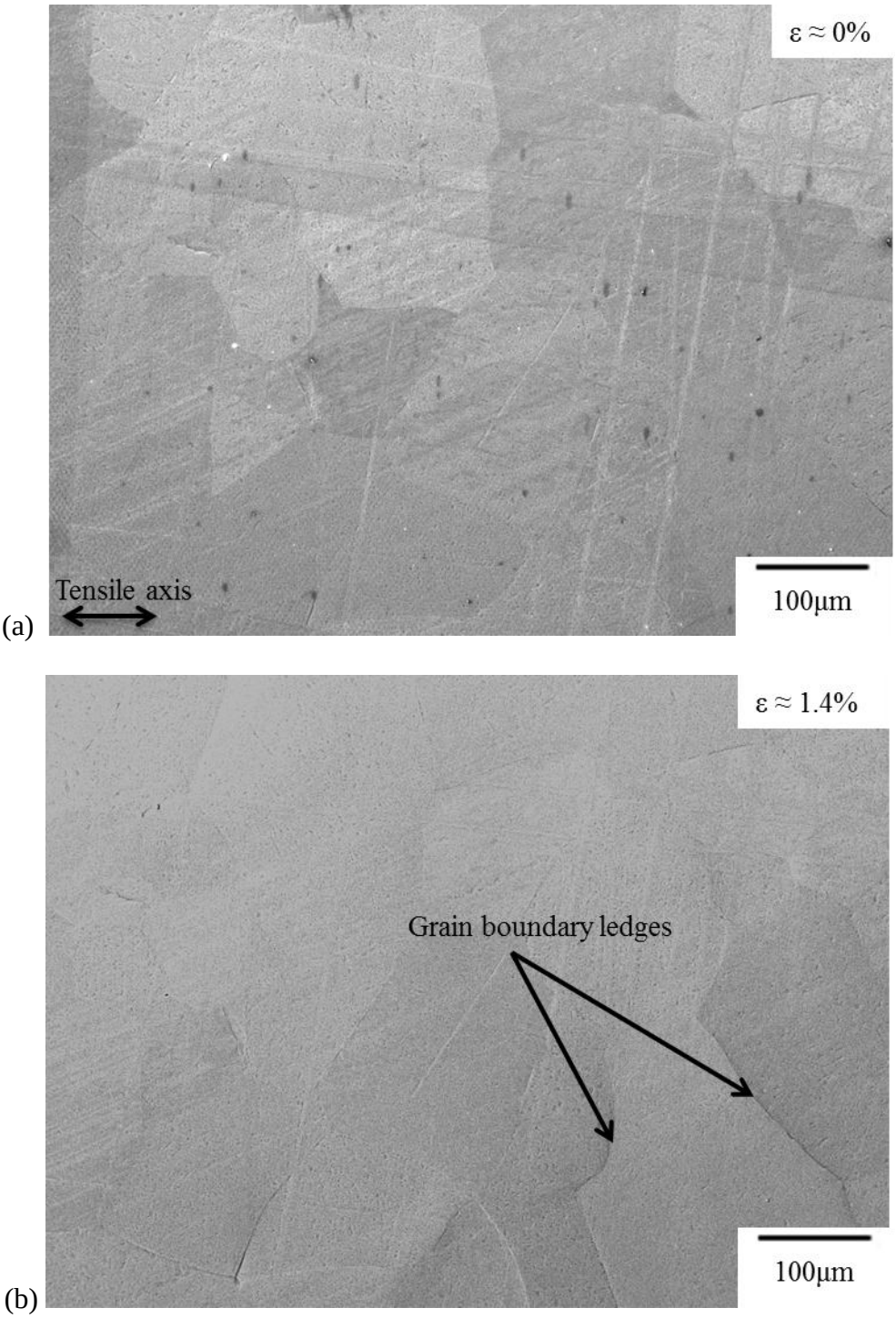

Figure 4.14 Sequential SE SEM images for CP Ti tensile-creep tested at 728K-45MPa: (a) undeformed; (b) ~1.4% strain,86h; (c) ~6.0% strain, 90h (when slip bands were first observed); (d) ~16.7% strain, 91.5h; (e) ~21.1%, 95h; and (f) ~23.2% strain,120h. Grain boundary ledges were observed at ~1.4% strain, prior to any dislocation slip becoming evident. The loading direction was horizontal.

Figure 4.14 (cont'd)

(c)

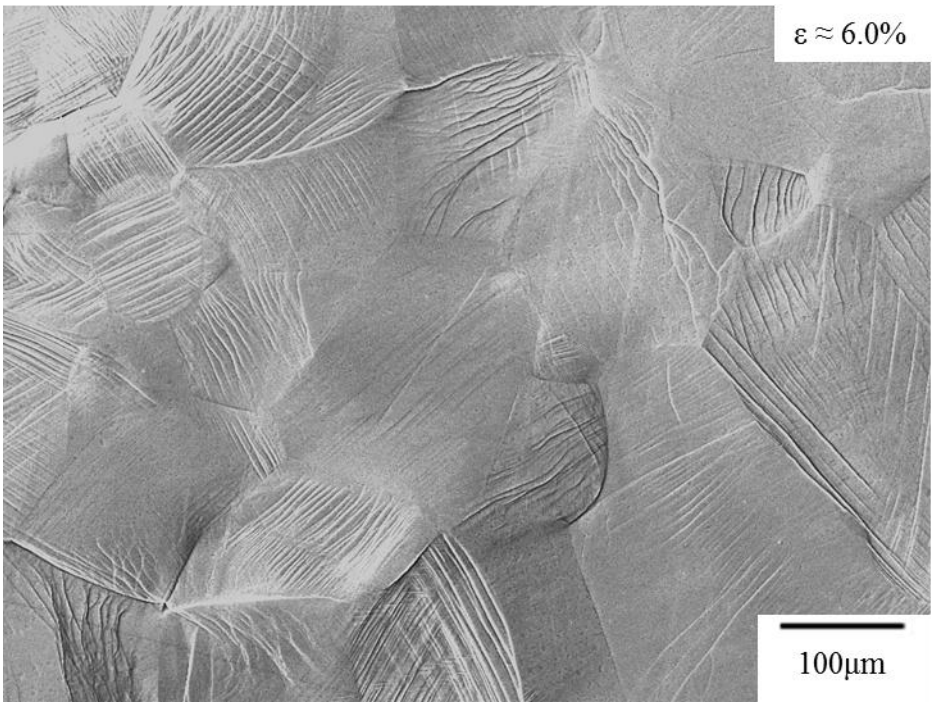

(d)

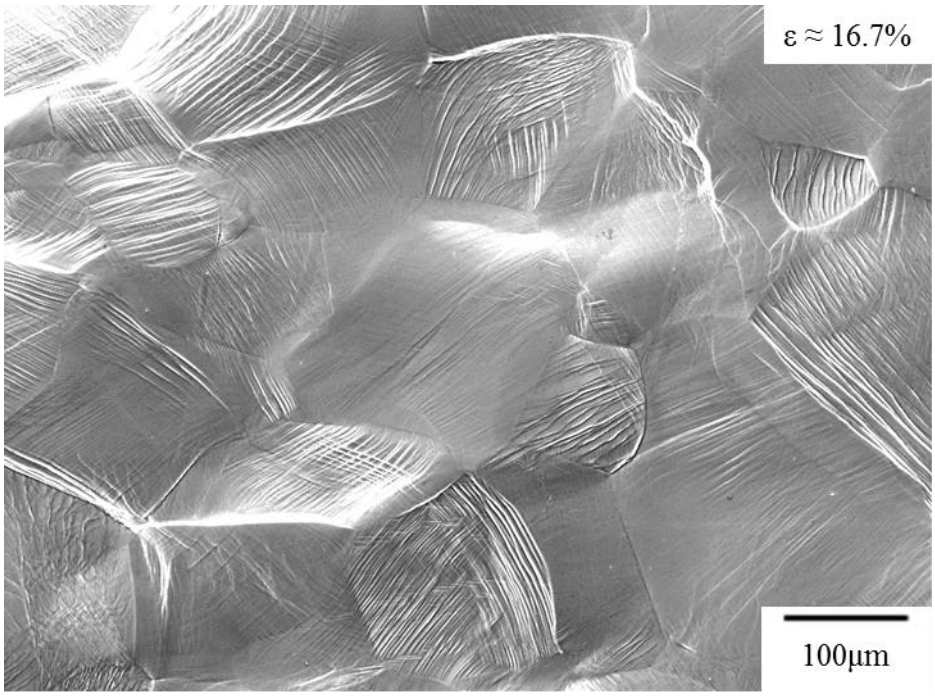

Figure 4.14 (cont'd)

(e)

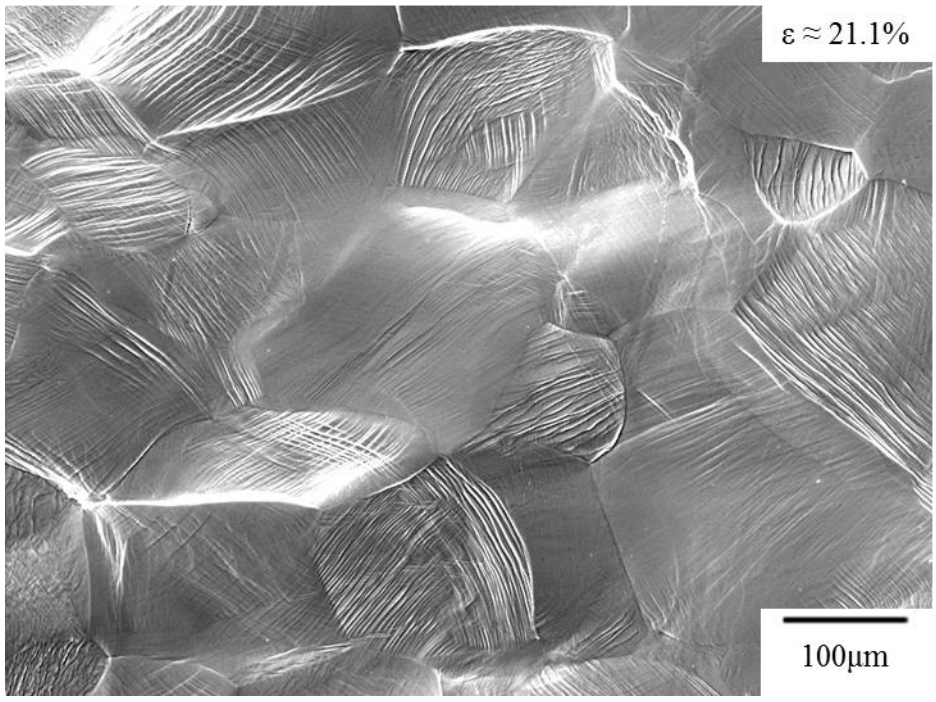

(f)

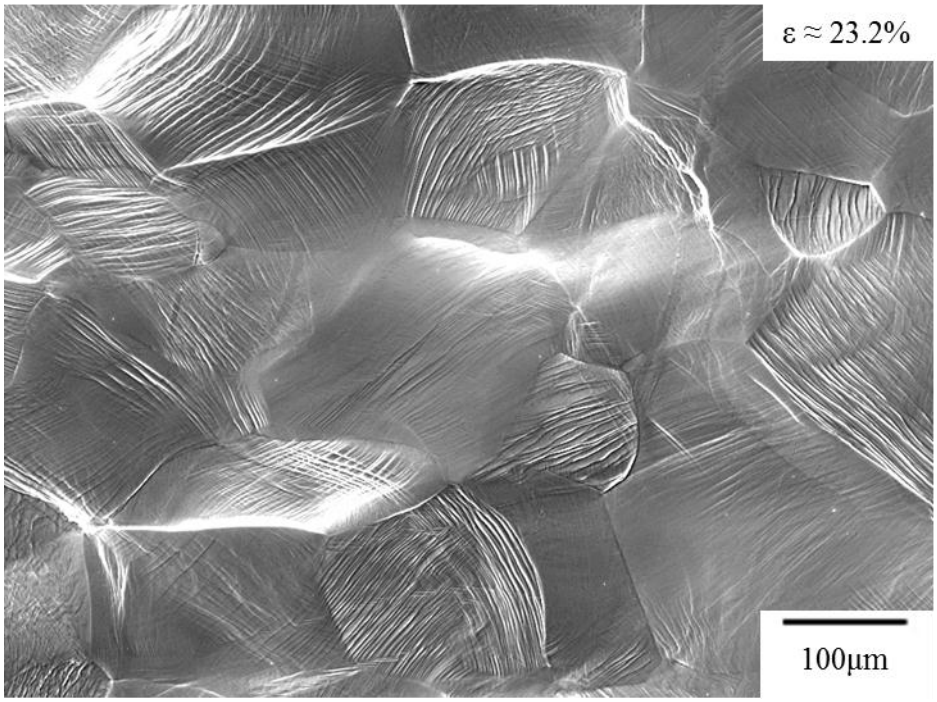

Slip-trace analysis was performed for 107 grains and 162 individual deformation systems were identified, see Figure 4.15. 15 basal (15/162≈9%), 104 prismatic (104/162≈64%), 22 pyramidal <a> (22/162≈14%), and 16 pyramidal <c+a> (16/162≈10%) slip were identified, along with 5 twinning systems (3%). Similar to the tension tests, prismatic slip was the dominant deformation mode, and it was activated over the largest global Schmid factor range (0-0.5). Basal, pyramidal <a>, and pyramidal <c+a> slip systems were only observed with Schmid factors greater than 0.25 and comprised 9%, 14%, and 10% of the total deformation systems, respectively (see Figure 4.15). Twinning was also observed but to a much lesser extent; i.e. only 3% of the total deformation systems (see Figure 4.15).

Figure 4.16 shows the stereographic triangles with the grain orientations plotted for basal, prismatic, pyramidal <a>, pyramidal <c+a>, and twinning deformation modes with Schmid factor contours overlaid. Similar to the tension tests for the CP Ti, grains with prismatic slip activated over the entire unit triangle. Some grains exhibited prismatic slip with very low Schmid factors (<0.1). Basal, pyramidal <a>, and pyramidal <c+a> slip and twinning were confined to the high Schmid factor regions.

Overall, dislocation slip was the primary deformation mechanism for both the CP Ti 728K-45MPa creep and the CP Ti 728K tensile test. Prismatic slip was the dominant deformation system under both testing conditions. There was less twinning activity during creep compared to the elevated temperature tensile test.

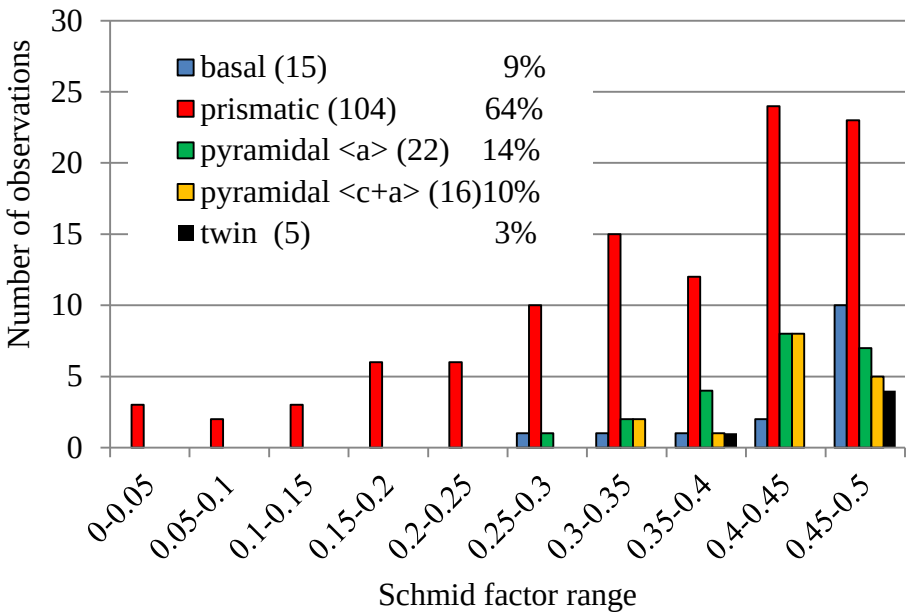

Figure 4.15 A histogram of the Schmid factor distribution of basal, prismatic, pyramidal <a>, and pyramidal <c+a> slip systems and T1 twinning systems for the CP Ti 728K-45MPa tensile-creep experiment after ~23.2% strain.

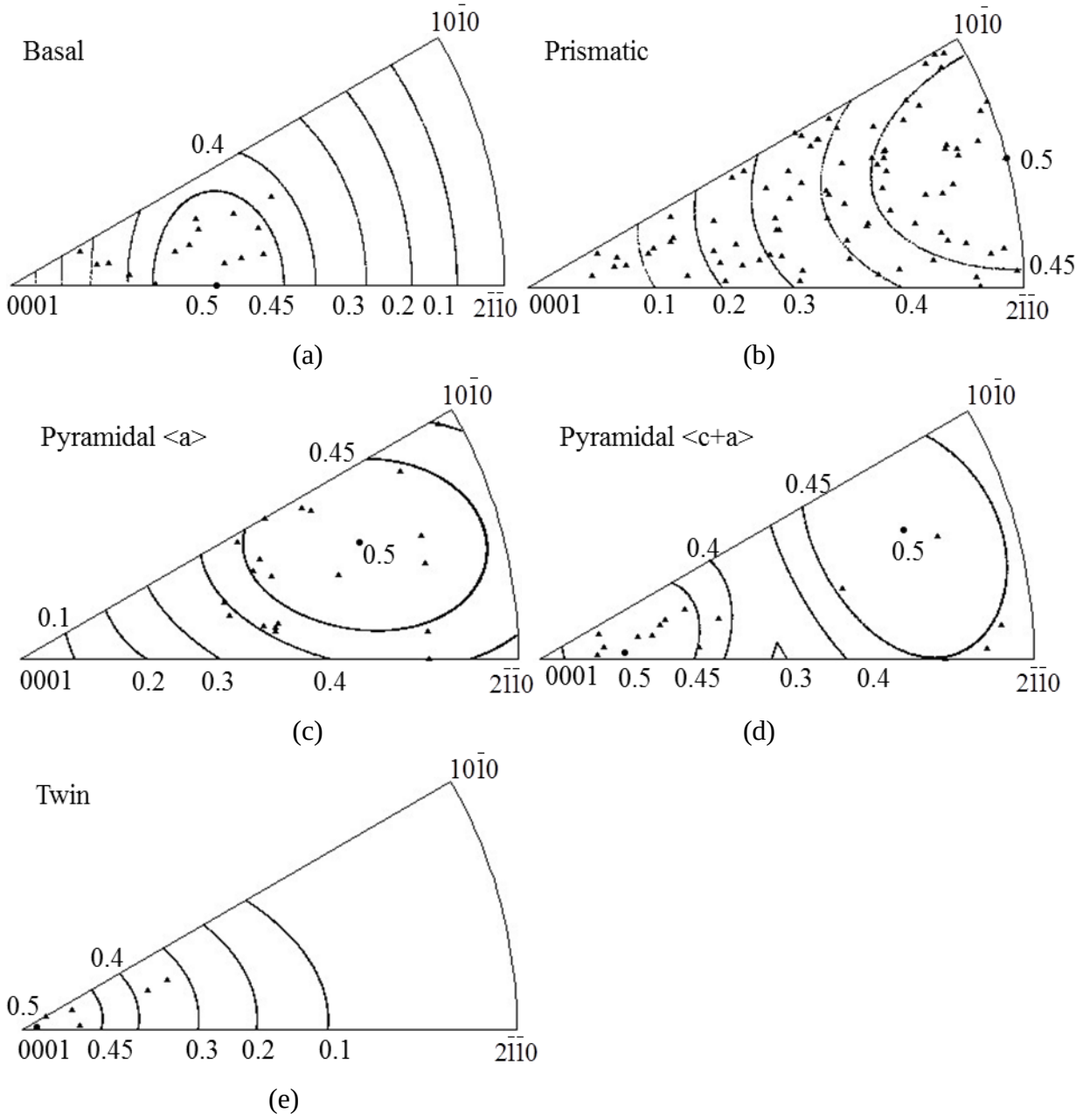

Figure 4.16 Unit triangle plots of grains which exhibited (a) basal, (b) prismatic, (c) pyramidal <a>, and (d) pyramidal <c+a> slip and (e) T1 twin for the CP Ti 728K-45MPa tensile-creep test deformed to ~23.2% strain with Schmid factor contours overlaid.

4.2 Ti-5Al-2.5Sn

4.2.1 Microstructure

The low- and high-magnification BSE and SE images of the as-received near-α Ti-5Al-2.5Sn alloy microstructure are shown in Figure 4.17. The BCC β phase was observed at some of the equiaxed α-phase grain boundaries and consisted of less than 1% of the specimen volume. The average α grain size was 39.5±10.0μm, as measured by the line-intercept method [ASTM 2004].

4.2.2 XRD

XRD was used to investigate the bulk texture of the as-received Ti-5Al-2.5Sn, shown in Figure 4.18. The XRD result shows a weak texture (an approximately four times random). The {0001} peak locations were on the 30° cone along the specimen normal direction. EBSD scans were also performed to investigate the texture for each of the *in-situ* tested specimens and the results of each specimen will be presented in the following sections. Macrozones were not observed in any of the Ti-5Al-2.5Sn specimens.

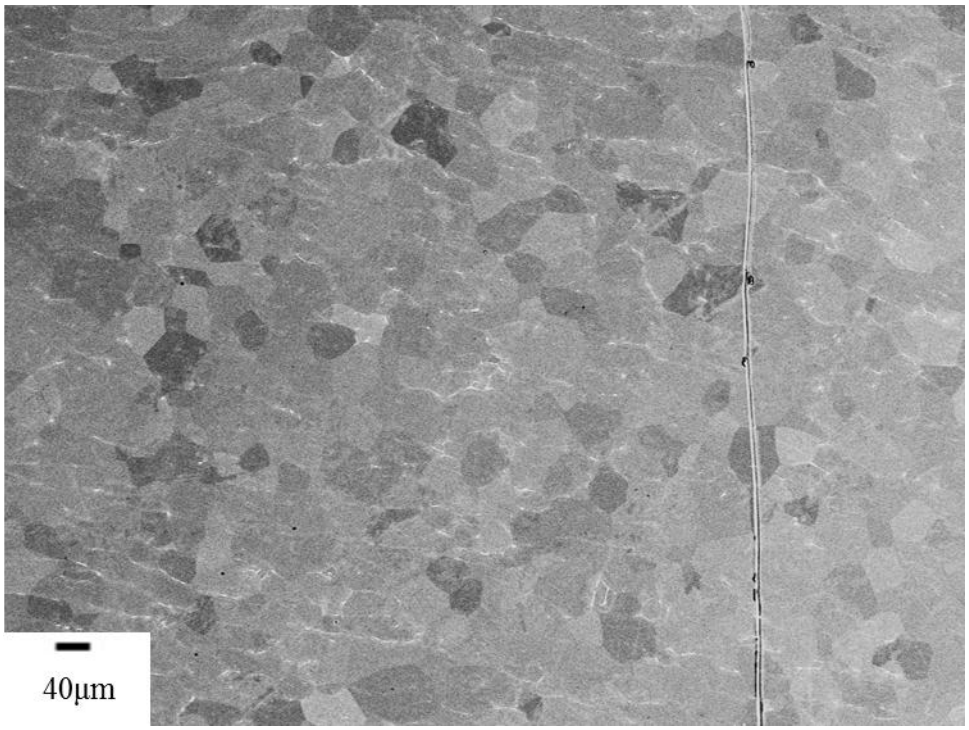

(c) Low-magnification BSE SEM image

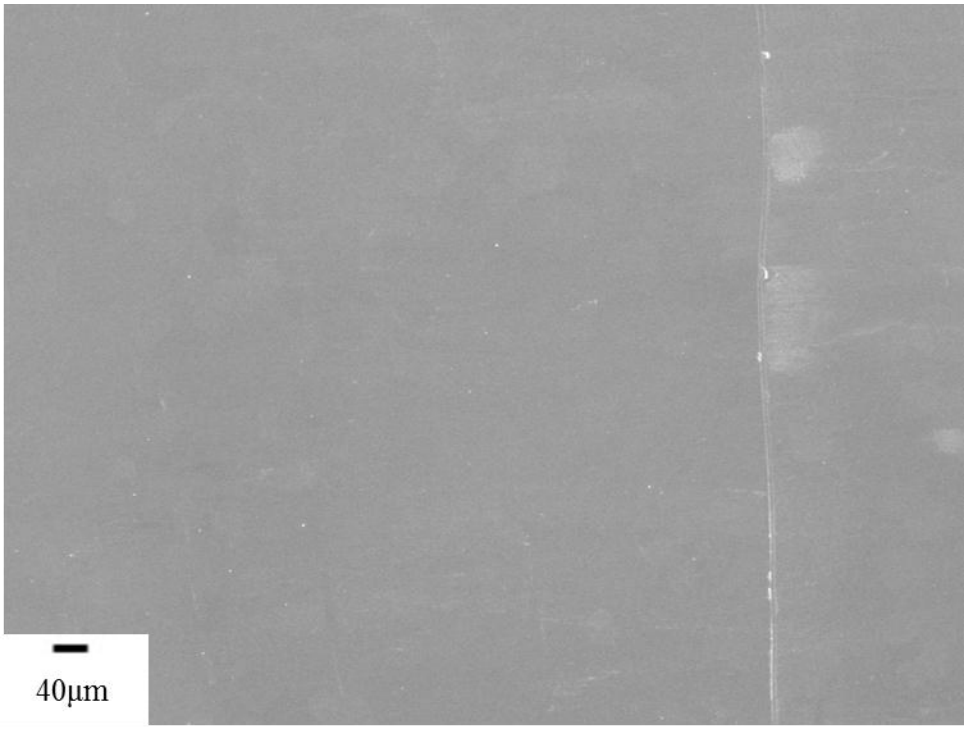

(d) Low-magnification SE SEM image

Figure 4.17 (a)-(b) Low- and (c)-(d) high-magnification SE SEM and BSE SEM images of the same area for the as-received near-α Ti-5Al-2.5Sn alloy. The intentional scratch on the right of (a) and (b) was used as a fiducial marker.

Figure 4.17 (cont'd)

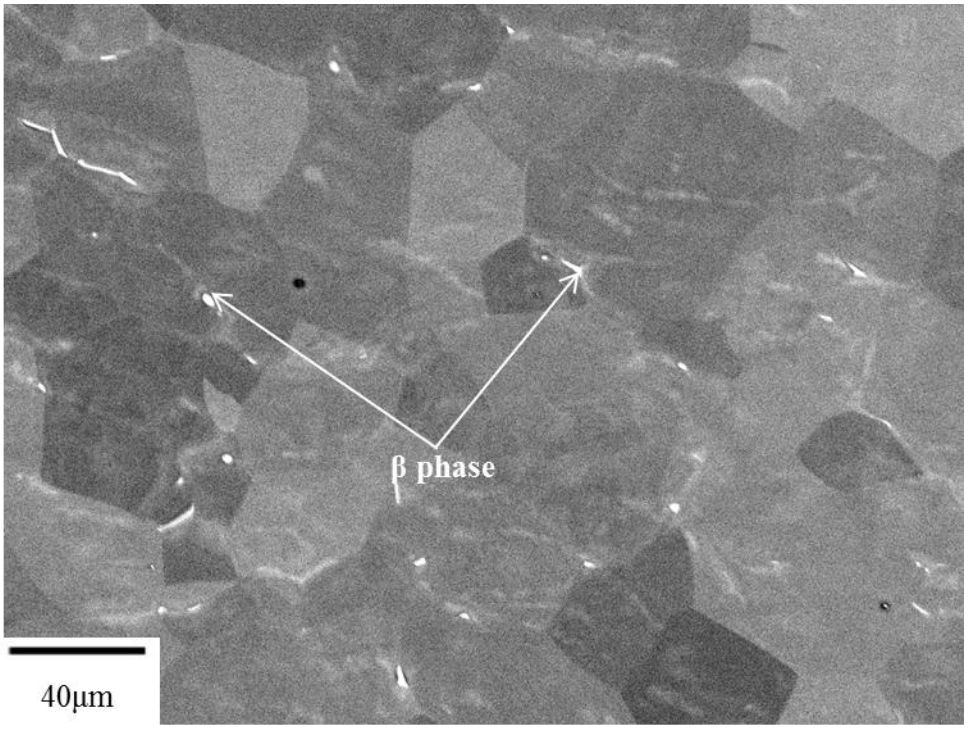

(c) High-magnification BSE SEM image

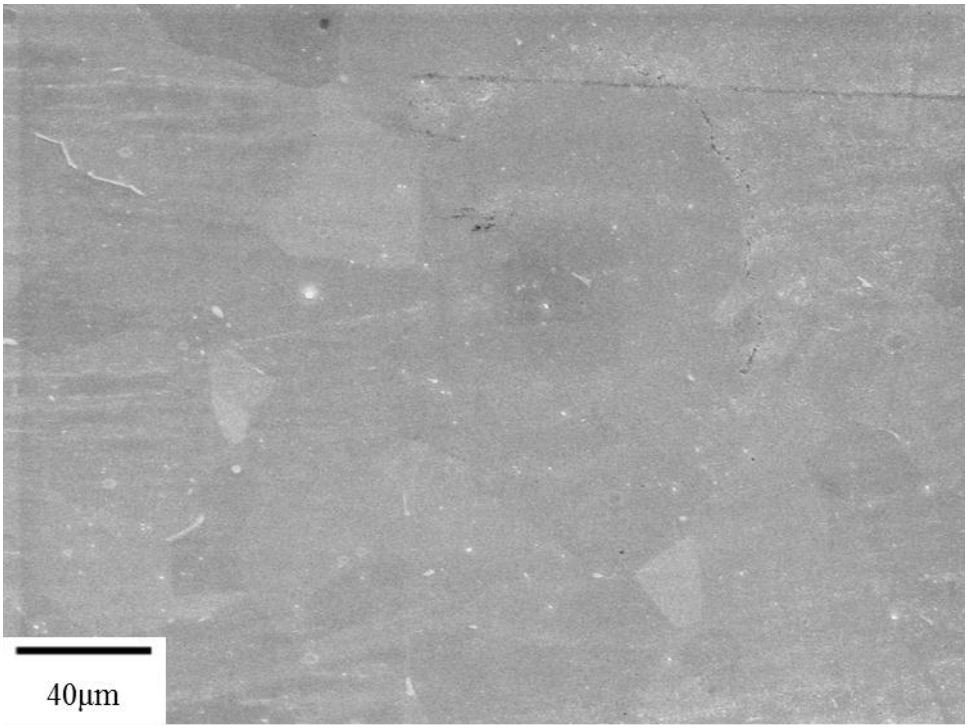

(d) High-magnification SE SEM image

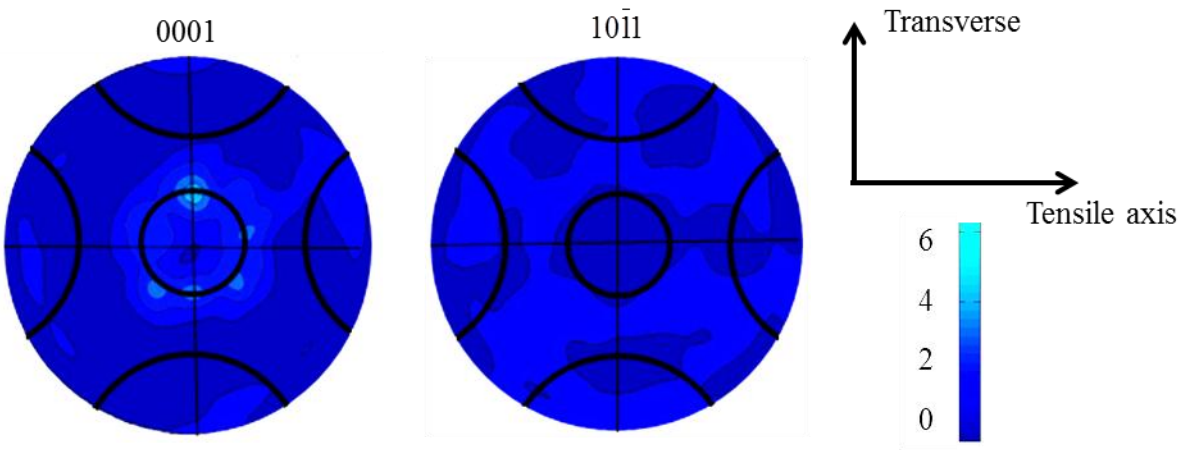

Figure 4.18 {0001} and $\{10\bar{1}1\}$ pole figures with 30° cones along the major axes of the Ti-5Al-2.5Sn alloy measured using XRD.

4.2.3 *In-situ* tension

In-situ tensile tests were performed on the Ti-5Al-2.5Sn at 296K and 728K. One test was performed for each temperature. The engineering stress versus displacement curves for the 296K and 728K tensile tests are illustrated in Figure 4.19. Similar to the CP Ti tension in Figure 4.2, load drops occurred when the tests were paused for imaging. None of the specimens were taken to failure and a minimum local strain of ~3.5% was achieved. The YS of the Ti-5Al-2.5Sn decreased from ~660MPa to ~330MPa with increasing temperature from 296K to 728K. These values are comparable to those found in the literature [Boyer et al. 1994], shown in Table 4.2.

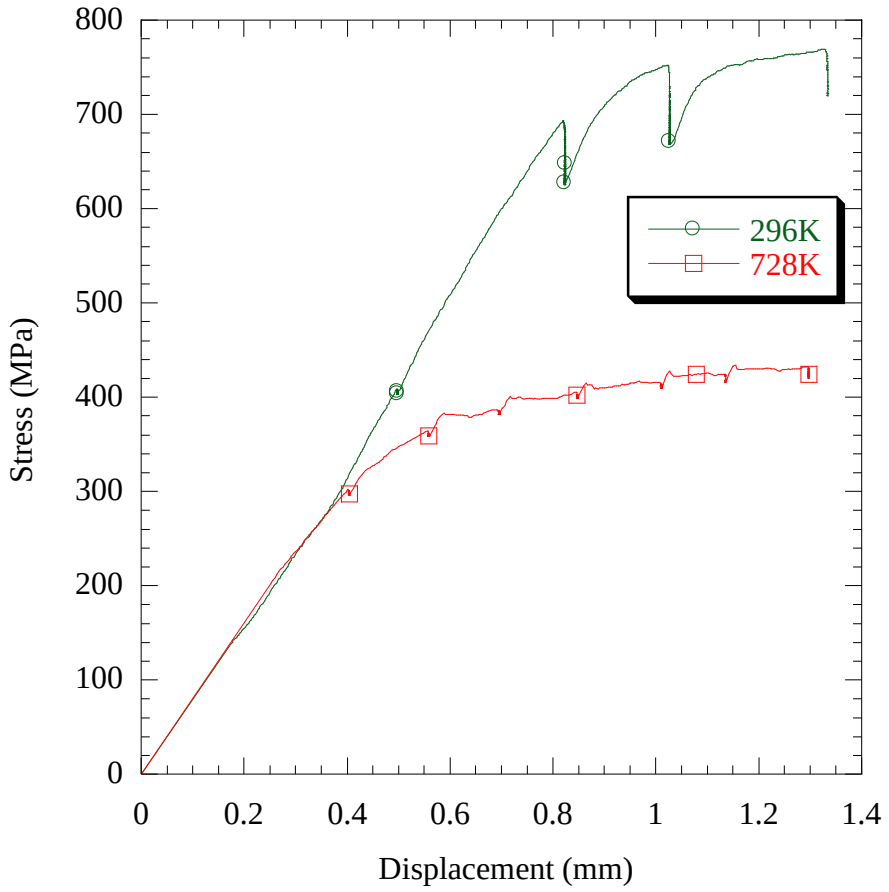

Figure 4.19 Stress vs. displacement plots for Ti-5Al-2.5Sn samples tensile tested at 296K and 728K. The load drops indicate that stress relaxation occurred when the tests were interrupted for imaging. The displacement values were taken from the testing systems, which included displacement in the grip region.

Table 4.2 Ti-5Al-2.5Sn tensile property comparison between the experiments in the current work and the Ti handbook by Boyer et al. [1994].

Test temperature	YS (MPa)	Max Stress (MPa)	YS (MPa) in Boyer et al.	UTS (MPa) in Boyer et al.	Comment
296K	~660	769	620	689	Minimum tensile properties
728K	~330	434	~400	450-500	Annealed material

4.2.3.1 296K tension

Figure 4.20 shows the EBSD IPF map in the tensile direction and the corresponding $\{0001\}$ and $\{10\bar{1}0\}$ pole figures from the gage section of the 296K tensile-tested specimen for Ti-5Al-2.5Sn. There were approximately 860 α grains in Figure 4.20. Ti-5Al-2.5Sn exhibited a weak texture (an approximately three times random). The value of the maximum intensity was similar to the XRD texture results in Figure 4.18 while the locations with the maximum intensities in Figure 4.20 varied from the XRD texture results. The locations with maximum intensities of the $\{0001\}$ pole figure in Figure 4.18 were on a 30° cone along the specimen normal, while they were near the circumference of the pole figure in Figure 4.20.

Figure 4.21 shows the *in-situ* BSE SEM images of the same area at different stress/strain levels for the Ti-5Al-2.5Sn tensile-tested specimen at 296K. Slip traces were first observed at a global stress of 690MPa (~0.5% strain, see Figure 4.21 (b)), which was just above the approximate YS (~660MPa). At ~0.5% strain, most of the slip traces were identified to be basal slip systems with Schmid factors greater than 0.37 (highlighted by blue lines). A few prismatic slip traces with high Schmid factors (highlighted by red lines) were also observed. After ~3.5% deformation, ~93% of grains exhibited slip and multiple slip traces within single grain were commonly observed. However, wavy slip traces were rare, indicating that cross-slip was not prevalent in the 296K tension deformation.

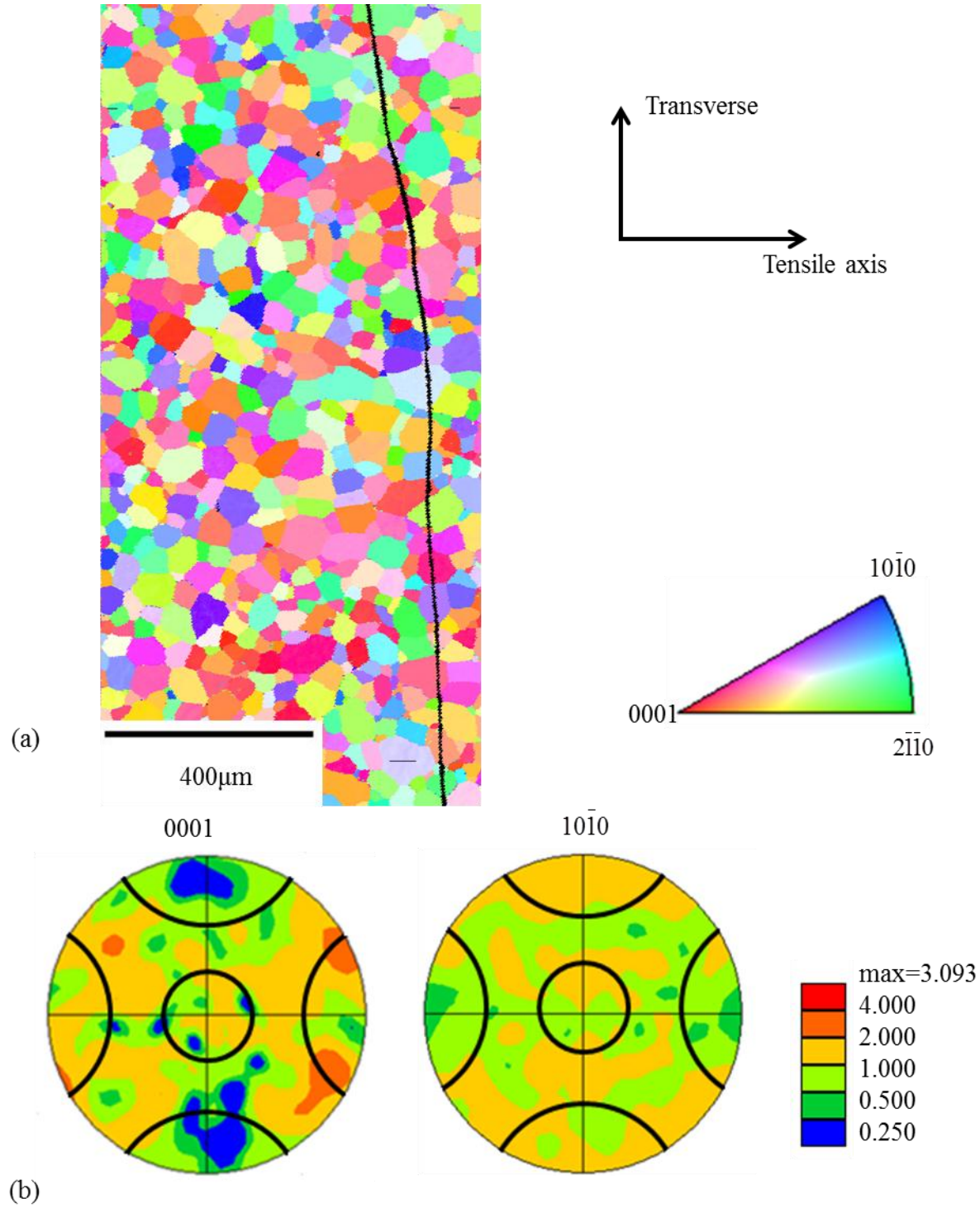

Figure 4.20 EBSD data of the Ti-5Al-2.5Sn 296K tensile-tested specimen: (a) EBSD IPF map in the tensile direction of the α-phase Ti containing approximately 860 α grains, (b) the {0001} and the $\{10\bar{1}0\}$ pole figures with 30° cones along the major axes. The intentional scratch on the right of the EBSD map was used as a fiducial marker. The loading direction was horizontal.

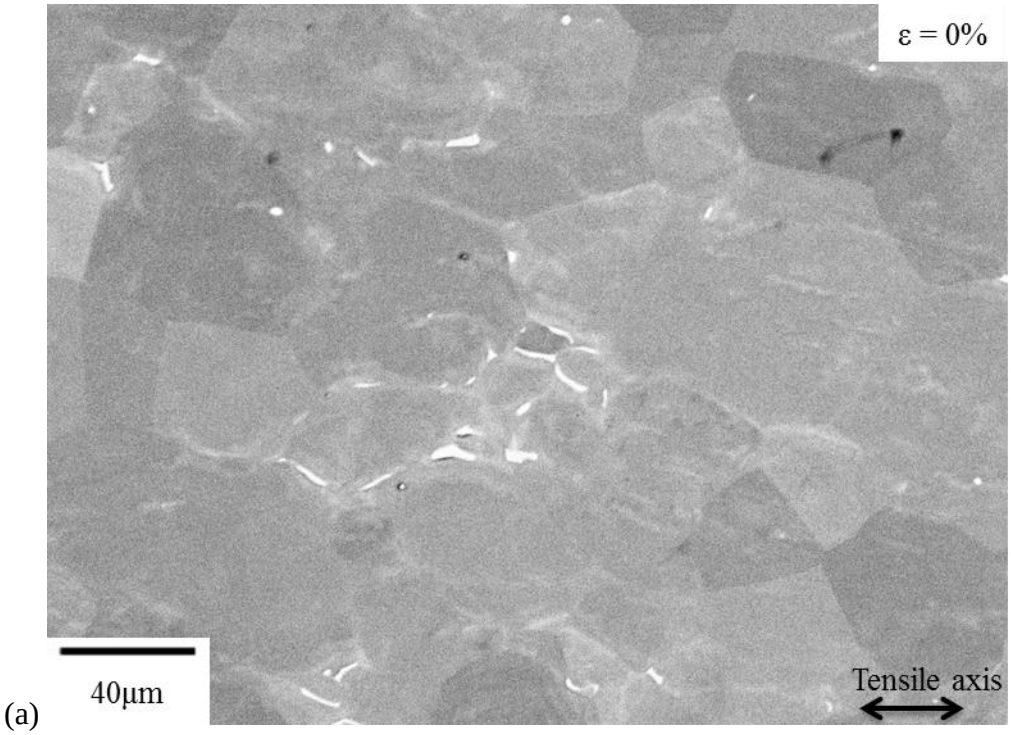

(a)

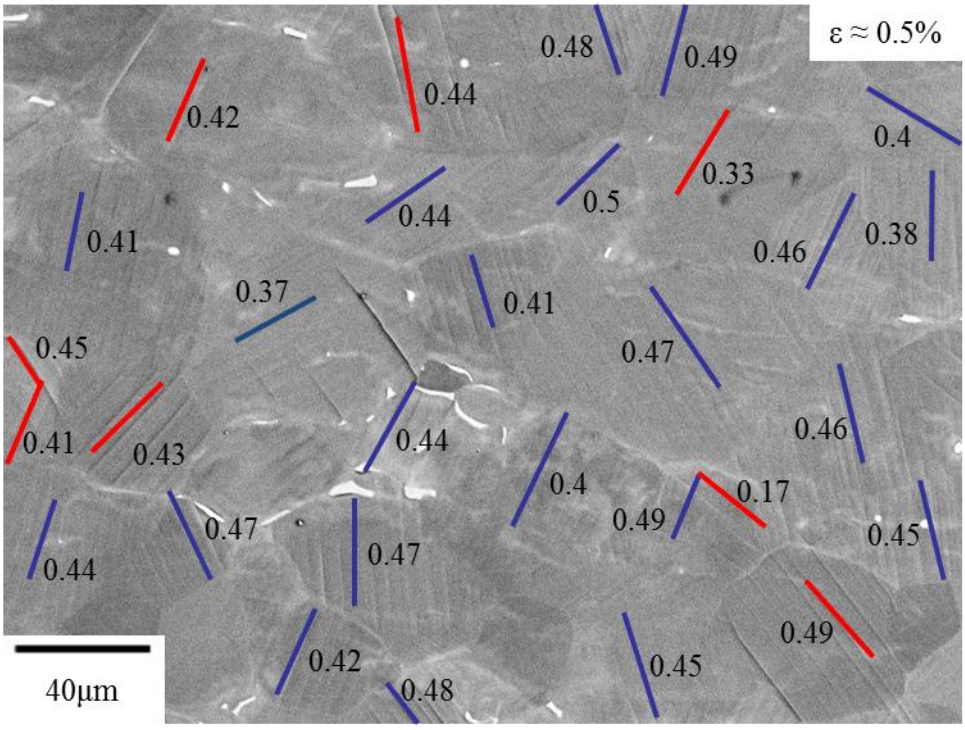

(b)

Figure 4.21 Sequential BSE SEM images for Ti-5Al-2.5Sn tensile tested at 296K: (a) undeformed, (b) 690MPa (~0.5% strain, when slip bands were first observed), the color-coded planes traces for prismatic slip (red) and basal slip (blue) are labeled along with their Schmid factors, (c) 746MPa (~1.6% strain), and (d) 762MPa (~3.5% strain). The loading direction was horizontal.

Figure 4.21(cont'd)

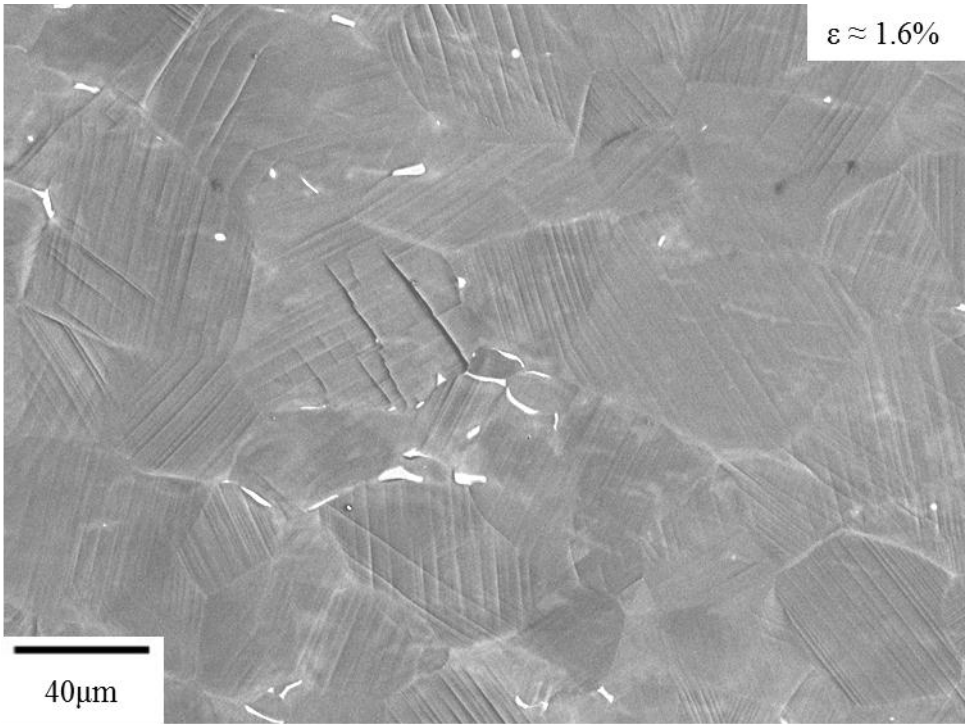

(c)

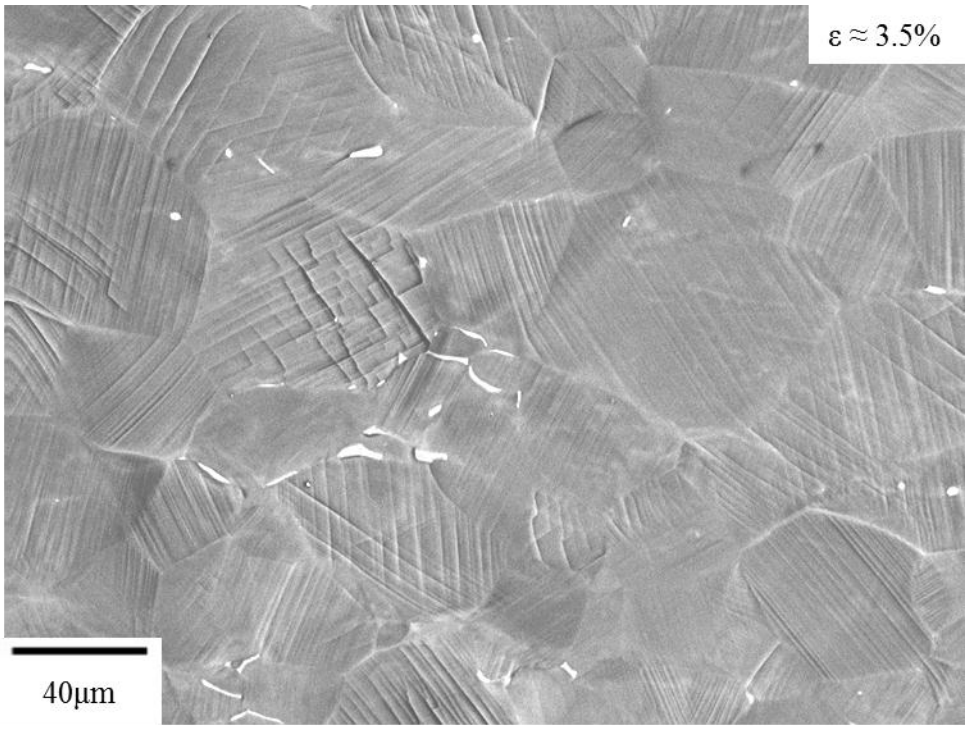

(d)

Figure 4.22 shows the EBSD IPF maps in the tensile direction for the same area in Figure 4.21 and the corresponding grain orientation spread distributions before and after deformation. Before deformation, the grain colors within each individual grain were relatively uniform and the grain orientation spread was within 1 degree, which is within the uncertainty of the typical EBSD angular measurements [Wilkinson 1996], as shown in Figure 4.22 (a) and (c). After ~3.5% strain, the grain orientation gradient increased up to two degrees, as shown in Figure 4.22 (b) and (c). Comparing Figure 4.22 (c) with the Figure 4.5 (c) for the CP Ti tensile tested at 296K, the extent of grain orientation spread after the deformation was much smaller in Figure 4.22 (c) for Ti-5Al-2.5Sn than in Figure 4.5 (c) for CP Ti. This is not surprise as the final strain imposed in the CP Ti (~8.4%) was larger than the Ti-5Al-2.5Sn (~3.5%).

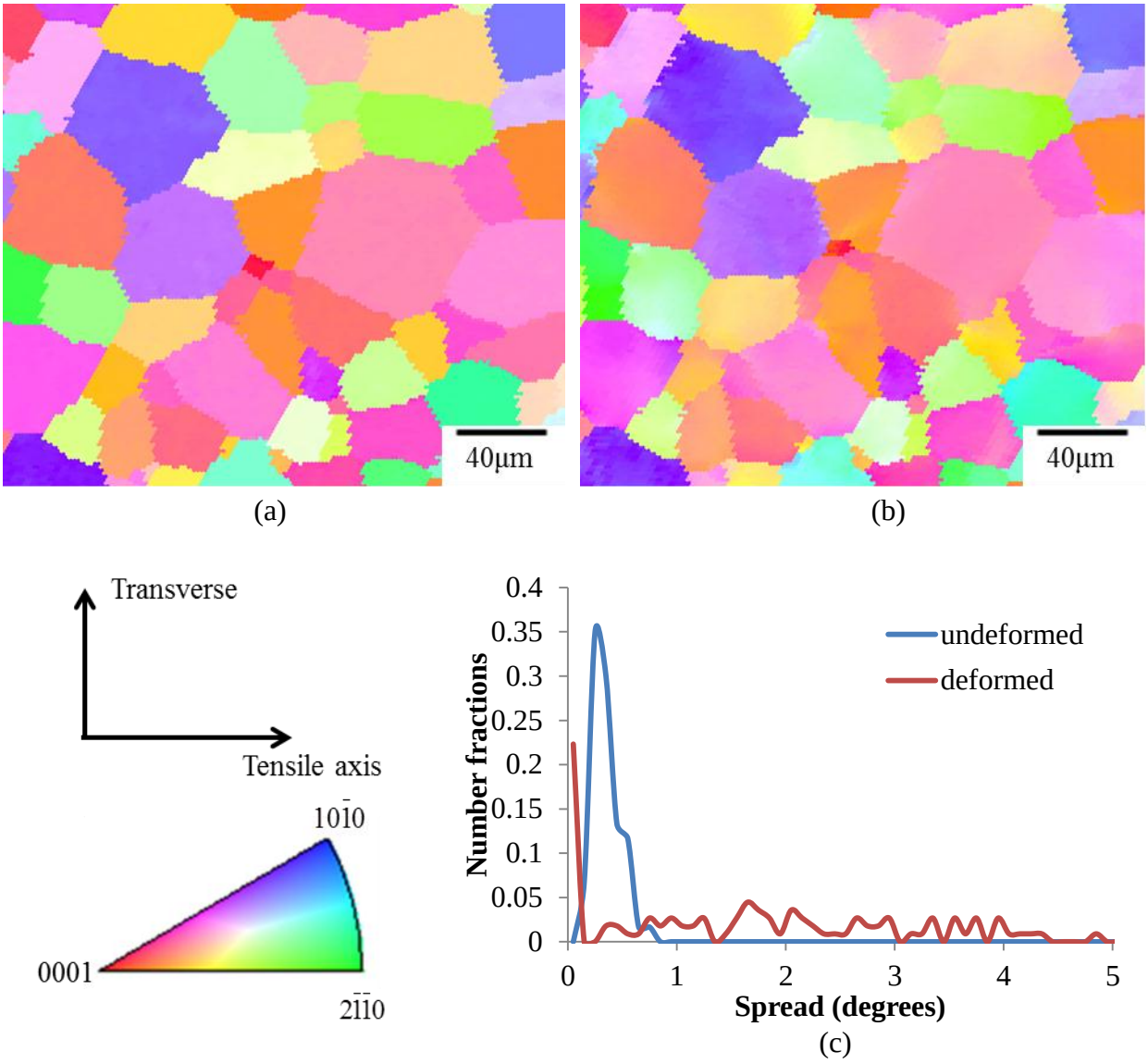

Figure 4.22 EBSD IPF maps in the tensile direction for the same area in the tensile-tested sample for Ti-5Al-2.5Sn at 296K (a) before and (b) after ~3.5% tensile strain. The grain orientation spread of the grains shown in (a) and (b) was plotted in (c).

The slip-trace technique was used to identify a total of 204 active slip systems in 137 α grains. In the 137 grains analyzed, 85 distinct basal slip systems (85/204≈42%) and 101 distinct prismatic slip systems (101/204≈50%) were identified (some grains exhibited multiple prismatic slip systems), with the remainder of the 204 active systems attributed to 7 pyramidal <a> (7/204≈3%) and 9 pyramidal <c+a> (9/204≈4%) slip systems and two T1 twinning systems (2/204≈1%). These observations indicated that basal and prismatic slip systems are the dominant deformation modes at 296K. Figure 4.23 summarizes the number of observations for the five deformation systems versus the global Schmid factor range. About 80% of the activated slip systems in these 137 grains exhibited Schmid factors greater than 0.3 for both basal and prismatic slip, based upon the global stress state tensor. As shown in Figure 4.23, the activation of basal slip was more associated with high Schmid factors, and basal slip with Schmid factors below 0.27 was not observed. However, some prismatic slip occurred with the corresponding Schmid factors less than 0.1, suggesting that prismatic slip was more easily activated than basal slip at 296K.

Figure 4.24 shows the stereographic triangles with the grain orientations plotted for basal, prismatic, pyramidal <a>, pyramidal <c+a>, and twinning deformation modes with Schmid factor contours overlaid. Basal, pyramidal <a>, and pyramidal <c+a> slip were generally confined to high Schmid factor regions. In contrast, prismatic slip was activated over the entire unit triangle (see Figure 4.24 (b)). Two T1 twins were observed and the Schmid factors were 0.27 and 0.47, respectively.

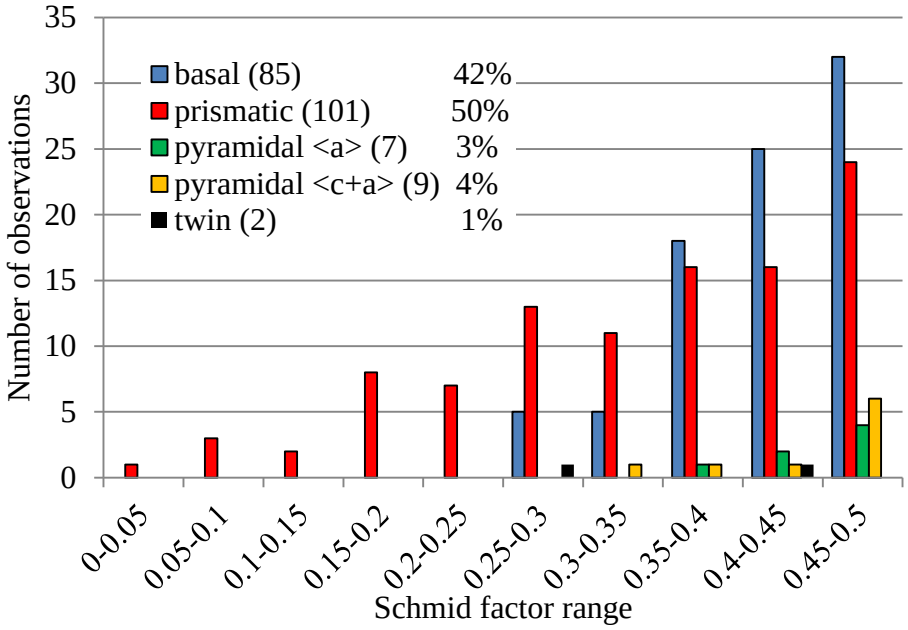

Figure 4.23 A histogram of the Schmid factor distribution of basal, prismatic, pyramidal <a>, and pyramidal <c+a> slip systems and T1 twinning systems for the Ti-5Al-2.5Sn 296K tension experiment after ~3.5% strain.

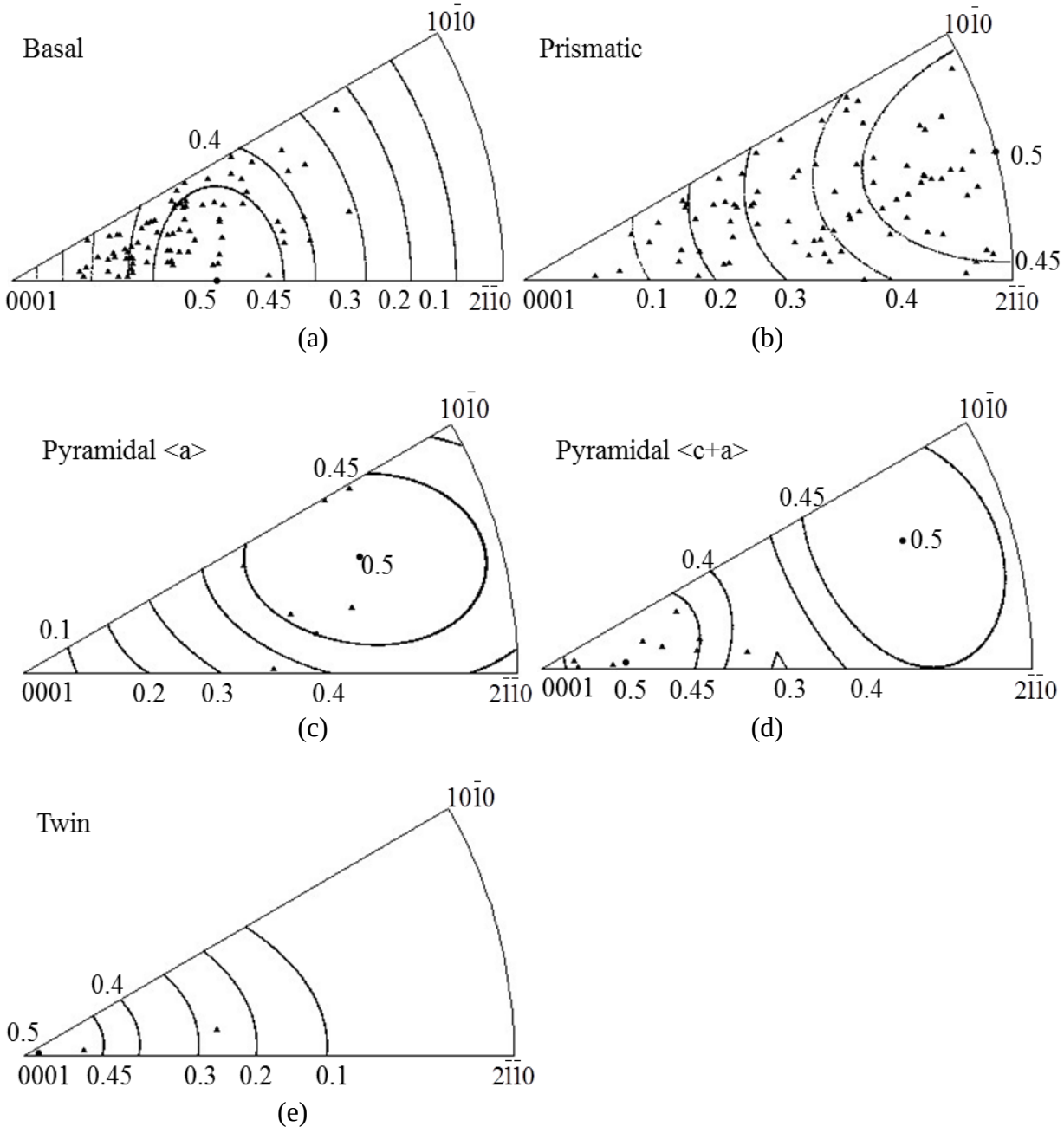

Figure 4.24 Unit triangle plots of grains which exhibited (a) basal, (b) prismatic, (c) pyramidal <a>, and (d) pyramidal <c+a> slip and (e) T1 twin for the Ti-5Al-2.5Sn 296K tension test deformed to ~3.5% strain with Schmid factor contours overlaid.

4.2.3.2 728K tension

Figure 4.25 shows an EBSD IPF map in the tensile direction and the corresponding $\{0001\}$ and $\{10\bar{1}0\}$ pole figures from the gage section of the 728K tensile-tested specimen for Ti-5Al-2.5Sn. There were approximately 870 α grains represented in Figure 4.25. Similar to the pole figures in Figure 4.20 and Figure 4.18, the 728K tensile specimen exhibited a weak texture (an approximately three times random). However, the locations with the maximum peak intensities in Figure 4.25 varied from the XRD texture results in Figure 4.18 and EBSD texture results in Figure 4.20.

Figure 4.26 shows the *in-situ* SE SEM images of the same area at different stress/strain levels for the Ti-5Al-2.5Sn tensile-tested specimen at 728K. Slip traces were first observed at a stress level of 301MPa (<0.5% strain, see Figure 4.26 (b)) and most of the slip traces were characterized to be basal slip systems with Schmid factors greater than 0.32 (highlighted by blue lines). Two prismatic slip systems (highlighted by red lines in Figure 4.26 (b)) were observed with Schmid factors of 0.19 and 0.49. In Figure 4.26 (b), slip traces were observed prior to the global yielding (~330MPa), indicating that microyielding occurred in this microstructural patch. After ~9% strain, ~94% grains exhibited slip traces and some grains exhibited more than one deformation system. Wavy slip lines were observed for grain labeled as "G" in Figure 4.26 (d), indicating the development of cross slip.

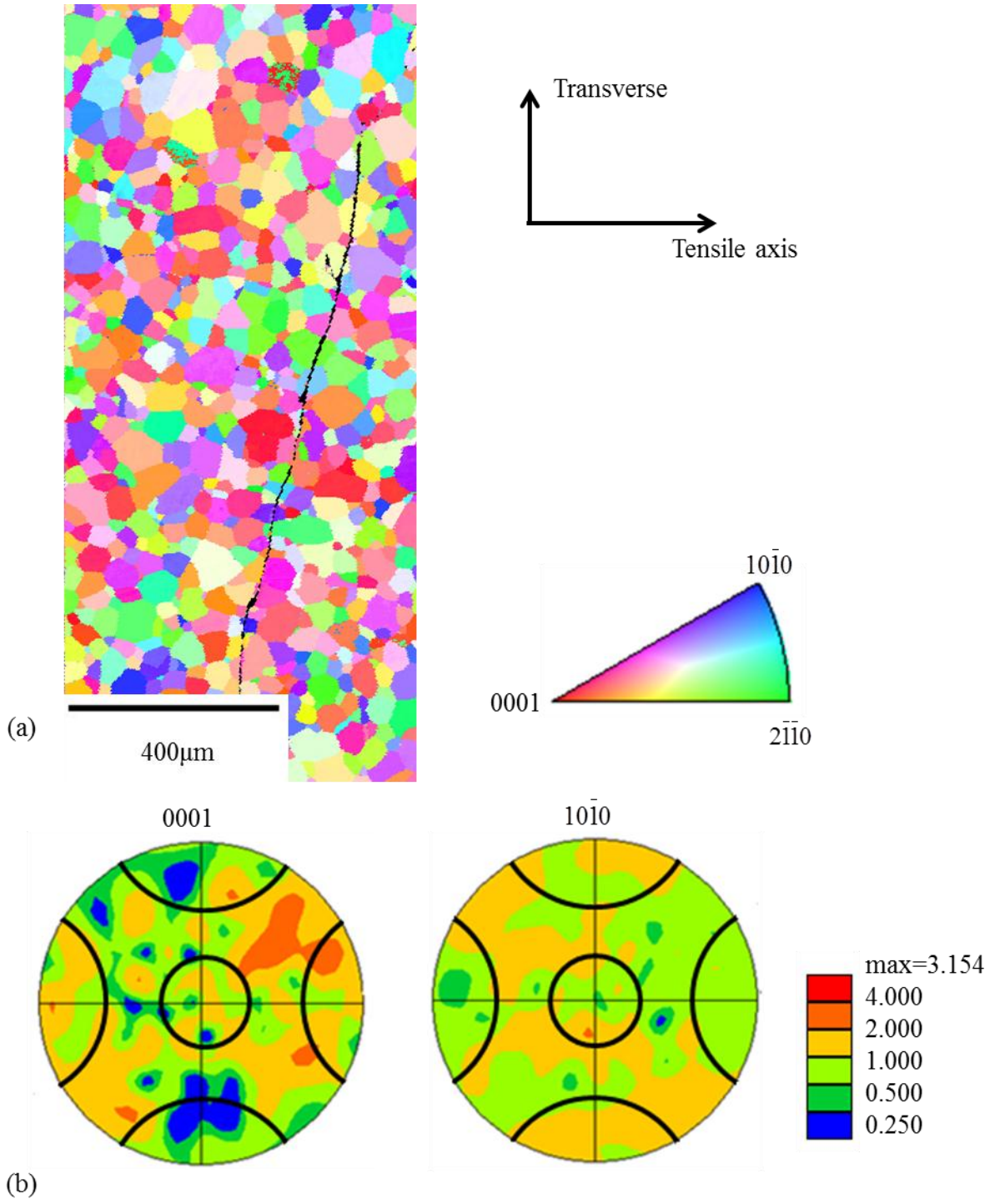

Figure 4.25 EBSD data of the Ti-5Al-2.5Sn 728K tensile-tested specimen: (a) EBSD IPF map in the tensile direction of the α-phase Ti containing approximately 870 α grains, (b) the {0001} and the $\{10\bar{1}0\}$ pole figures with 30° cones along the major axes. The intentional scratch in the middle of the EBSD map was used as a fiducial marker. The loading direction was horizontal.

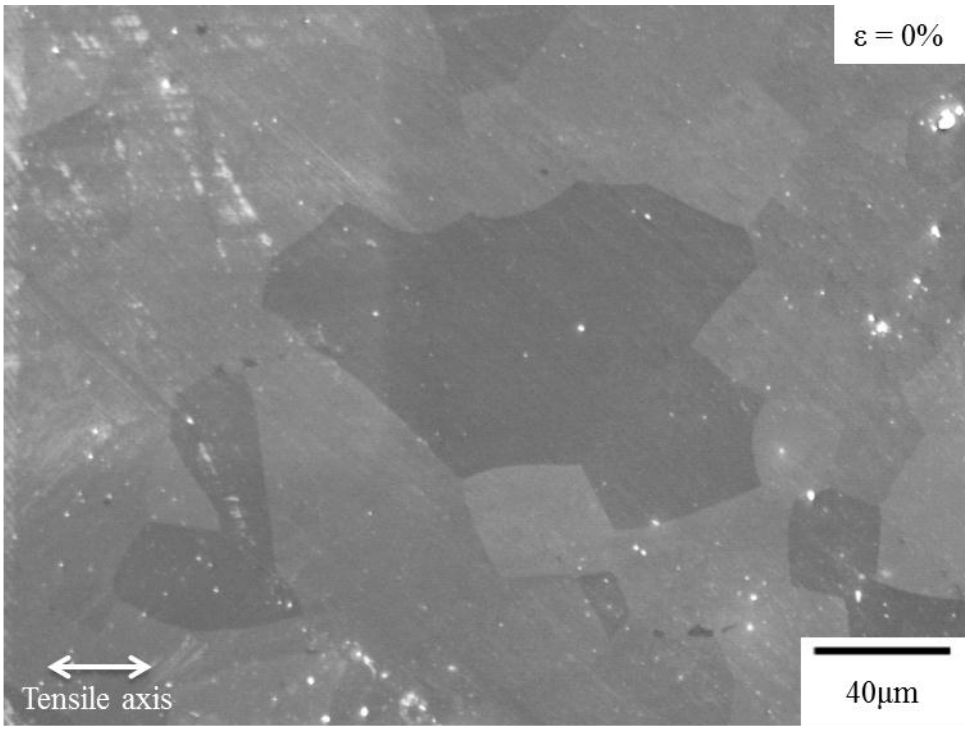

(a)

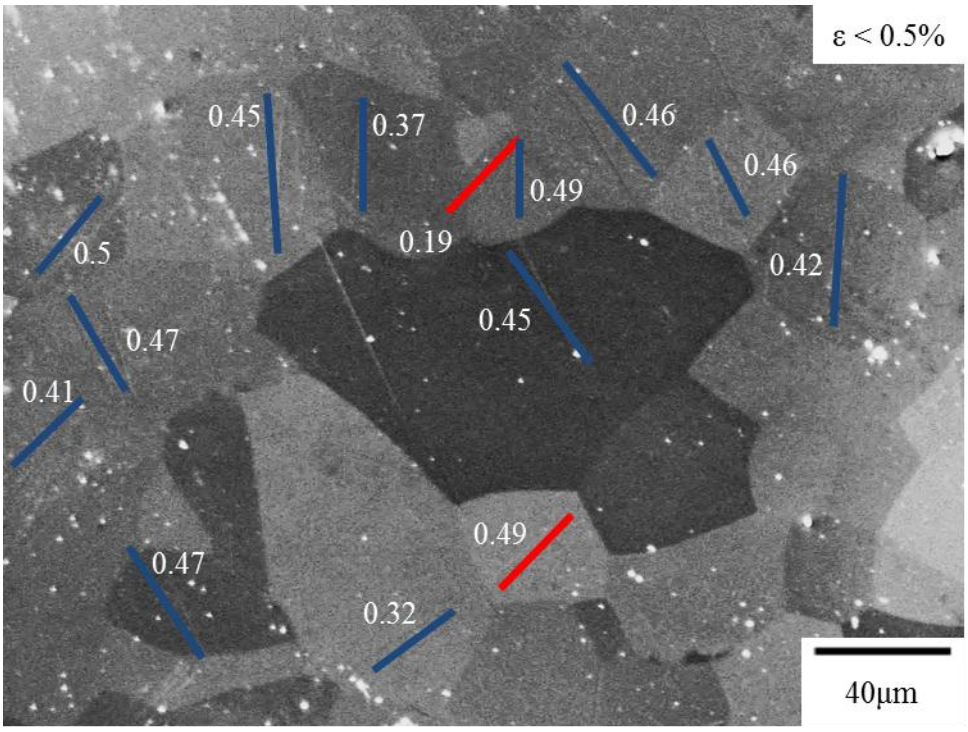

(b)

Figure 4.26 Sequential SE SEM images for Ti-5Al-2.5Sn tensile tested at 728K: (a) undeformed, (b) 301MPa (<0.5% strain, when slip bands were first observed), the color-coded planes traces for prismatic slip (red) and basal slip (blue) are labeled along with their Schmid factors, (c) 359MPa (~2.8% strain), and (d) 426MPa (~9% strain). Grain G in (d) is the cross slipped grain analyzed in Figure 4.29. The loading direction was horizontal.

Figure 4.26 (cont'd)

(c)

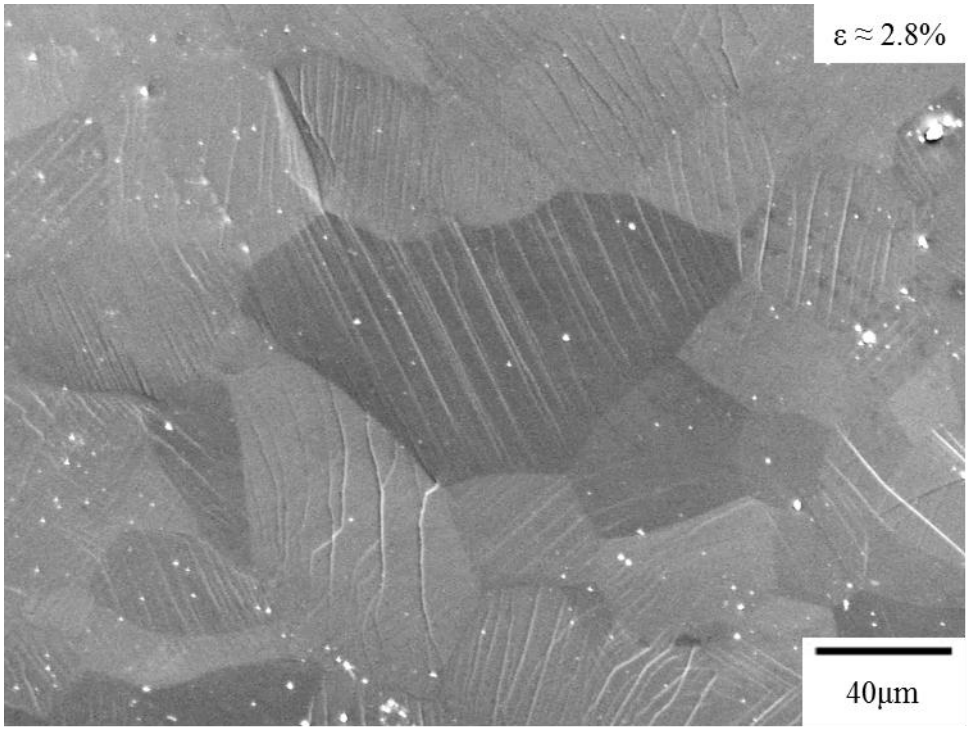

(d)

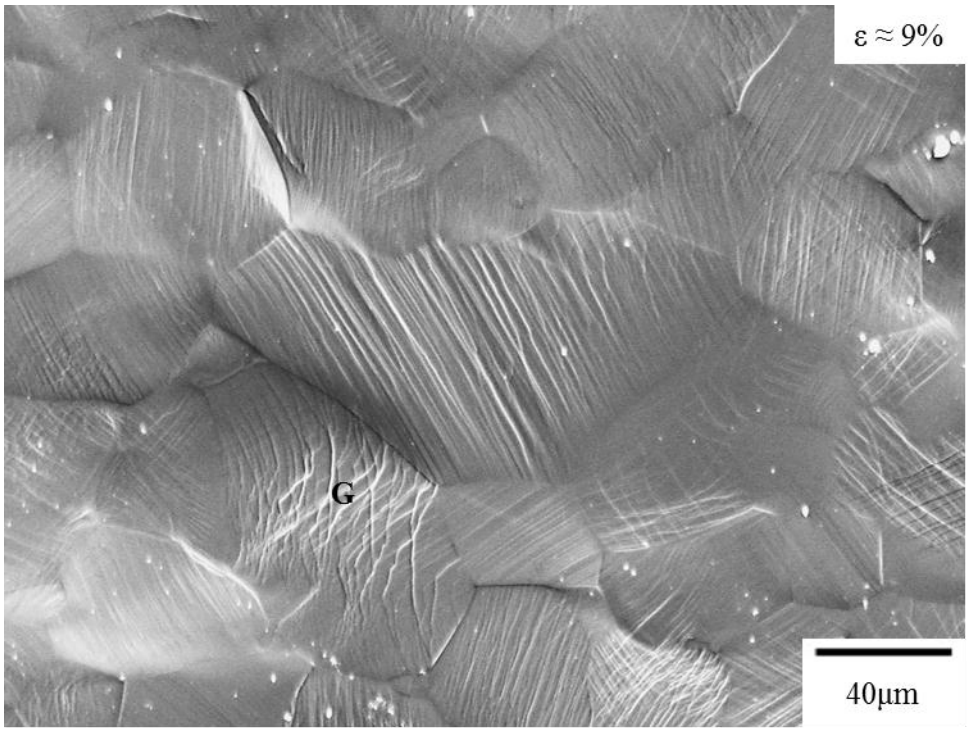

193 active slip systems were identified in 122 grains, with the distribution histogram shown in Figure 4.27. 81 basal (81/193≈42%), 90 prismatic (90/193≈47%), 10 pyramidal <a> (10/193≈5%), and 12 pyramidal <c+a> (12/193≈6%) were observed. More than 95% of the slipped grains exhibited basal or prismatic slip. These observations suggest that basal and prismatic slip systems are the main deformation modes at 728K. In Figure 4.27, both basal and prismatic slip systems were observed for global Schmid factors as low as 0.15. This is in contrast with the observation at 296K for Ti-5Al-2.5Sn where no basal slip was observed for systems with Schmid factors below 0.27. Prismatic slip was observed in a large Schmid factor range at 728K, similar to the observations at 296K. This is consistent with the fact that the CRSS for basal slip decreases more rapidly with higher temperatures compared to prismatic slip [Williams et al., 2002]. Pyramidal <a> and pyramidal <c+a> slip were observed to a less extent compared with basal and prismatic slip. Pyramidal <a> and pyramidal <c+a> slip systems were only activated with Schmid factors greater than 0.3. Unlike at 296K, twinning was not observed at 728K.

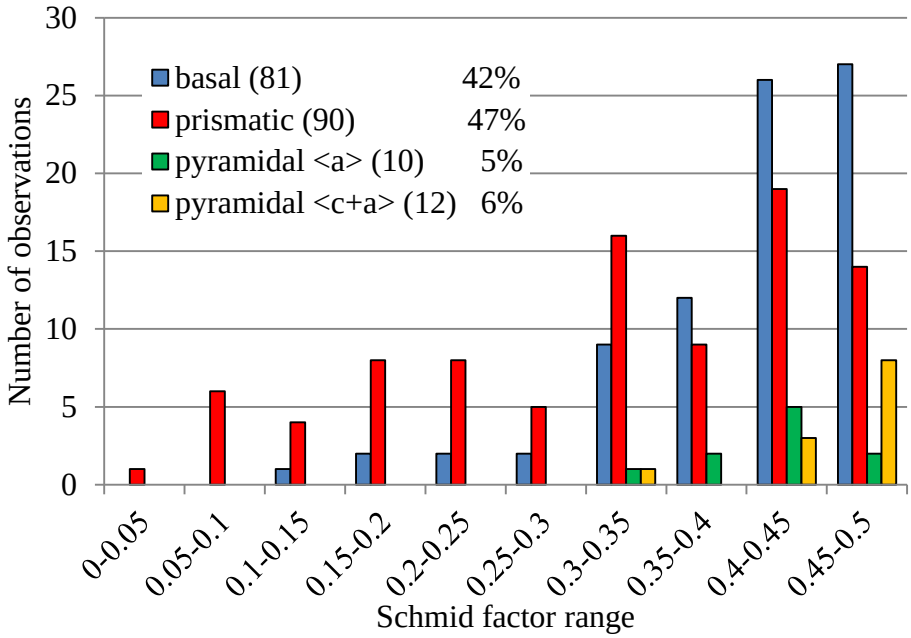

Figure 4.27 A histogram of the Schmid factor distribution of basal, prismatic, pyramidal <a>, and pyramidal <c+a> slip systems for the Ti-5Al-2.5Sn 728K tension experiment after ~9% strain.

Figure 4.28 shows the stereographic triangles with the grain orientations plotted for basal, prismatic, pyramidal <a>, and pyramidal <c+a> slip with Schmid factor contours overlaid. Generally, basal slip was confined to grains with high Schmid factors. Basal slip was observed in a few grains with Schmid factor as low as 0.1-0.2. Similar to the 296K tension for Ti-5Al-2.5Sn, grains with prismatic slip was activated over the entire stereographic triangle (see Figure 4.24 (b) and Figure 4.28 (b)). A few grains exhibited pyramidal <a> and pyramidal <c+a> slip and the grain orientations of these grains were located at the regions with high Schmid factors for pyramidal <a> and pyramidal <c+a> slip.

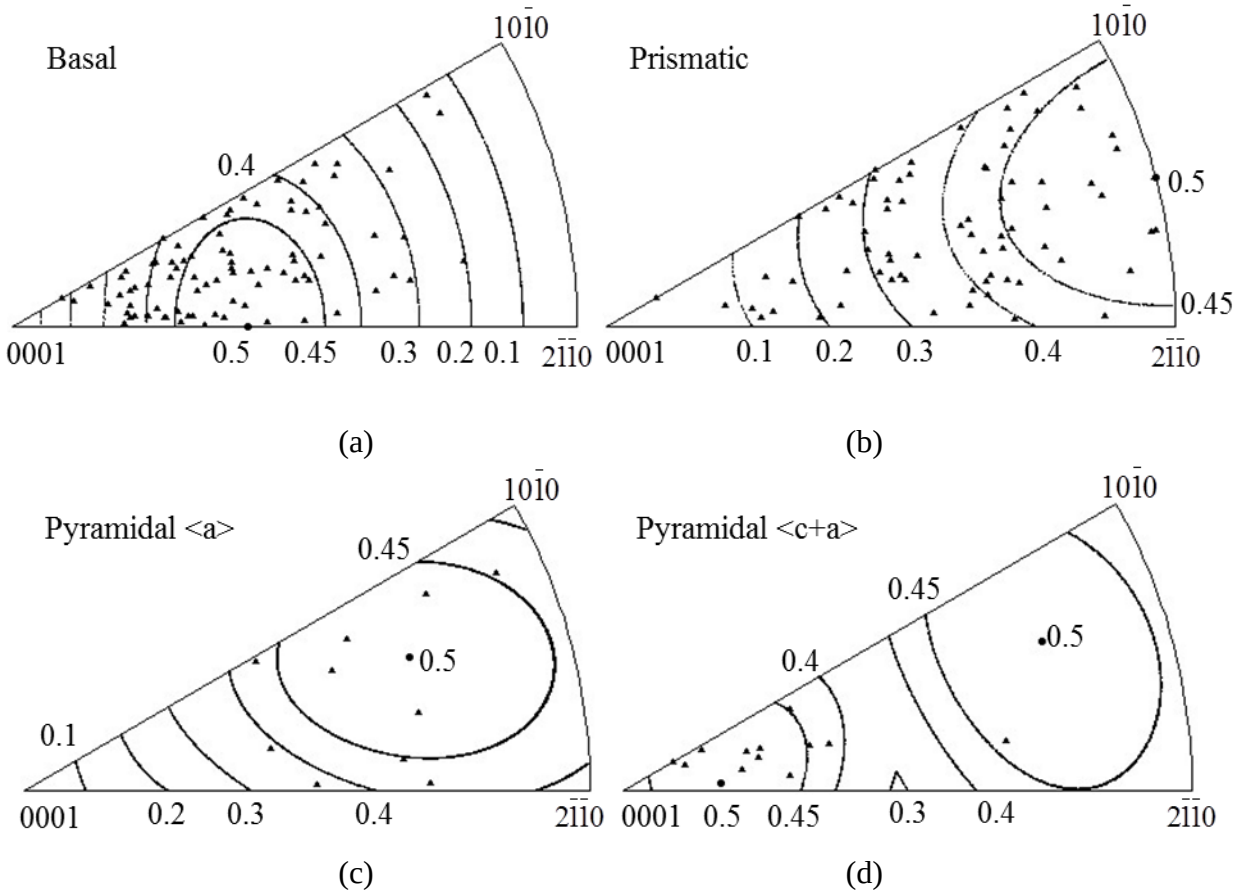

Figure 4.28 Unit triangle plots of grains which exhibited (a) basal, (b) prismatic, (c) pyramidal <a>, and (d) pyramidal <c+a> slip for the Ti-5Al-2.5Sn 728K tension test deformed to ~9% strain with Schmid factor contours overlaid.

The development of wavy slip lines, indicative of cross slip, was first observed at a strain level of ~2.8%. The development of cross slip in grain "G" in Figure 4.26 (d) is shown in a series of SE SEM images with ~2.8%, 3.5%, 4.4%, and 9% strains in Figure 4.29. Trace analysis of the slip lines indicated that slip in the $[\bar{2}110]$ direction on (0001) basal, prismatic, and pyramidal planes was involved in the cross-slip with the common screw dislocation Burgers vector of $[\bar{2}110]$. These three slip systems exhibited relatively high Schmid factors of 0.3, 0.32, and 0.42, respectively. Figure 4.29 (e) represents the HCP unit cell with the activated slip systems, where the shaded planes show the slip plane and arrows indicate the sense of shear.

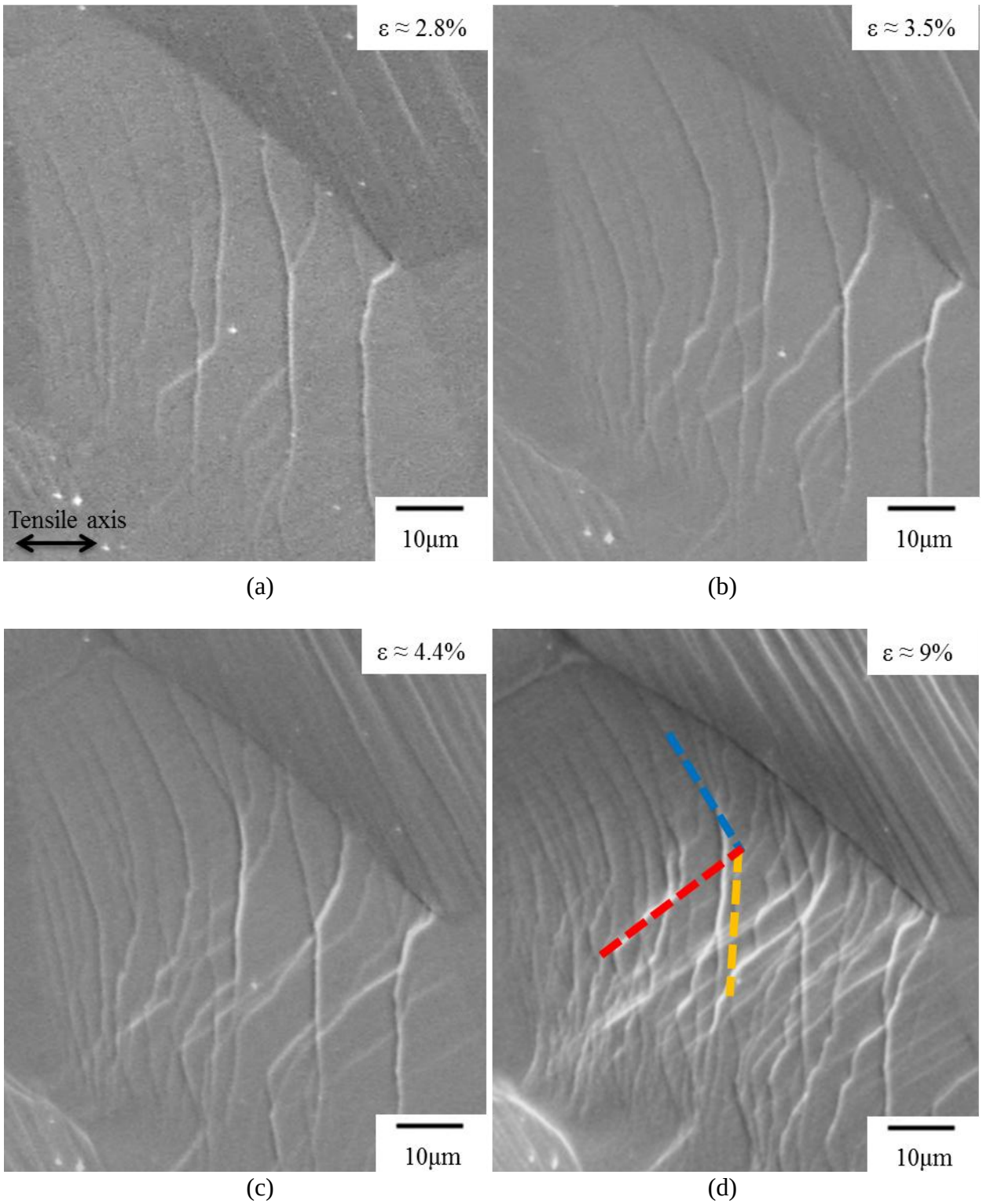

Figure 4.29 Cross-slip evolution in grain "G" (see Figure 4.26 (d) in the Ti-5Al-2.5Sn 728 K tension test) at various strain levels (a) ~2.8%, (b) ~3.5%, (c) ~4.4%, (d) ~9%, and (e) represents the activated slip systems where the shaded planes show the slip plane and arrows indicate the sense of shear. The loading direction was horizontal.

Figure 4.29 (cont'd)

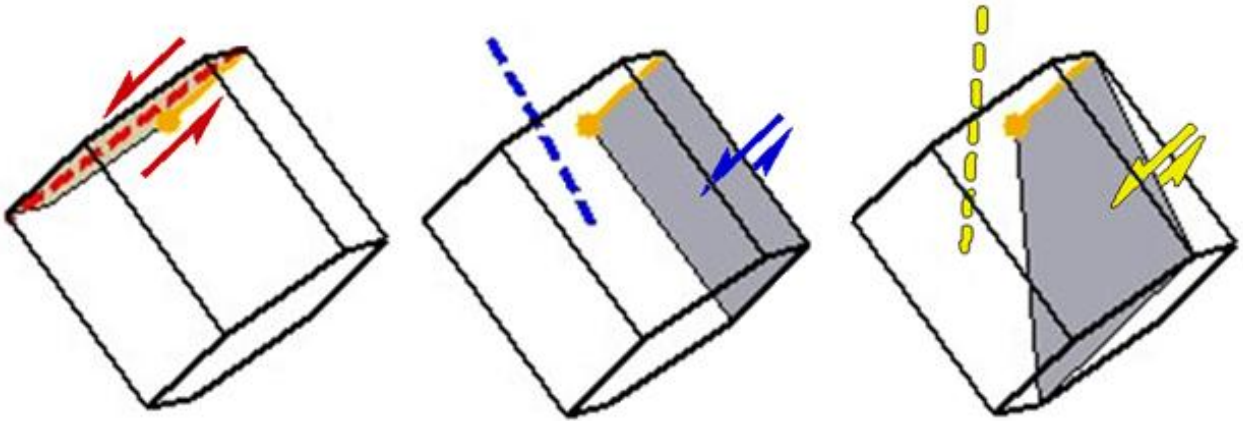

Basal (0001)[$\bar{2}$110] Schmid factor =0.3

Prismatic (01$\bar{1}$0) [$\bar{2}$110] Schmid factor=0.32

Pyramidal <a> (01$\bar{1}$1) [$\bar{2}$110] Schmid factor=0.42

(e)

Overall, with increasing temperature, there was no significant change of the relative activation of the different deformation systems for Ti-5Al-2.5Sn (except for the twining which was completely suppressed at elevated temperature). Basal and prismatic slip were the primary deformation systems at both 296K and 728K. Compared to 296K tension test, more cross-slip was observed at the elevated temperature. In chapter 6, the relative CRSS values for the different deformation system types at 296K and 728K will be calculated and compared.

4.2.4 *In-situ* creep

In-situ creep tests were performed on Ti-5Al-2.5Sn at 728K and 763K. At 728K, creep tests were performed with constant stresses of 250MPa and 300MPa, which are equivalent to 76% and 91% of the yield stress at 728K. At 763K, creep tests were performed with constant stresses of 200MPa and 250MPa. A minimum of ~15.3% strain was achieved for all of the four creep tests and none of the specimens were deformed to failure. The dominant deformation mechanisms under different applied stresses and temperatures are presented in this section. The relative activation of the different deformation systems during different creep conditions is also presented. Cracks were observed in all of the four creep tests. The relationship between the crystallographic orientation/misorientation and the grain boundary/triple point cracks will be discussed later in Chapter 5. Overall, compared with the tension tests, the creep tests revealed less dislocation slip and more GBS. When slip occurred, basal slip was dominant.

4.2.4.1 *In-situ* 728K-250MPa creep

Figure 4.30 shows an EBSD IPF map in the tensile direction and the corresponding {0001} and $\{10\bar{1}0\}$ pole figures from the gage section of the 728K-250MPa creep tested specimen for Ti-5Al-2.5Sn. There were approximately 870 α grains in Figure 4.30. Similar to the bulk XRD in Figure 4.18 and EBSD results in Figure 4.20 and Figure 4.25, the maximum peak intensity was approximately three times random and this specimen was weakly textured. However, the peak locations of the {0001} pole figure in Figure 4.30 (b) varied from all the previous texture measurements and the peak locations of any two of the {0001} pole figures from Figure 4.18, Figure 4.20, Figure 4.25, and Figure 4.30 were different, suggesting that the

Ti-5Al-2.5Sn lacked any symmetric texture characteristics (i.e. peaks were found at random orientations).

Sequential SE SEM images of the same area taken at different strains during the 728K-250MPa tensile-creep experiment are shown in Figure 4.31. Visible offsets were noticed at grain boundaries. These offsets were typically observed out of the plane of the image (i.e. vertical) and were referred as grain boundary ledges. These grain boundary ledges formed at strains less than 0.5%, prior to any slip traces becoming evident, as shown in Figure 4.31 (b). These ledges continued to form with increasing strain, while only a few grains developed observable slip traces (see Figure 4.31 (f)). After ~16.5% strain, ~10% of the total number of observed grains exhibited slip traces. Figure 4.31 (f) shows the identified slip traces for this microstructural patch. Five basal slip systems (highlighted by blue lines) and one prismatic slip system (highlighted by red line) were observed. However, GBS was more prevalent, suggesting that dislocation slip did not contribute to the strain as much as GBS. Figure 4.32 shows a higher magnification SE SEM image that shows the details of GBS, which was evidenced by the protrusion of the grain labeled as “P” and the recess of the grain labeled as “R”. Some of the observed grain boundary ledges eventually evolved into grain boundary cracks, as illustrated in Figure 4.33.

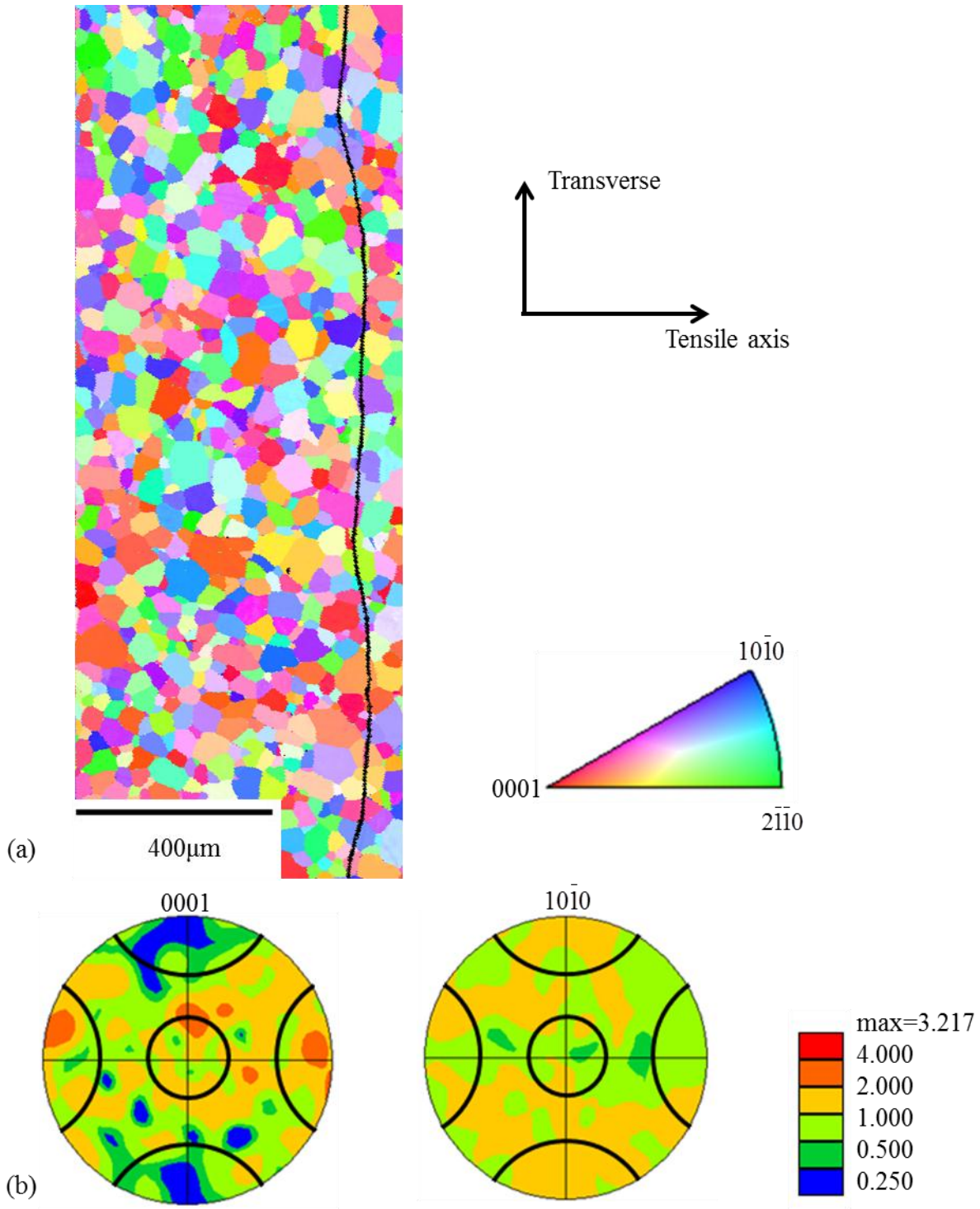

Figure 4.30 EBSD data of the Ti-5Al-2.5Sn 728K-250MPa creep tested specimen: (a) EBSD IPF map in the tensile direction of the α-phase Ti containing approximately1000 α grains, (b) the $\{0001\}$ and the $\{10\bar{1}0\}$ pole figures with 30° cones along the major axes of grain orientations in (a). The intentional scratch on the right of the EBSD map was used as a fiducial marker. The loading direction was horizontal.

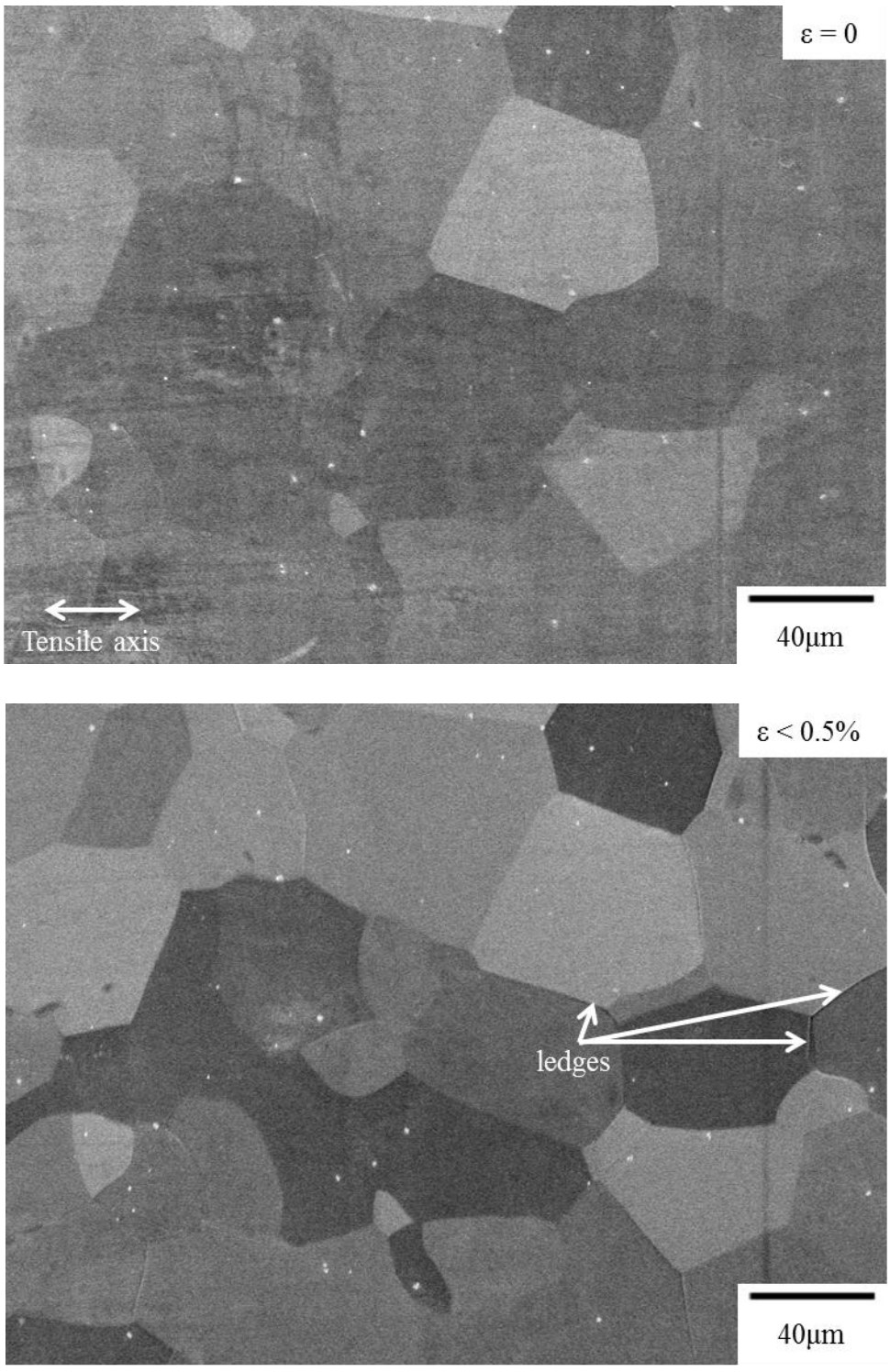

(a)

(b)

Figure 4.31 Sequential SE SEM images for Ti-5Al-2.5Sn tensile-creep tested at 728K-250MPa: (a) undeformed; (b) <0.5% strain, 0.5 h; (c) ~1.6% strain, 19.5 h; (d) ~5.1% strain, 46; (e) ~9.5% strain, 50 h; (f) ~16.5% strain, 56 h, the color-coded planes traces for prismatic slip (red) and basal slip (blue) are labeled along with their Schmid factors. The loading direction was horizontal.

Figure 4.31 (cont'd)

(c)

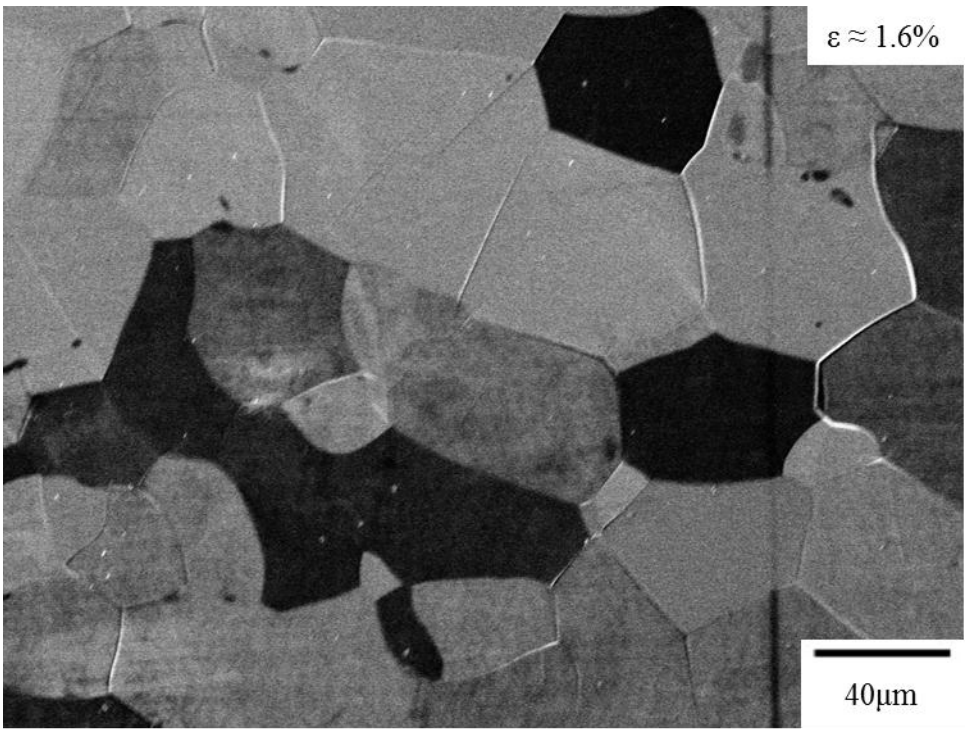

(d)

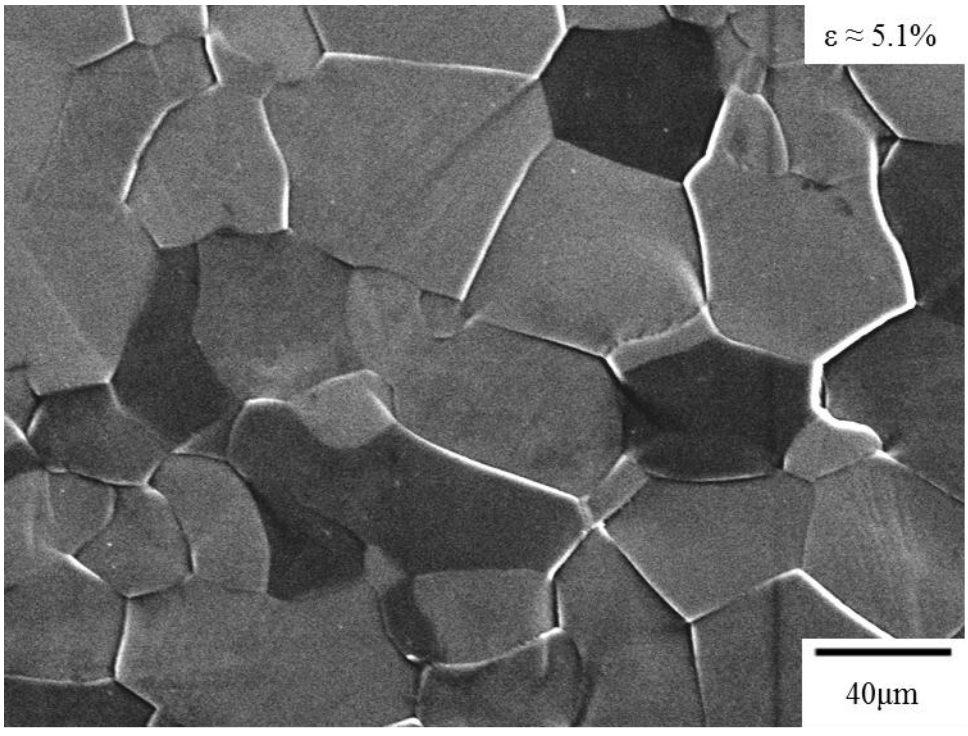

Figure 4.31 (cont'd)

(e)

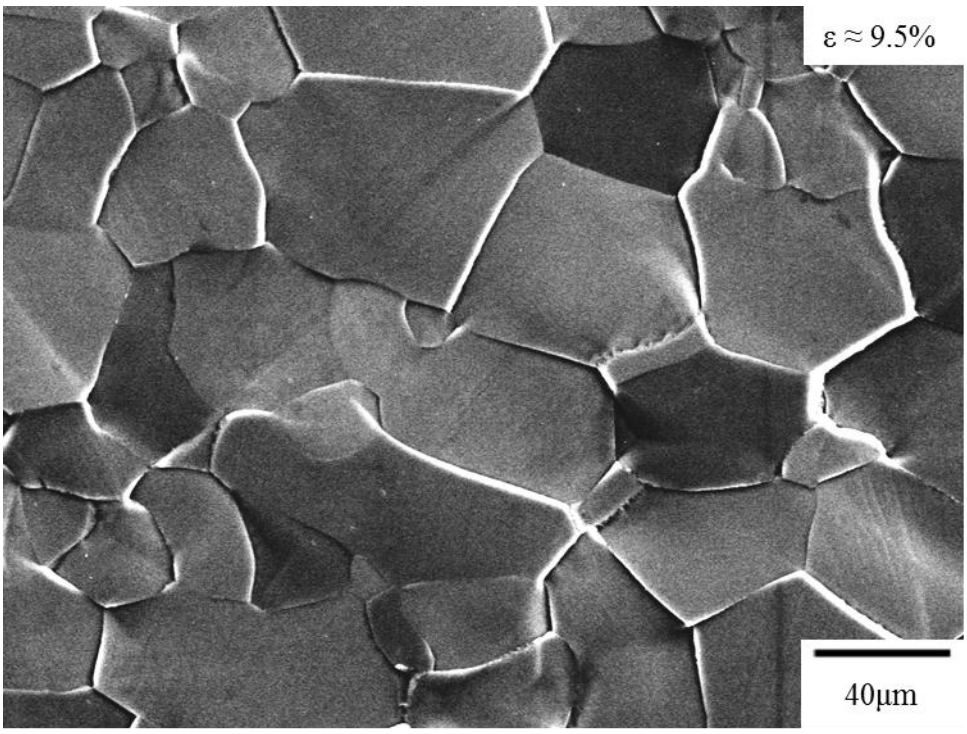

(f)

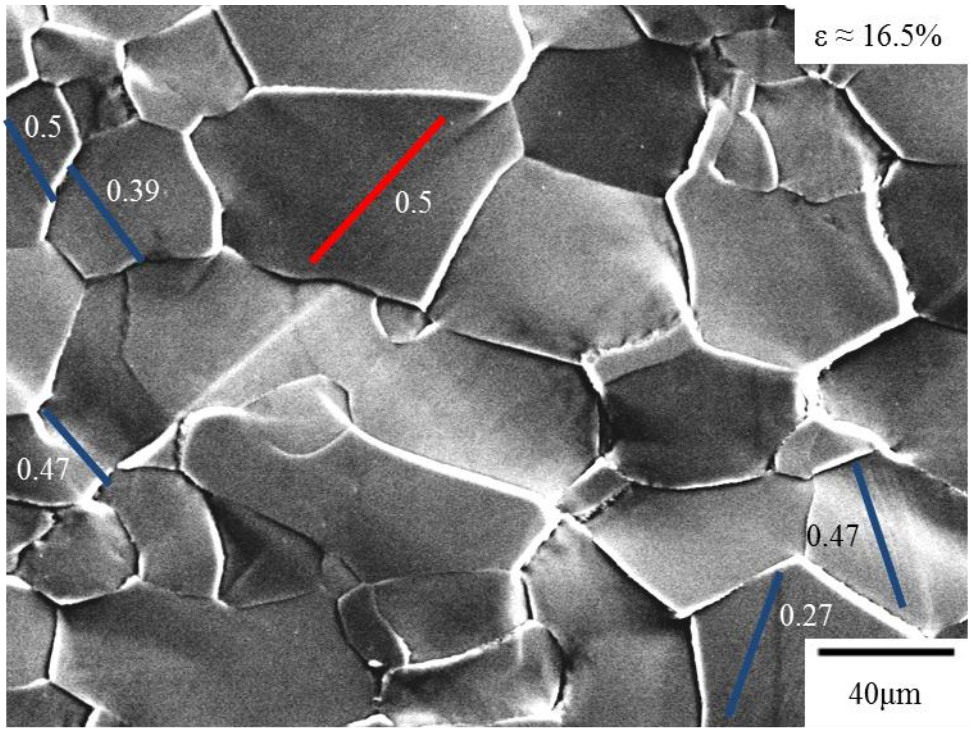

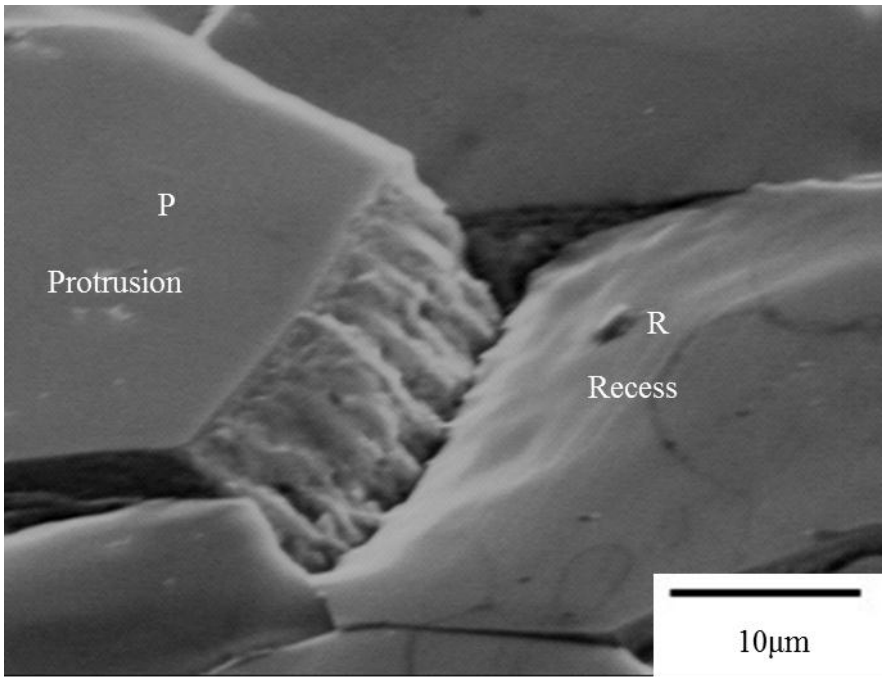

Figure 4.32 SE SEM photomicrograph of a grain boundary ledge which displaced approximately 16μm and was evidenced by the protrusion in the grain labeled P and recess in the grain labeled R for the Ti-5Al-2.5Sn 728K-250MPa creep experiment after ~16.5% strain. The loading direction was horizontal.

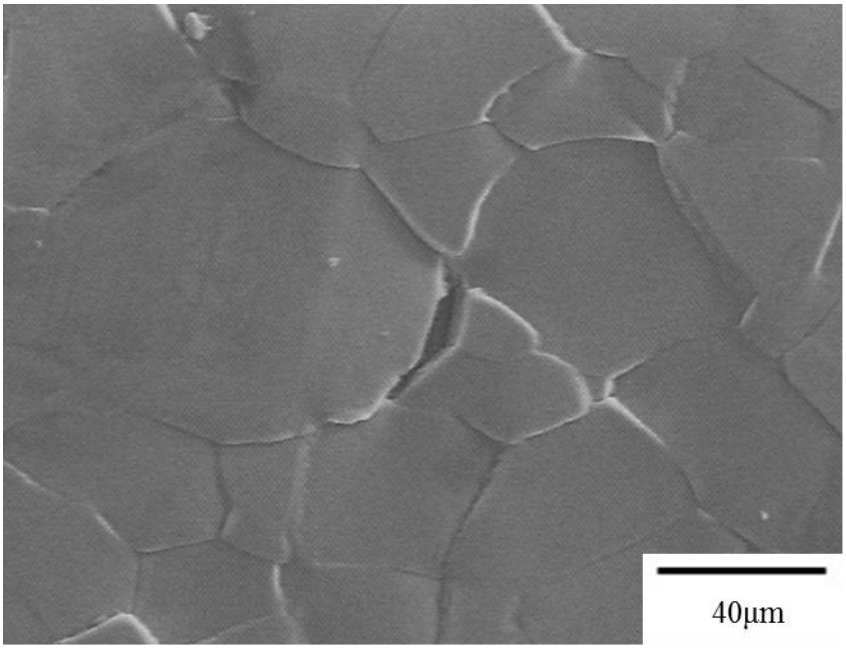

Figure 4.33 SE SEM photomicrograph illustrating grain boundary cracking during the Ti-5Al-2.5Sn 728K-250MPa tensile-creep experiment deformed to ~16.5% strain. The loading direction was horizontal.

Figure 4.34 shows the EBSD IPF maps in the tensile direction for the same area in Figure 4.31 and the corresponding grain orientation spread before and after the deformation. Before the deformation, the majority of grains exhibited an orientation spread less than one degree, which is within the uncertainty of the EBSD angular measurements [Wilkinson 1996]. After ~16.5% strain, a grain orientation gradient developed up to 6 degrees. This gradient was more often observed in "soft" grains (blue and green) than "hard" grains (red), see Figure 4.34 (b).

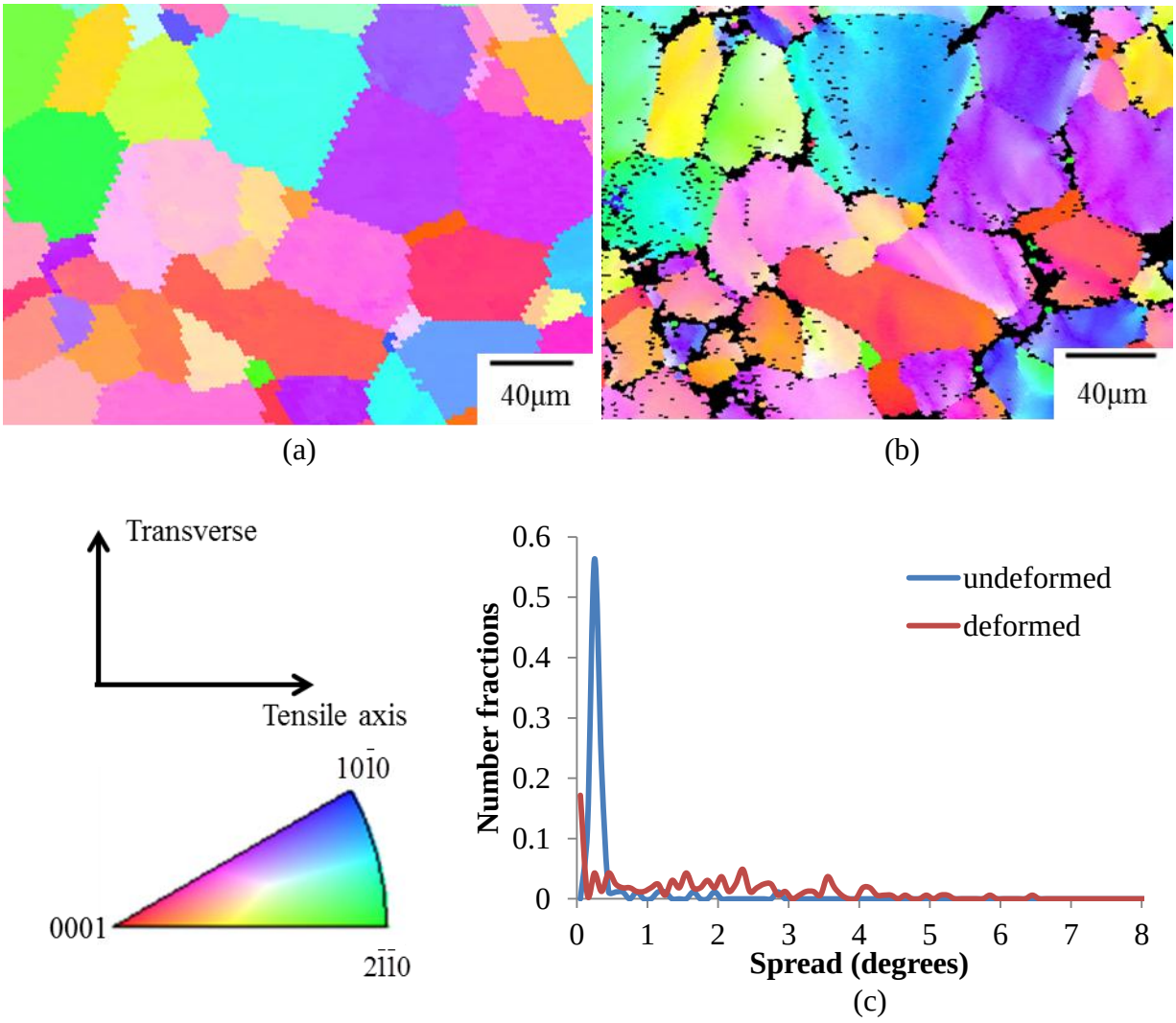

Figure 4.34 EBSD IPF maps in the tensile direction for the same area in the 728K-250MPa tested sample for Ti-5Al-2.5Sn (a) before and (c) after ~16.5% tensile strain. The grain orientation spread of the grains shown in (a) before and (b) after the deformation was plotted in (c).

45 slip systems were identified in the 44 grains exhibiting slip traces, with 35 basal slip system traces observed (35/45≈78%), indicating that the majority of the grains that exhibited slip traces deformed by basal slip (see Figure 4.35). In the 35 basal slip systems, 32 basal slip systems were activated with Schmid factors greater than 0.35. Three basal slip systems were activated with relatively small Schmid factors (0.15–0.3) in three separate grains in which the Schmid factors of prismatic slip systems were less than 0.05. This suggests that the activation of these three basal slip systems were the result of strain accommodation. Prismatic slip systems comprised only a small fraction (7/45≈16%) of the identified slip systems, and all had Schmid factors greater than 0.4. This is in contrast to the tension tests where a large fraction of prismatic slip was observed (50% at 296K and 47% at 728 K), and prismatic slip was activated over the entire Schmid factor range. Only one pyramidal <a> (1/44≈2%) and two pyramidal <c+a> slip (2/44≈4%) systems were observed. Compared with the higher strain rate tensile experiments, GBS and basal slip systems were more favored during creep.

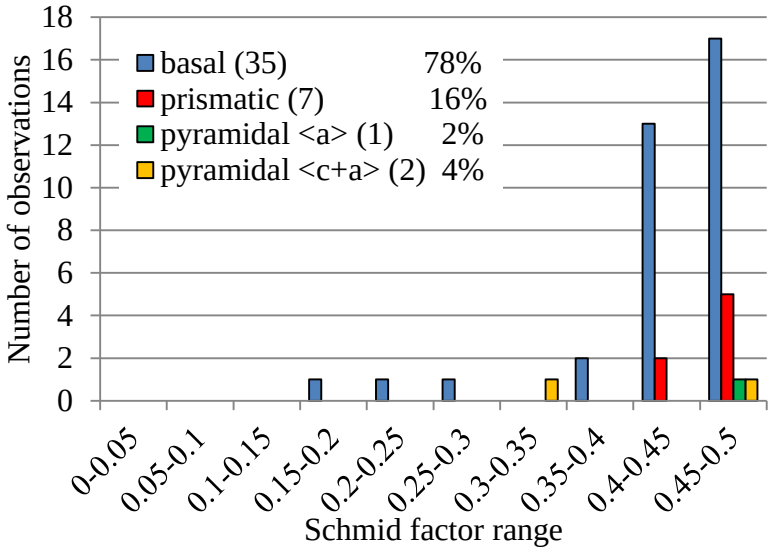

Figure 4.35 A histogram of the Schmid factor distribution of basal, prismatic, pyramidal <a>, and pyramidal <c+a> slip systems for the Ti-5Al-2.5Sn 728K-250MPa creep experiment after ~16.5% strain.

Figure 4.36 shows the stereographic triangles with the grain orientations plotted for basal, prismatic, pyramidal <a>, and pyramidal <c+a> slip with Schmid factor contours overlaid. Basal slip was the dominant deformation system type and the orientations of grains with basal slip were more confined to high Schmid factor regions. Grains with prismatic slip were only observed in grains with Schmid factors greater than 0.4, which is in contrast to the tension tests for the Ti-5Al-2.5Sn, and prismatic slip was observed in grains with Schmid factors of prismatic slip below 0.2.

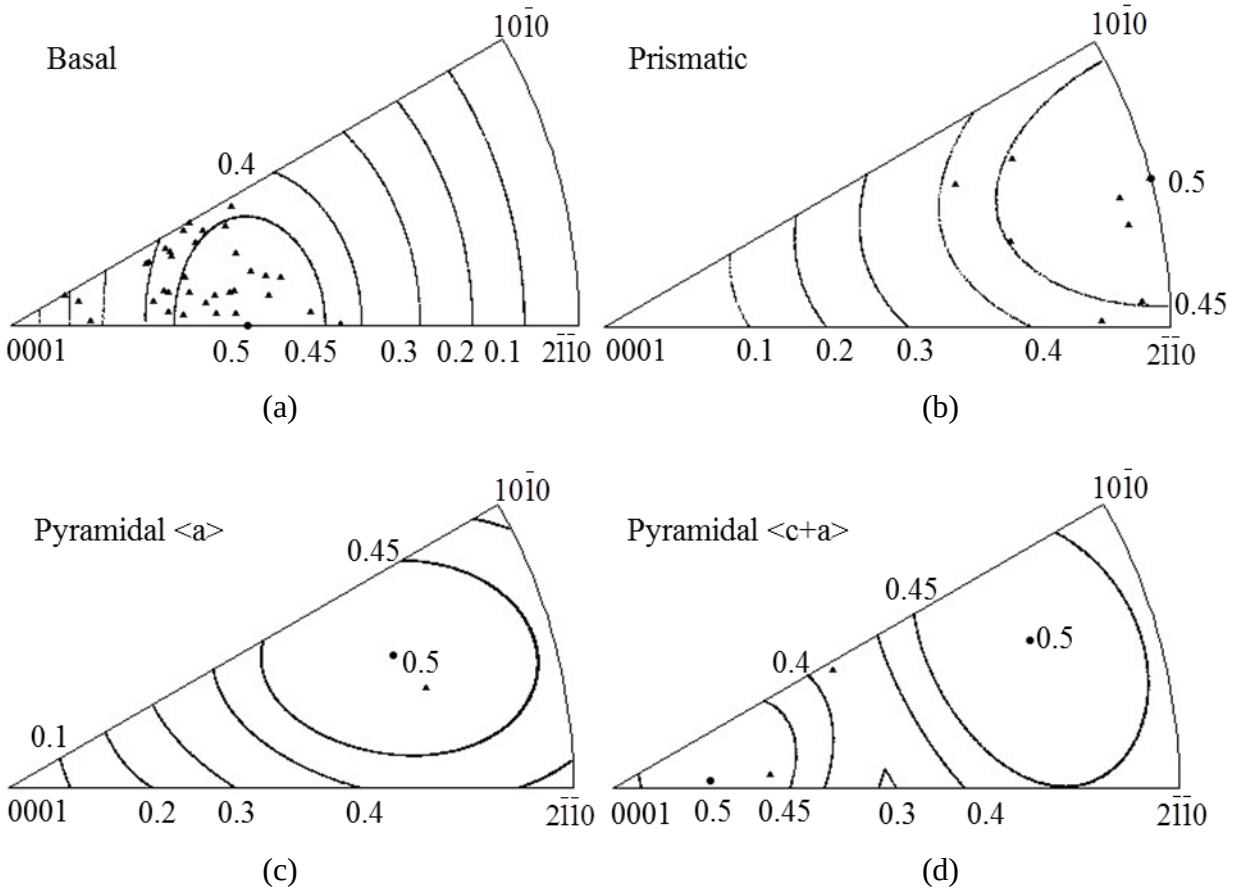

Figure 4.36 Unit triangle plots of grains which exhibited (a) basal, (b) prismatic, (c) pyramidal <a>, and (d) pyramidal <c+a> slip for the Ti-5Al-2.5Sn 728K-250MPa creep test deformed to ~16.5% strain with Schmid factor contours overlaid.

The misorientation angles between grain pairs on either side of a given grain boundary ledge, as well as the angle between the boundary trace and the loading direction, were analyzed for 26 boundaries where ledges formed at less than 0.5% strain (Figure 4.31 (b)) and the data are presented in Figure 4.37. The y-axis represents the normalized fraction of the number of observations in a particular angular range. For the equiaxed α grains, the angle between boundary traces and the loading axis should be almost evenly distributed between 0° and 90°. However, there was a strong correlation between the boundary trace angles and the ledge formation. Ledges tended to form at boundaries orientated perpendicular or nearly perpendicular to the loading direction. More than 90% of the ledges formed at grain boundaries where the angles between the boundary and the loading axis were greater than 60°. Moreover, compared with the total grain boundary misorientation distribution, ledges also tended to form at boundaries with large misorientation angles (greater than 30°). Of the 26 ledges that formed at less than 0.5% strain, 23 ledges formed at boundaries with high misorientation angles and large angles between the boundary traces and the loading axis (>60°). Only one formed at a low angle boundary and this boundary was orientated 75° to the loading direction. Two boundaries were observed to form ledges at boundaries with trace angles from 30° to 60° and these two boundaries had misorientation angles of 75° and 70°. Thus, high misorientation angles and high angles between the boundary and the loading axis were both associated with the formation of grain boundary ledges.

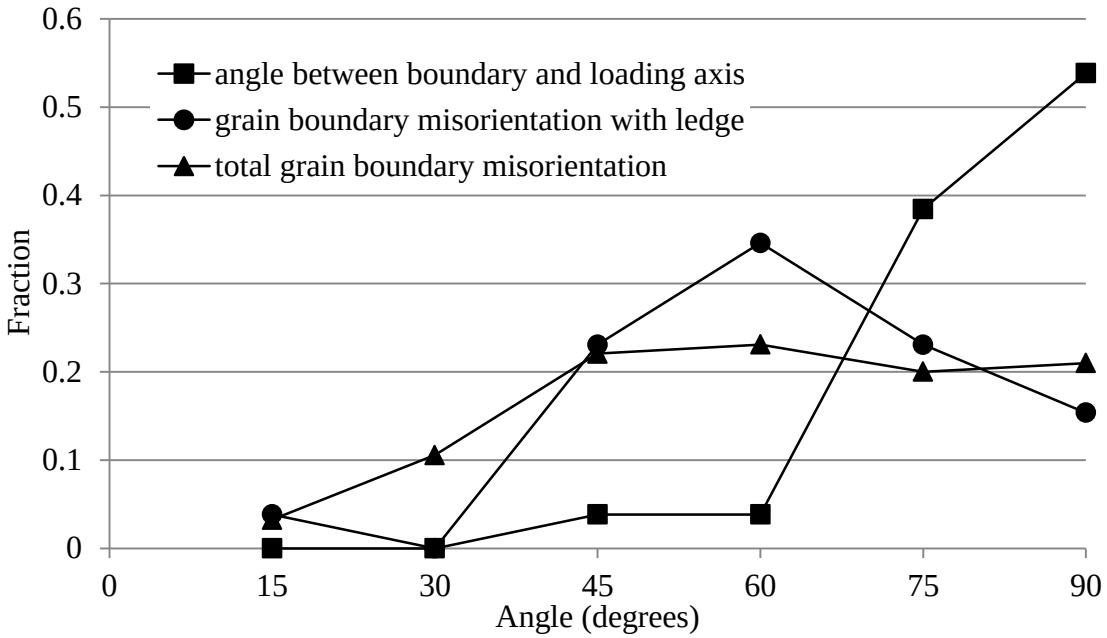

Figure 4.37 The y-axis represents the normalized fraction of grain boundaries for 26 grains that exhibited ledges at less than 0.5% strain during the Ti-5Al-2.5Sn 728K-250MPa creep experiment. The x-axis represents the angular range for either the angle between the grain boundary and the tensile-creep axis or the grain boundary misorientation angle. The plot for the total grain boundary misorientation includes all the grain boundaries in the microstructural patch analyzed (>500), where only 26 of the grain boundaries exhibited ledges.

4.2.4.2 *In-situ* 728K-300MPa creep

Figure 4.38 shows an EBSD IPF map in the tensile direction and the corresponding {0001} and $\{10\bar{1}0\}$ pole figures from the gage section of the 728K-300MPa creep tested specimen for Ti-5Al-2.5Sn. There were approximately 1050 α grains in Figure 4.38. This specimen was weakly textured and the maximum peak intensity was approximately three times random, which was similar to the bulk XRD resulted provided in Figure 4.18 and previous EBSD scan results shown in Figure 4.20, Figure 4.25, and Figure 4.30. As the Ti-5Al-2.5Sn lacked any symmetric texture characteristic, it is no surprise that the peak locations of the {0001} pole figure in Figure 4.38 were different from the previous EBSD results.

Figure 4.39 shows sequential SE SEM images of the same area taken at various strains for the 728K-300MPa creep test. Like the 728K-250MPa creep test, grain boundary ledges were observed early in the deformation (<0.5% strain), however, more slip traces were observed for this specimen compared to the 728K-250MPa tested specimen. As shown in Figure 4.39 (b), the majority of the slip traces were identified to be basal (highlighted by blue lines) and prismatic slip (highlighted by red lines). The global Schmid factor ranges associated with these slip systems were 0.37-0.50 for basal slip and 0.33-0.48 for prismatic slip, suggesting that the resolved shear stresses on these slip systems were relatively high. With larger deformation, more grains exhibited slip traces and grain boundary sliding/ledges were more evident. Wavy slip lines associated with cross-slip were observed at ~4% strain (see Figure 4.39 (c)). After ~21.4% strain, ~86% of the total number of observed grains exhibited slip traces. This is significantly greater than the ~10% value exhibited by the 728K-250MPa creep sample. It is expected that more slip activity would be present at 300MPa, which is close to the measured YS (~330MPa) at

728K. Some of the observed grain boundary ledges eventually evolved into grain boundary cracks, as illustrated in Figure 4.40.

Slip trace analysis was performed for 121 grains and a total of 146 slip systems were identified, as shown in Figure 4.41. In the 146 active slip systems, 65 were basal slip systems (65/146=45%) and 71 were prismatic slip systems (71/146=49%), which was different from the creep experiment performed at 728K-250MPa, where 78% of the slip systems were basal slip. Pyramidal <a> and pyramidal <c+a> only comprised a small portion of the identified slip systems. Most of the basal and prismatic slip systems were activated with relatively large Schmid factors (>0.3). In the 728K-250MPa creep test, prismatic slip only comprised 16% of deformation systems and the Schmid factors of these prismatic slip systems were above 0.4. This is not the case for the 728K-300MPa creep test, where prismatic slip was more active (49%) and observed over a larger Schmid factor range (0.1~0.5). The pronounced prismatic activity in the 300MPa experiment indicated that prismatic slip becomes easier to activate with increasing stress. The almost equal activity of basal and prismatic slip for the 728K-300MPa was similar to the observations for the tensile tests (Figure 4.23 and Figure 4.27). This may be attributed to the higher creep stress 300MPa, which is close to the measured YS (~330MPa) at 728K. Overall, the results of the slip trace analysis from this test were more similar to the tensile experiments than the lower stress 728K-250MPa creep experiment.

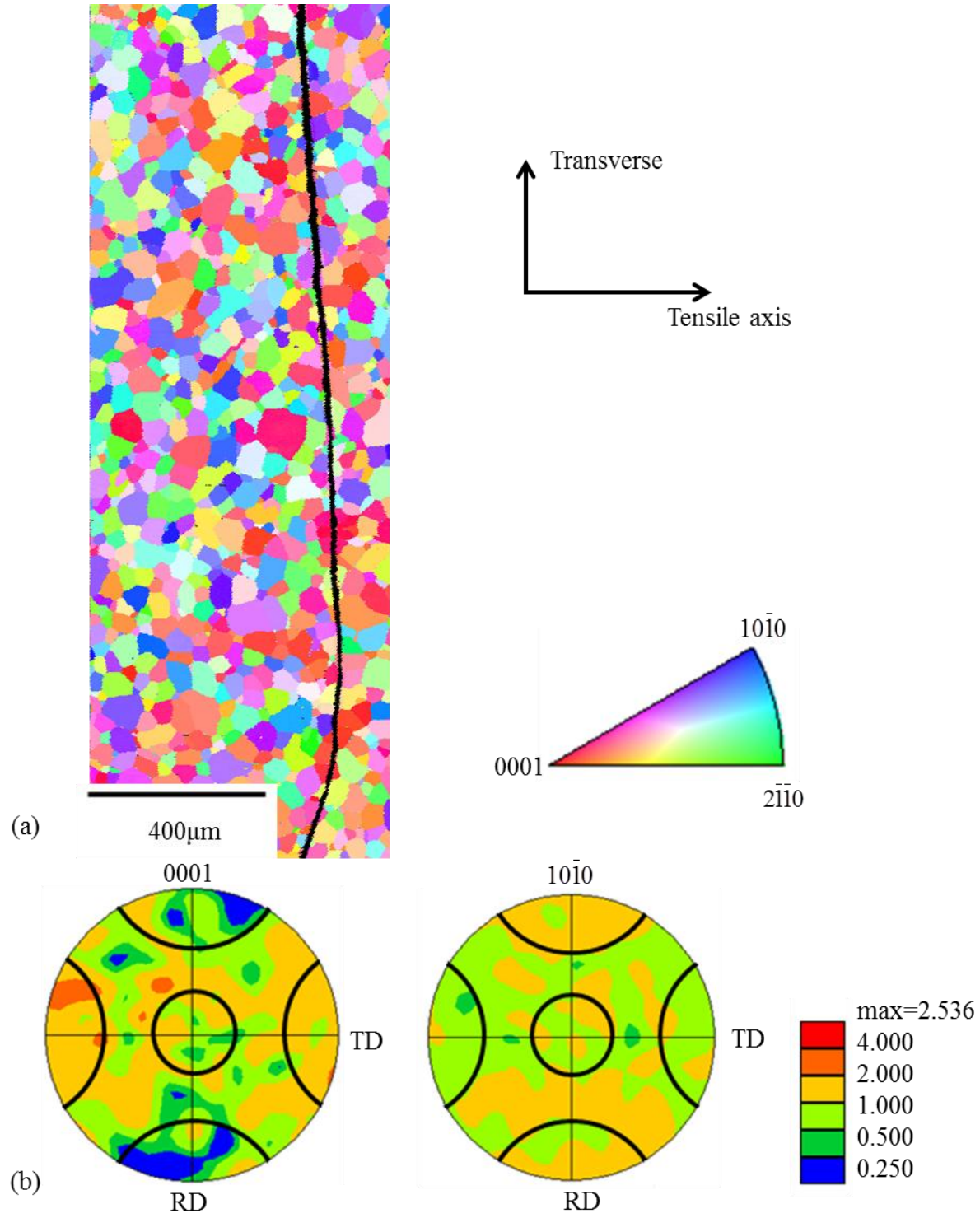

Figure 4.38 EBSD data of the Ti-5Al-2.5Sn 728K-300MPa creep tested specimen: (a) EBSD IPF map in the tensile direction of the α-phase Ti containing approximately 1050 α grains, (b) the $\{0001\}$ and the $\{10\bar{1}0\}$ pole figures with 30 ° cones along the major axes. The intentional scratch on the right of the EBSD map was used as a fiducial marker. The loading direction was horizontal.

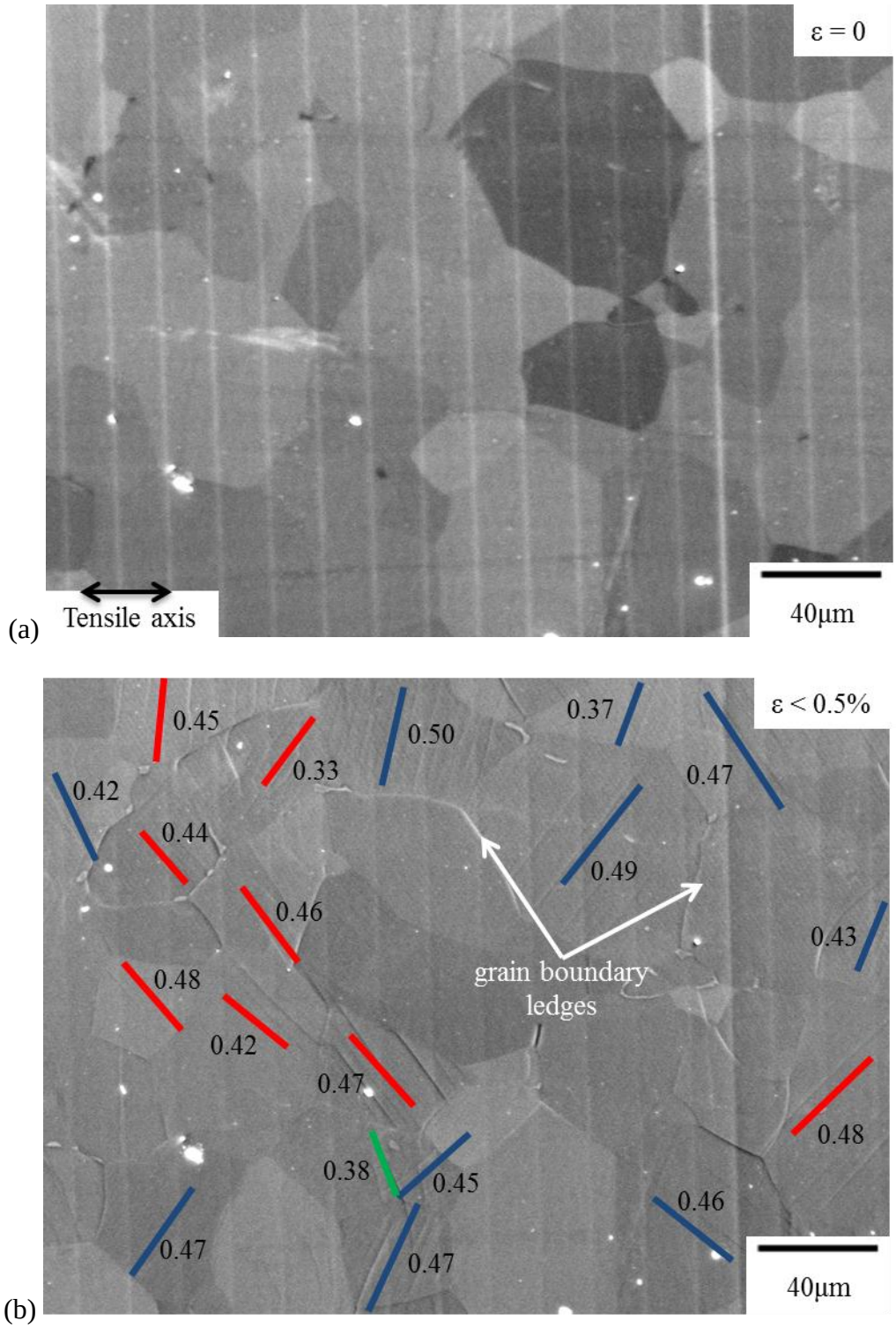

Figure 4.39 Sequential SE SEM images for Ti-5Al-2.5Sn tensile-creep tested at 728K-300MPa: (a) before loading; (b) <0.5% strain, 8 min, the color-coded planes traces for prismatic slip (red), basal slip (blue), and pyramidal <a> (green) are labeled along with their Schmid factors; (c) ~4% strain, 9 h; (d) ~9% strain, 24 h; (e) ~16.4%, 31; (f) ~21.4% strain, 32 h. The loading direction was horizontal. The vertical lines evident in (a), (b), and (c) were imaging artifacts.

Figure 4.39 (cont'd)

(c)

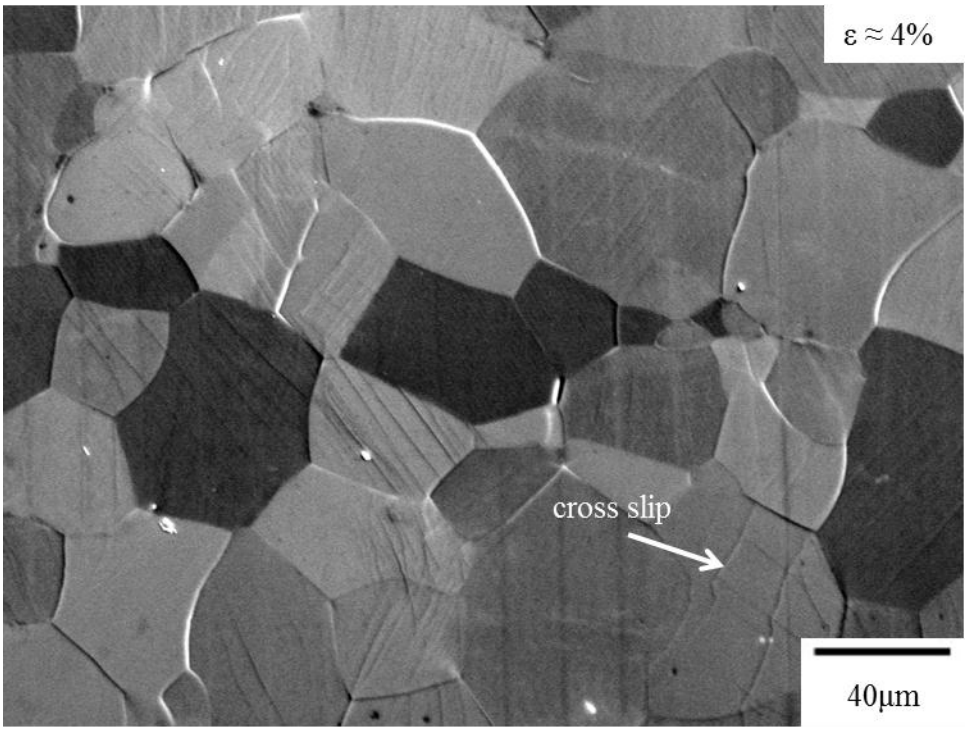

(d)

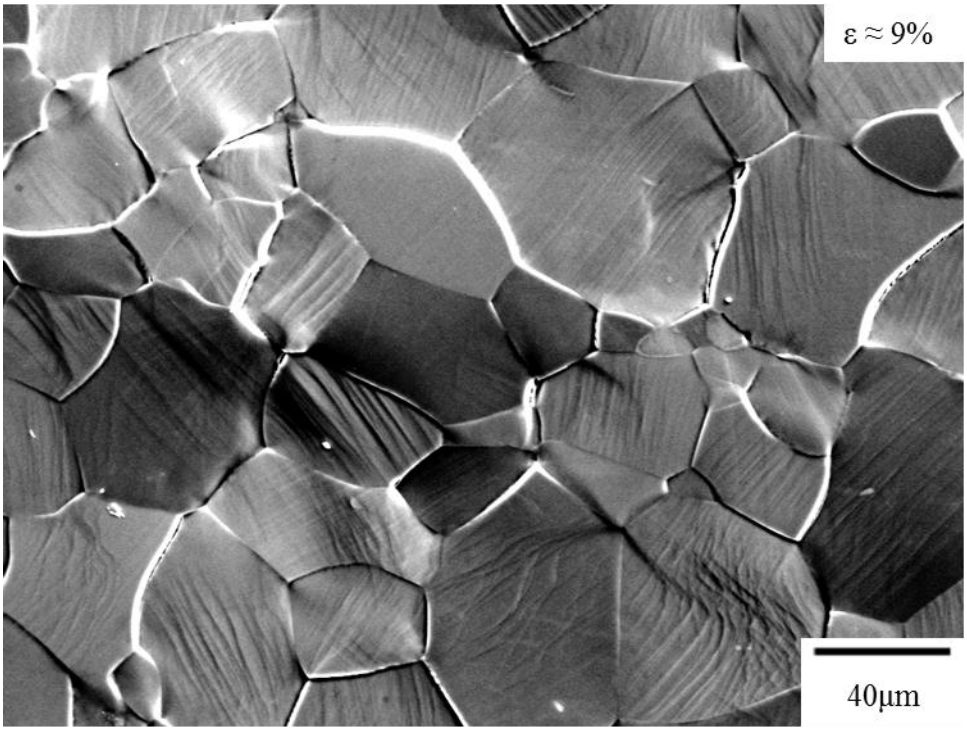

Figure 4.39 (cont'd)

(e)

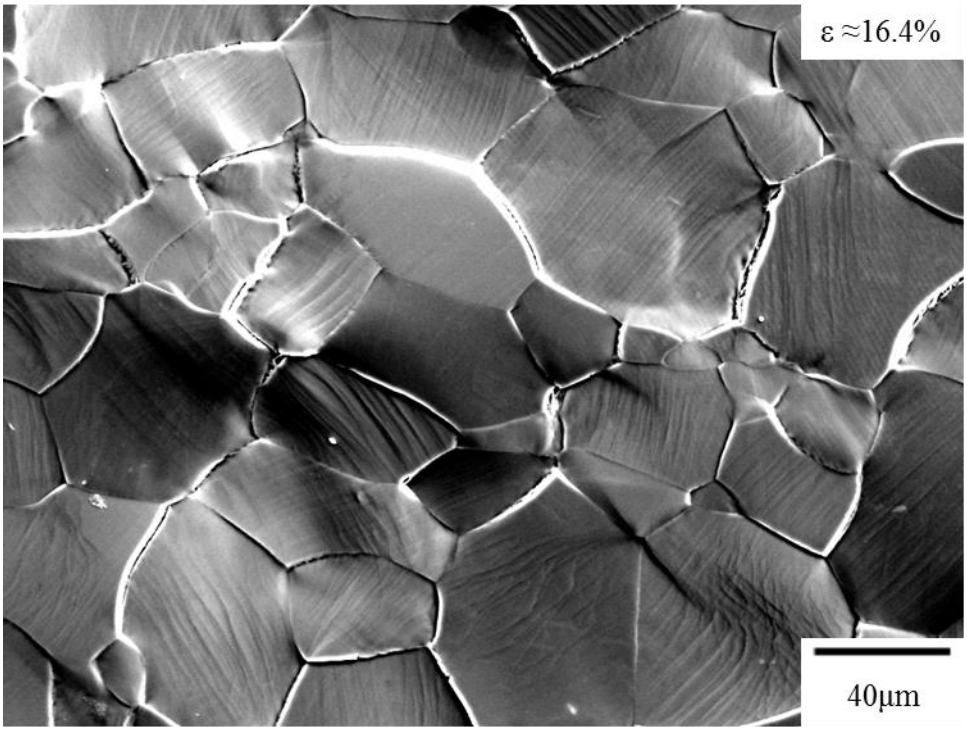

(f)

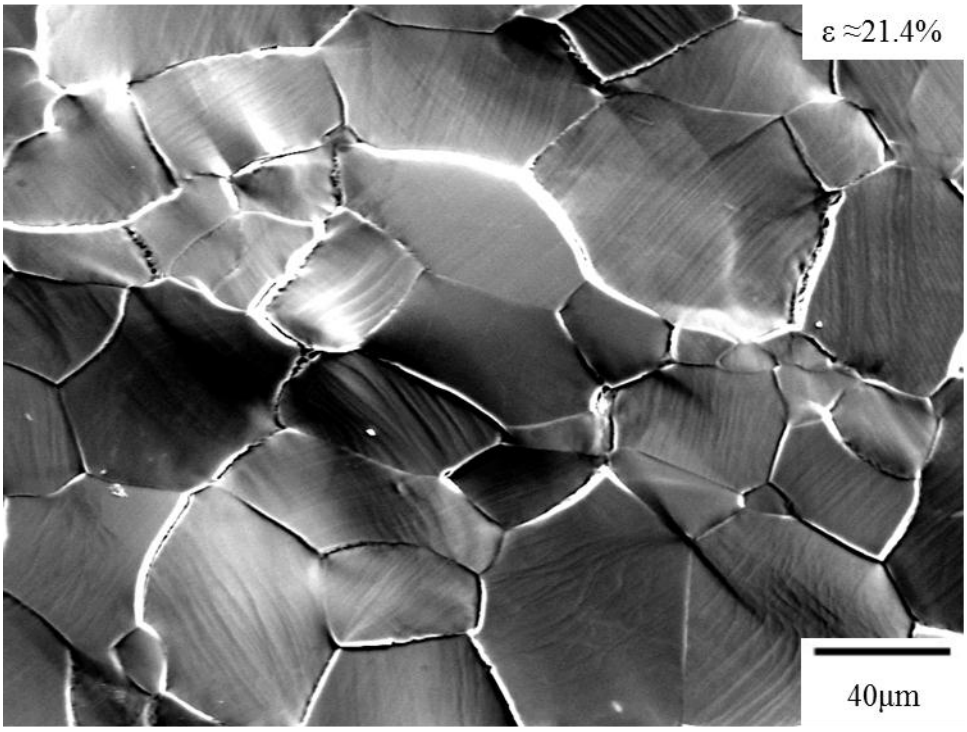

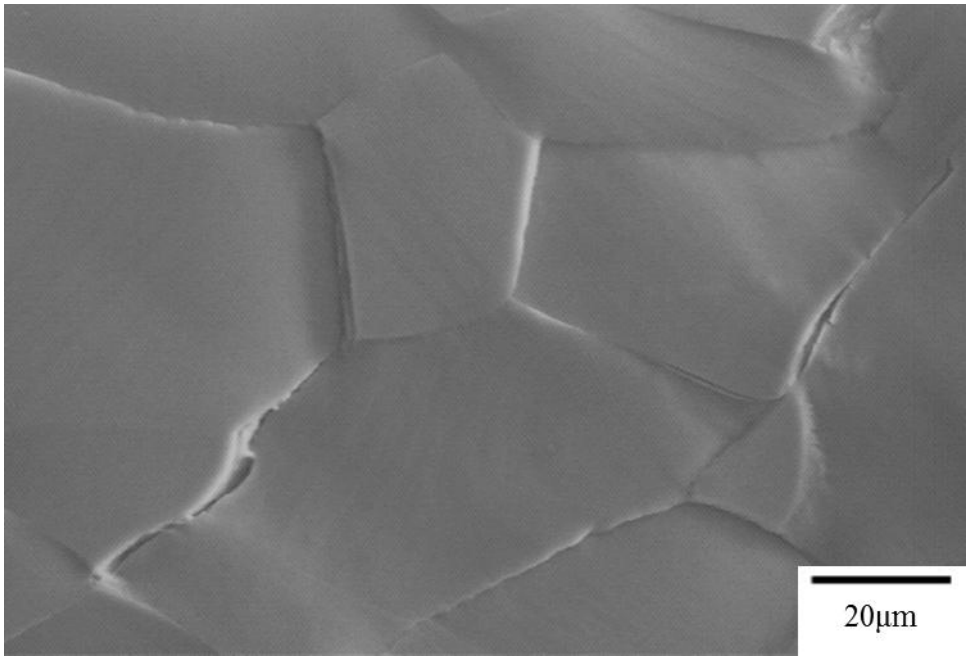

Figure 4.40 SE SEM photomicrograph illustrating grain boundary cracking during the Ti-5Al-2.5Sn 728K-300MPa tensile-creep experiment after ~21.4% strain. The loading direction was horizontal.

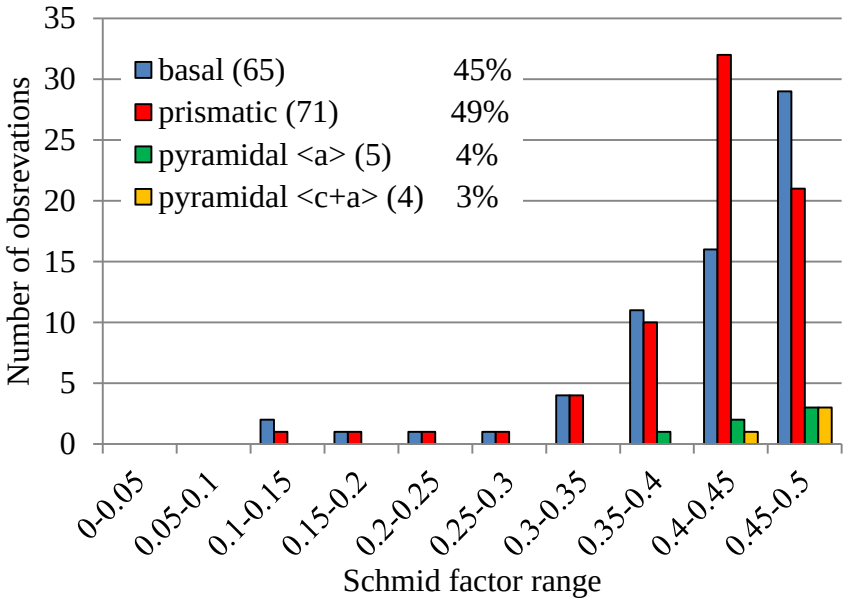

Figure 4.41 A histogram of the Schmid factor distribution of basal, prismatic, pyramidal <a>, and pyramidal <c+a> slip systems for the Ti-5Al-2.5Sn 728K-300MPa creep experiment after ~21.4% strain.

Figure 4.42 shows the stereographic unit triangles with the grain orientations plotted for basal, prismatic, pyramidal <a>, and pyramidal <c+a> slip with Schmid factor contours overlaid. Generally, grains with these four types of deformation systems were confined to high Schmid factor regions. Some grains exhibited basal and prismatic slip were found at regions with Schmid factors as low as 0.1 for these types of slip systems, which was similar to the tension tests performed at 296K and 728K. In addition, the distribution of the grain orientations with prismatic slip (see Figure 4.42 (b)) was also more like tension (Figure 4.24 (b) and Figure 4.28 (b)) other than the lower stress 250MPa creep test. This may be due to the higher stress level of 300MPa, which was close to the YS (~330MPa) at 728K.

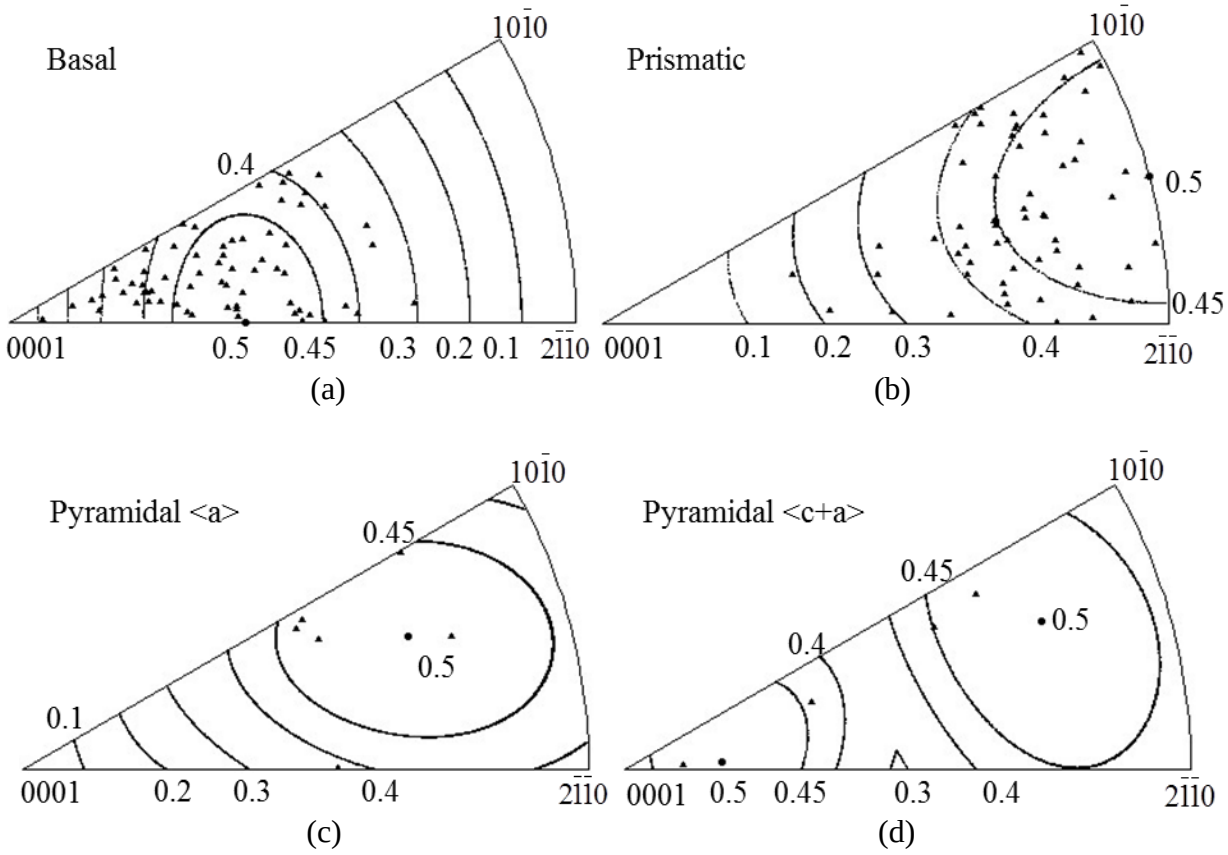

Figure 4.42 Unit triangle plots of grains which exhibited (a) basal, (b) prismatic, (c) pyramidal <a>, and (d) pyramidal <c+a> slip for the Ti-5Al-2.5Sn 728K-300MPa creep test deformed to ~21.4% strain with Schmid factor contours overlaid.

4.2.4.3 *In-situ* 763K-200MPa creep

Figure 4.43 shows an EBSD IPF map in the tensile direction and the corresponding {0001} and $\{10\bar{1}0\}$ pole figures from the gage section of the 763K-200MPa tensile-creep tested specimen for Ti-5Al-2.5Sn. There were approximately 700 α grains in Figure 4.43. This specimen exhibited a weak texture (an approximately three times random), which is similar to the bulk XRD results in Figure 4.18 and other EBSD results shown in Figure 4.20, Figure 4.25 and Figure 4.38. Again, the locations with the maximum peak intensities varied from the previous EBSD and XRD results.

Figure 4.44 shows the sequential SE SEM images of the same area acquired at various strains for the 763K-200MPa tensile-creep test. Some grain boundary ledges formed at less than 0.5% strain. Later in the deformation, almost all the grain boundaries formed ledges. Several grains exhibited slip traces at ~2.9% strain. After ~24.8% strain in Figure 4.44 (c), 6 grains exhibited 6 slip systems, where three were basal slip and three were prismatic slip. The Schmid factor ranges associated with these 6 slip systems were 0.37-0.5 for basal slip and 0.36-0.44 for prismatic slip. However, the extent of slip activity was much less than the higher-stress creep test (728K-300MPa) and the tensile tests. Instead, GBS was prevalent.

After ~24.8% strain, about 15% of the observed grains exhibited slip and 46 slip systems were identified in the 43 grains. As shown in Figure 4.45, 34 out of a total of 46 slip systems were found to be basal slip systems (34/46≈74%) and 11 were prismatic (11/46≈24%). Only one pyramidal <a> slip system was observed with a Schmid factor 0.48 (1/46≈2%). Similar to the 728K-250MPa creep test (see Figure 4.35), the majority of the activated slip systems were basal slip and the associated Schmid factor range was 0.25–0.5 for the 763K-200MPa creep test. Although a few grain exhibited slip, dislocation slip was not prevalent in the examined regions,

and instead grain boundary ledge formation and cracking appeared to be the preferred way to accommodate the strain. After ~24.8% strain, cracking was observed at triple points and grain boundaries (see Figure 4.46).

Figure 4.47 shows stereographic triangles with the grain orientations plotted for basal, prismatic, and pyramidal <a> slip systems with Schmid factor contours overlaid. Generally, the majority of the slip systems were confined to grains with the Schmid factors greater than 0.3. Two basal slip were observed with grain orientations orientated with intermediate Schmid factor values (0.2-0.3). Overall, the deformation behavior of the 763K-200MPa creep test was similar to the 728K-250MPa creep test.

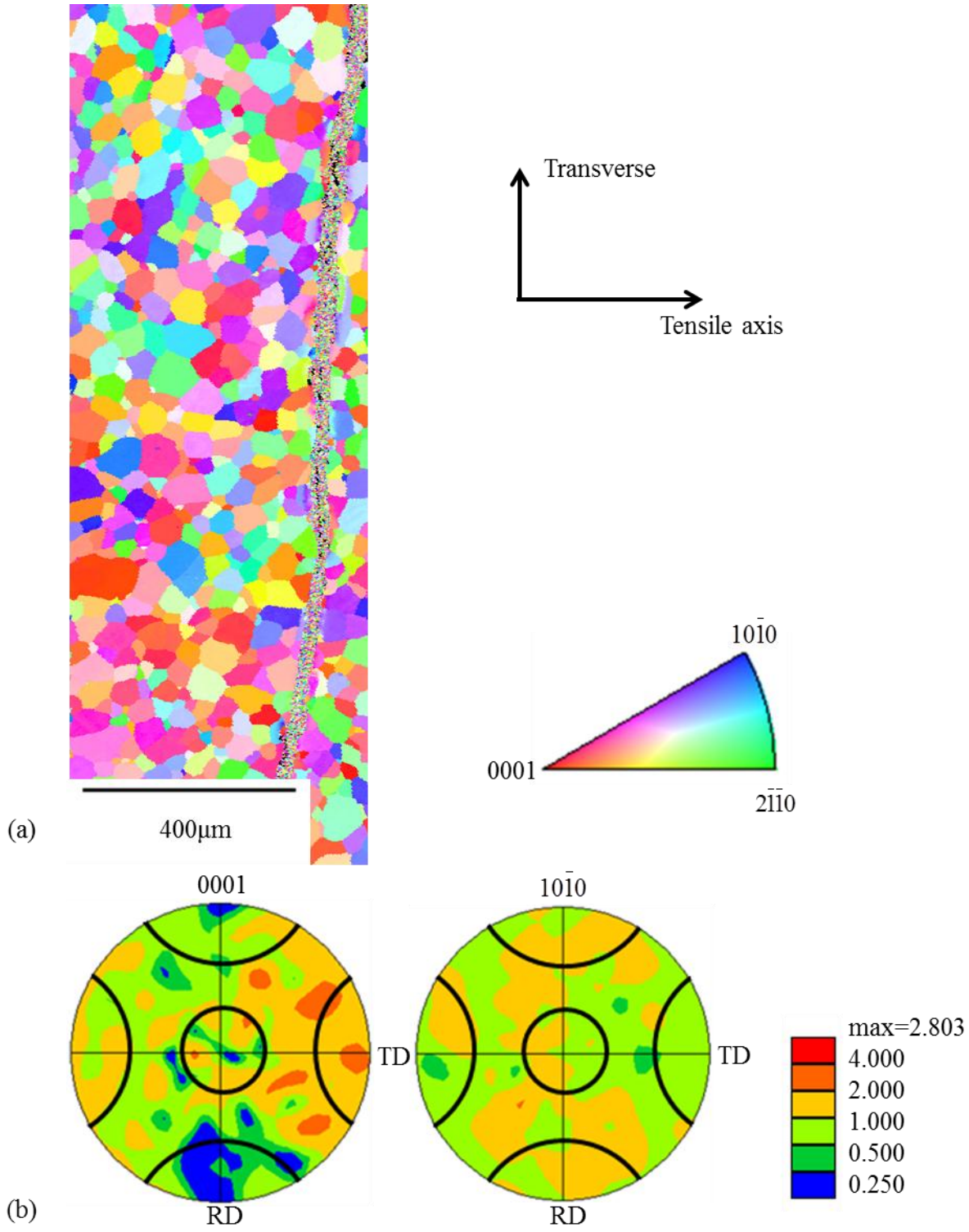

Figure 4.43 EBSD data of the Ti-5Al-2.5Sn 763K-200MPa creep tested specimen: (a) EBSD IPF map in the tensile direction of the α-phase Ti containing approximately 700 α grains, (b) the {0001} and the $\{10\bar{1}0\}$ pole figures with 30 ° cones along the major axes. The intentional scratch on the right of the EBSD map was used as a fiducial marker. The loading axis was horizontal.

(a)

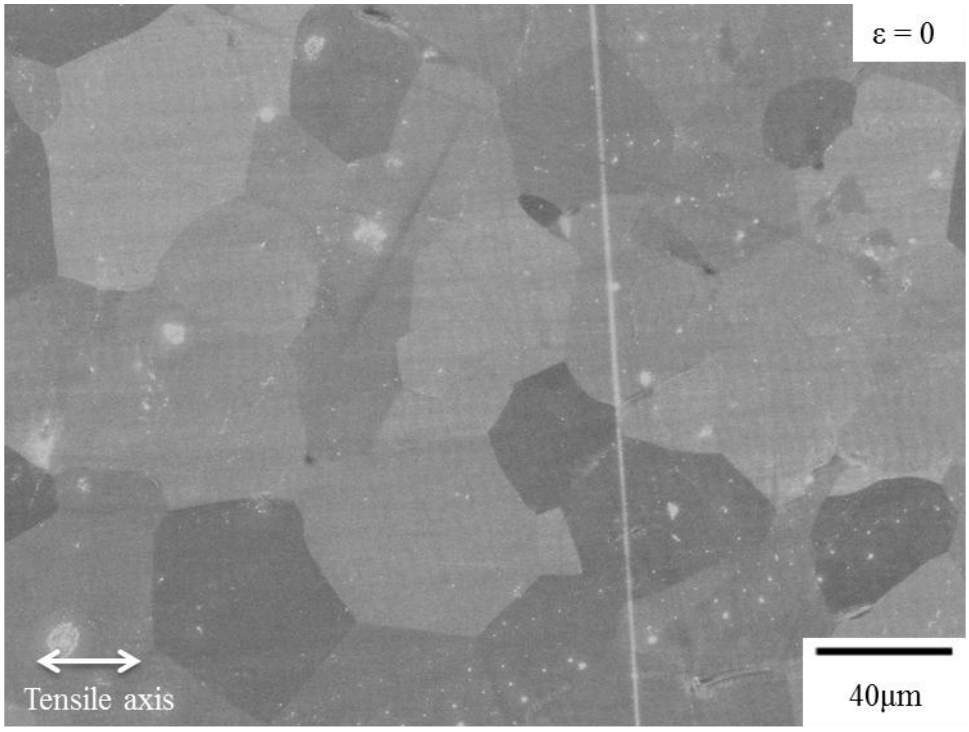

Figure 4.44 Sequential SE SEM images for Ti-5Al-2.5Sn tensile-creep tested at 763K-200MPa: (a) before loading; (b) <0.5% strain, 9 h; (c) ~2.9% strain, 24 h; (d) ~8.3% strain, 30 h; (e) ~21.2% strain, 70 h; (f) ~24.8% strain, 94 h, the color-coded planes traces for prismatic slip (red) and basal slip (blue) are labeled along with their Schmid factors. The loading direction was horizontal. Note that ledges were first apparent in (b) and grew larger with increased deformation. Some grain boundary offsets were also observed in the later stages of the deformation as observed by the vertical fiducial scratch migration.

Figure 4.44 (cont'd)

(b)

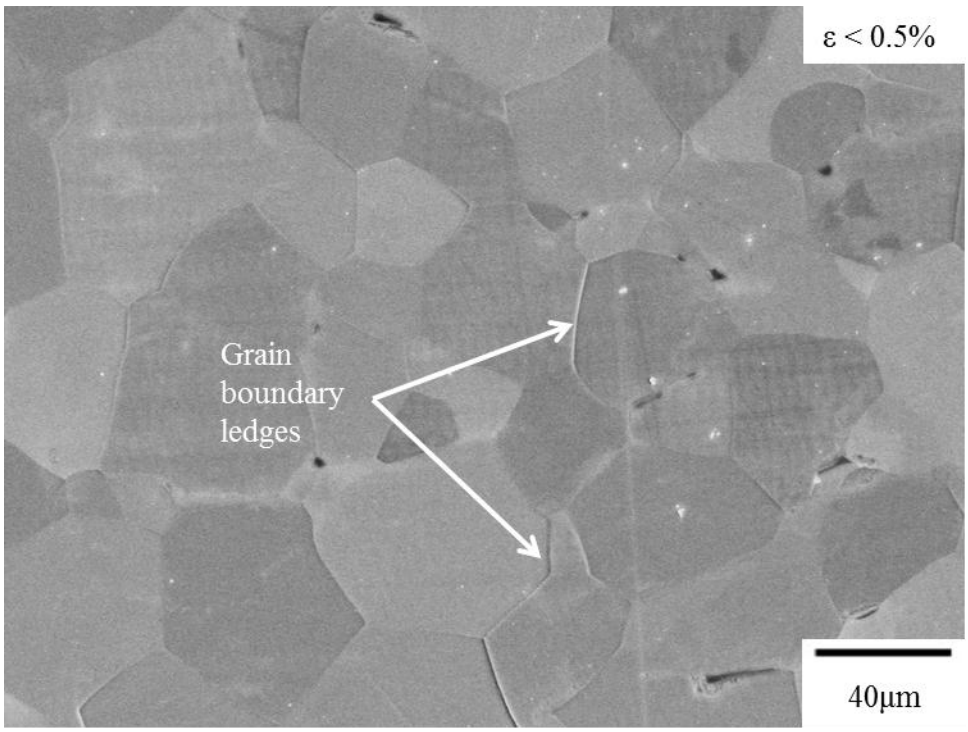

(c)

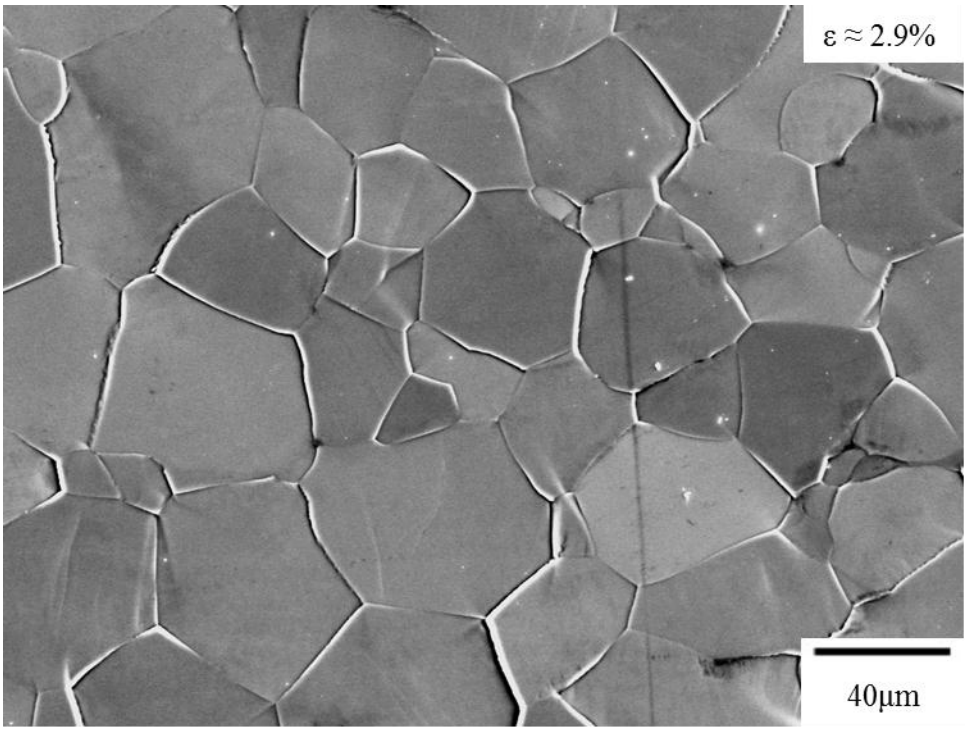

Figure 4.44 (cont'd)

(d)

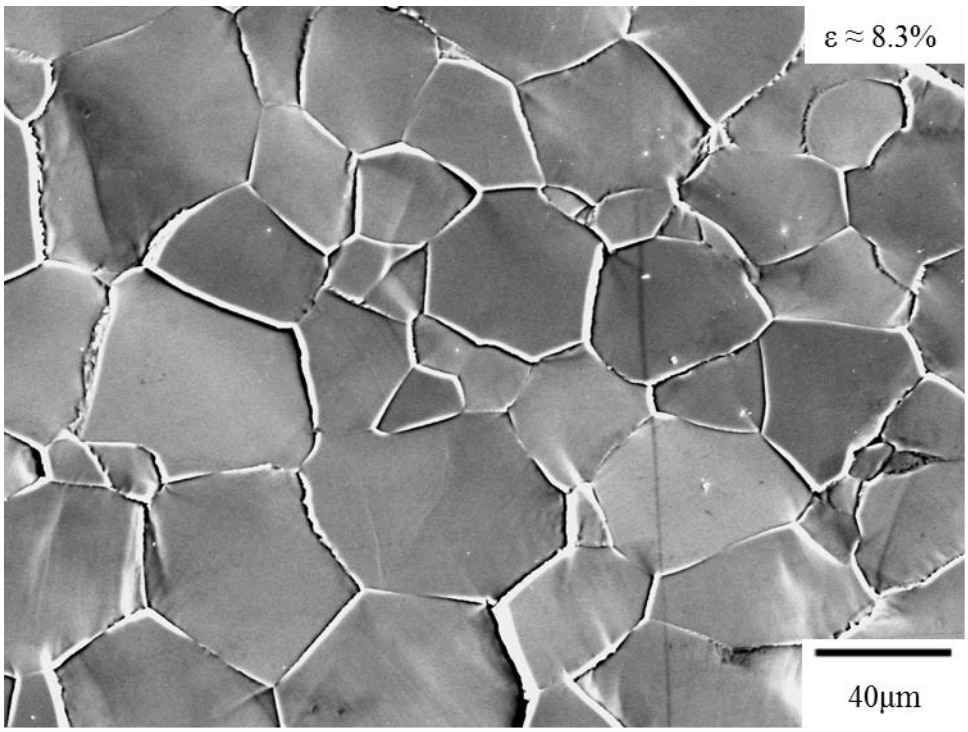

(e)

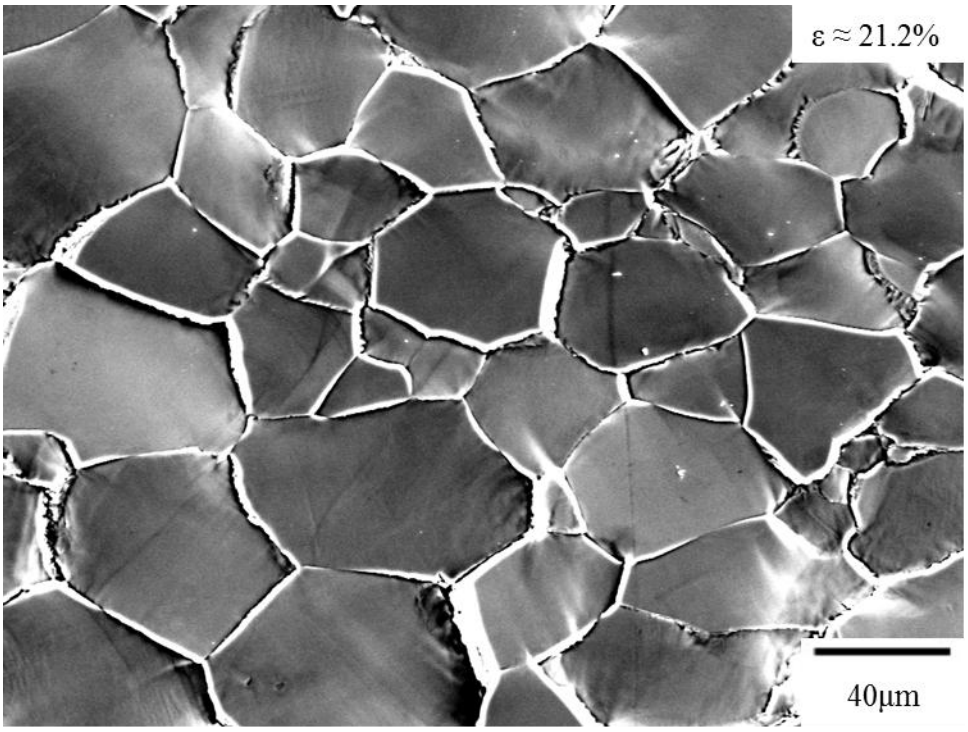

Figure 4.44 (cont'd)

(f)

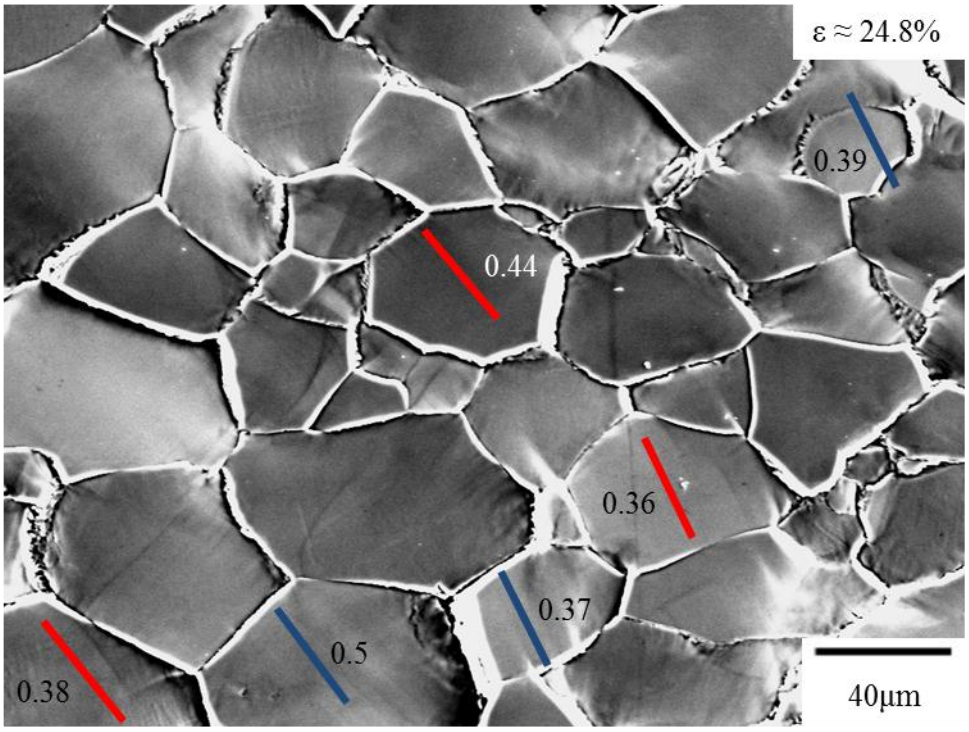

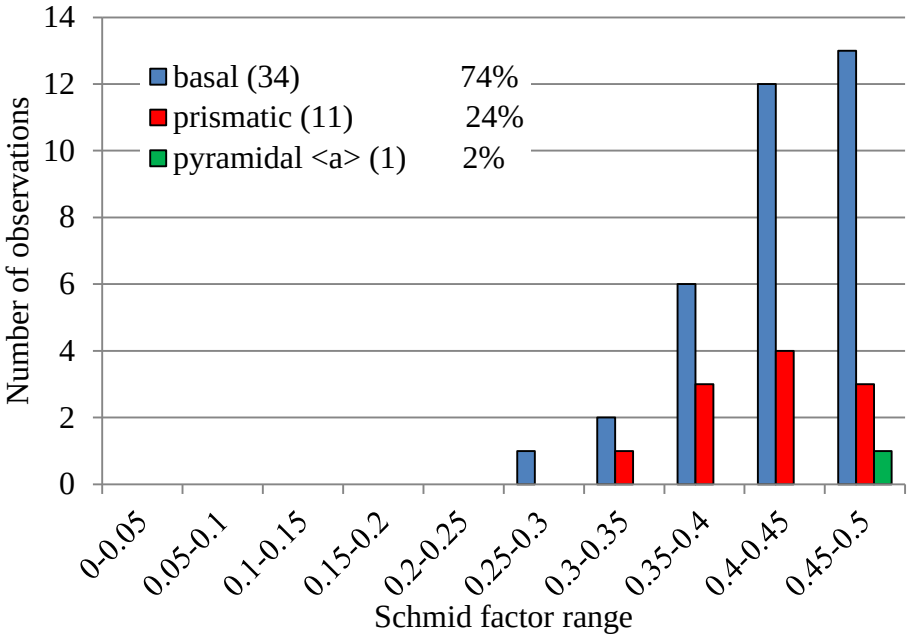

Figure 4.45 A histogram of the Schmid factor distribution of basal, prismatic, and pyramidal <a> slip systems for the Ti-5Al-2.5Sn 763K-200MPa tensile-creep experiment after ~24.8% strain.

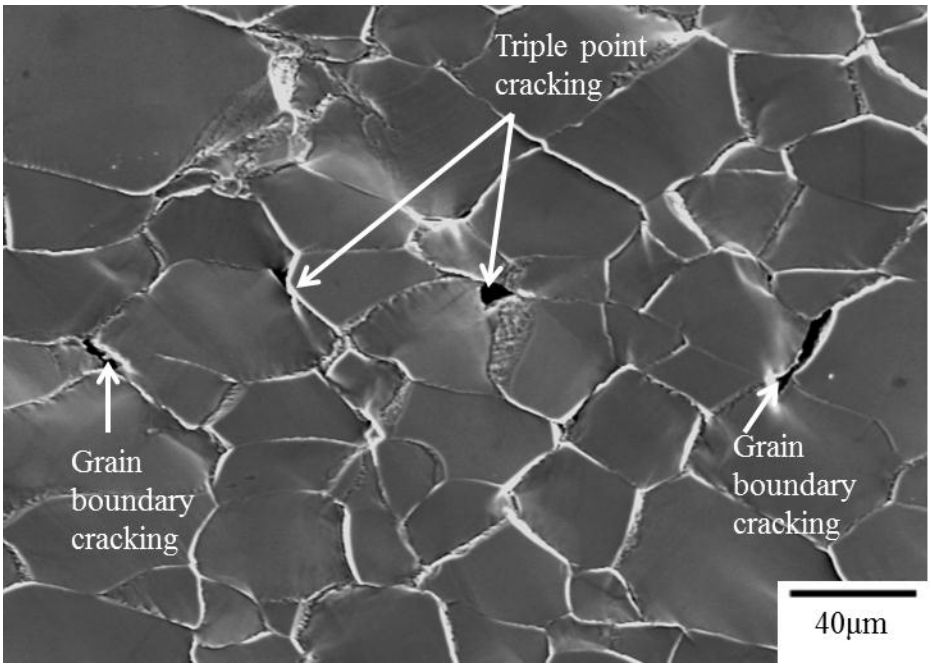

Figure 4.46 SE SEM photomicrograph illustrating grain boundary cracking during the Ti-5Al-2.5Sn 763K-200MPa tensile-creep experiment after ~24.8% strain. The loading direction was horizontal.

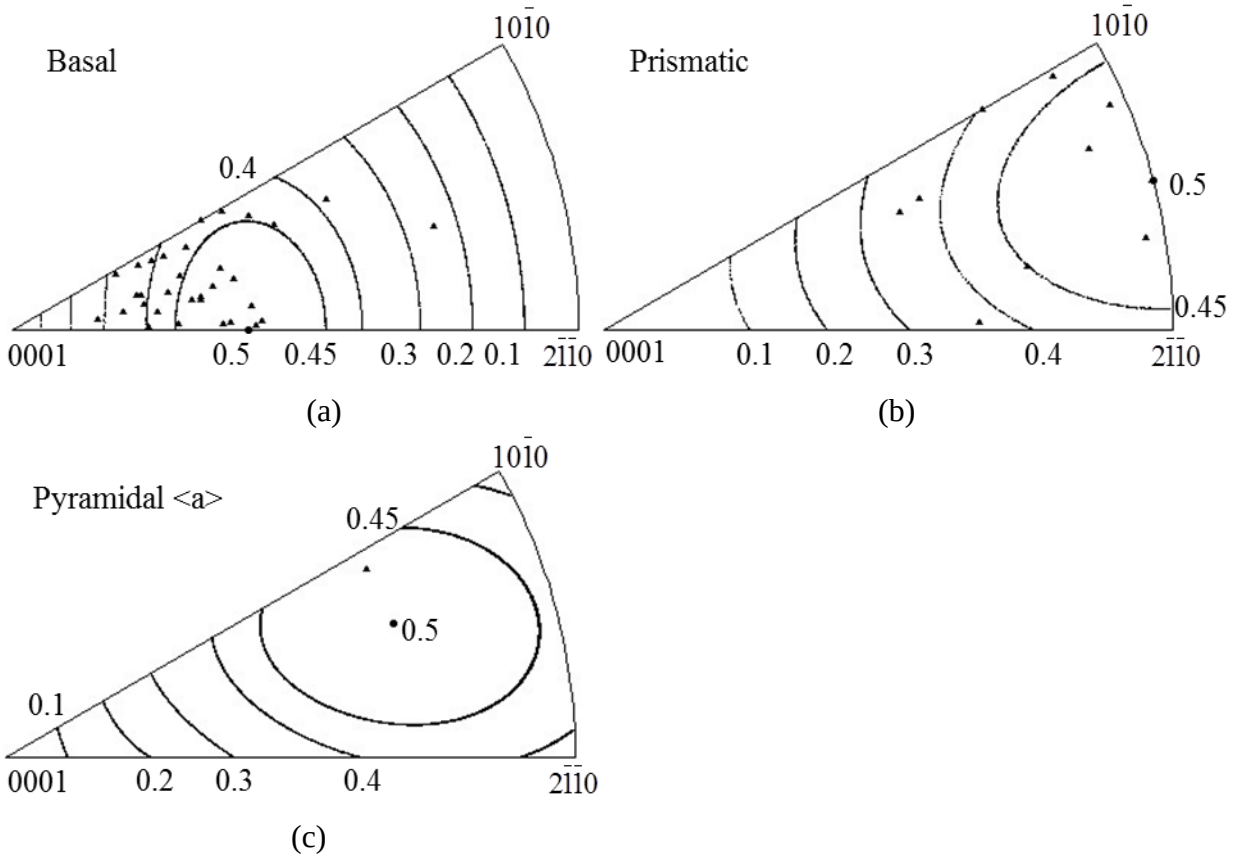

Figure 4.47 Unit triangle plots of grains which exhibited (a) basal, (b) prismatic, and (c) pyramidal <a > slip for the Ti-5Al-2.5Sn 763K-200MPa creep test deformed to ~24.8% strain with Schmid factor contours overlaid.

4.2.4.4 *In-situ* 763K-250MPa creep

Figure 4.48 shows an EBSD IPF map in the tensile direction and the corresponding {0001} and {$10\bar{1}0$} pole figures from the gage section of the 763K-250MPa creep tested specimen for Ti-5Al-2.5Sn. There were approximately 650 α grains in Figure 4.48. Like the other Ti-5Al-2.5Sn specimens, the 763K-250MPa creep specimen also exhibited a weak texture (an approximately three times random) and the locations with the maximum peak intensities in Figure 4.48 varied from the previous tested specimens of Ti-5Al-2.5Sn.

Figure 4.49 shows *in-situ* SE SEM images of the same area acquired during the 763K-250MPa creep experiment. At ~5.5% strain in Figure 4.49 (c), grain boundary ledges and slip traces were observed. Four prismatic (highlighted by red lines), three basal (highlighted by blue lines), and one pyramidal <c+a> slip systems (highlighted by yellow line) were observed for this microstructural patch after ~5.5% strain. With increasing strain, more grain boundary ledges formed and more grains exhibited slip traces. The slip traces were planar and cross slip was not prevalent. Some grain boundary ledges eventually formed cracks, shown in Figure 4.50.

After ~15.3% strain, 43 out of 64 grains (43/64≈67%) showed evidence for 44 activated slip systems. About 24 (24/44≈59%) of the activated slip systems exhibited basal slip and 17 (17/44≈39%) displayed prismatic slip. The trace analysis showed that all of the activated slip systems had Schmid factors greater than 0.3 (with one exception for a prismatic slip system with a Schmid factor of 0.23), as shown in Figure 4.51. At 763K, more prismatic slip and less basal slip was activated than in the sample creep-tested at 728K-250MPa. Thus, temperature plays an important role in determining which slip systems are activated.

Figure 4.52 shows the stereographic triangles with the grain orientations plotted for basal, prismatic, pyramidal <a>, and pyramidal <c+a> slip with Schmid factor contours overlaid. Similar to other creep tests, most of the slip systems were confined to grains with high Schmid factors. Compared with the 763K-200MPa creep test in Figure 4.47 (b), there were more prismatic slip systems in the regions corresponding to high Schmid factors for prismatic slip during the high stress 763K-250MPa creep test (see Figure 4.52 (b)), suggesting that prismatic slip was preferred at higher stresses during creep. The effect of stress on the relative activity of different slip systems during creep will be further discussed in Chapter 5.

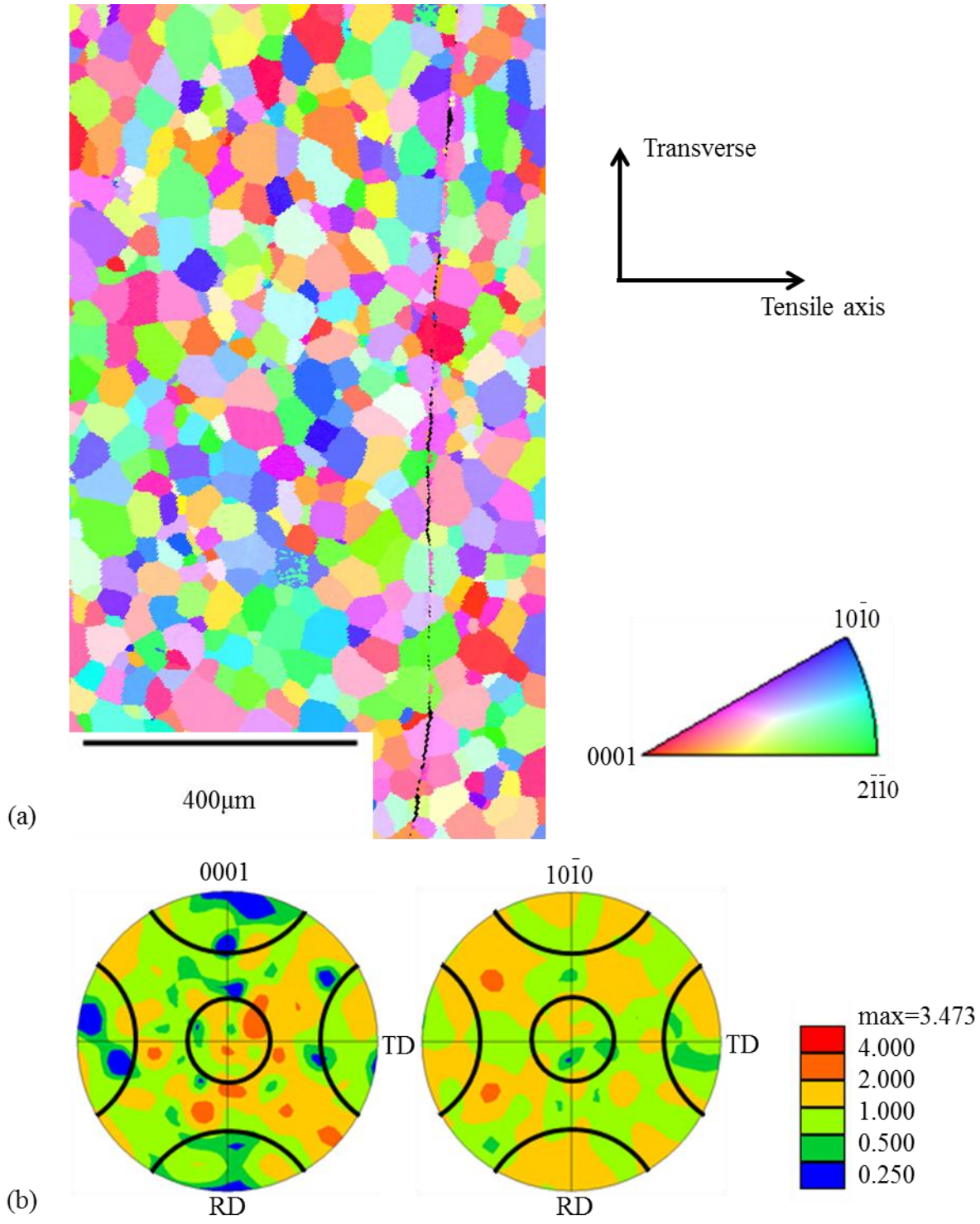

Figure 4.48 EBSD data of the Ti-5Al-2.5Sn 763K-250MPa creep tested specimen: (a) EBSD IPF map in the tensile direction of the α-phase Ti containing approximately 650 α grains, (b) the {0001} and the $\{10\bar{1}0\}$ pole figures with 30 ° cones along the major axes. The intentional scratch on the right of the EBSD map was used as a fiducial marker. The loading direction was horizontal.

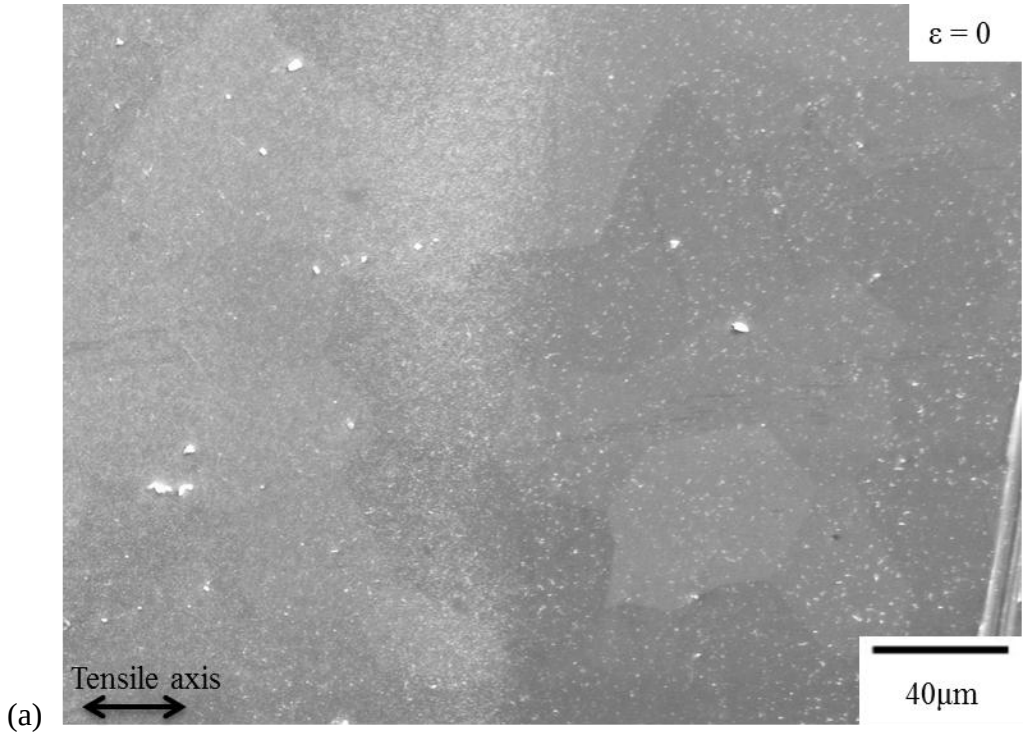

(a)

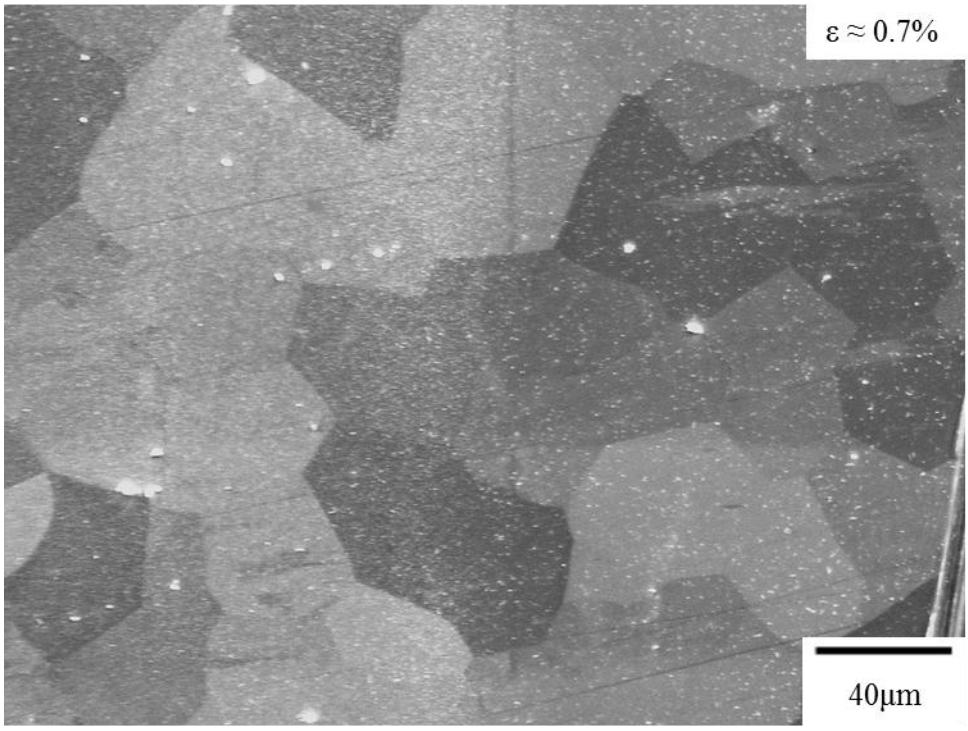

(b)

Figure 4.49 Sequential SE SEM images for Ti-5Al-2.5Sn tensile- creep tested at 763K-250MPa: (a) before loading; (b) 0.7% strain, 8 h; (c) ~5.5% strain, 23 h, the color-coded planes traces for prismatic slip (red), basal slip (blue), and pyramidal <c+a> (yellow) are labeled along with their Schmid factors; (d) ~8% strain, 34 h; (e) ~12% strain, 56 h; (f) ~15.3% strain, 59 h. The loading direction was horizontal.

Figure 4.49 (cont'd)

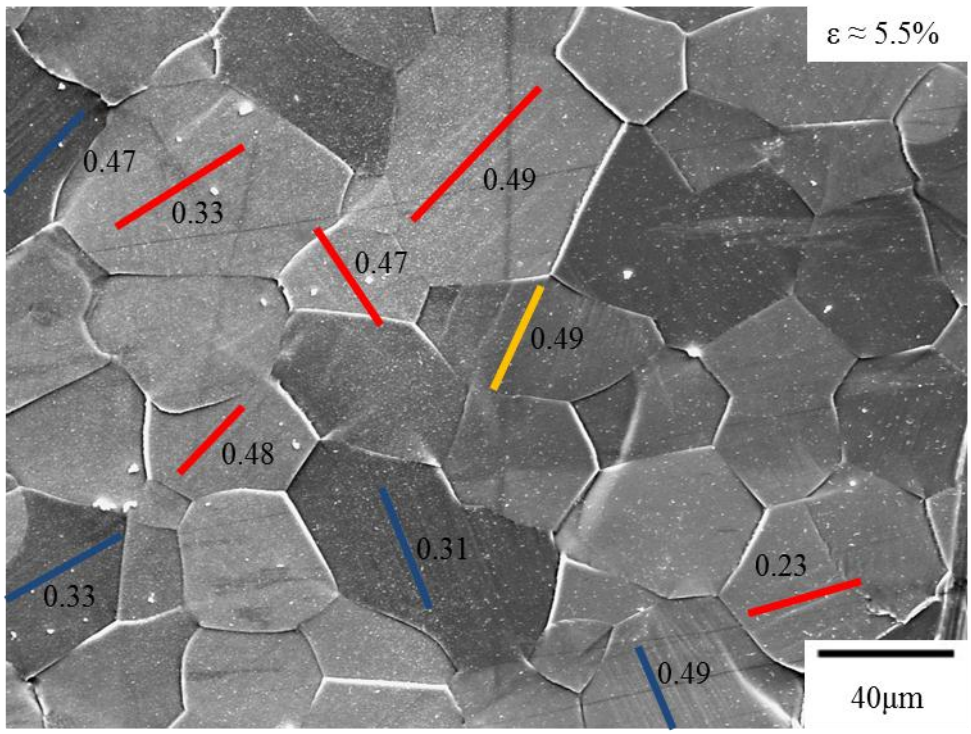

(c)

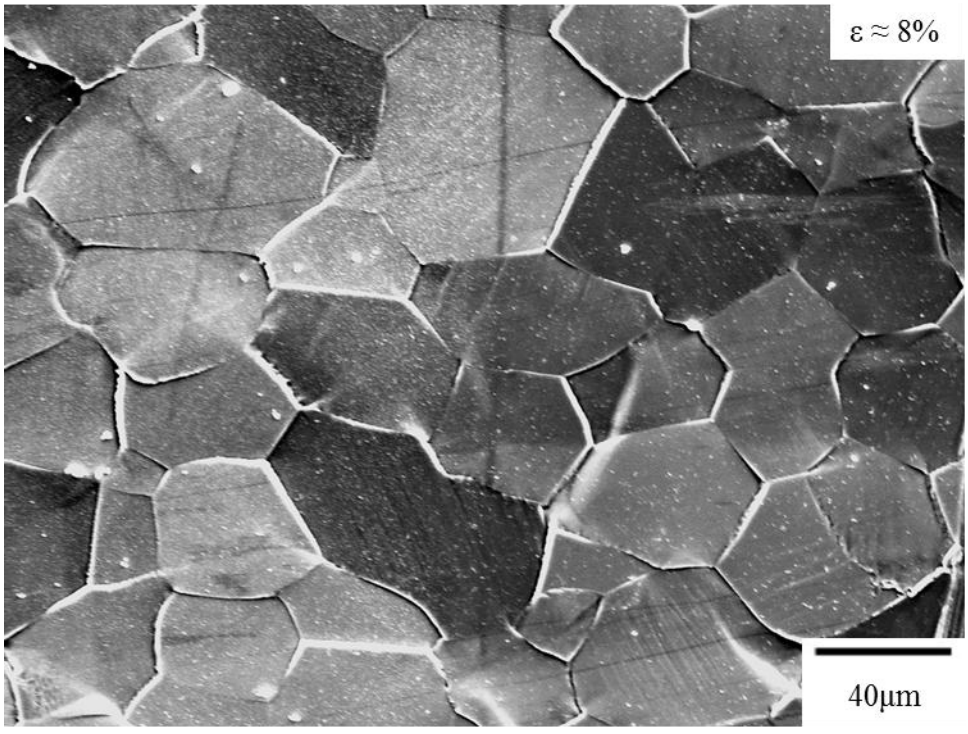

(d)

Figure 4.49 (cont'd)

(e)

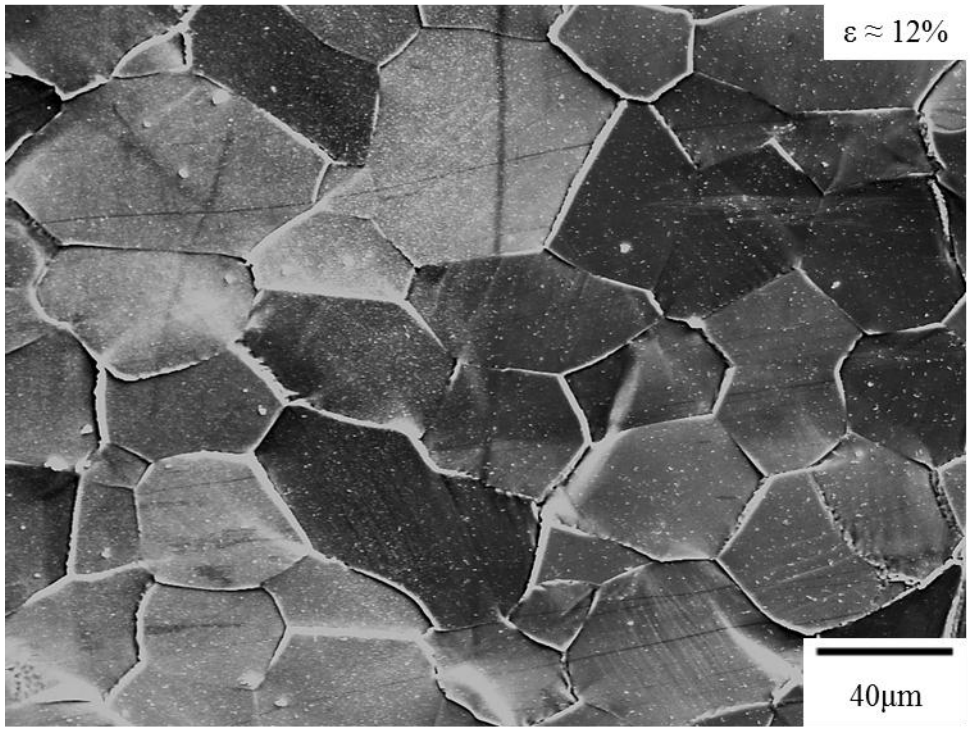

(f)

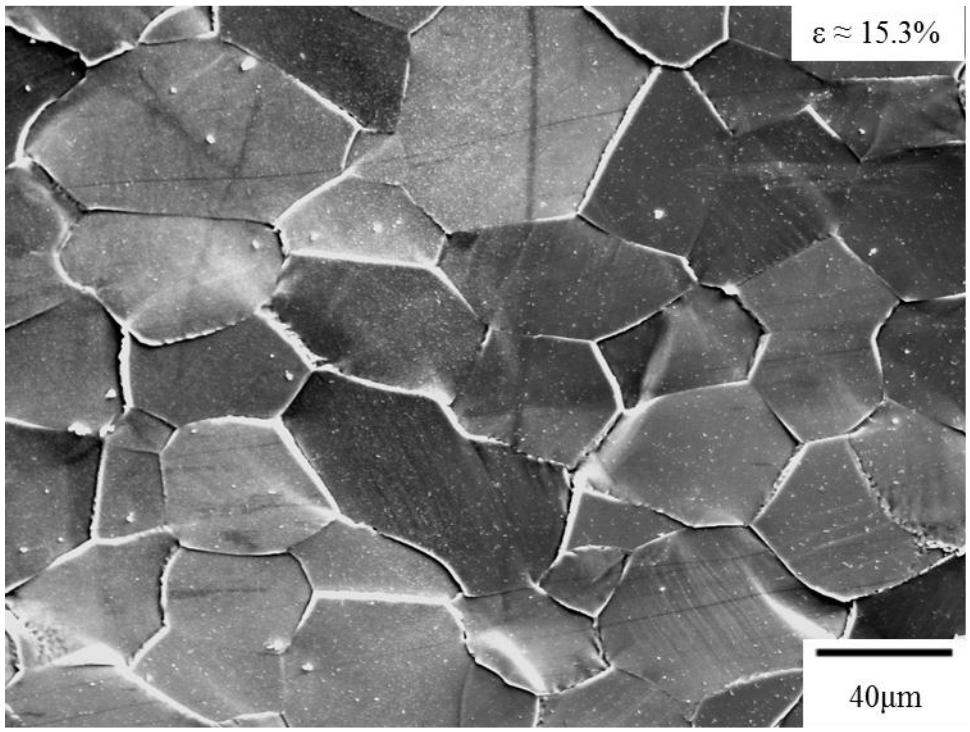

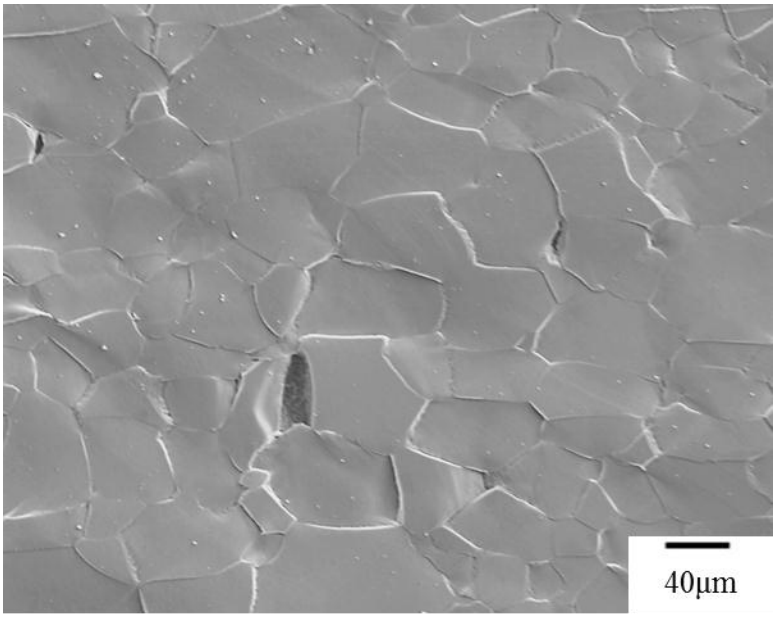

Figure 4.50 SE SEM photomicrograph illustrating grain boundary cracking during the Ti-5Al-2.5Sn 763K-250MPa tensile-creep experiment after ~15.3% strain. The loading direction was horizontal.

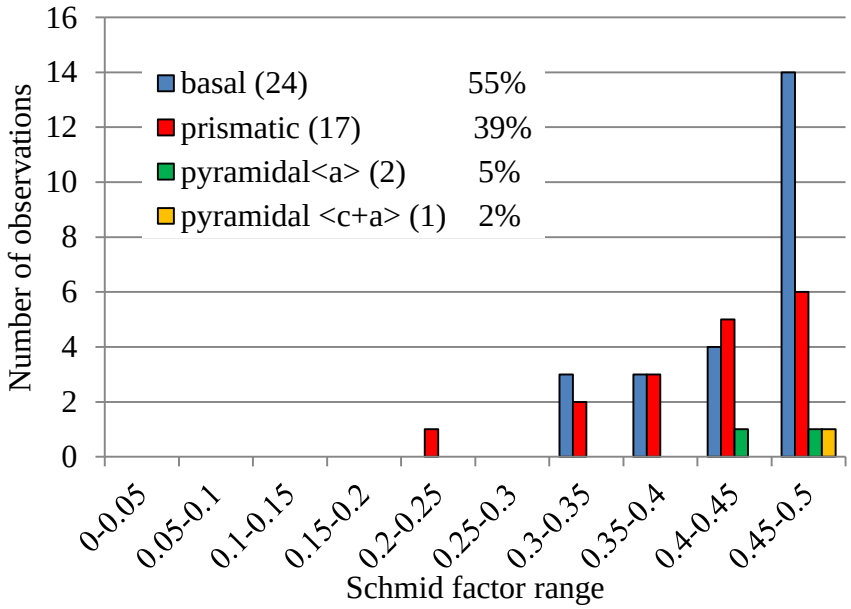

Figure 4.51 A histogram of the Schmid factor distribution of basal, prismatic, and pyramidal <a> slip systems for the Ti-5Al-2.5Sn 763K-250MPa tensile-creep experiment after ~15.3% strain.

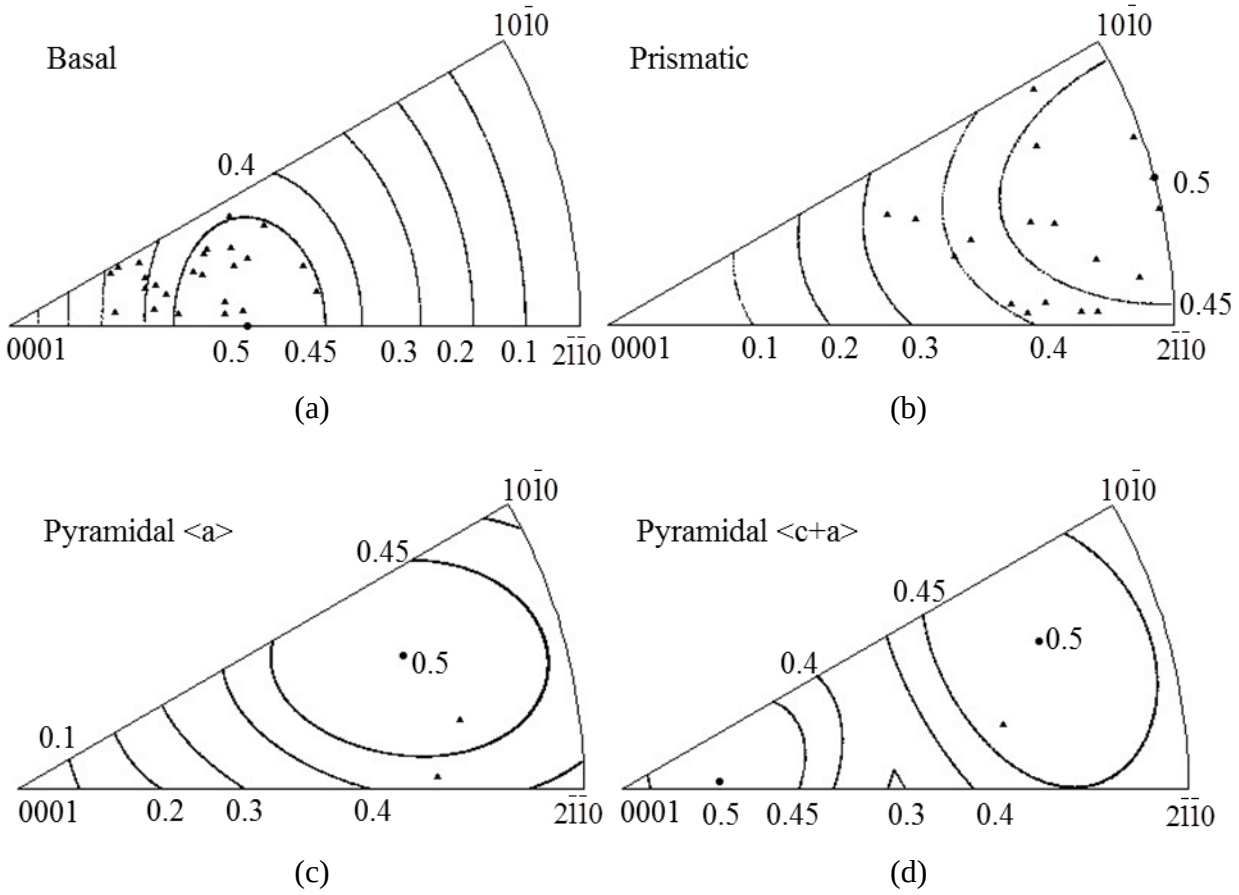

Figure 4.52 Unit triangle plots of grains which exhibited (a) basal, (b) prismatic, (c) pyramidal <a >, and pyramidal<c+a> slip for the Ti-5Al-2.5Sn 763K-250MPa creep test deformed to ~15.3% strain with Schmid factor contours overlaid.

4.2.5 GBS analysis

Grain boundary ledges were characterized for the four deformed Ti-5Al-2.5Sn creep specimens using a digital optical microscope (VHX-600). Figure 4.53 shows an example of a grain boundary ledge measurement for the 763K-200MPa creep-tested specimen. Figure 4.53 (a) and (b) illustrates two optical microscope images taken with grain "1" and grain "2" in focus, respectively. Note that the minimum increment of the working distance was set to be 0.2μm. The difference of the two working distances associated with Figure 4.53 (a) and (b) was 4.4μm. Therefore, the step height between grain "1" and "2" was estimated to be 4.4μm. For each Ti-5Al-2.5Sn creep specimen, the step height was measured for 90 distinct grain boundaries within the *in-situ* imaged areas shown in Figure 4.31, Figure 4.39, Figure 4.44, and Figure 4.49. Figure 4.54 represents the distribution of the step heights for each of the creep specimens. Most of the step heights were less than 5μm. The 763K-200MPa creep specimen exhibited the largest range for the step heights in all of the four creep specimens, and two ledges were found to have step heights greater than 10μm.

Table 4.3 summarizes GBS analysis results performed on the Ti-5Al-2.5Sn creep deformed specimens. Almost all of the grain boundaries analyzed exhibited measurable amount of GBS. The average grain boundary step heights were 2.1μm, 2.0μm, 3.8μm, and 1.8μm for the 728K-250MPa, 728K-300MPa, 763K-200MPa, and 763K-250MPa creep deformed specimens, respectively. The strain accommodated by GBS (GBS strain) was calculated by using the average grain boundary step height divided by the average grain diameter of the Ti-5Al-2.5Sn alloy (39.5μm, see section 4.2.1). Therefore, the corresponding GBS strains of these four creep specimens were 5.3%, 5.1%, 9.7%, and 4.4%, respectively. The strain in loading direction was estimated by measuring the relative displacements of obvious microstructural features on SEM

images acquired before and after deformation. The final strains of the four creep tests were ~16.5%, ~21.4%, ~24.8%, and ~15.3%, respectively. The contribution of GBS to the strain in the loading direction was estimated by the ratio of GBS strain and the final strain in the loading. For example, the contribution of GBS to the strain in the loading direction was calculated to be 32.2% (GBS strain (5.3%) divided by the strain (~16.5%) in the loading direction) for the 728K-250MPa creep deformed specimen. In Table 4.3, at 728K, increasing the creep stress from 250MPa to 300MPa, the contribution of GBS to the strain in the loading direction decreased from 32.2% to 23.6%. This statement was supported by a statistical t-test with 95% confidence (P=0.0104). A similar trend was also observed at 763K, where the contribution of GBS to the strain in the loading direction decreased from 39.0% to 29.0% with increasing creep stresses from 200MPa to 250MPa. This statement was also supported by a statistical t-test with 95% confidence (P=0.0035). Therefore, at the same temperature, GBS was enhanced by decreasing the applied creep stress level. This is consistent with Ashby and Crossman's study, which found that GBS becomes more extensive with decreasing stress at constant temperature [Crossman et al. 1975]. It is noted that the method of calculating the contribution of GBS to the strain in the loading direction is based on a rough assumption that the extent of GBS in the loading direction of the sample is the same as the sample normal direction.

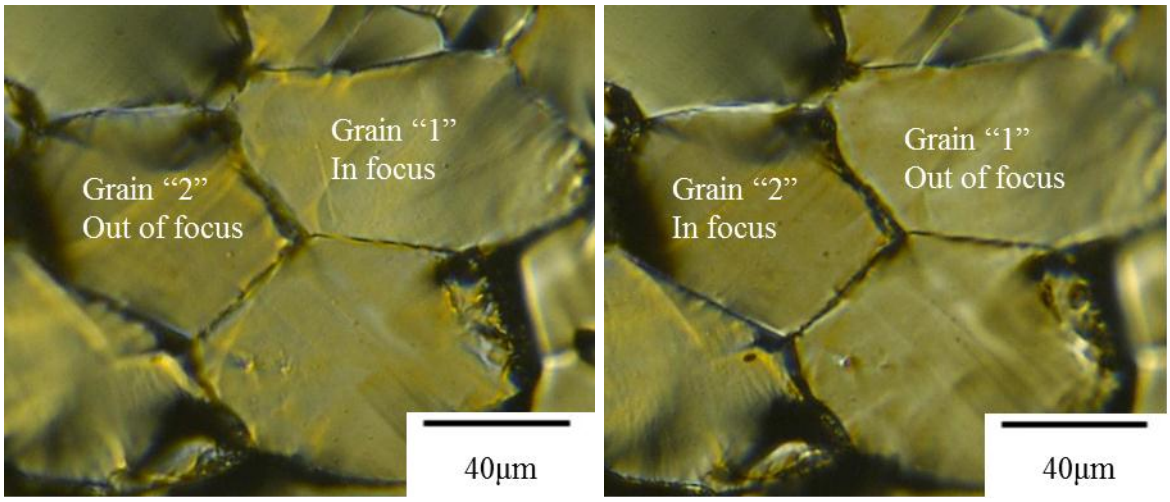

(a) (b)

Figure 4.53 Optical microscope images showing (a) grain "1" in focus and (b) grain "2" in focus with an associated z-direction step height of 4.4μm for the 763K-200MPa creep specimen after ~24.8% strain.

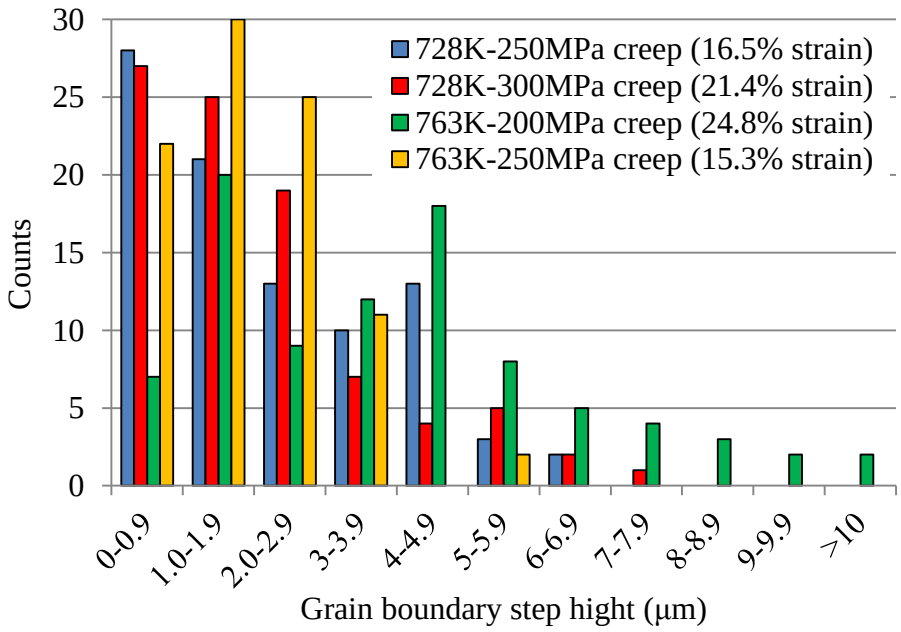

Figure 4.54 The grain boundary step height distributions of the four Ti-5Al-2.5Sn creep tested specimens. The final local strains were listed in parenthesis.

Table 4.3 Summary of GBS analysis on Ti-5Al-2.5Sn creep specimens.

	Creep testing conditions			
	728K-250MPa	728K-300MPa	763K-200MPa	763K-250MPa
Number of GBs analyzed	90	90	90	90
Number of GBs exhibited sliding	89	87	90	88
Average GB step height	2.1μm	2.0μm	3.8μm	1.8μm
Standard deviation	1.59μm	1.68μm	2.62μm	1.07μm
GBS strain	5.3%	5.1%	9.7%	4.4%
Strain in the loading direction	16.5%	21.4%	24.8%	15.3%
Contribution of GBS to the strain in the loading direction	32.2%	23.6%	39.0%	29.0%

4.2.6 3D XRD analysis

Synchrotron 3D XRD was performed on the Ti-5Al-2.5Sn 728K-250MPa tensile-creep tested specimen to provide supplemental information about the dislocation arrangement beneath the specimen surface, which could not be acquired by the slip trace analysis technique and the traditional two-dimensional (2D) EBSD technique. For a dislocation-free specimen, the diffraction patterns (i.e. Laue patterns) are sharp points. After deformation, the diffraction patterns may not be sharp points. This is related to lattice defects such as dislocations. The presence of dislocations may affect the shape of the diffraction spots, resulting in streaks or elongated spots. Therefore, 3D XRD can be used to investigate the subsurface dislocation content.

For the Ti-5Al-2.5Sn 728K-250MPa tensile-creep specimen deformed to ~16.5% strain, 90% of the grains did not exhibit slip traces on surface and most of the grain boundaries developed ledges. Figure 4.55 shows a SE SEM image of the 728K-250MPa tensile-creep tested specimen after ~16.5% strain and the corresponding EBSD IPF map in the tensile direction. In Figure 4.55, a grain boundary ledge with a vertical displacement of 14μm was developed at the

right side of grain “3” and no slip trace was observed in this grain. A 3D XRD line scan along the tensile axis was performed using a step size of 2μm inside grain 3. The length of this line scan was 34μm. Figure 4.56 shows the subsurface map of this line scan and the diffraction patterns. In Figure 4.56, some diffraction patterns exhibited streaked or elongated spots, suggesting dislocation content beneath the surface. However, no surface slip traces were observed. Based on the shape of the diffraction spots, the subsurface of grain “3” was divided into 6 distinct regions. The representative indexed diffraction patterns from each of the 6 regions are shown in Figure 4.56. The orange, gold, red, and pink regions (i.e. a-d regions) exhibited streaked spots. The grey regions exhibited diffused spots (i.e. e-f regions). These observations suggest that although no slip traces are observed at surface, this does not mean that subsurface regions don’t exhibit slip activity. Furthermore, the change of the shape of the diffraction patterns may indicate the presence of more than one dislocation slip system beneath specimen surface. The dislocations associated with the different regions are not the focus of this dissertation. This could be the target of the future work.

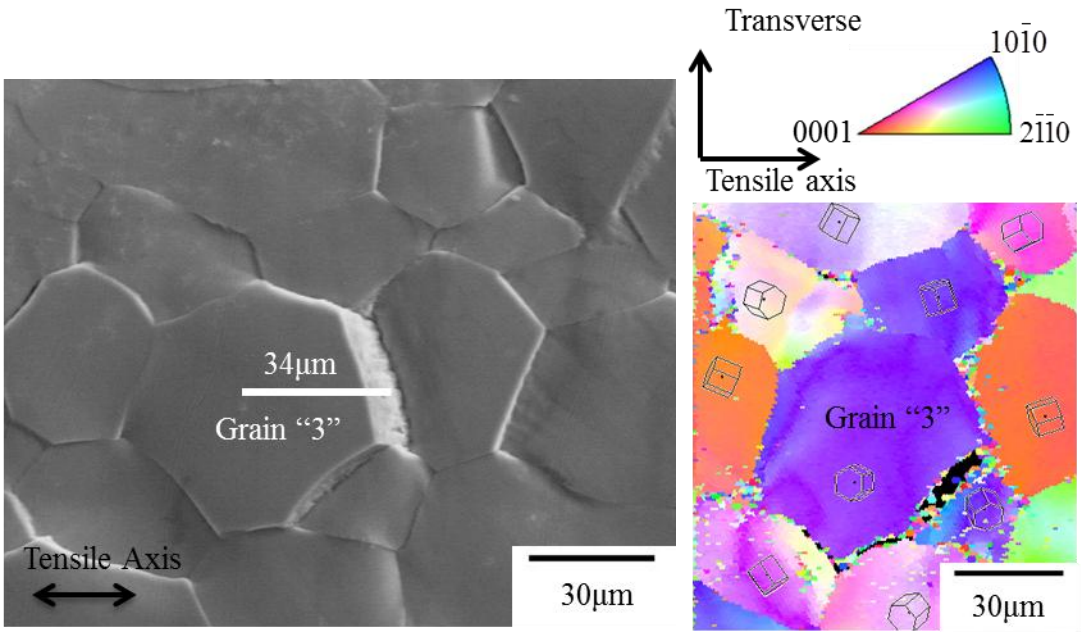

(a) (b)

Figure 4.55 (a) A SE SEM image of the 728K-250MPa tensile-creep tested specimen after ~16.5% strain. Most of the grains did not show surface slip traces. A 34μm 3D XRD line scan along the tensile axis was performed in grain 3. (b) An EBSD orientation map for the same region with the grain orientations depicted by the overlaid unit cells.

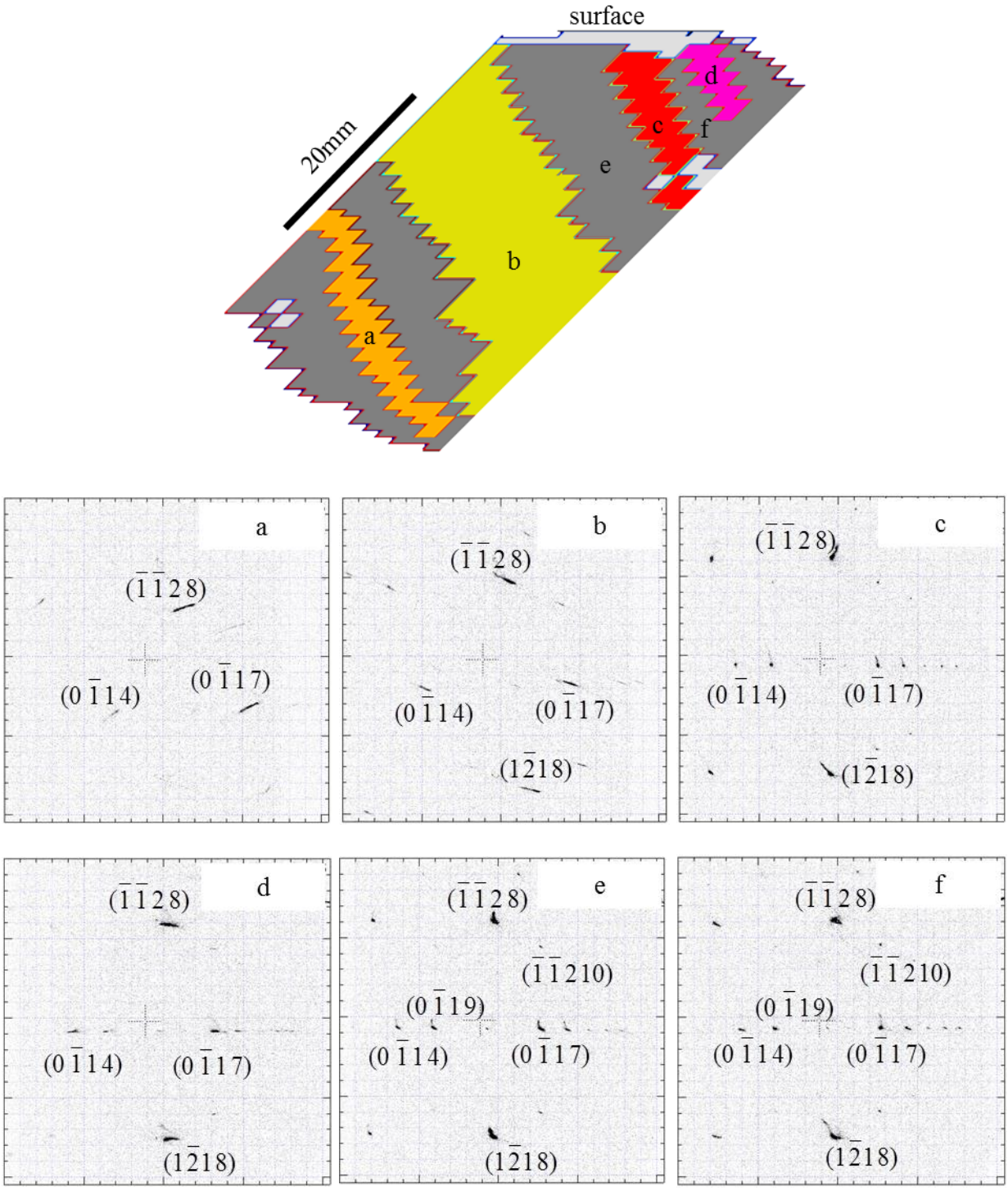

Figure 4.56 Results from the 3D XRD line scan in grain "3" for the 728K-250MPa tensile-creep tested specimen after ~16.5% strain. The orange, gold, red, and pink regions show peak streaks along different directions. The representative diffraction patterns of six pixels labeled a-f from the six different regions are shown.

4.3 Ti-3Al-2.5V

4.3.1 Microstructure

The two Ti-3Al-2.5V plates (i.e. plate 1 and plate 2) exhibited similar microstructures. The low- and high-magnification SE SEM images of the as-received near-α Ti-3Al-2.5V alloy microstructure are shown in Figure 4.57. The bright phase in Figure 4.57 is the β phase, which comprised 6.1±1.1% of the total volume as measured through image analysis, and is distributed along the α/α grain boundaries and at triple points. Contrast variations observed in the darker α grains are a consequence of the electron channeling effect coupled with the variation in α grain orientation. Using a method described by Glavicic et al. [2003a and 2003b], it was determined that sometimes several α grains shared a common β variant and that the β orientations varied in different places. The average α grain size was 5.1±0.8μm in both plates. This analysis suggests that the size of the prior β grains was ~10-20μm and that the microstructural patch shown in Figure 1 originated from β grains with a variety of grain orientations. It was ruled out that the microstructure could have been transformed from one parent β orientation.

4.3.2 XRD

XRD was performed to investigate the bulk texture of the as-received Ti-3Al-2.5V plate 1, shown in Figure 4.58. The Ti-3Al-2.5V alloy exhibited a moderate texture with the intensity no stronger than ~6 times random. In Figure 4.58, most of the c-axis orientations in the {0001} pole figure were aligned within 30° of the transverse direction and the corresponded three $\{10\bar{1}0\}$ peaks were along the tensile axis. Prismatic slip was favored for activation in such bulk texture. For plate 2, the texture was not measured by XRD and the textures of specimens cut from plate 2 were measured by EBSD instead and will be presented in section 4.3.3.

(a)

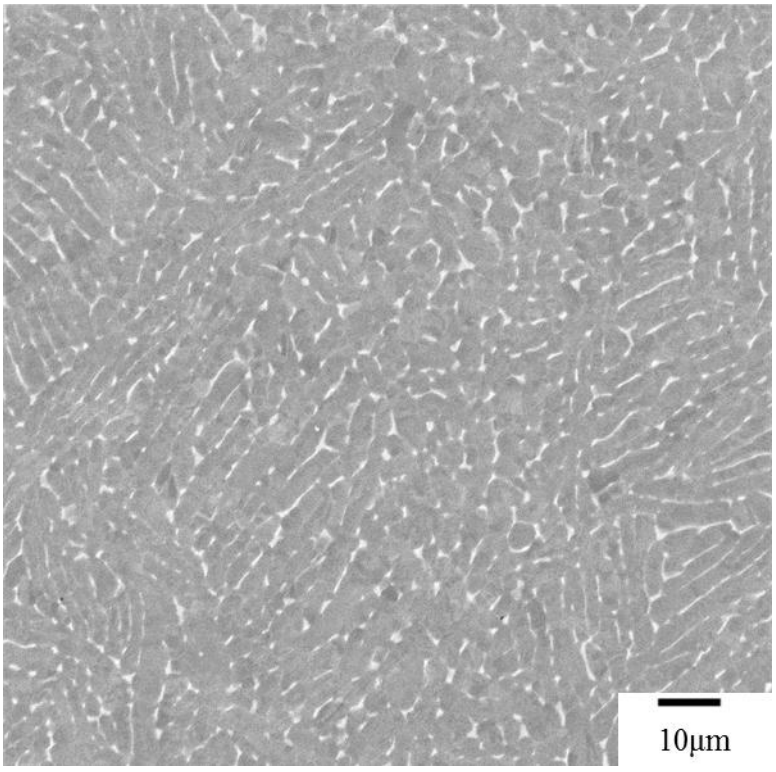

(b)

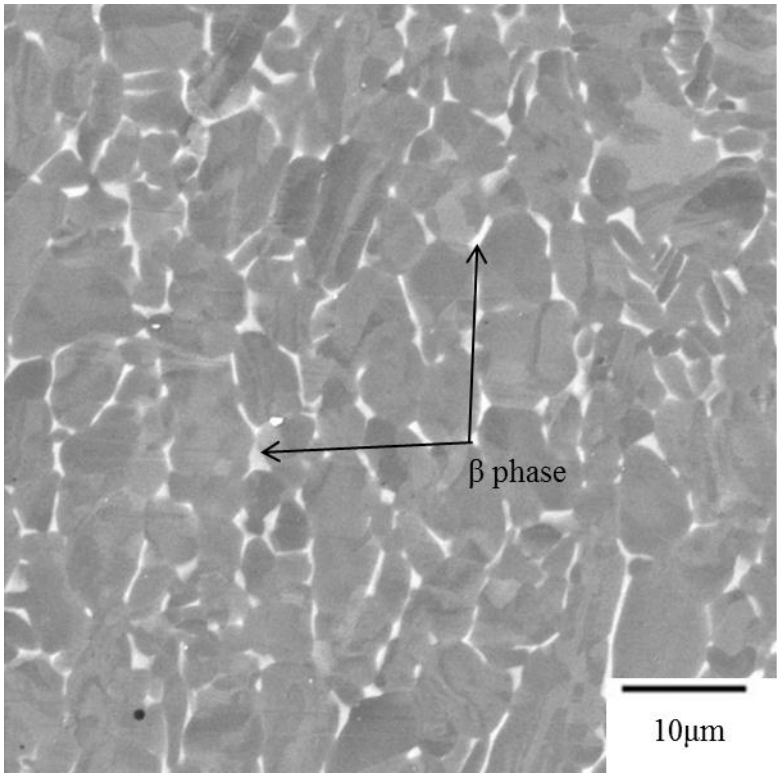

Figure 4.57 (a) Low- and (b) high-magnification SE SEM images of the as-received Ti-3Al-2.5V alloy.

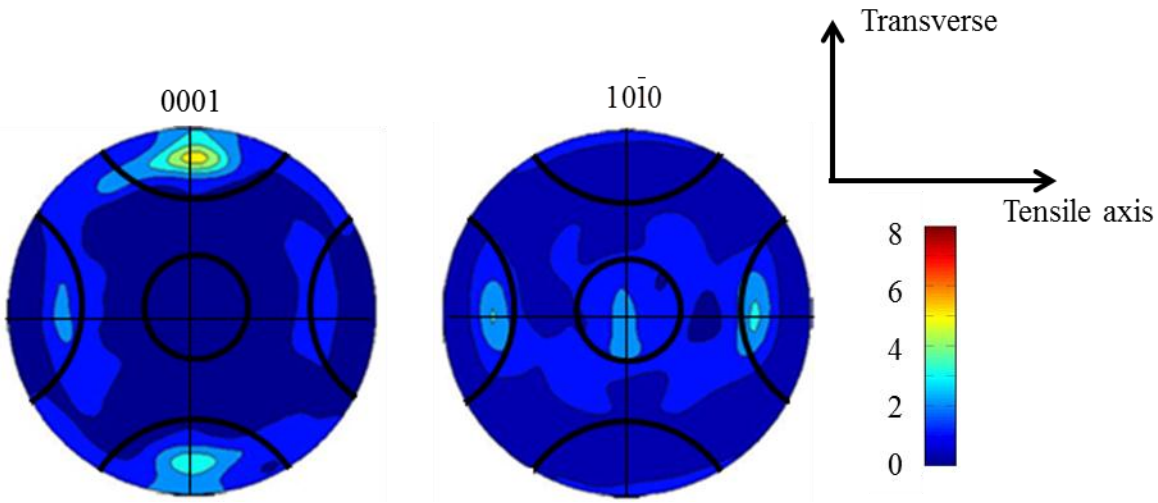

Figure 4.58 {0001} and {$10\bar{1}0$} pole figures with 30° cones along the major axes of the Ti-3Al-2.5V alloy from plate 1measured using XRD.

4.3.3 *In-situ* tension

One specimen from each plate was tensile deformed at 296K and 728K. The engineering stress versus displacement curves for the 296K and 728K tensile tests are illustrated in Figure 4.59. None of the specimens were taken to failure, but a minimum local strain of ~6.5% was achieved. The stress-displacement curve of plate 1 deformed at 296K was similar to that of plate 2 deformed at 296K, except that the YS was slightly lower. The stress-displacement curves collected at 728K show that the yield stresses of plate 1 and plate 2 exhibited no significant difference. Overall, from 296K to 728K, the YS of Ti-3Al-2.5V decreased from ~560MPa for plate 1 and ~600MPa for plate 2 to ~250MPa for both plates.

Table 4.4 shows a good agreement of the YS and the UTS values obtained in the current study and the corresponding values found in the Ti handbook by Boyer et al. [1994]. At 296K, the UTS and the YS values in the literature were in a wide range and this is may be due to the small compositional differences, the heat treatment differences, and the texture differences of the tested specimens. It is noted that only the maximum temperature at which the YS and the UTS

of Ti-3Al-2.5V were found in the literature is 598K and the corresponding YS and UTS values at 598K were 300MPa and 500MPa respectively. Since increasing temperature leads to a decrease in the YS and the UTS values, the YS and the UTS at 728K should be below the values found at 598K. This is the case for the values found in the current study.

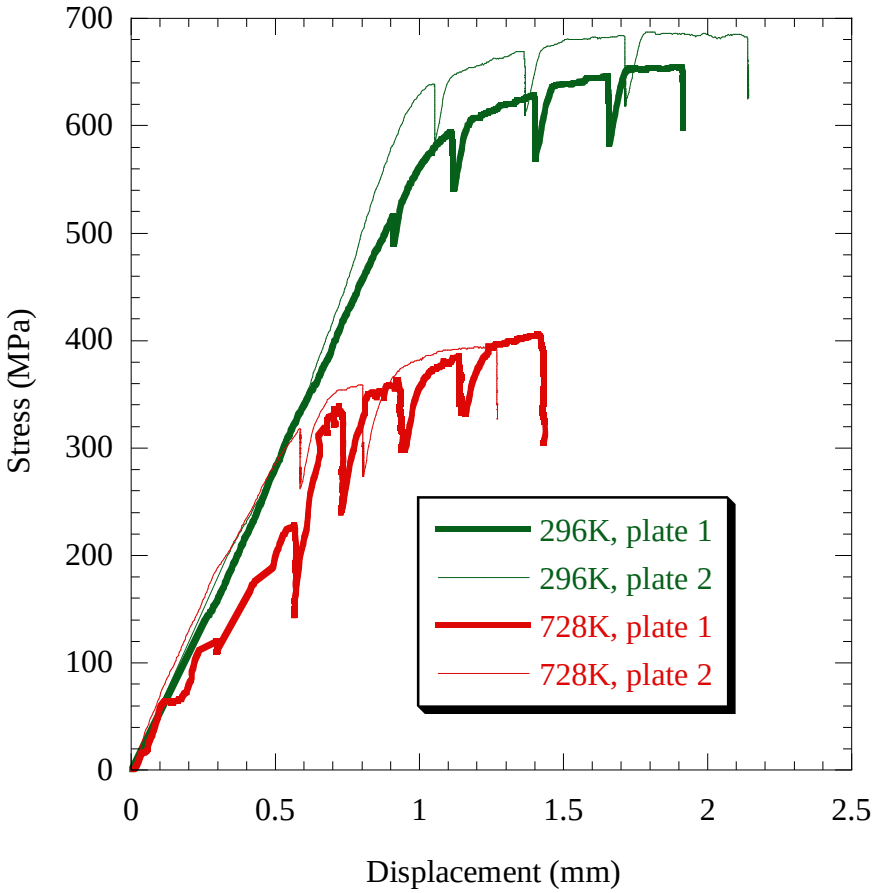

Figure 4.59 Stress vs. displacement plots for Ti-3Al-2.5V samples tensile tested at 296K and 728K. The load drops indicate that stress relaxation occurred when the tests were interrupted for imaging. The displacement values included displacements in both gage section and the grip regions.

Table 4.4 Ti-3Al-2.5V tensile property comparison between the experiments in the current work and the Ti handbook by Boyer et al. [1994].

Test temperature	YS (MPa)	Max Stress (MPa)	YS (MPa) in Boyer et al.	UTS (MPa) in Boyer et al.	Comment
296K	~580	687	450-725	585-1035	
728K	~250	406	<300	<500	Only found for temp. below 598K

4.3.3.1 296K tension

4.3.3.1.1 Plate 1

Figure 4.60 shows the EBSD IPF map in the tensile direction and the corresponding {0001} and $\{10\bar{1}0\}$ pole figures from the gage section of the plate 1 tensile tested at 296K. There were approximately 720 α grains in Figure 4.60. This specimen exhibited a moderate texture (an approximately 6 times random), where most of the c-axis orientations were aligned within 30 ° of the transverse direction and the corresponded three $\{10\bar{1}0\}$ peak locations were along the tensile axis. The EBSD texture result was similar to the bulk XRD result in Figure 4.58. Most of the grains in Figure 4.60 (a) exhibited soft orientations (green color), where prismatic slip was favored for activation.

Sequential SE SEM images of the same area taken at different strains during the 296K tensile experiment of plate 1 are shown in Figure 4.61. No slip traces were observed within the elastic limit even for stresses as high as 510MPa. Slip traces were first observed in some α grains at 595MPa (~2% strain), which was just after global yielding (~560MPa). In Figure 4.61 (b), the slip traces were difficult to see and one grain was magnified to show an example of slip traces observed in this grain. At ~2% strain, most of the traces were identified with prismatic slip with Schmid factors greater than 0.4 (highlighted by red lines in Figure 4.61 (b)). Basal slip was not observed in this microstructural patch. Usually only a single slip system was identified in each grain. After ~6.5% strain, only ~15% of grains exhibited slip and significant surface was observed at the α/β phase boundaries.

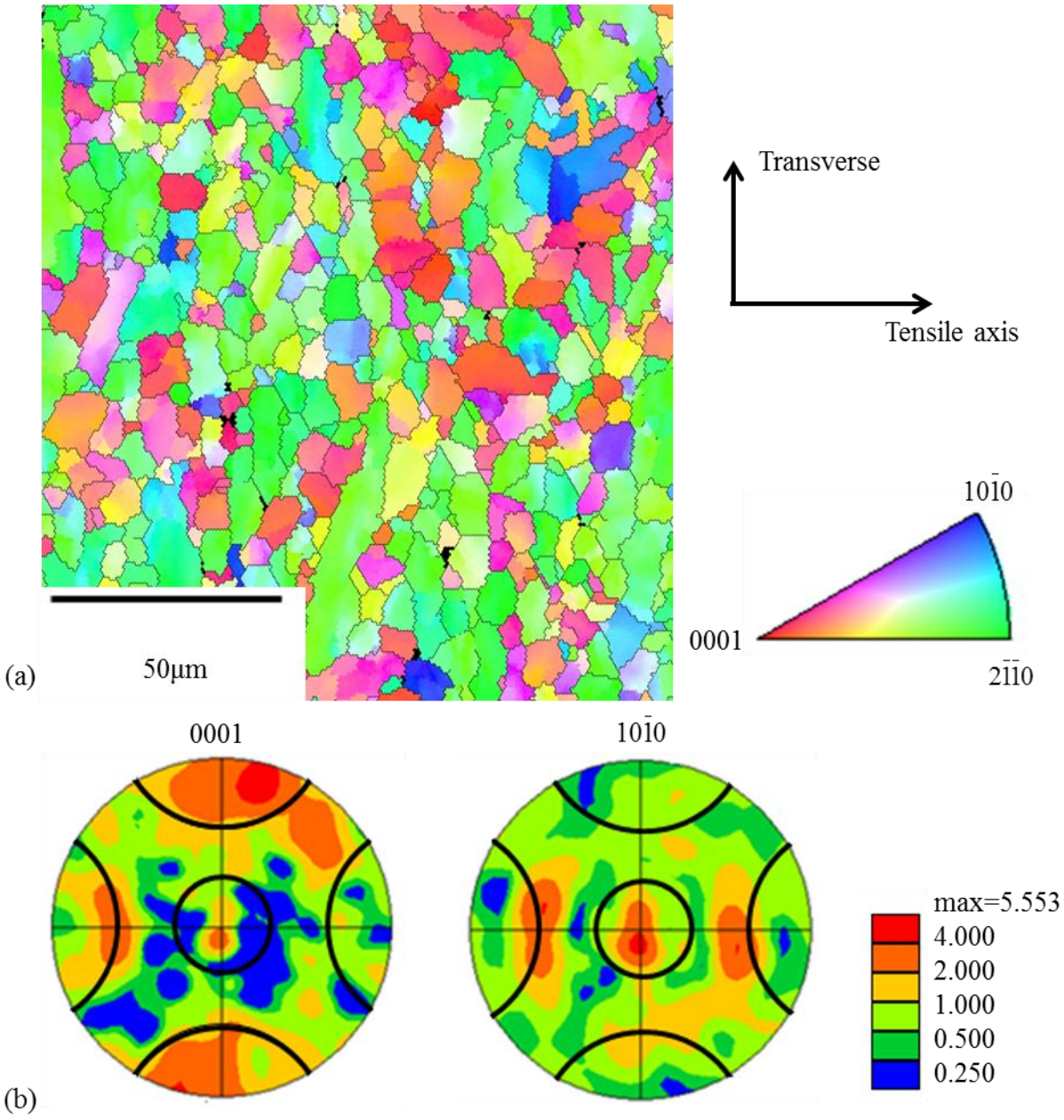

Figure 4.60 EBSD data of the specimen from the Ti-3Al-2.5V plate 1 tensile tested at 296K: (a) EBSD IPF map in the tensile direction of the α-phase Ti containing approximately 720 α grains, (b) the {0001} and the $\{10\bar{1}0\}$ pole figures with 30° cones along the major axes. The loading direction was horizontal.

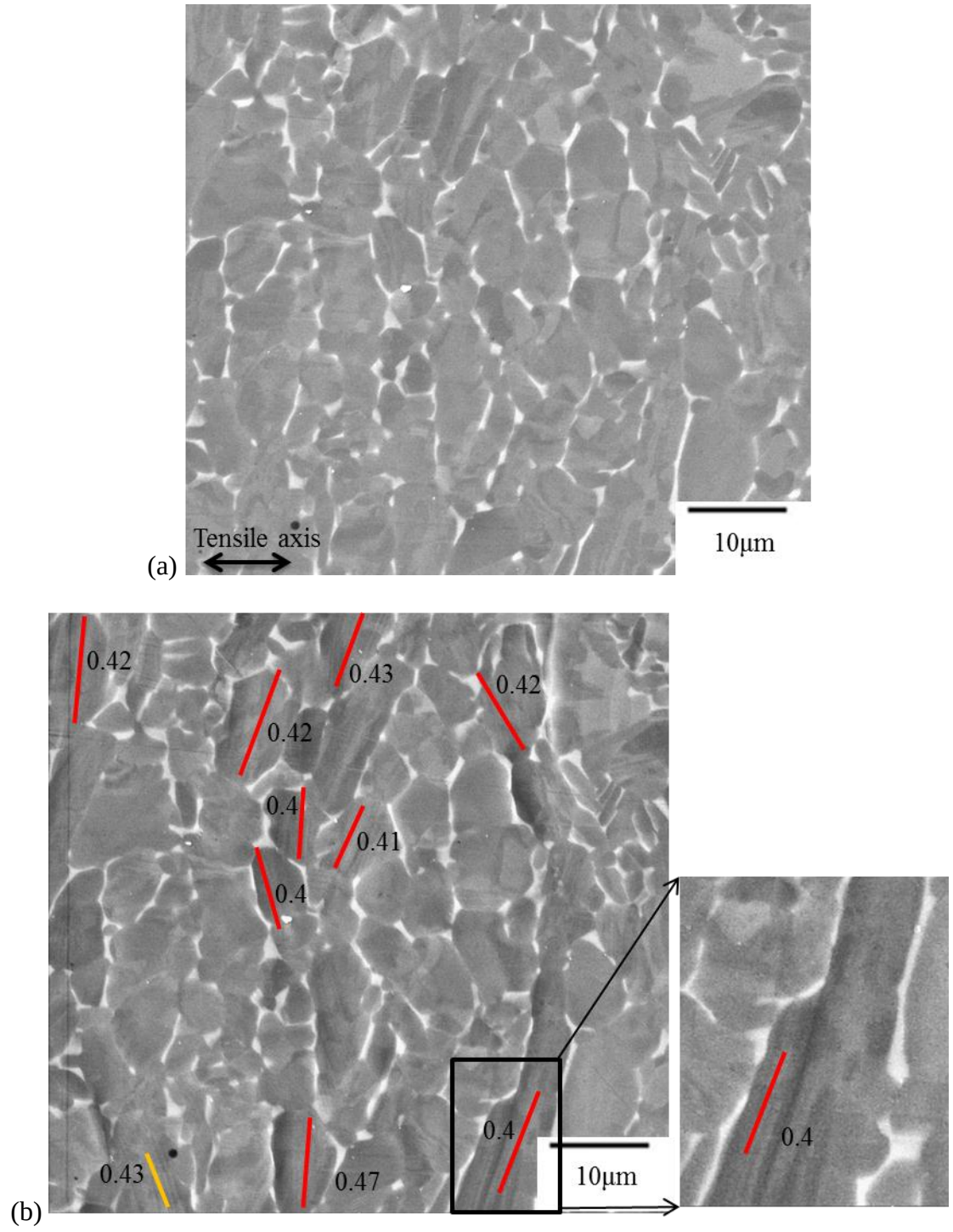

Figure 4.61 Sequential SE SEM images for the Ti-3Al-2.5V plate 1 tensile tested at 296K: (a) undeformed, (b) 595MPa (~2.0% strain, when slip bands were first observed), the color-coded planes traces for prismatic slip (red) and pyramidal <c+a> (orange) are labeled along with their Schmid factors and one grain outlined in black was magnified (see insert) to show an example of observations of slip traces, (c) 646MPa (~4.9% strain), and (d) 656MPa (~6.5% strain) were acquired. The loading direction was horizontal.

Figure 4.61 (cont'd)

(c)

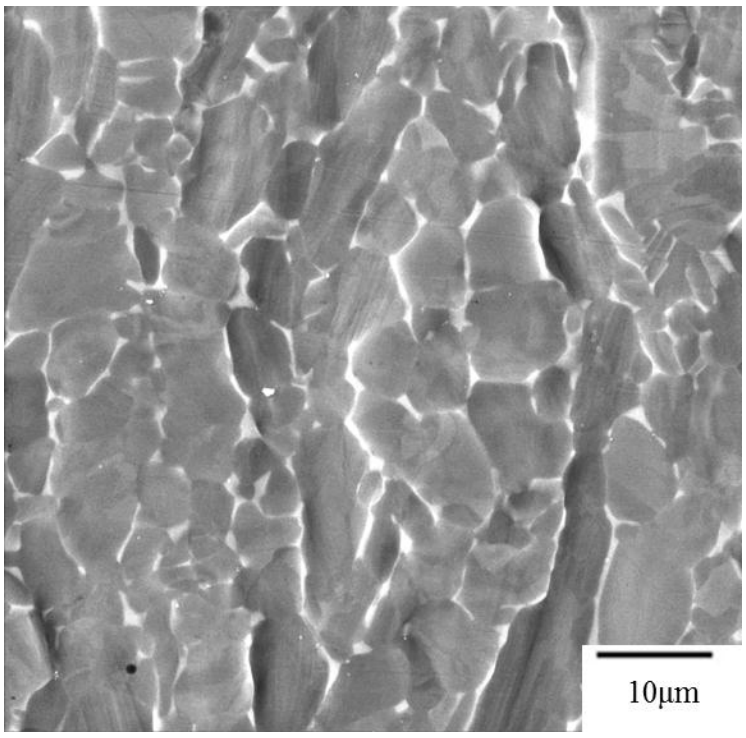

(d)

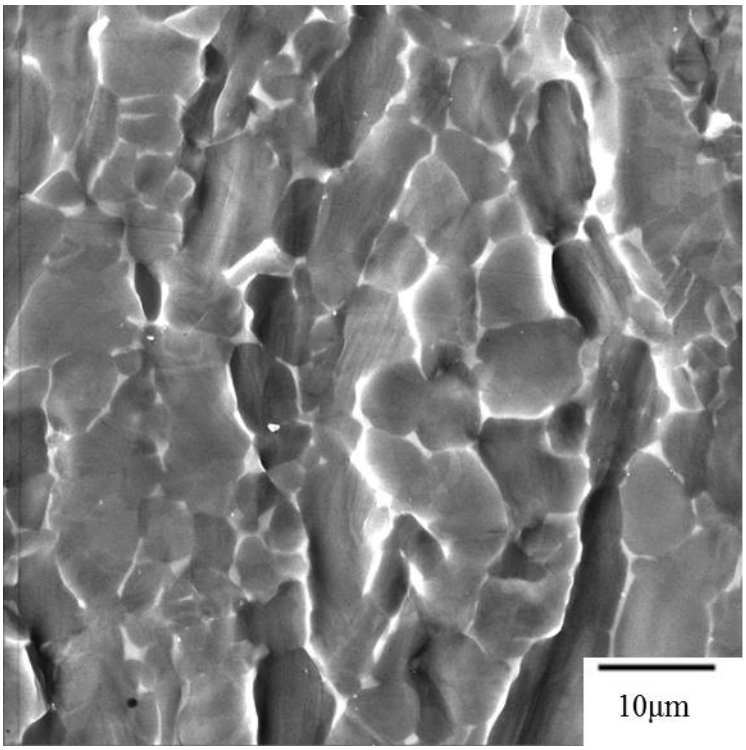

Twinning was an active deformation mode in the plate 1 tested at 296K. Due to the fine α-phase grain size and low contrast in these grains, it was often hard to distinguish between the twin and the parent grain [Leo Praksah et al. 2010], see Figure 4.61. Therefore, twins were found by comparing EBSD maps collected before and after deformation, as twinned regions show large orientation changes in grains, as illustrated in Figure 4.62. The particular twinning systems were characterized by determining the misorientation between the parent and the twin; an $\sim 85^\circ$ misorientation indicates a T1 twin and the rotation axis determines which of the six $< 2\bar{1}\bar{1}0 >$ T1 twinning system was active [Christian and Mahajian 1995]. In Figure 4.62, two parent grains are outlined in red in Figure 4.62 (a) and (b) and black in Figure 4.62 (c) and (d). The misorientation across the parent and twin grains in the misorientation profiles in Figure 4.62 (e) and (f) showed that there was $\sim 85^\circ$ misorientation between the twins and the corresponding parent grains. Note that only T1 twinning was observed for the Ti-3Al-2.5V alloy. Comparison of the EBSD maps before and after straining revealed that no grains had completely reoriented due to twinning.

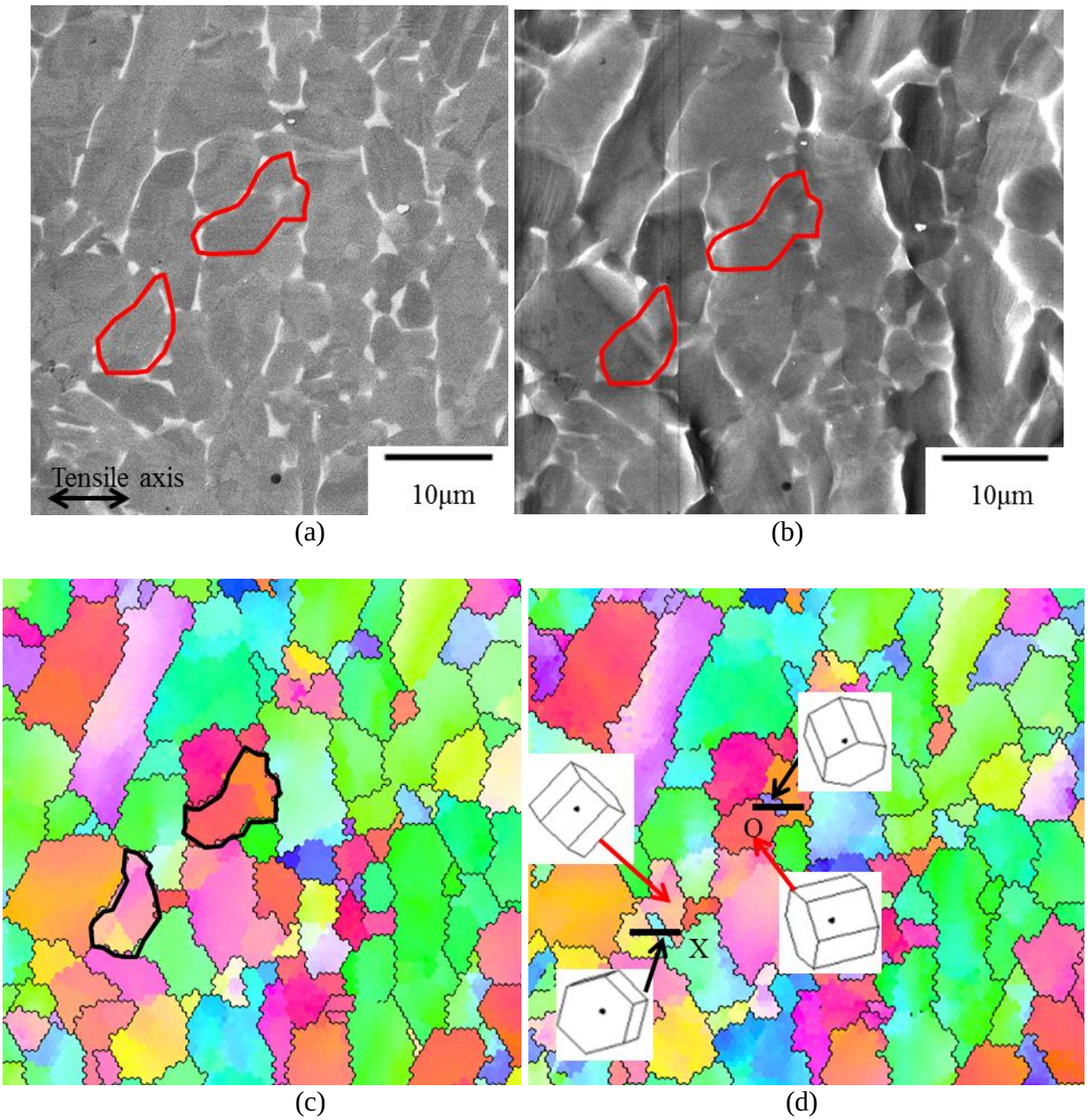

Figure 4.62 (a) Undeformed and (b) deformed microstructure patch which exhibited deformation twinning during the 296K tension test of plate 1 after ~6.5% strain with the corresponding EBSD orientation map (c) before and (d) after deformation. The grains highlighted in red in (a) and (b) indicated the parent grains where the twins formed. The red arrows in (d) point to the parent orientation and the black arrows indicate the newly-formed twin orientations. (e) The color code of EBSD maps. Two misorientation profiles across the parent and twin grains are plotted in (f) and (g), corresponding to lines X and O in (d).

Figure 4.62 (cont'd)

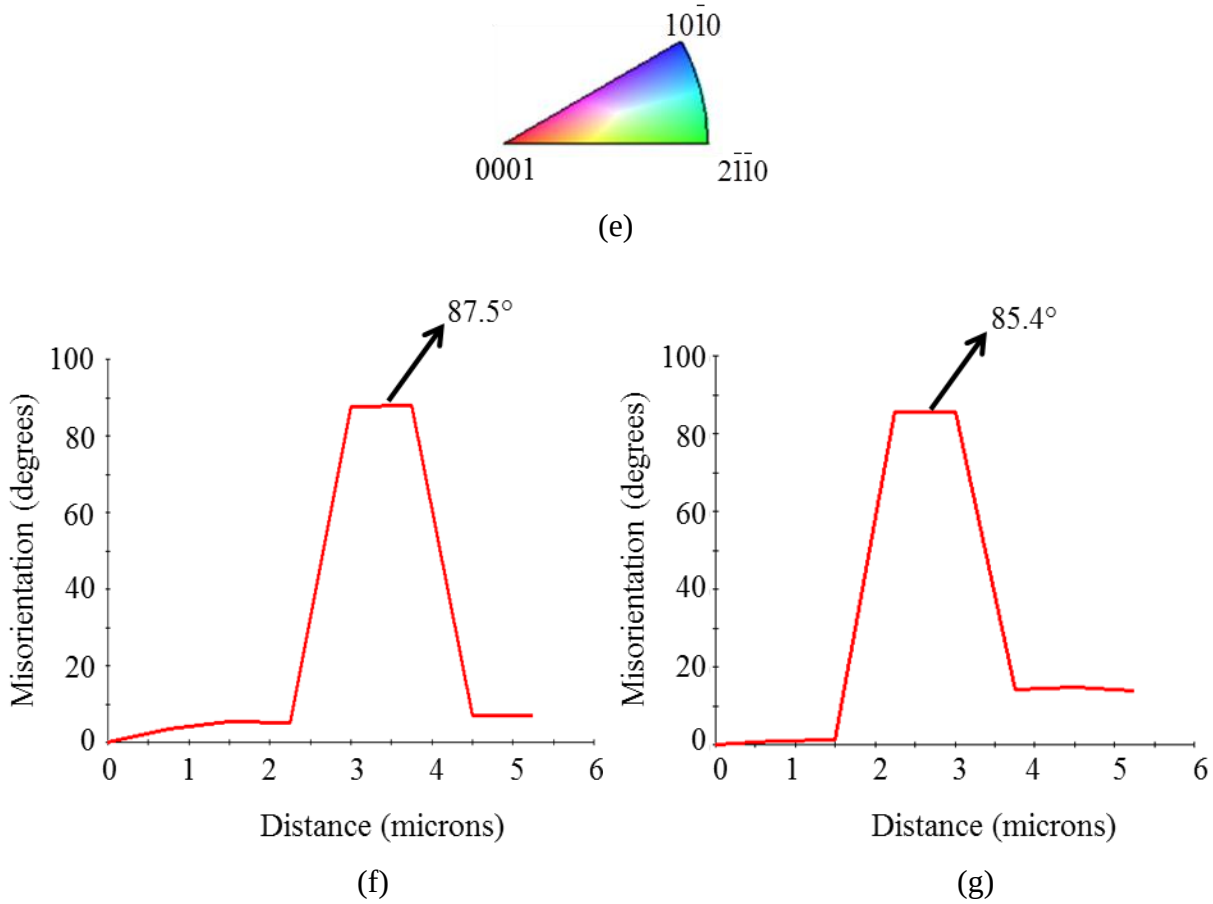

The slip-trace technique was used to identify 128 active deformation systems in 125 α grains. Of the 128 active slip systems, 102 of them (80%) were identified to be for prismatic slip. There were some instances of T1 twinning (12/128≈10%), basal slip (2/128≈2%), pyramidal <a> slip (9/128≈7%), and pyramidal <c+a> slip (2/128≈2%). A histogram shown in Figure 4.63 illustrates the basal, prismatic, pyramidal <a>, pyramidal <c+a> slip, and T1 twinning distribution with respect to the global Schmid factors after ~6.5% strain. The activation of the different deformation systems was correlated with high Schmid factors as 76% of the active deformation systems exhibited global Schmid factors greater than 0.4.

Figure 4.64 shows stereographic triangles with the grain orientations plotted for basal, prismatic, pyramidal <a>, pyramidal <c+a>, and twinning deformation modes with Schmid factor contours overlaid. In Figure 4.64 (b), grains in which prismatic slip was activated were concentrated in the lower right corner of the unit triangle, where prismatic slip systems had high Schmid factors. Grains in which basal, pyramidal <a>, and pyramidal <c+a> slip systems were activated were also confined to the corresponding high Schmid factor regions (>0.4).

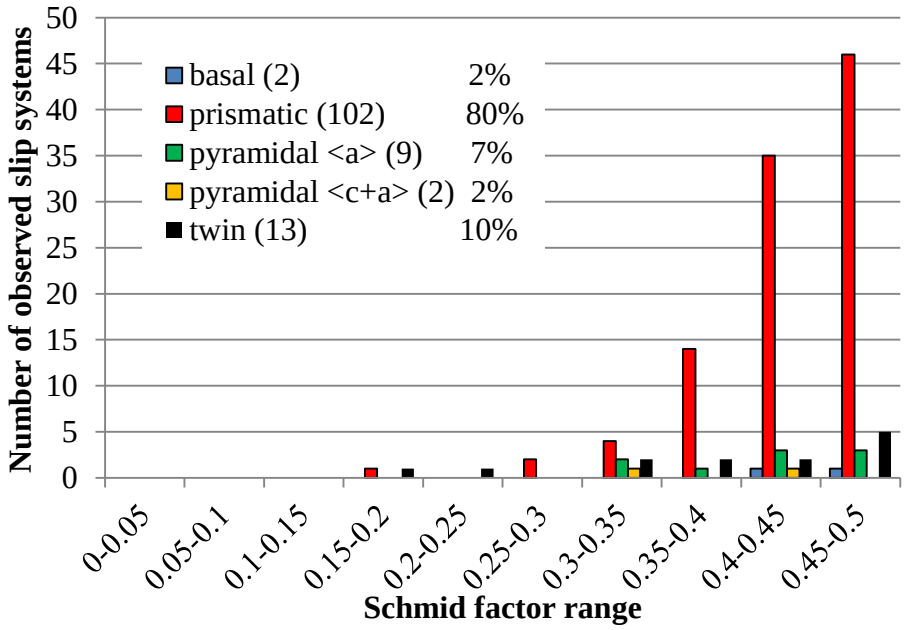

Figure 4.63 A histogram of the Schmid factor distribution of basal, prismatic, pyramidal <a>, and pyramidal <c+a> slip systems and T1 twinning systems for the Ti-3Al-2.5V plate 1 tensile tested at 296K after ~6.5% strain.

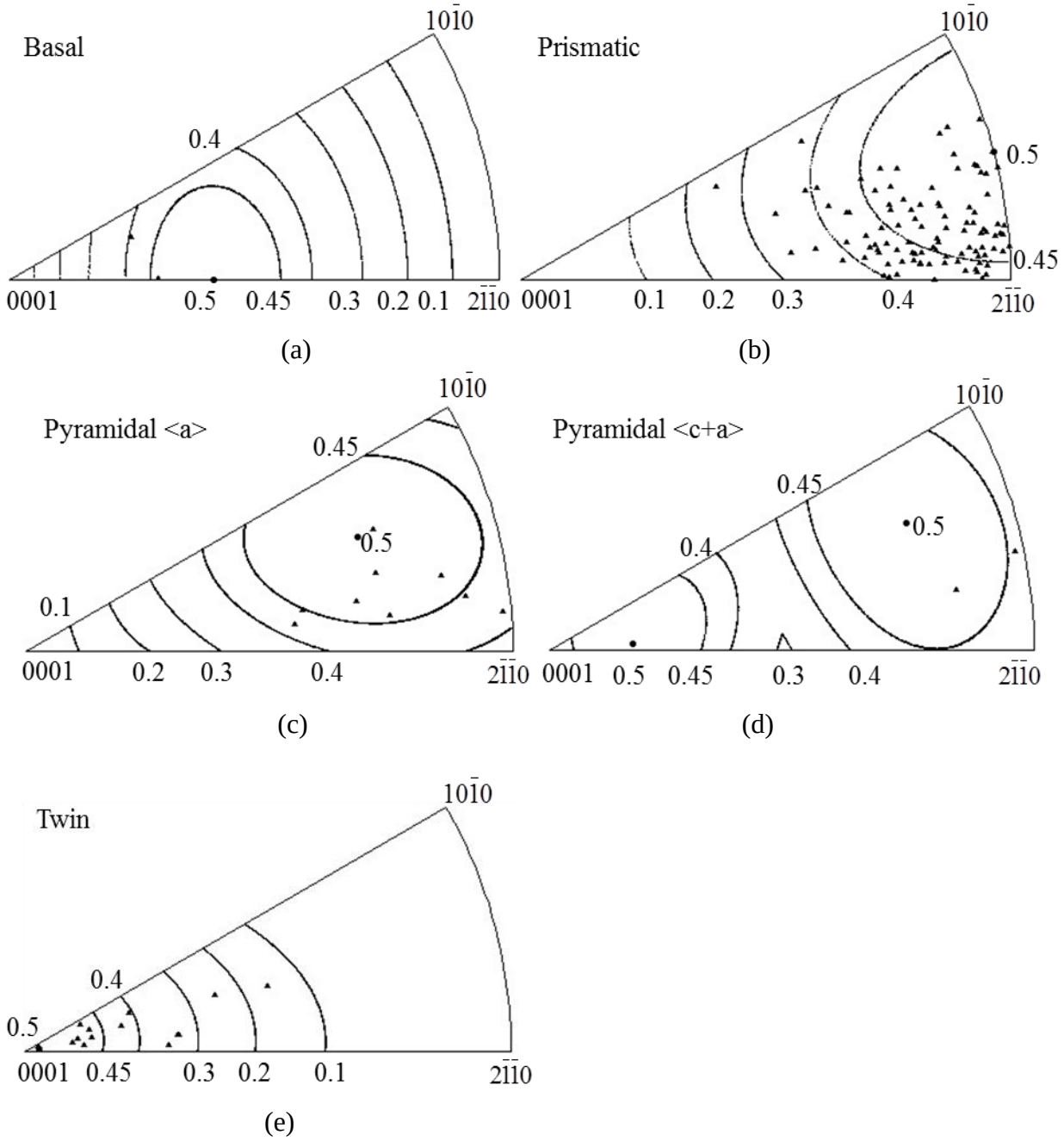

Figure 4.64 Unit triangle plots of grains which exhibited (a) basal, (b) prismatic, (c) pyramidal <a>, (d) pyramidal <c+a>, and (e) T1 twin deformation systems for the Ti-3Al-2.5V plate 1 tensile tested at 296K after ~6.5% strain with Schmid factor contours overlaid.

4.3.3.1.2 Plate 2

A 296K tensile test was performed for Ti-3Al-2.5V plate 2, which exhibited a different texture, shown in Figure 4.65. Unlike the texture of plate 1 tested at 296K, which was dominated by the soft orientations (i.e. green orientations), a variety of grain orientations were observed in Figure 4.65 (a) and the peak locations of the {0001} pole figure in Figure 4.65 (b) were distributed in multiple locations. Such a texture did not strongly favor any particular deformation system.

Sequential SE SEM images of the same area taken at different strains during the 296K tensile experiment of plate 2 are shown in Figure 4.66. After ~10.5% deformation, about 25% of grains exhibited slip traces and 124 active deformation systems were identified in the 117 α grains, shown in Figure 4.67. More than 69% of the observed deformation systems activated had Schmid factors greater than 0.4. Similar to plate 1 tested at 296K, prismatic slip was the most active deformation system, and it comprised 48% of the total slip systems observed. However, this percentage is much smaller than that for plate 1 tested at 296K, where prismatic slip comprised 80% of the total observed deformation systems. Correspondingly, the percentages of basal, pyramidal <a>, pyramidal <c+a>, and T1 twins increased from 2%, 7%, 2%, and 9% respectively for specimen from plate 1 tested at 296K to 8%, 15%, 6%, and 23% for specimen from plate 2 tested at 296K. The observation of extensive twinning suggests that this is a significant deformation system in Ti-3Al-2.5V at 296K.

Figure 4.68 shows the stereographic unit triangles with the grain orientations plotted for basal, prismatic, pyramidal <a>, and pyramidal <c+a> slip with Schmid factor contours overlaid. Similar to plate 1 tested at 296K, the majority of grains exhibiting active deformation systems were confined to high Schmid factor regions. Unlike plate 1 tested at 296K that grains in which

prismatic slip was activated were more concentrated near the $<2\bar{1}\bar{1}0>$ corner in the unit triangle, these grains in plate 2 tested at 296K were more evenly distributed in regions with Schmid factors greater than 0.3. Two grains with basal slip exhibited Schmid factors smaller than 0.3, see Figure 4.68 (a).

Overall, it appears that the texture has strong effect on the deformation system distributions in plate 1 and plate 2. The effect of texture on the deformation system activation will be discussed in Chapter 5. The relative CRSS values of the different deformation systems in Ti-3Al-2.5V plate 1 and plate 2 will be discussed in Chapter 6.

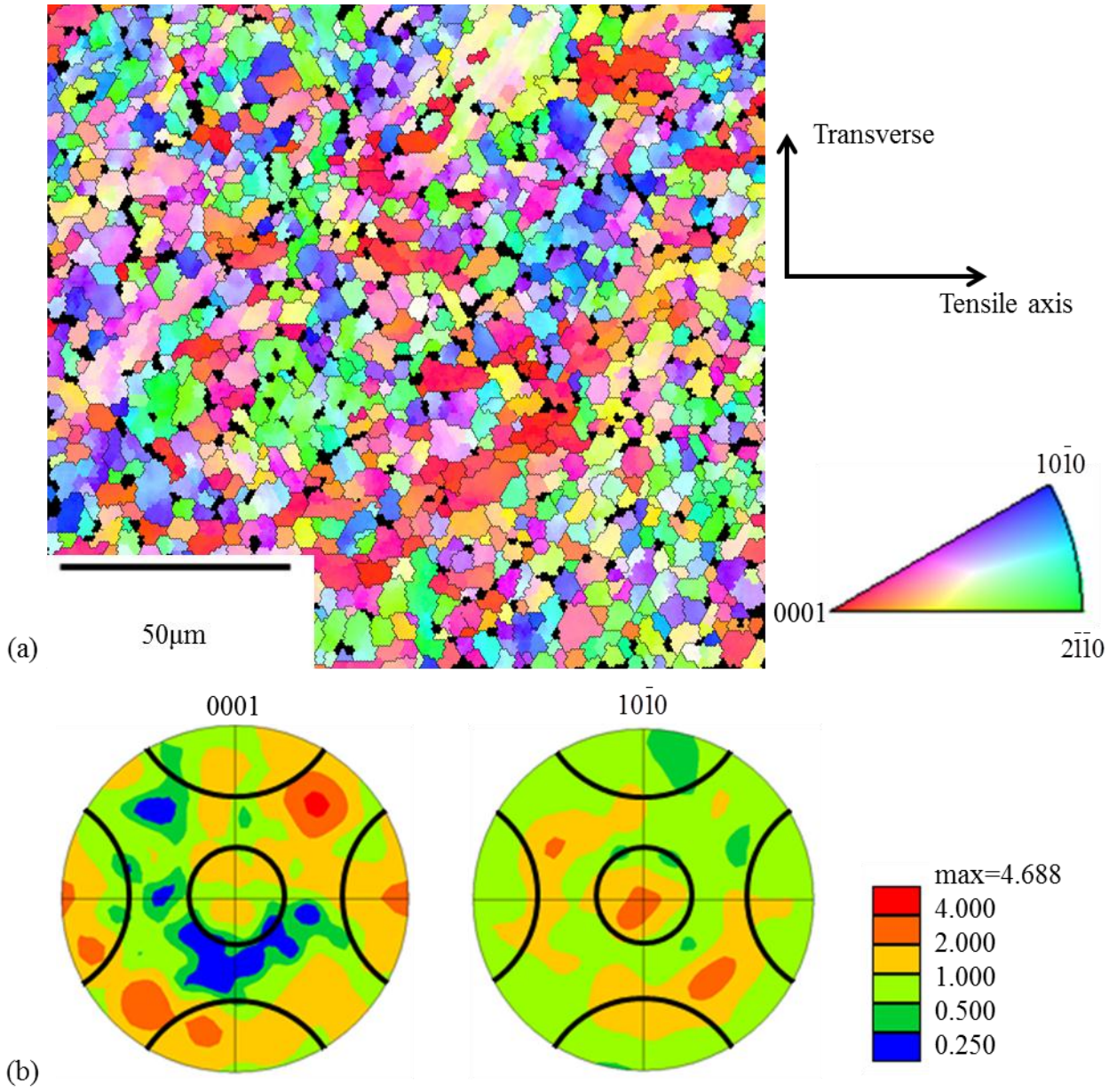

Figure 4.65 EBSD data of the specimen from the Ti-3Al-2.5V plate 2 tensile tested at 296K: (a) EBSD IPF map in the tensile direction of the α-phase Ti containing approximately 1200 α grains, (b) the {0001} and the $\{10\bar{1}0\}$ pole figures with 30° cones along the major axes. The loading direction was horizontal.

(a)

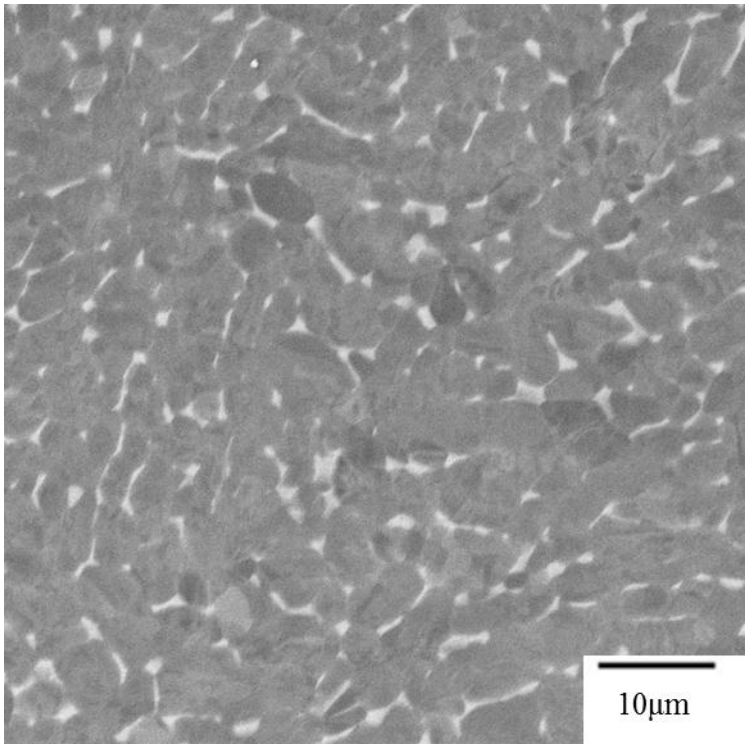

(b)

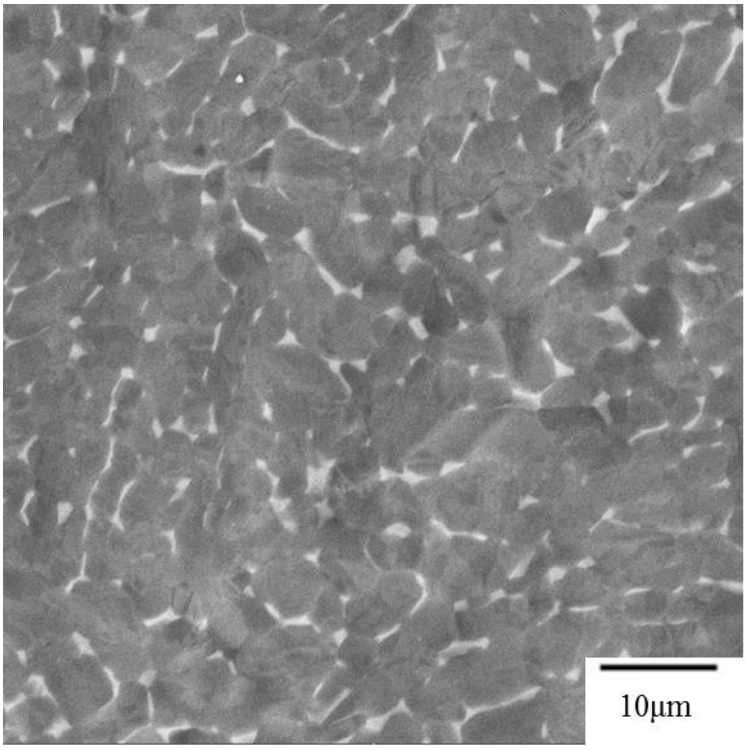

Figure 4.66 Sequential SE SEM images for the Ti-3Al-2.5V plate 2 tensile tested at 296K: (a) undeformed, (b) 619MPa (~1.6% strain), (c) 648MPa (~3.8% strain), and (d) 685MPa (~10.5% strain) were acquired. The loading direction was horizontal.

Figure 4.66 (cont'd)

(c)

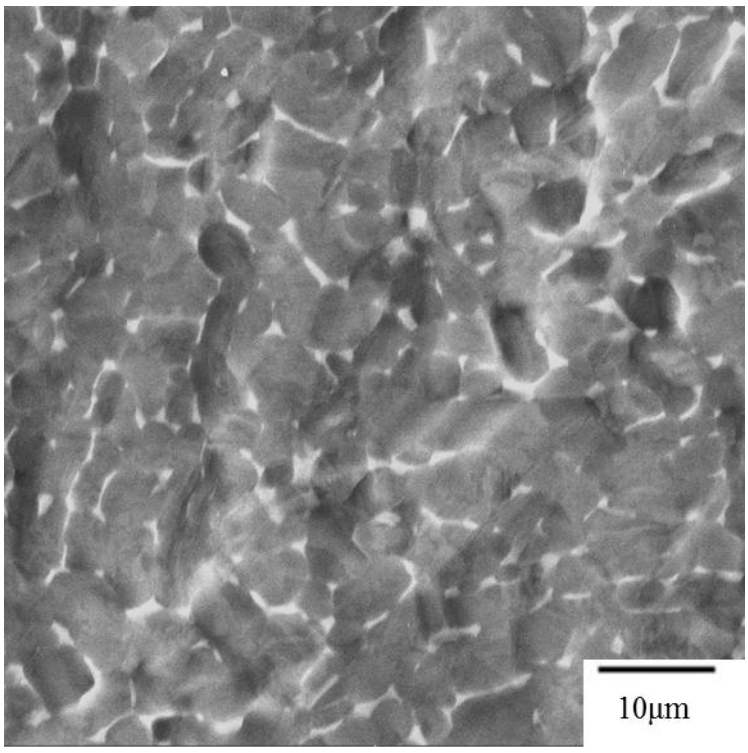

(d)

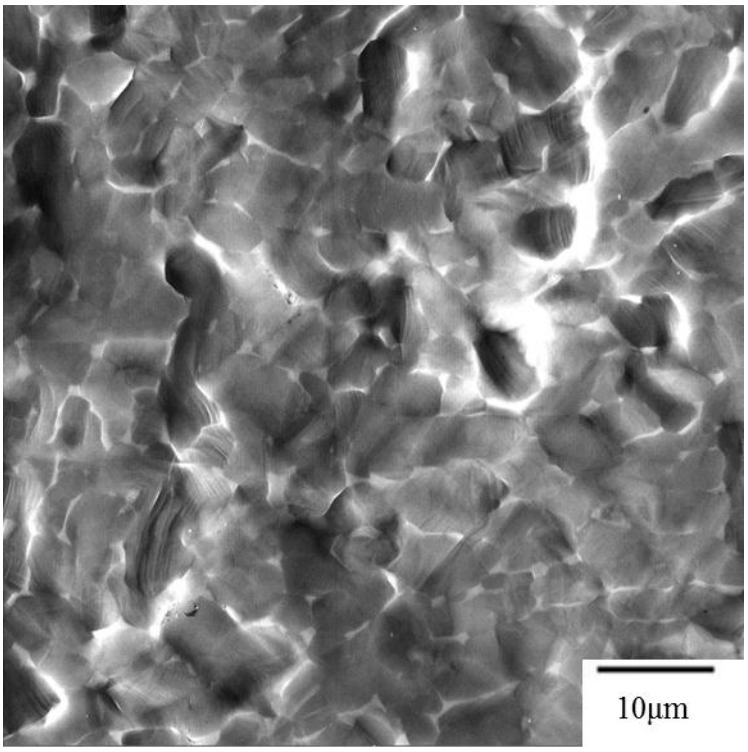

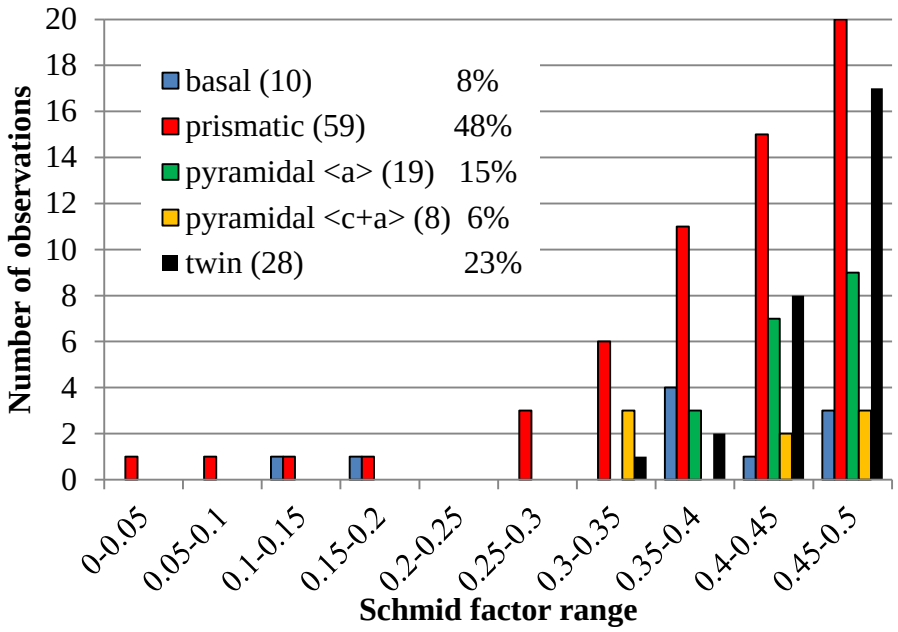

Figure 4.67 A histogram of the Schmid factor distribution of basal, prismatic, pyramidal <a>, and pyramidal <c+a> slip systems and T1 twinning systems for the Ti-3Al-2.5V plate 2 tensile tested at 296K after ~10.5% strain.

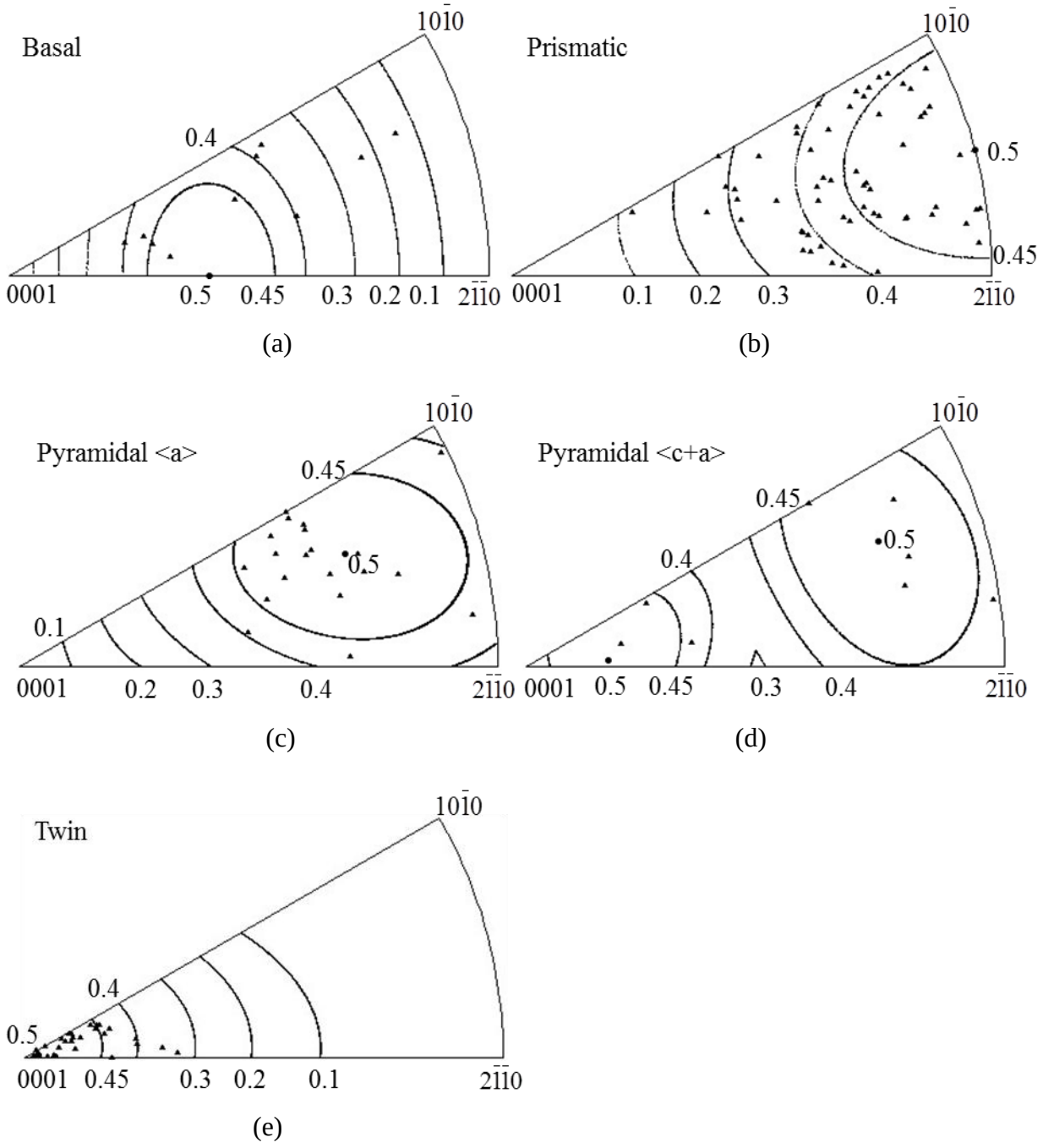

Figure 4.68 Unit triangle plots of grains which exhibited (a) basal, (b) prismatic, (c) pyramidal <a>, (d) pyramidal <c+a>, and (e) T1 twinning deformation systems for the Ti-3Al-2.5V plate 2 tensile tested at 296K after ~10.5% strain with Schmid factor contours overlaid.

4.3.3.2 728K tension

4.3.3.2.1 Plate 1

Figure 4.69 shows the EBSD IPF map in the tensile direction and the corresponding $\{0001\}$ and $\{10\bar{1}0\}$ pole figures from the gage section of the 728K tested specimen for Ti-3Al-2.5V plate 1. There were approximately 1150 α grains in Figure 4.69 with an approximately 5 times random moderate texture. The texture of the specimen from plate 1 tested at 728K was similar to the texture of the specimen from the same plate tested at 296K, where most of the c-axis orientations were aligned within $30°$ of the transverse direction and the corresponding three $\{10\bar{1}0\}$ peak locations were along the tensile axis.

Sequential SE SEM images taken of plate 1 tensile deformed at 728K at 0%, ~5.6%, and ~9.7% strain are shown in Figure 4.70. After ~9.7% strain, about 45% of grains exhibited slip traces. Grain boundary relief, suggesting sliding, was observed during the deformation. Compared to the plate 1 deformed at 296K, (compare Figure 4.61 (d) and 4.70 (b) both at ~6% strain), the extent of the surface relief was much more dramatic at 728K, which is likely to result from an increase in the grain boundary mobility assisted by the elevated temperature.

The active slip systems, which were determined for 112 slip traces in 105 α grains, are shown in Figure 4.71. Among the 112 active deformation systems analyzed, 7 were basal (6%), 75 were prismatic (67%), 19 were pyramidal <a> (17%), 7 were pyramidal <c+a> slip systems (6%), and 4 were T1 twins (4%). Prismatic slip was the primary slip system and it occurred over a wide Schmid factor range (0.25-0.5), while the rest of the deformation systems accounted for a much smaller portion of the total active deformation systems. T1 twins were only observed with Schmid factors greater than 0.4. The stereographic unit triangle plots in Figure 4.72 show that the majority of grains were confined to the high Schmid factor regions.

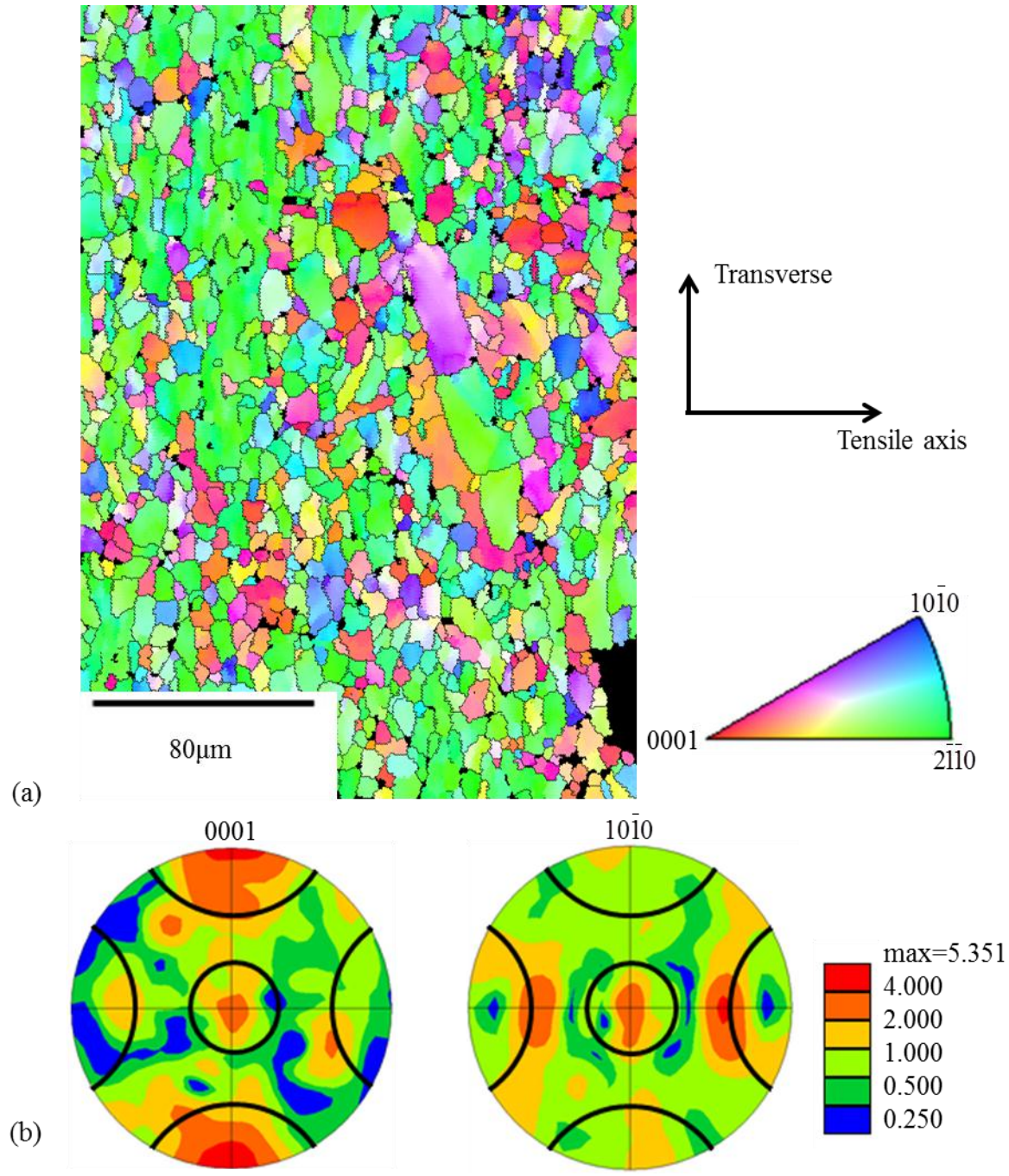

Figure 4.69 EBSD data of the specimen from the Ti-3Al-2.5V plate 1 tensile tested at 728K: (a) EBSD IPF map in the tensile direction of the α-phase Ti containing approximately 1250 α grains, (b) the {0001} and the $\{10\bar{1}0\}$ pole figures with 30° cones along the major axes. The loading direction was horizontal.

(a)

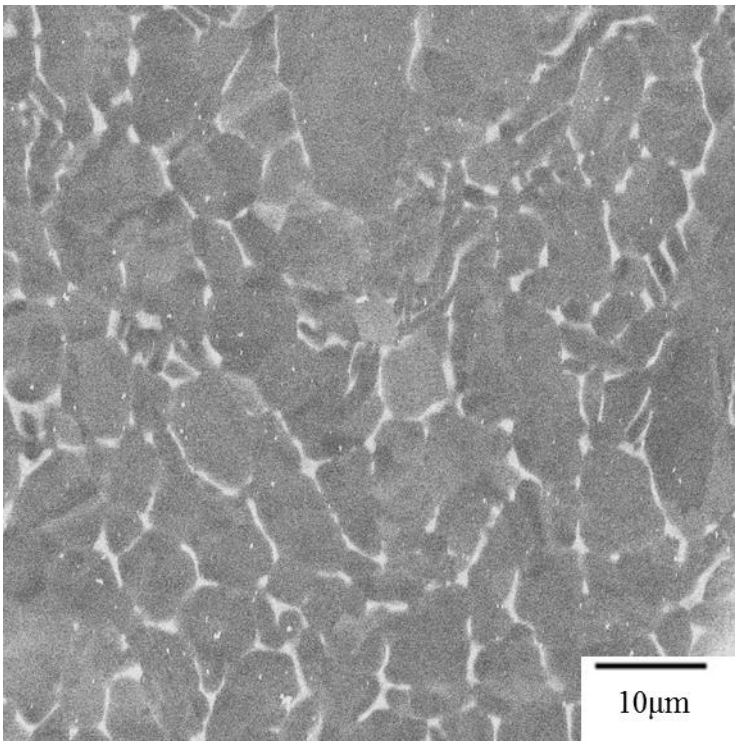

(b)

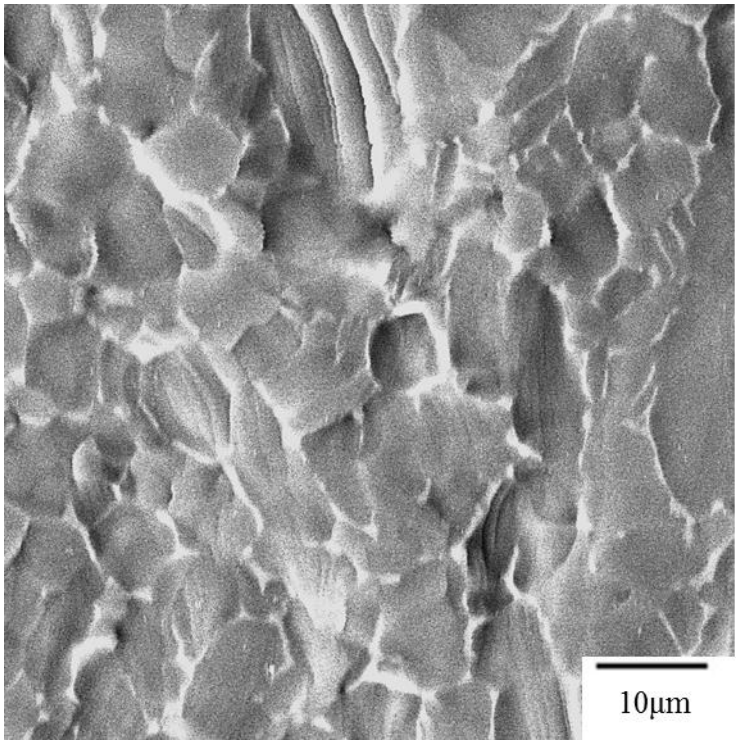

Figure 4.70 Sequential SE SEM images for the Ti-3Al-2.5V plate 1 tensile tested at 728K: (a) undeformed, (b) 379MPa (~5.6% strain), and (c) 403MPa (~9.7% strain) were acquired. The loading direction was horizontal.

Figure 4.70 (cont'd)

(c)

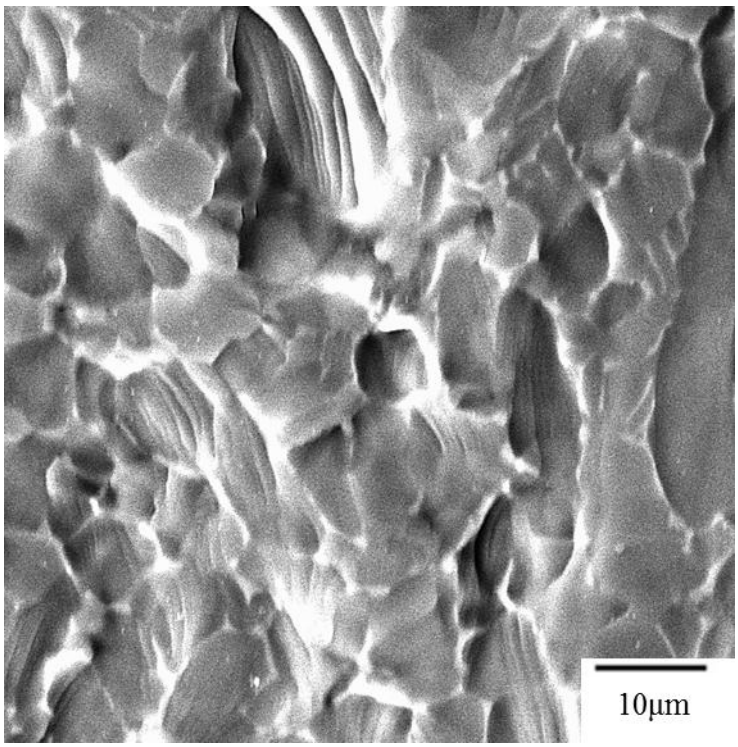

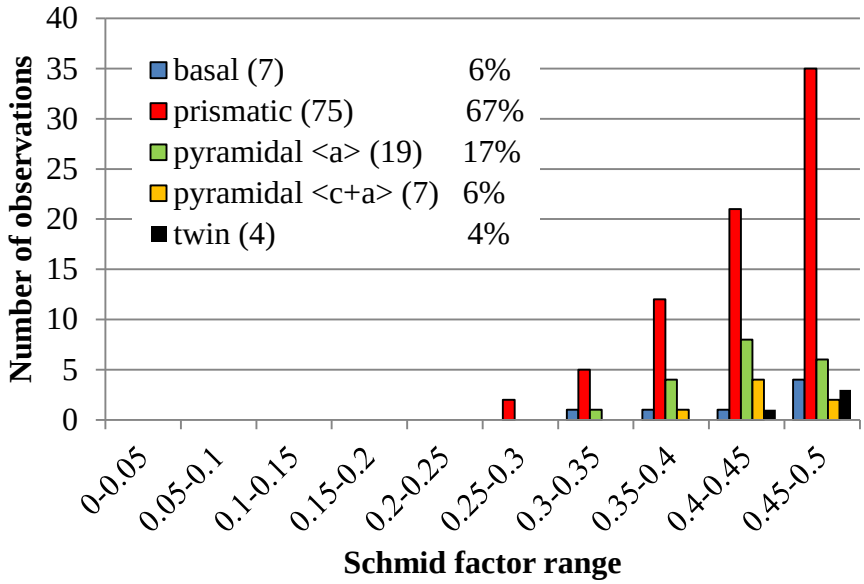

Figure 4.71 A histogram of the Schmid factor distribution of basal, prismatic, pyramidal <a>, and pyramidal <c+a> slip systems and T1 twinning systems for the Ti-3Al-2.5V plate 1 tensile tested at 728K after ~9.7% strain.

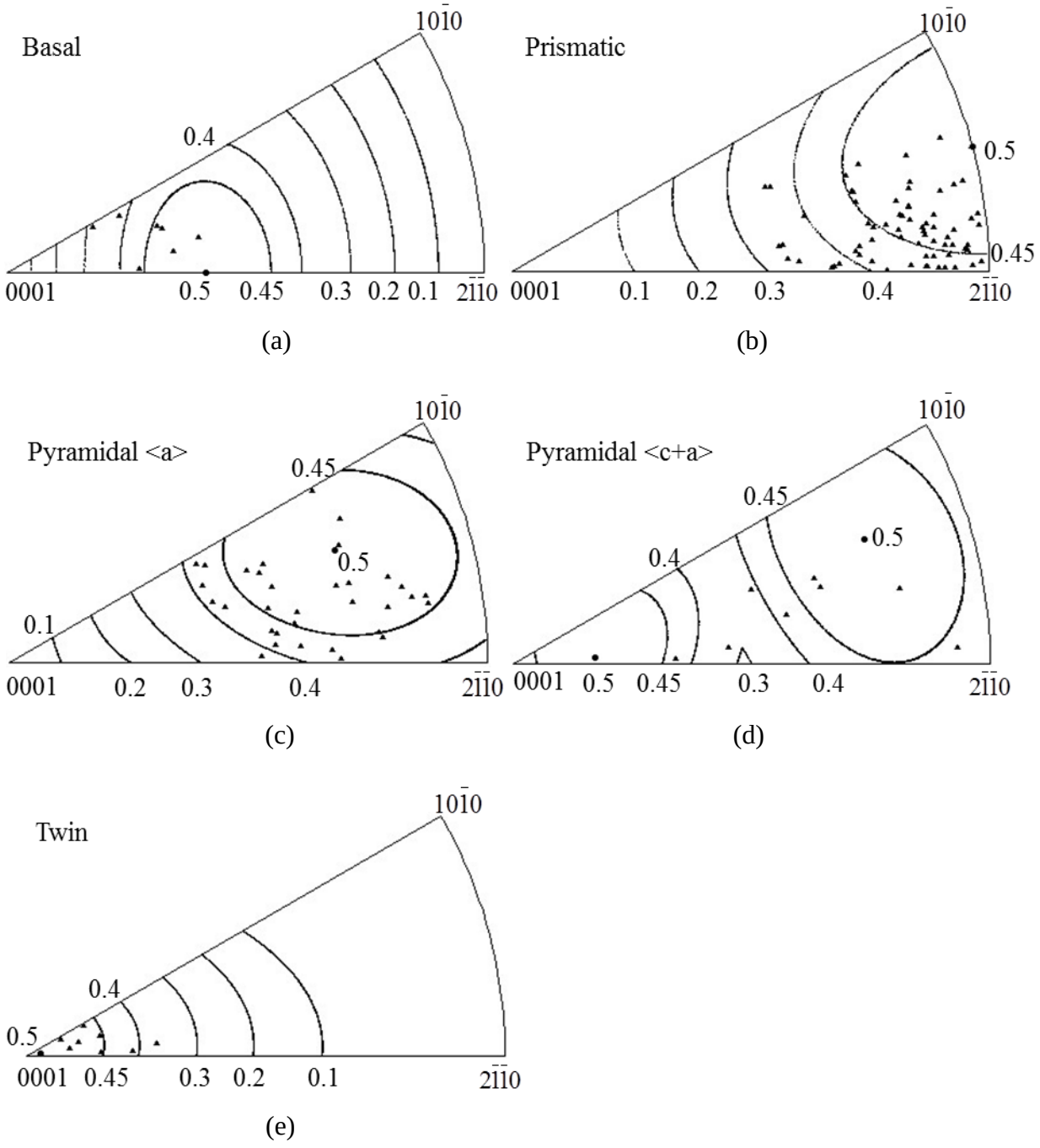

Figure 4.72 Unit triangle plots of grains which exhibited (a) basal, (b) prismatic, (c) pyramidal <a>, (d) pyramidal <c+a>, and (e) T1 twin deformation systems for the Ti-3Al-2.5V plate 1 tensile tested at 728K after ~9.7% strain with Schmid factor contours overlaid.

4.3.3.2.2 Plate 2

Similar to 296K tensile tests, a duplicate 728K tensile test was performed on a specimen from the Ti-3Al-2.5V plate 2. Figure 4.73 shows the EBSD IPF map in the tensile direction and the corresponding {0001} and $\{10\bar{1}0\}$ pole figures from the gage section of this specimen. Similar to plate 2 tested at 296K, Figure 4.73 shows a more random distribution of the texture and Schmid factors were not heavily biased for any particular deformation systems.

Figure 4.74 shows sequential SE SEM images of the same area taken from the Ti-3Al-2.5V plate 2 during 728K tension test. Similar to plate 1 tested at 728K, both dislocation slip and surface relief were observed. About ~54% of grains exhibited slip traces. The active deformation modes were determined for 133 deformation systems in 130 α grains; 19 were basal (14%), 65 were prismatic (49%), 33 were pyramidal <a> (25%), 8 were pyramidal <c+a> (6%), and 8 were T1 twins (8%), shown in Figure 4.75. This indicates that prismatic slip was the dominant deformation system for plate 2 tested at 728K, which was also the case for plate 1 at 728K. However, prismatic slip accounted for a lower percentage of the total observed deformation systems in plate 2 (49%) compared with plate 1 (67%). Most slip occurred with Schmid factors greater than 0.3 and no slip system with a global Schmid factor below 0.1 was observed. T1 twinning was the only twinning mode observed and the Schmid factors associated with these twins were greater than 0.35.

Figure 4.76 shows the stereographic unit triangles with the grain orientations plotted for basal, prismatic, pyramidal <a>, and pyramidal <c+a> slip with Schmid factor contours overlaid. Most of grains exhibited prismatic slip and a number of grains exhibited pyramidal <a> slip. Similar to other tensile-tested Ti-3Al-2.5V specimens, the majority of grains were distributed in the high Schmid factor regions.

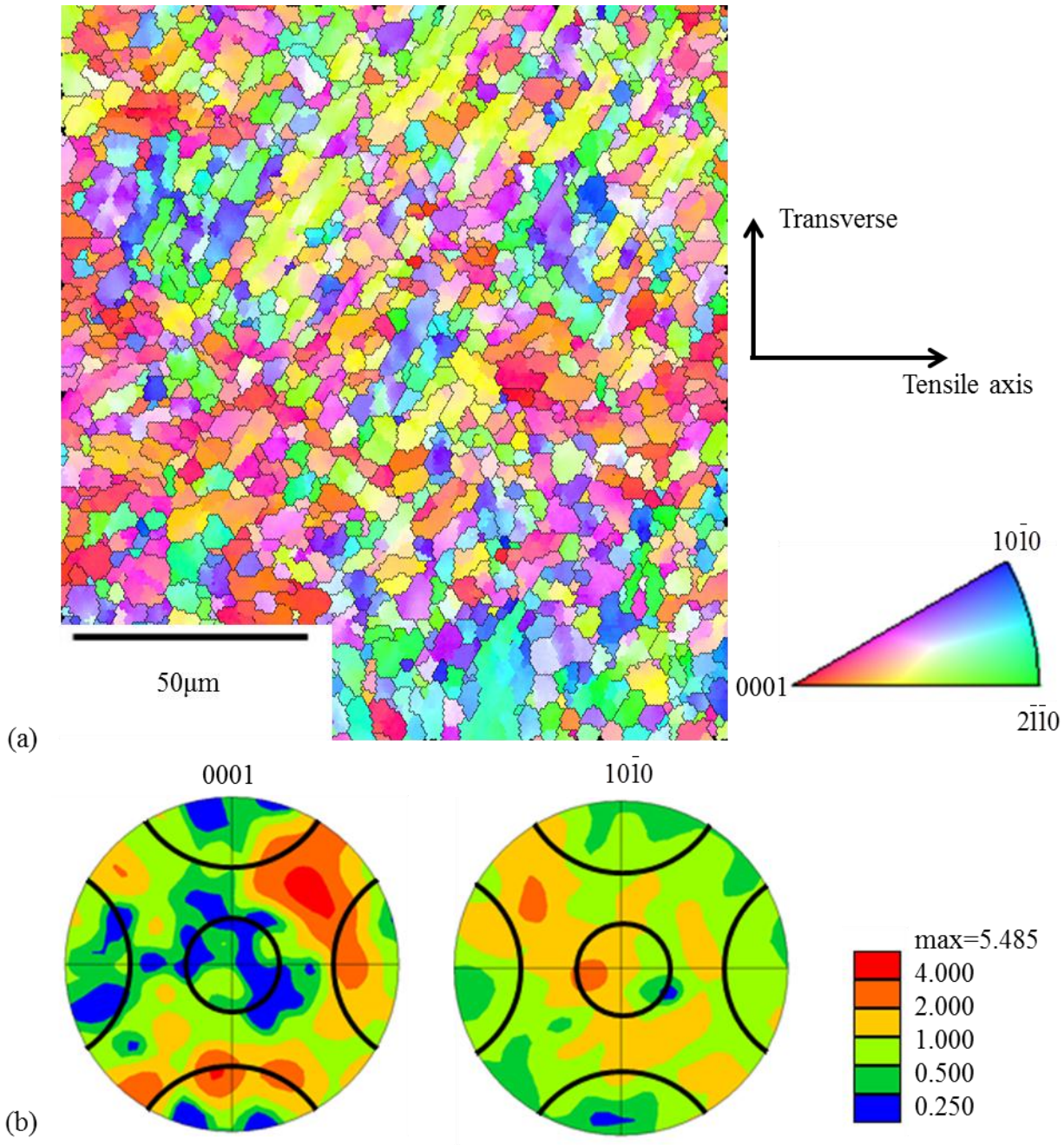

Figure 4.73 EBSD data of the specimen from the Ti-3Al-2.5V plate 2 tensile tested at 728K: (a) EBSD IPF map in the tensile direction of the α-phase Ti containing approximately 960 α grains, (b) the {0001} and the $\{10\bar{1}0\}$ pole figures with 30 ° cones along the major axes. The loading direction was horizontal.

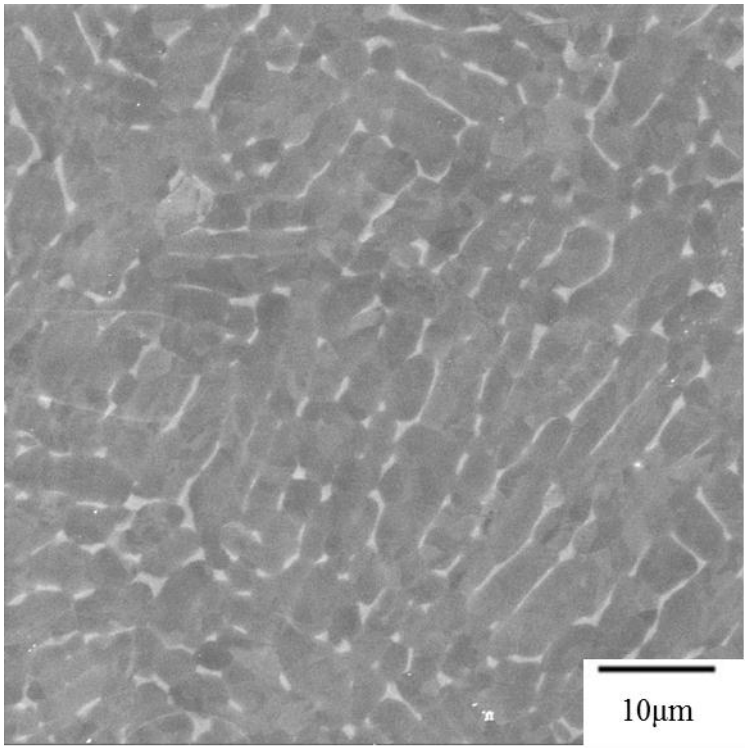

Figure 4.74 Sequential SE SEM images for the Ti-3Al-2.5V plate 2 tensile tested at 728K: (a) undeformed, (b) 309MPa (~3.7% strain), (c) 357MPa (~7.1% strain), and (d) 394MPa (~16.2% strain) were acquired. The loading direction was horizontal.

Figure 4.74 (cont'd)

(c)

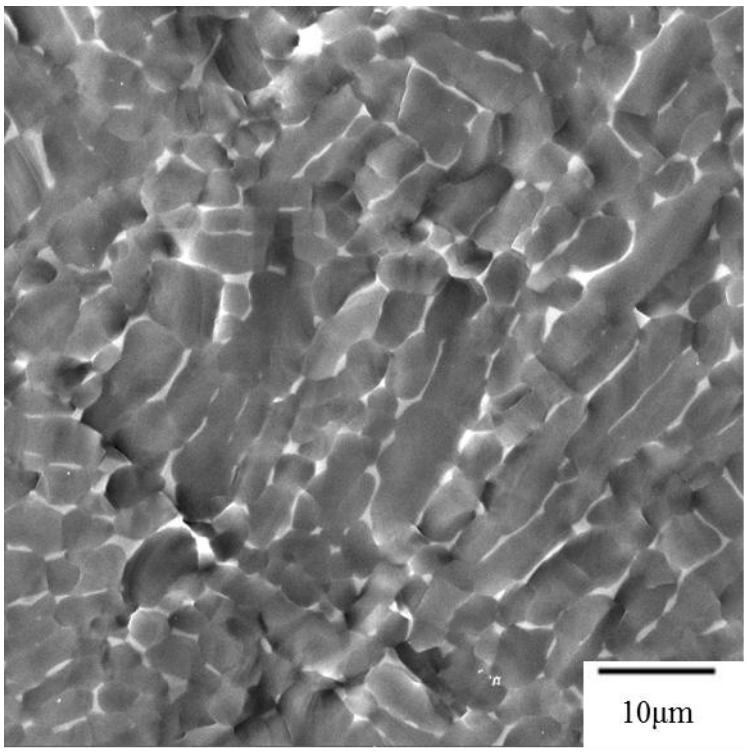

(d)

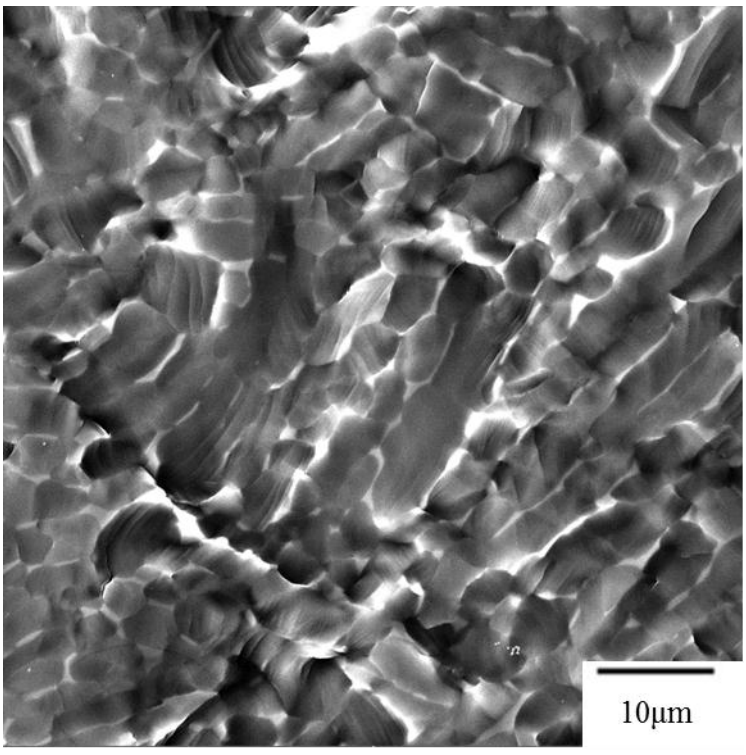

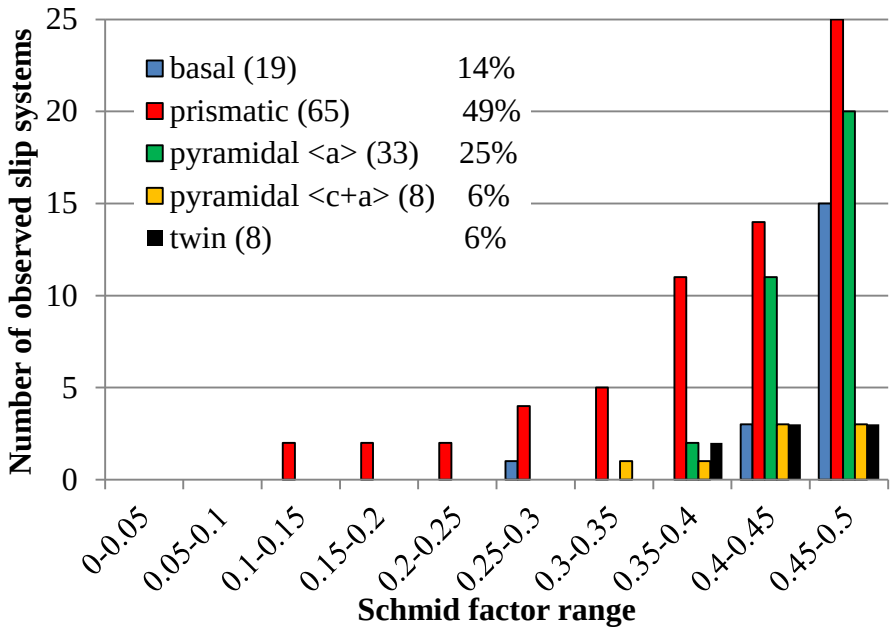

Figure 4.75 A histogram of the Schmid factor distribution of basal, prismatic, pyramidal <a>, and pyramidal <c+a> slip systems and T1 twinning systems for the Ti-3Al-2.5V plate 2 tensile tested at 728K after ~16.2% strain.

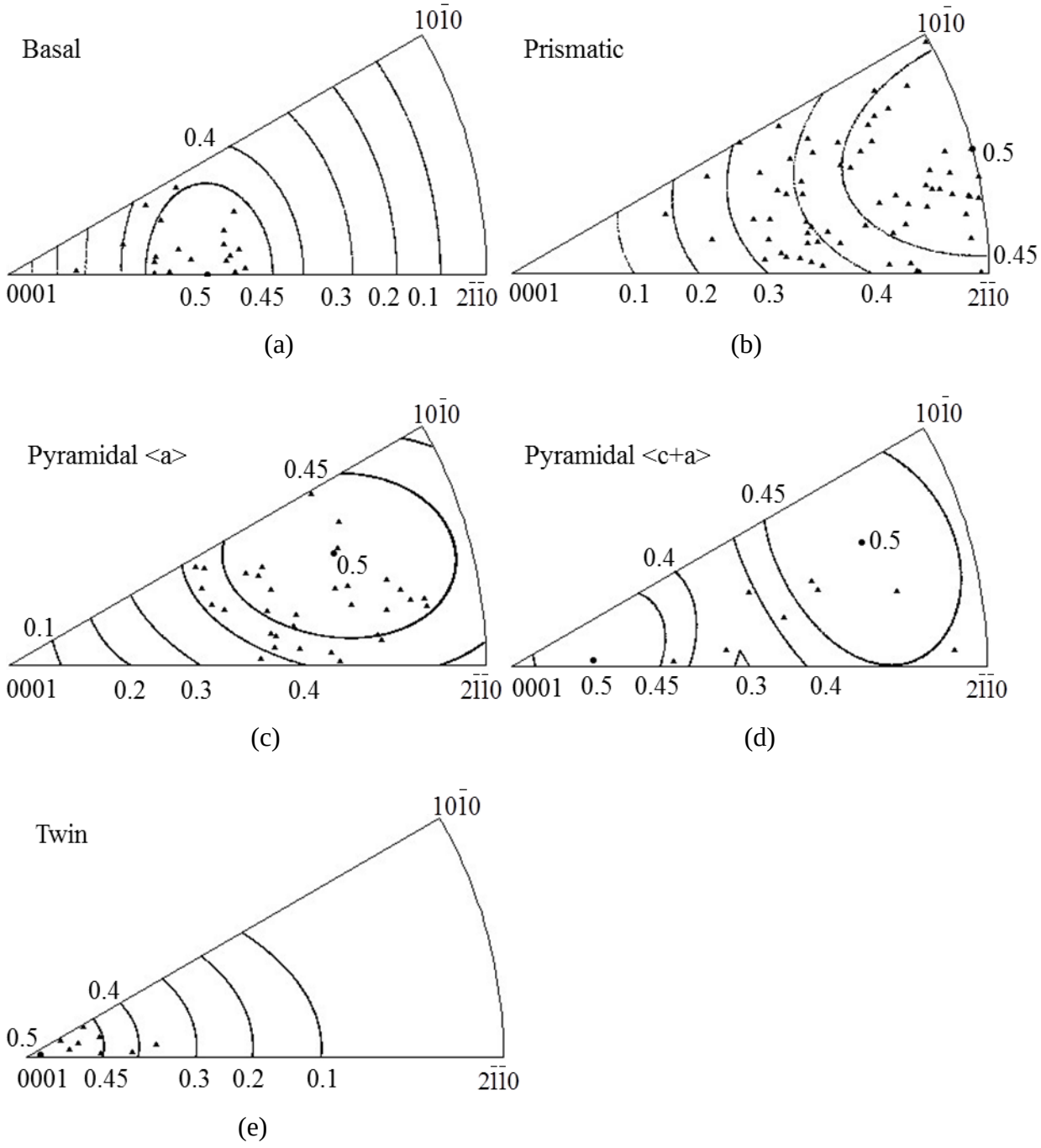

Figure 4.76 Unit triangle plots of grains which exhibited (a) basal, (b) prismatic, (c) pyramidal <a>, (d) pyramidal <c+a>, and (e) T1 twin deformation systems for the Ti-3Al-2.5V plate 2 tensile tested at 728K after ~16.2% strain with Schmid factor contours overlaid.

4.3.4 *In-situ* 728K-180MPa creep

One *in-situ* creep test was performed on a specimen from the Ti-3Al-2.5V plate 1 at 728K with a constant stress of 180MPa, which was equivalent to 72% of the YS at 728K. Figure 4.77 shows an EBSD IPF map in the tensile direction and the corresponding {0001} and $\{10\bar{1}0\}$ pole figures from the gage section of the 728K-180MPa creep tested specimen for Ti-3Al-2.5V plate 1. The texture of the creep tested specimen is similar to the specimens from the same plate 1 tested at 296K and 728K, where a moderate texture was observed and the majority of the c-axis were aligned within 30 ° of the transverse direction.

Sequential SE SEM images taken during the 728K-180MPa (~0.72 YS) tensile-creep experiment are shown in Figure 4.78. Grain boundary ledges were distinguishable after ~1.4% strain. Almost all the grain boundaries developed some degree of ledges after ~11.7% strain. Approximately 5% of the total number of grains exhibited slip traces, indicating that dislocation slip was not the dominant deformation mechanism and GBS accommodated the majority of the deformation. This is evident in Figure 4.78 (f), where only a few grains exhibited slip traces.

23 slip traces in 23 grains were determined. Figure 4.79 shows the deformation system distribution with respect to the Schmid factors. No slip systems with Schmid factors below 0.35 were observed, indicating that Schmid factor calculated based on global stress state can be an effective parameter associated with the slip system activation. The stereographic unit triangle plots also show that grains in which slip systems were identified were confined in the Schmid factor regions, see Figure 4.80. Out of 23 active slip systems, 1 was basal (4%), 16 were prismatic (70%), 4 were pyramidal <a> (17%), and 2 were pyramidal <c+a> slip (9%). Prismatic slip was the primary slip system, which is similar to that observed for the tensile tests at 296K and 728K. Twinning was not observed during the creep experiment, which is unlike the

relative high strain rate tensile tests at the same temperature that twinning was an active deformation mode.

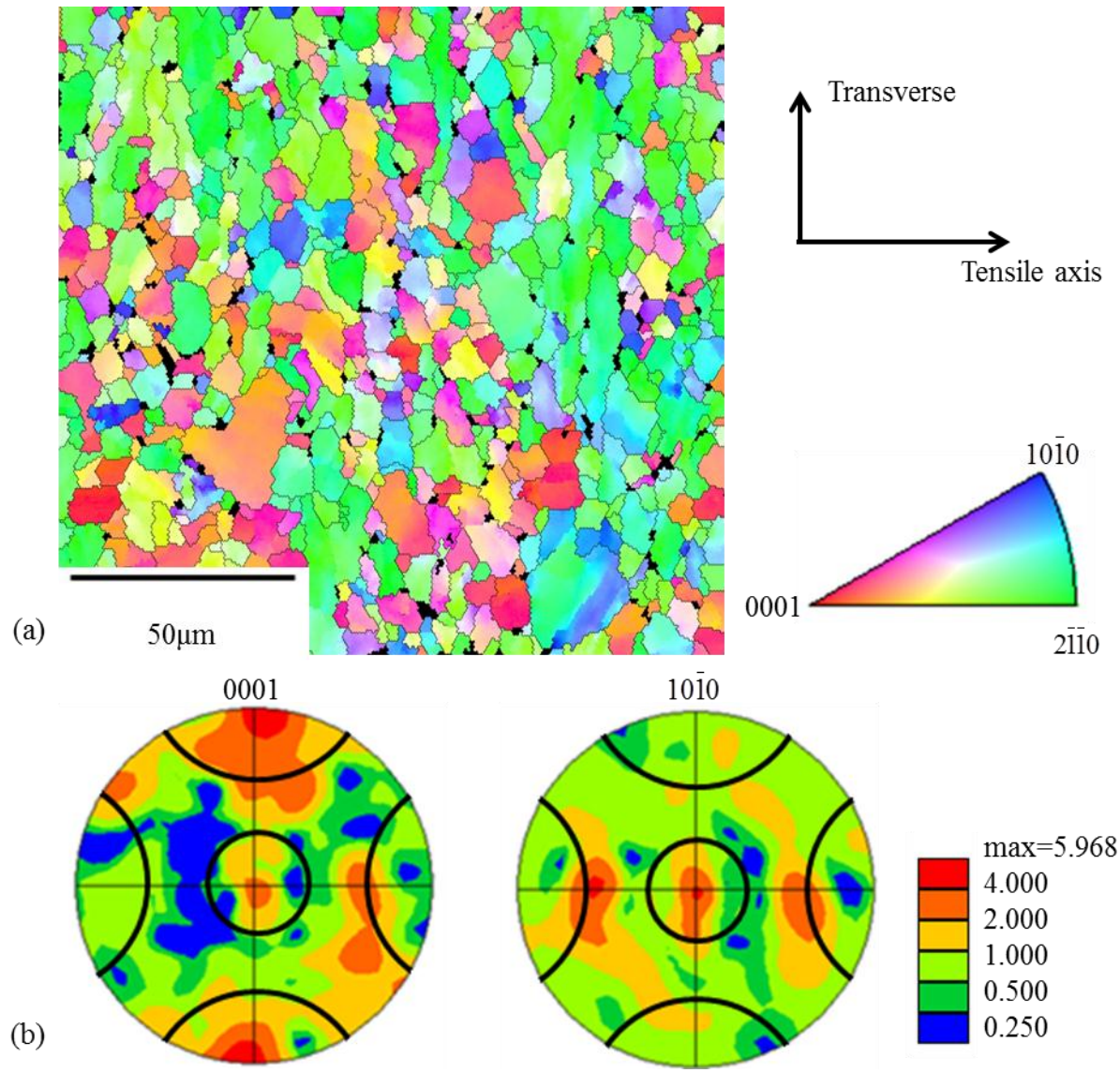

Figure 4.77 EBSD data of the 728K-180MPa tensile-creep tested specimen for the Ti-3Al-2.5V plate 1: (a) EBSD IPF map in the tensile direction of the α-phase Ti containing approximately 750 α grains, (b) the {0001} and the $\{10\bar{1}0\}$ pole figures with 30 ° cones along the major axes. The loading direction was horizontal.

(a)

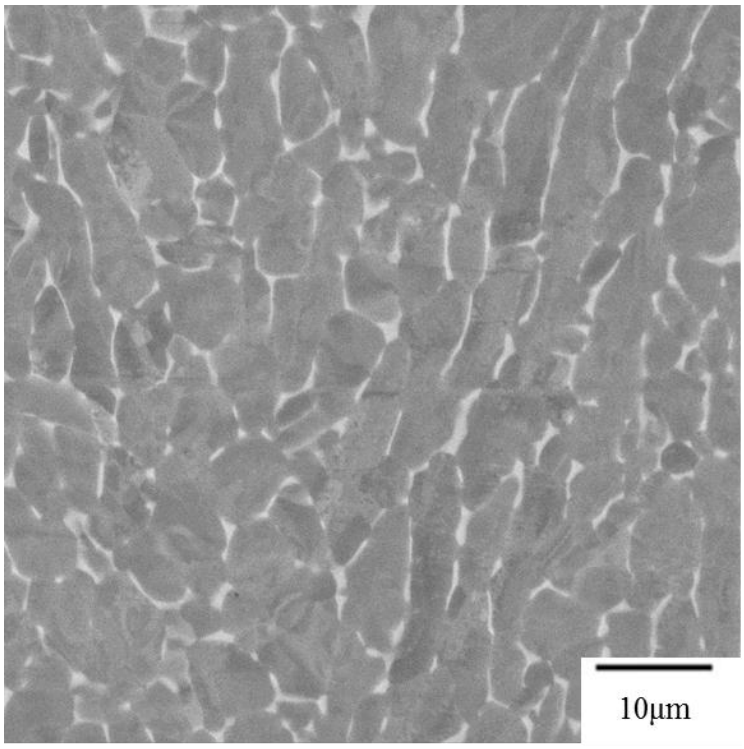

(b)

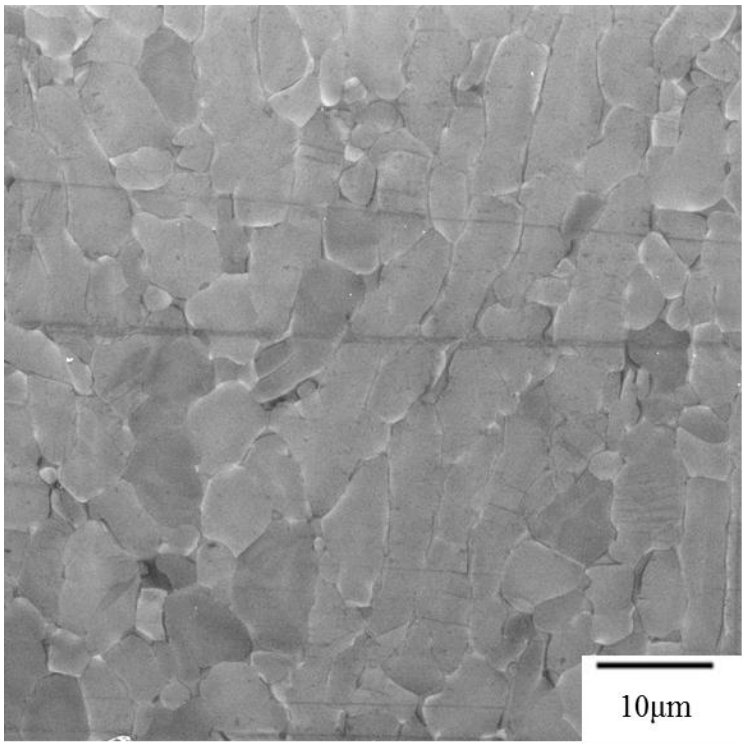

Figure 4.78 Sequential SE SEM images for the Ti-5Al-2.5Sn plate 1 tensile-creep tested at 763K-250MPa: (a) before loading; (b) 0.7% strain, 43 h; (c) ~1.4% strain, 94 h; (d) ~3.6% strain, 126 h; (e) ~6.6% strain, 186 h; (f) ~11.7% strain, 245 h. The loading direction was horizontal.

Figure 4.78 (cont'd)

(c)

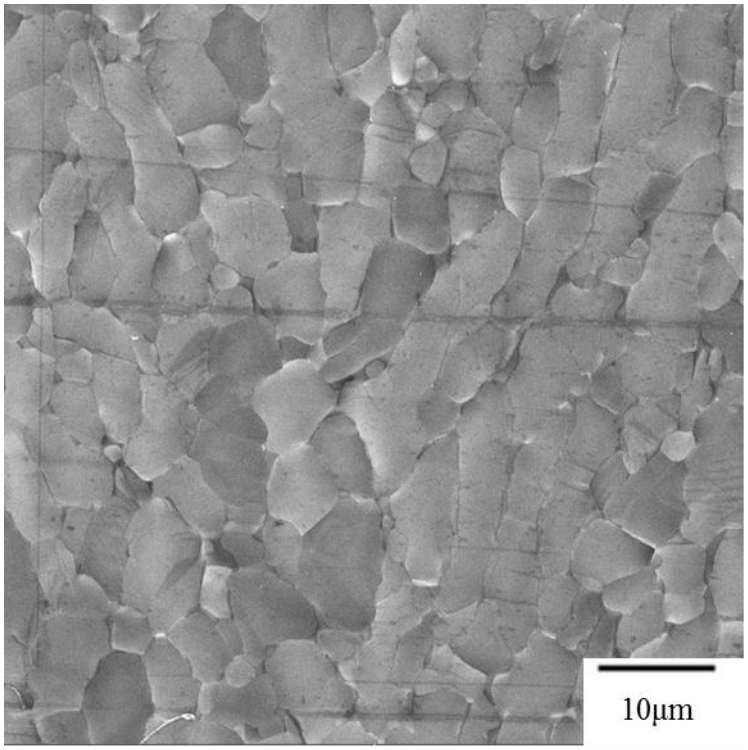

(d)

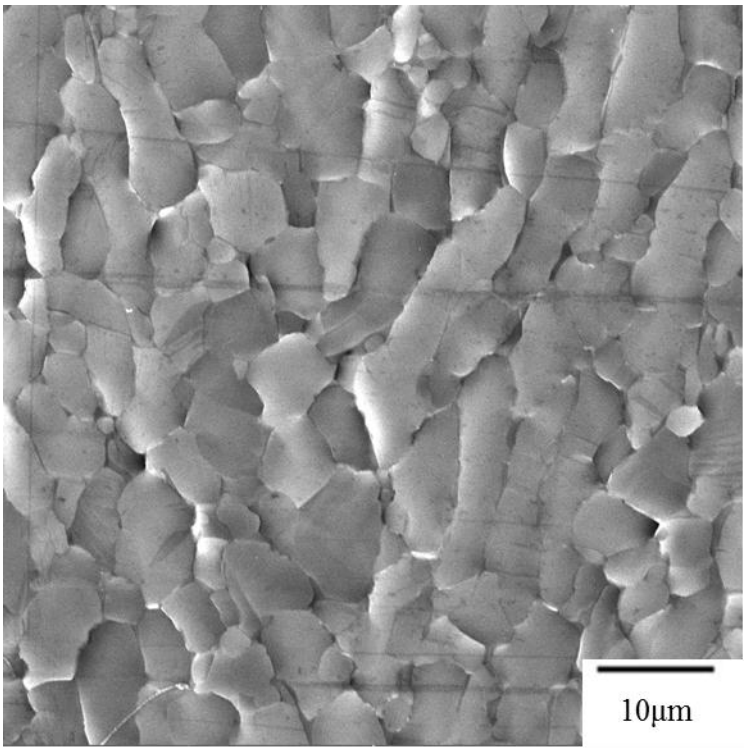

Figure 4.78 (cont'd)

(e)

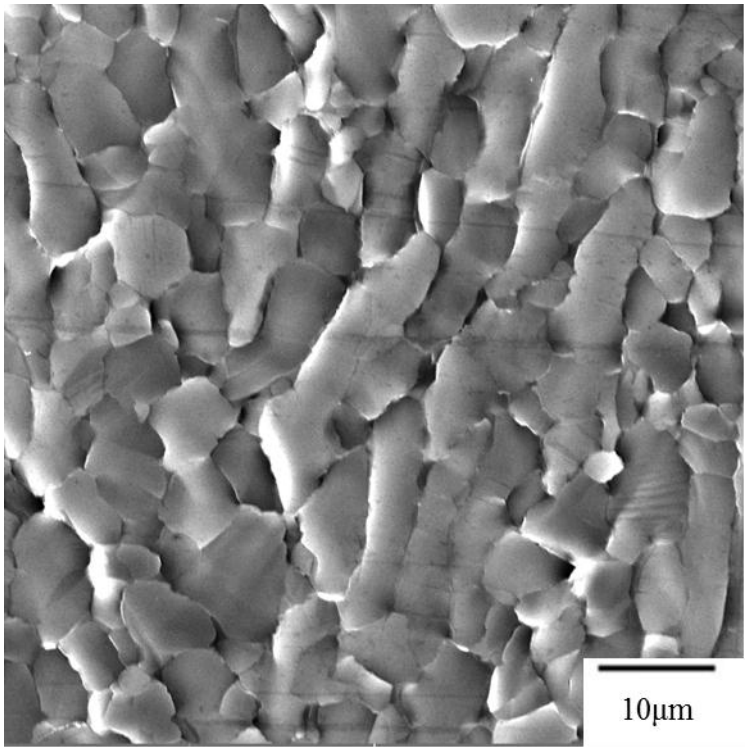

(f)

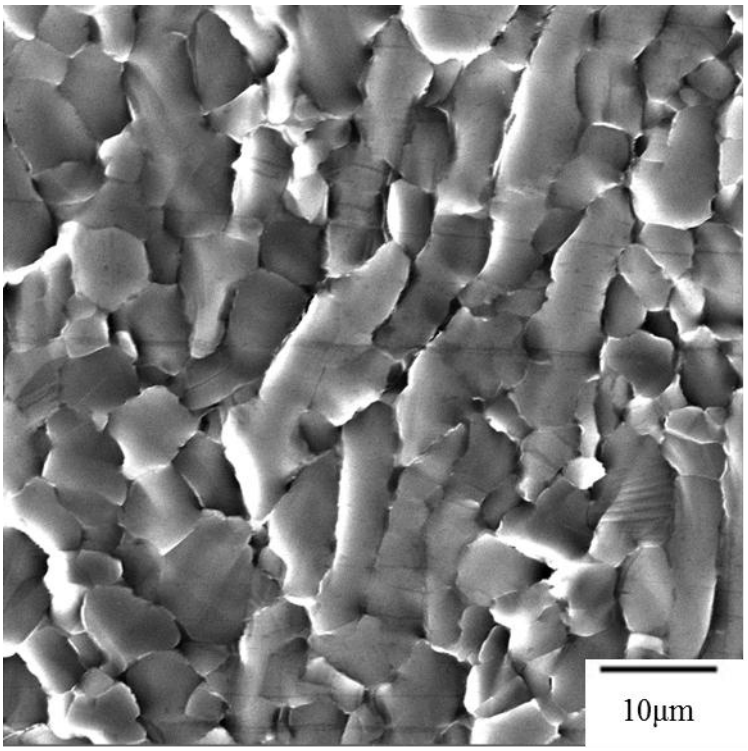

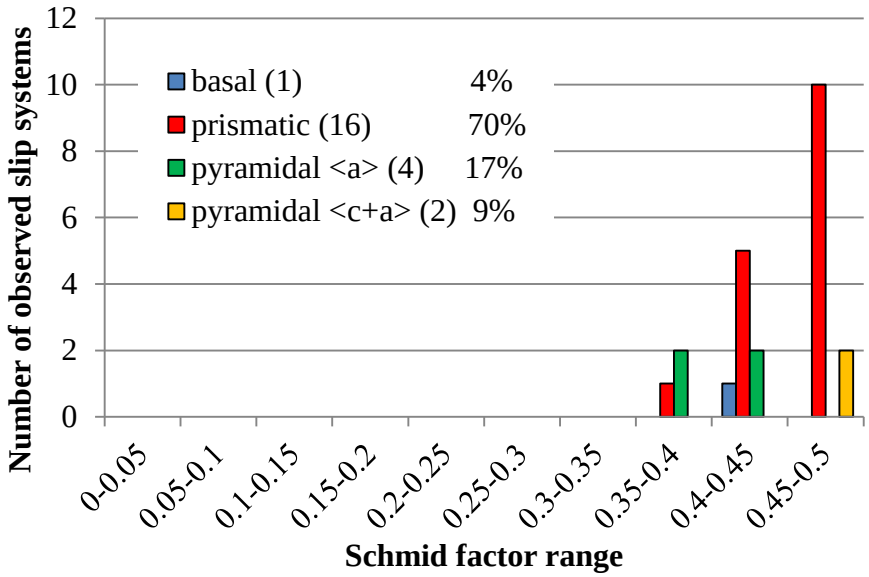

Figure 4.79 A histogram of the Schmid factor distribution of basal, prismatic, pyramidal <a>, and pyramidal <c+a> slip systems for the Ti-3Al-2.5V plate 1 tensile-creep tested at 728K and 180MPa after ~11.7% strain.

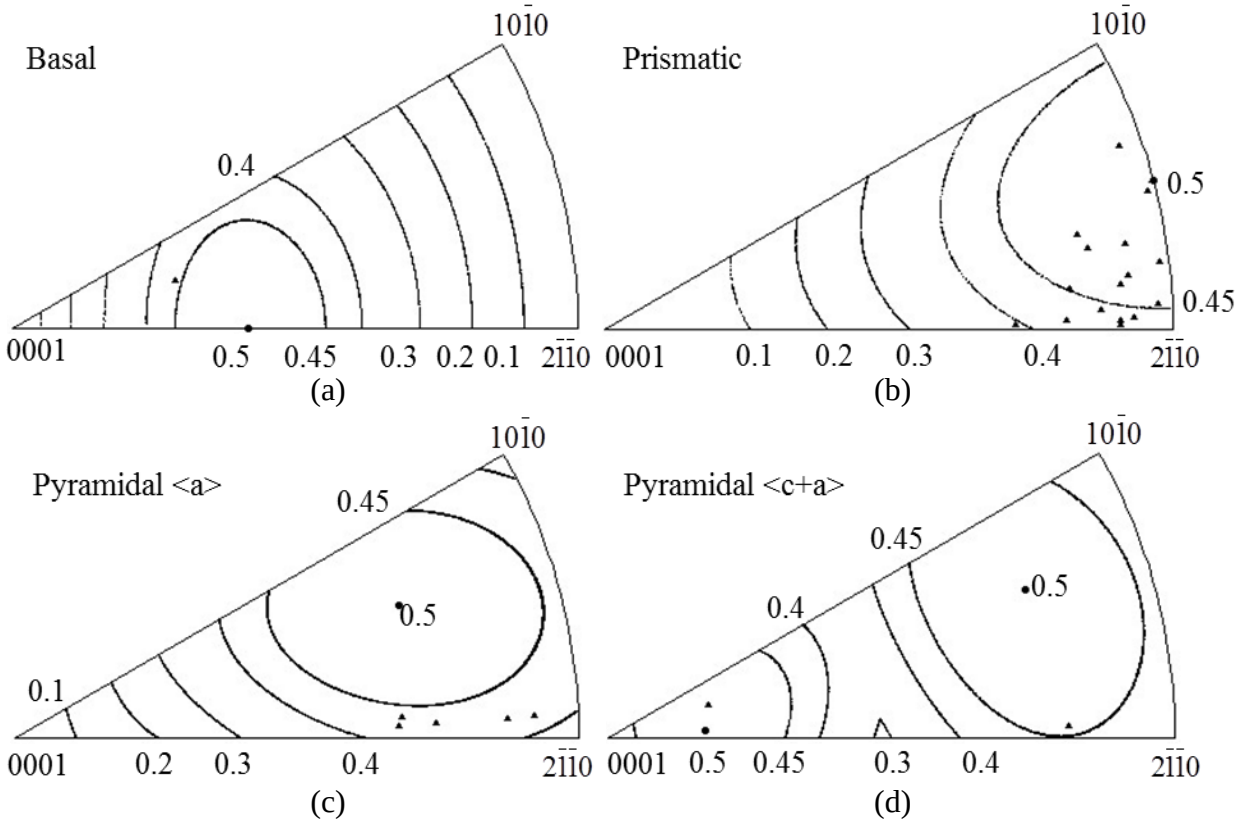

Figure 4.80 Unit triangle plots of grains which exhibited (a) basal, (b) prismatic, (c) pyramidal <a>, and (d) pyramidal <c+a> slip for the Ti-3Al-2.5V plate 1 tensile-creep tested at 728K and 180MPa after ~11.7% strain with Schmid factor contours overlaid.

4.4 Ti-6Al-4V

4.4.1 Microstructure

Figure 4.81 illustrates the low- and high-magnification BSE images of the as-received two-phase α+β Ti-6Al-4V microstructure. The microstructure was characterized to be bimodal; i.e. it was a combination of lamellar colonies and equiaxed grains. The Ti-6Al-4V alloy examined in the present study exhibited 49.9±3.4% of the equiaxed primary α (α_p) grains and 50.1±3.4% of the lamellar colony microstructure. The colony microstructure included secondary α (α_s) platelets (dark phase, 31.9±3.2% of the total volume) separated by thin layers of the β phase (light phase, 18.2±3.2% of the total volume). In Figure 4.81, both α_p and α_s appear dark due to the enrichment by the α-phase stabilizer Al, which had low atomic number. The β phase appears white or gray due to the enrichment by the relatively heavy β-phase stabilizer, V. The average α_p grain size was 6.4±4.4μm.

(a)

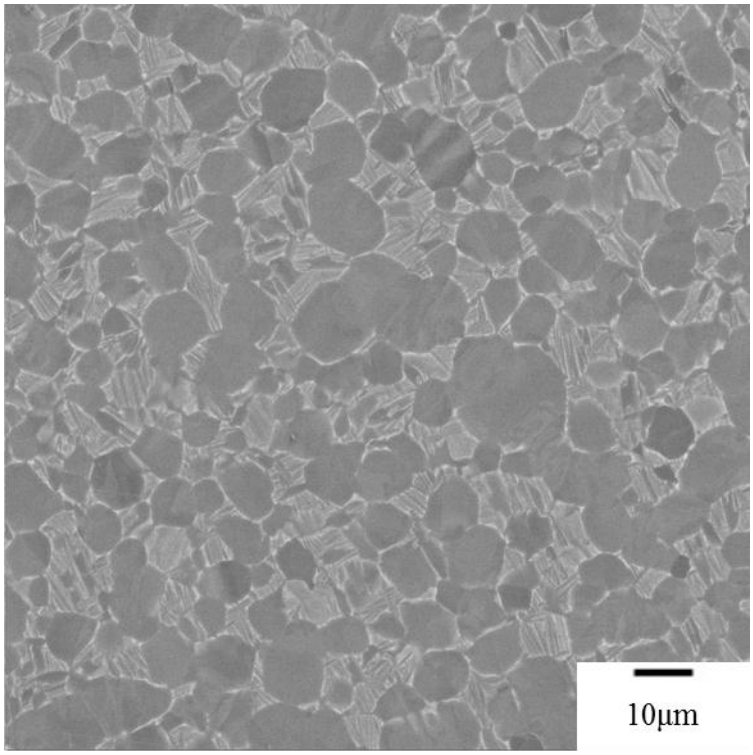

(b)

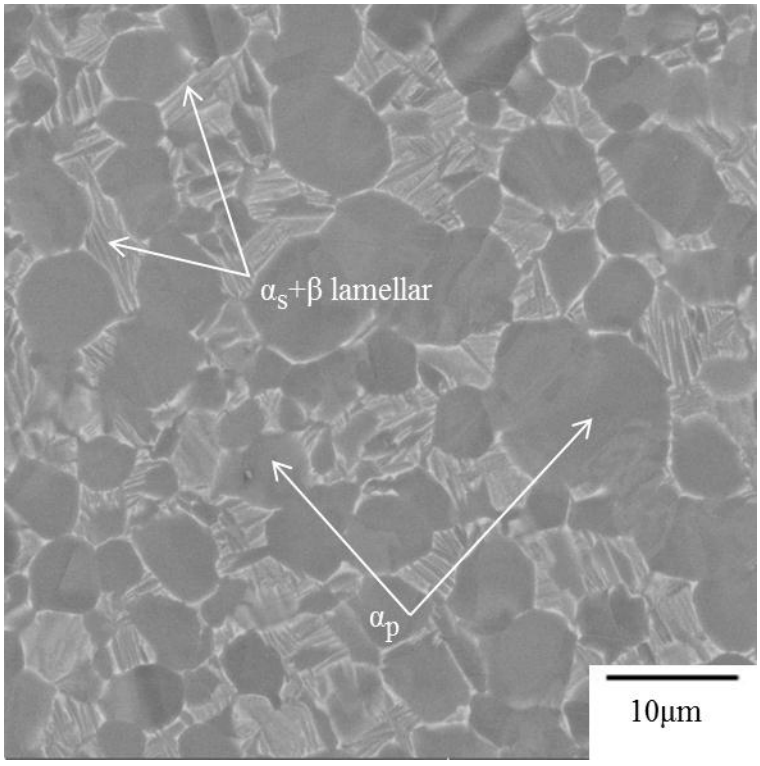

Figure 4.81 (a) Low- and (b) high-magnification BSE SEM images of the as-received α+β two phase Ti-6Al-4V alloy microstructure.

4.4.2 Macrozone

Macrozones were observed in Ti-6Al-4V. Figure 4.82 shows an IPF EBSD map in the tensile direction of an area of 1.3×2.4mm in a Ti-6Al-4V specimen. In Figure 4.82, hard orientations (i.e. red orientations) dominated in the upper region and were highlighted by a red circle while soft orientations (i.e. blue and green orientations) dominated in the lower region and were highlighted by a blue circle. Thus, two macrozones were present in this area. These macrozones can strongly affect the activation of the different deformation modes. For example, for a uniaxial tension test along the horizontal direction, in the hard-orientation dominated regions, both T1 twinning and pyramidal <c+a> slip had high Schmid factors and therefore were favored for activation during deformation. In contrast, in the soft-orientation dominated regions, prismatic slip exhibited high Schmid factors and was favored for activation. Therefore, areas that were chosen for performing slip trace analysis were intentionally chosen to not fall within a single macrozone, so that one deformation mode was not strongly preferred over another.

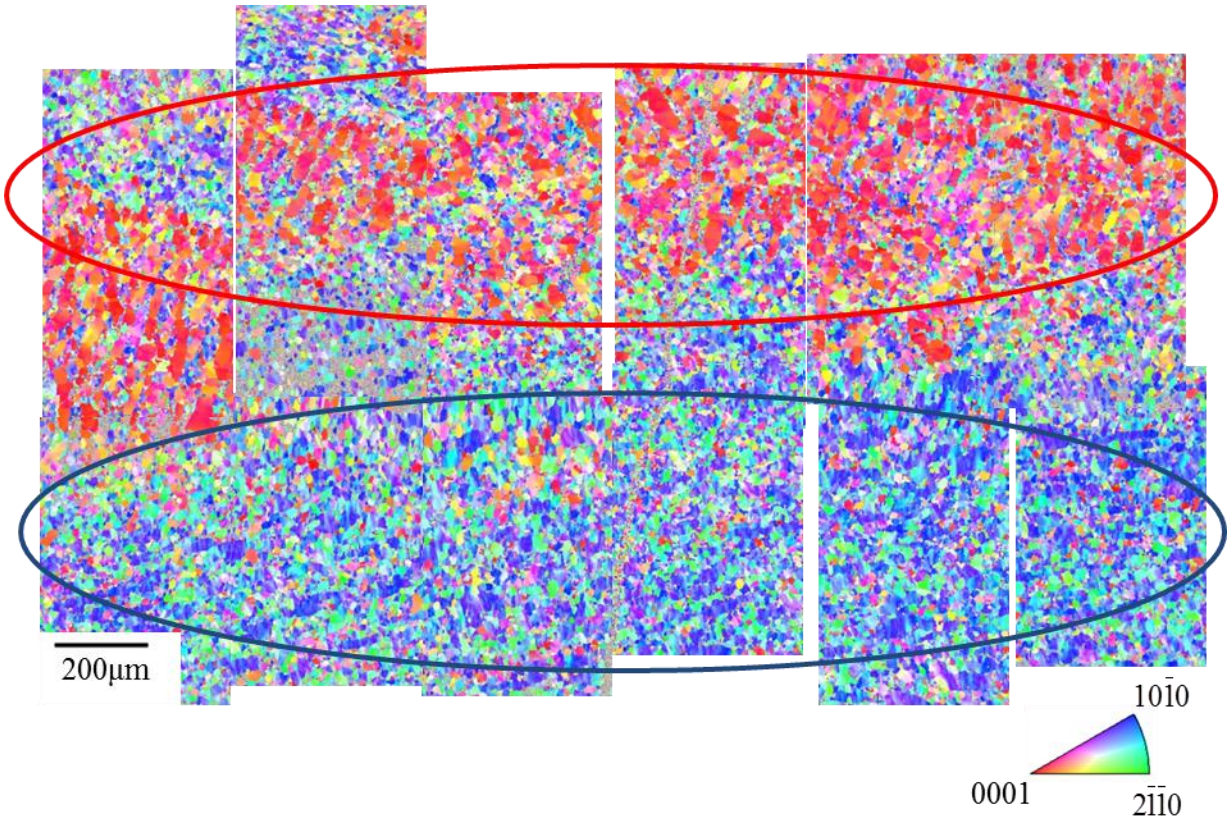

Figure 4.82 EBSD IPF map in the tensile direction of Ti-6Al-4V showing two macrozones highlighted by red and blue circles in a 1.3mm×2.4mm area.

4.4.3 *In-situ* tension

In-situ tensile tests were performed on Ti-6Al-4V at 296K and 728K. For each temperature, two tests were performed. Specimens A and B were deformed at 296K. Specimens C and D were performed at 728K. The four tensile specimens were machined from the same plate.

The engineering stress versus displacement curves for the 296K and 728K tensile tests are illustrated in Figure 4.83. It is noted that the engineering stress versus displacement curve of specimen B was not shown because an error occurred during the test, resulting in inaccurate stress data. A minimum of ~6.3% strain was imposed on each specimen. With increasing temperature, the YS of Ti-6Al-4V decreased from ~810MPa to ~420MPa. The YS and the

maximum stress observed at 296K were comparable with the values found in the literature, shown in Table 4.5. The YS and the maximum stress at 728K are slightly lower than the typical values found in the literature.

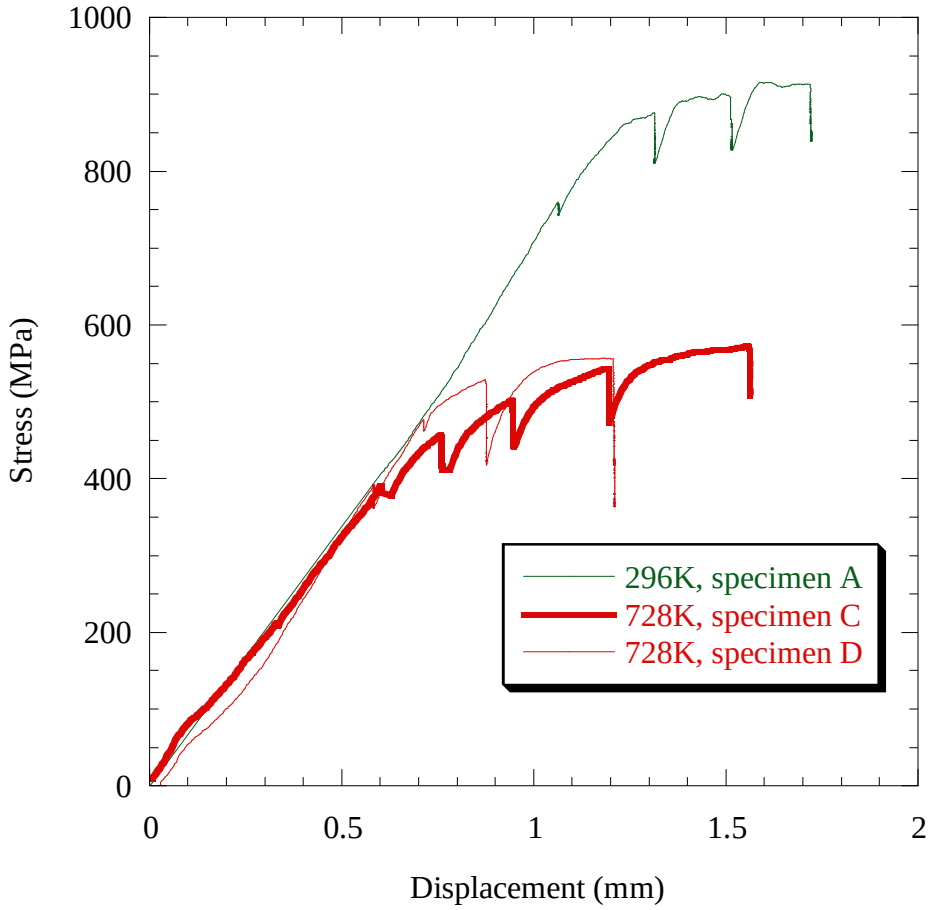

Figure 4.83 Stress vs. displacement plots for Ti-6Al-4V samples tensile tested at 296K and 728K. The load drops indicate that stress relaxation occurred when the tests were interrupted for imaging. The displacement values included displacements in both the gage section and the grip regions.

Table 4.5 Ti-6Al-4V tensile property comparison between the experiments in the current work and the Ti handbook by Boyer et al. [1994].

Test temperature	YS (MPa)	Max Stress (MPa)	YS in Boyer et al. (MPa)	UTS in Boyer et al. (MPa)	Comment
296K	~810	915	760-1103	830-1172	
728K	~420	572	~500	~650	Typical values

4.4.3.1 296K tension

4.4.3.1.1 Specimen A

For Ti-6Al-4V, within the α+β lamellar colonies, the β phase was often too thin to be indexed using the current Mira 3 SEM/EBSD system with a step size as small as 0.75μm. Thus, the resulting IPF EBSD maps exhibited only the α phase for the α+β lamellar colonies although the BSE SEM images clearly indicate the presence of the β phase. For example, Figure 4.84 (a) shows an undeformed microstructural patch of the Ti-6Al-4V alloy with two lamellar colonies highlighted and named as "X" and "Y". The corresponding EBSD IPF map in the tensile direction in Figure 4.84 (b) showed that these two lamellar colonies were indexed as α grains. In addition to the fact that the β-phase thin layers made the identification of β-phase difficult, another reason was that the α_s grains and the β thin layers within a single colony structure usually maintained the Burgers relationship and that the misorientations across α_s platelets within a single colony were less than 3° [Salem at al. 2008]. Hence, the α_s grains and the β thin layers together were indexed as a single HCP α grain by the EBSD software and a single orientation (i.e. single color in EBSD map) was assigned to all the lamellae in a given lamellar colony. Similar results have also been reported by Bridier et al. [2005] and Salem et al. [2008].

Figure 4.85 shows the EBSD IPF map in the tensile direction and the corresponding {0001} and $\{10\bar{1}0\}$ pole figures from a selected area of the gage section of the 296K tensile-tested specimen A. This area was chosen because it contained both hard and soft orientations and was not dominated by a single macrozone. There were approximately 1460 α grains (including α_p grains and lamellas) presented in Figure 4.85 (a). This area exhibited a strong texture (approximately 10 times random), where the majority of c-axis orientations in the {0001}

pole figures were aligned within 30° cones along the major axes. Such texture slightly favored the activation of prismatic slip and twinning over basal slip.

Figure 4.86 shows *in-situ* SE SEM images acquired during the 296K tension test of the Ti-6Al-4V specimen A. At ~2.4% strain, slip traces were first observed. These slip traces were identified to be associated with basal and prismatic slip systems with the Schmid factors greater than 0.4. Only one prismatic slip trace was identified with a low Schmid factor (0.11) and basal slip was also observed in the same grain with a Schmid factor of 0.45. With increasing strain, more grains exhibited slip traces. After ~6.3% strain in Figure 4.86 (d), slip was preferentially observed within the α_p grains and ~50% of the α_p grains exhibited slip traces. The slip traces were planar and cross slip was not observed. Usually, only one slip system was observed for each grain that exhibited slip traces. Much fewer deformation systems were activated in the $\alpha+\beta$ lamellar colonies compared to the equiaxed α_p grains. This was also the case for the other Ti-6Al-4V specimens tested at 296K and 728K, which will be presented later. Therefore, the analysis of the deformation modes was focused on the α_p grains. In Figure 4.86 (d), a T1 twin was observed with a Schmid factor of 0.48. This twin exhibited an 87.6° misorientation about the $<2\bar{1}\bar{1}0>$ axis with respect to the parent grain.

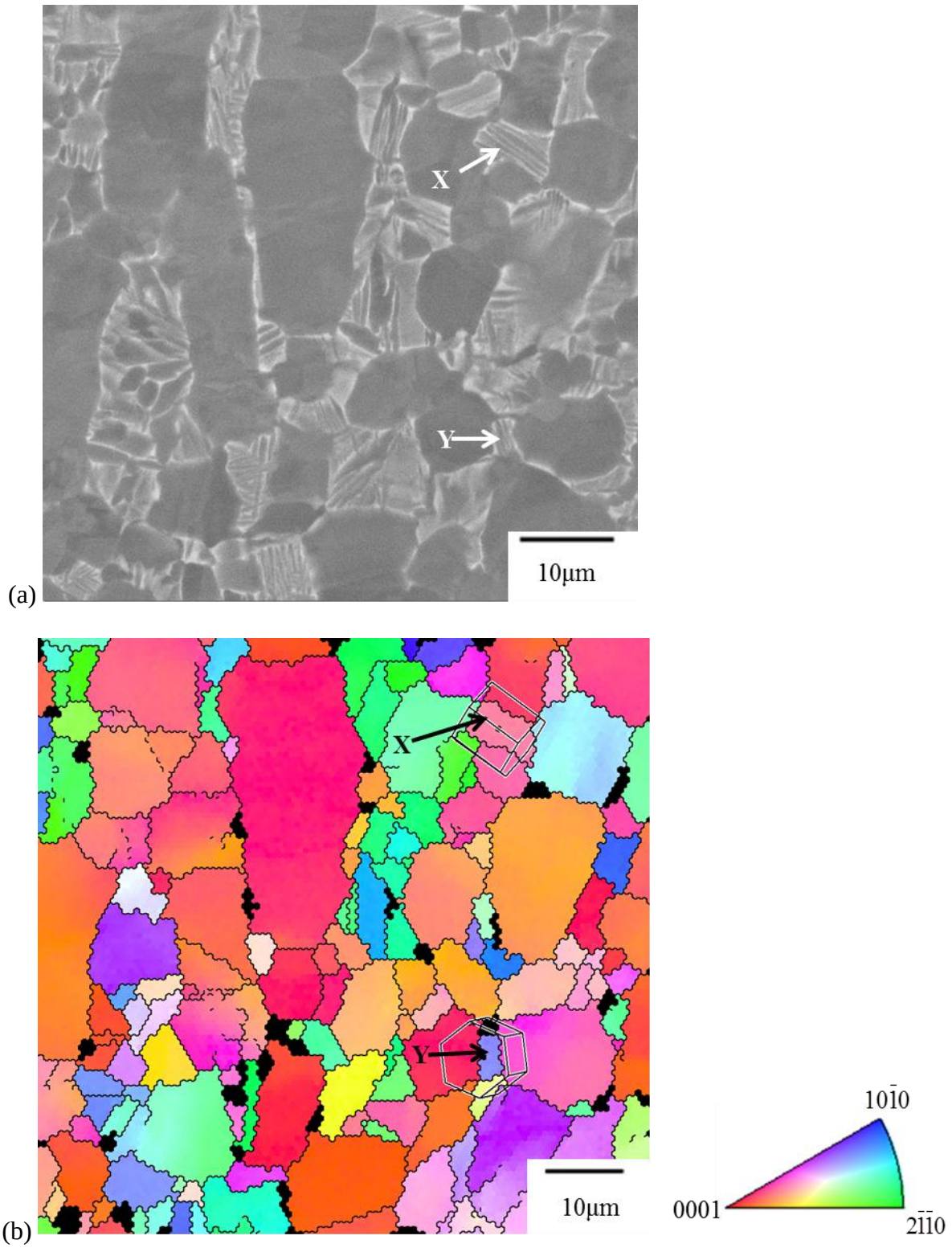

Figure 4.84 (a) A BSE SEM image showing an undeformed Ti-6Al-4V microstructure with two lamellar colonies highlighted as "X" and "Y". (b) The corresponding IPF EBSD map in the tensile direction showing that the orientations of the lamellar colonies, "X" and "Y", were erroneously indexed as the α phase only.

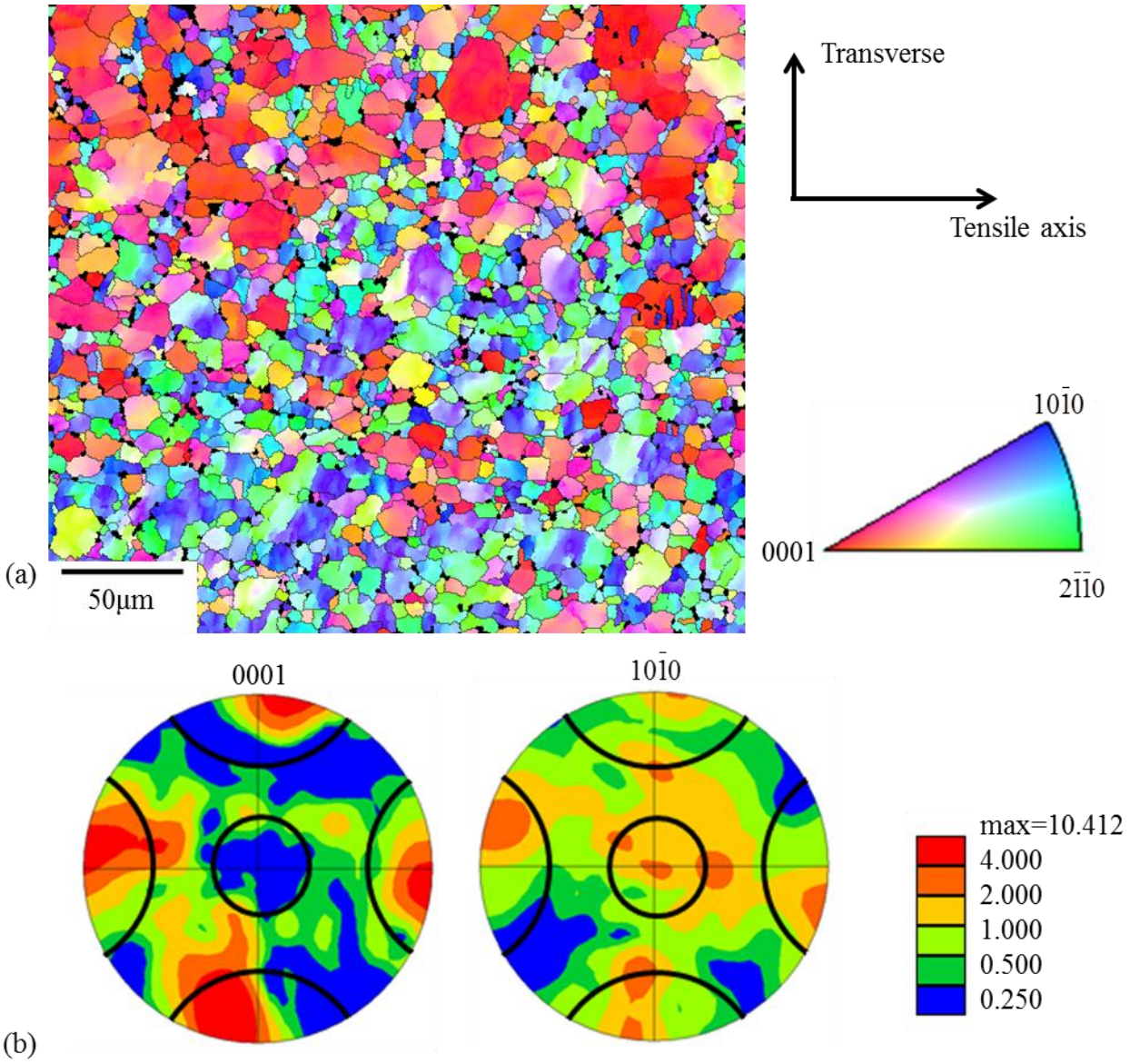

Figure 4.85 EBSD data of the Ti-6Al-4V 296K tensile-tested specimen A: (a) EBSD IPF map in the tensile direction of the α-phase Ti containing approximately 1460 α grains, (b) the {0001} and the $\{10\bar{1}0\}$ pole figures with 30 ° cones along the major axes. The loading direction was horizontal.

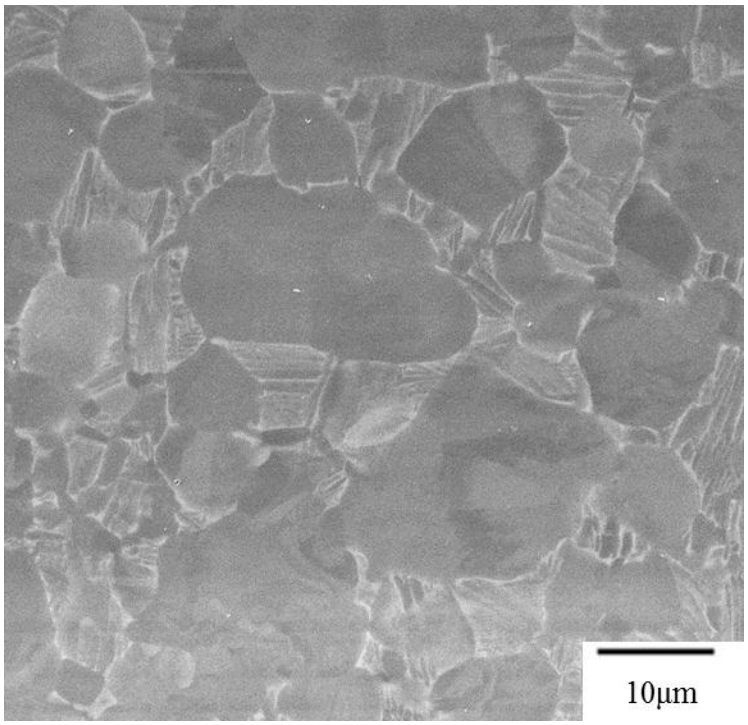

(a)

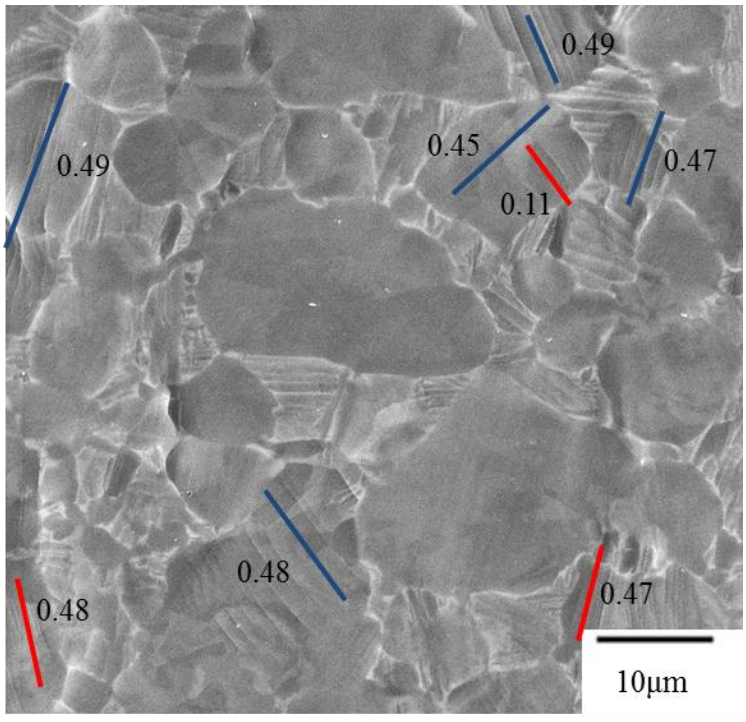

(b)

Figure 4.86 Sequential SE SEM images for Ti-6Al-4V specimen A tensile tested at 296K: (a) undeformed, (b) 876MPa (~2.4% strain), the color-coded planes traces for prismatic slip (red) and basal slip (blue) are labeled along with their Schmid factors (c) 901MPa (~4.1% strain), and (d) 916MPa (~6.3% strain). The black plane trace in (d) is for T1 twin and its Schmid factor was 0.48. The loading direction was horizontal.

Figure 4.86 (cont'd)

(c)

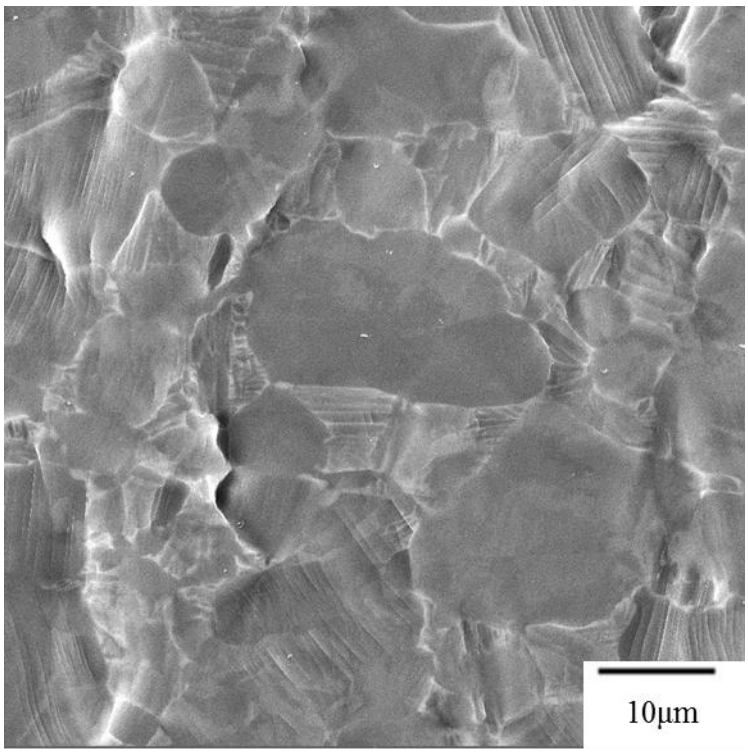

(d)

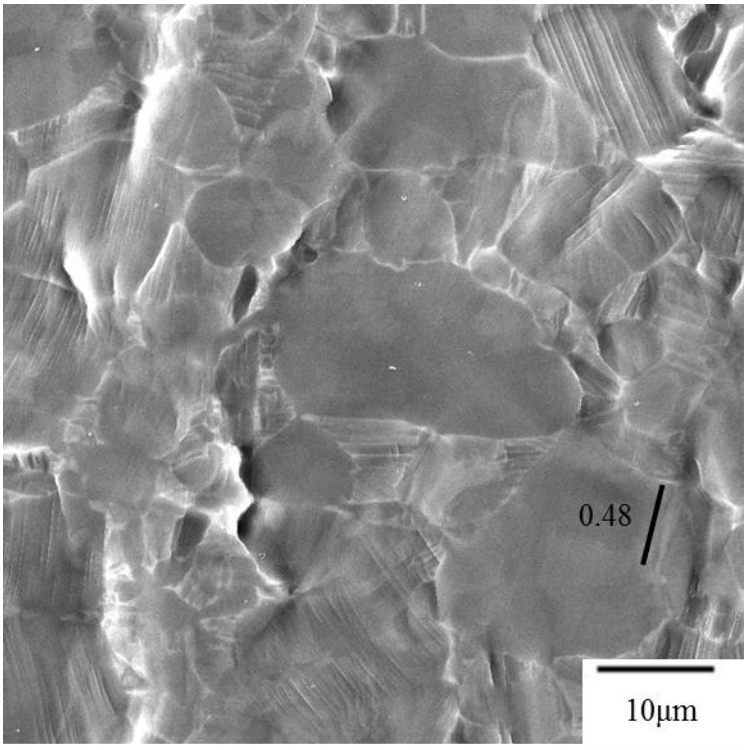

A total of 313 deformation systems were determined for 297 grains, shown in Figure 4.87. In the 297 grains analyzed, 113 basal slip systems (36%) and 147 prismatic slip systems (47%) were observed, indicating that both of the basal and prismatic slip systems were the dominant deformation modes at 296K tension. Pyramidal <a> and pyramidal <c+a> contributed 8% and 6% of the total deformation systems, respectively. 10 T1 twins (3%) were observed. This suggests that twinning was an active deformation system but not a dominant deformation system for Ti-6Al-4V at 296K. As shown in Figure 4.87, the active deformation systems were associated with high Schmid factors and no slip system with a Schmid factor lower than 0.15 was observed.

Figure 4.88 shows the stereographic triangles with the grain orientations plotted for basal, prismatic, pyramidal <a>, pyramidal <c+a>, and twinning deformation modes with Schmid factor contours overlaid. As seen in Figure 4.88, grains with prismatic slip were confined to the high Schmid factor regions. This is similar to that observed in the 296K tension tests for both Ti-3Al-2.5V plates. Unlike the 296K tension tests for CP Ti and Ti-5Al-2.5Sn, where some grains with Schmid factors below 0.1 were activated and grains with prismatic slip were activated over the entire stereographic triangles, prismatic slip was only observed when the Schmid factor was greater than 0.2 for Ti-6Al-4V at 296K. Most of grains that exhibited basal, pyramidal <a>, pyramidal <c+a>, and twinning were also within regions where the high Schmid factor was high.

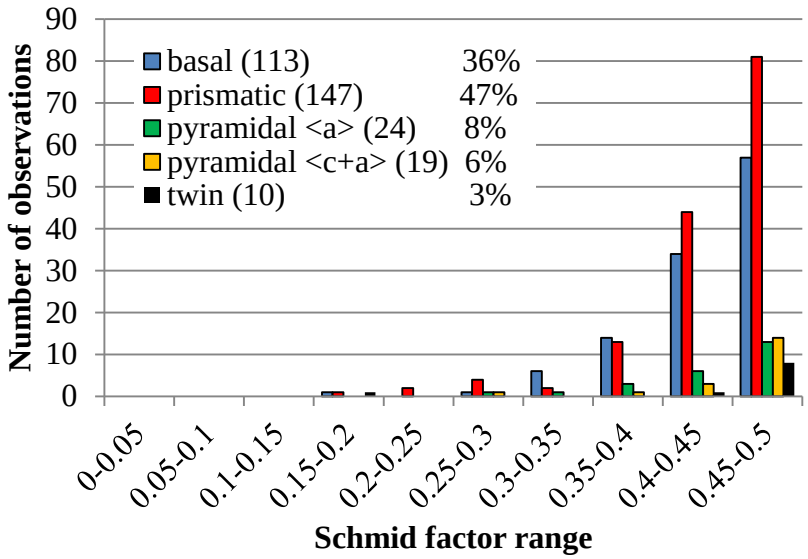

Figure 4.87 A histogram of the Schmid factor distribution of basal, prismatic, pyramidal <a>, and pyramidal <c+a> slip systems and T1 twinning systems for the Ti-6Al-4V 296K tensile specimen A after ~6.3 % strain.

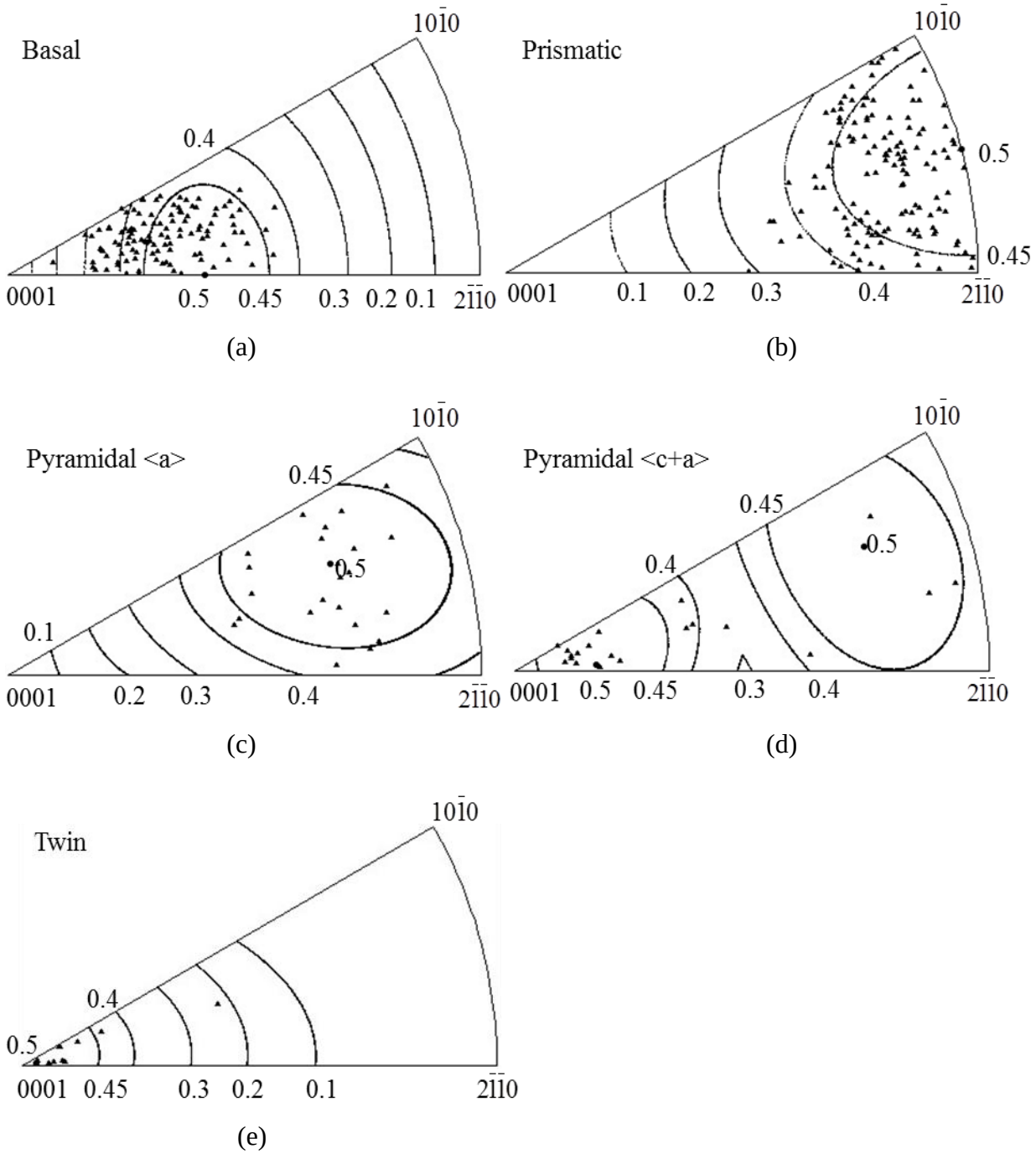

Figure 4.88 Unit triangle plots of grains which exhibited (a) basal, (b) prismatic, (c) pyramidal <a>, (d) pyramidal <c+a>, and (e) T1 twin deformation systems for the Ti-6Al-4V 296K tensile specimen A deformed to ~6.3% strain with Schmid factor contours overlaid.

4.4.3.1.2 Specimen B

A second 296K tensile test was performed for the Ti-6Al-4V specimen B. Figure 4.89 shows the EBSD IPF map in the tensile direction and the corresponding {0001} and $\{10\bar{1}0\}$ pole figures from a selected area of the gage section of specimen B. There were approximately 1480 α grains (including α_p grains and α+ β lamellar colonies) represented in Figure 4.89 (a) and the maximum peak intensity of the texture was approximately 9 times random. Similar to the texture of the specimen A in Figure 4.84, the texture of the specimen B contained both hard and soft orientations and the majority of the c-axis orientations in the {0001} pole figure of specimen B were aligned within 30 °cones of the major axes.

Figure 4.90 shows a deformed microstructural patch from the Ti-6Al-4V specimen B after ~8.2% strain. In Figure 4.90, ~82% of the α_p grains exhibited slip traces. A total of 228 active deformation systems were identified in the 214 α_p grains, as summarized in Figure 4.91. Similar to specimen A, both basal and prismatic slip were the dominant deformation modes as they were associated with 83% of all the slip traces analyzed for specimen B (basal 40% and prismatic 43%, see Figure 4.91). Both basal and prismatic slip were typically observed with Schmid factors greater than 0.4. This was also the case for the pyramidal <a> and pyramidal <c+a> slip. Only 4 T1 twins (2%) were observed, indicating twinning was not a dominant deformation mode in Ti-6Al-4V at 296K. The Schmid factors associated with these four T1 twins were greater than 0.45.

Figure 4.92 shows stereographic triangles with the grain orientations plotted for basal, prismatic, pyramidal <a>, pyramidal <c+a>, and T1 twin deformation modes with Schmid factor contours overlaid. Similar to the specimen A, most of grains in which basal and prismatic slip

were identified were activated within the high Schmid factor regions. Twinning was only observed in the left corner of the stereographic triangle, where T1 twins had high Schmid factors.

Overall, the activity of the different deformation modes in specimen A and B was similar. This activity will be compared with the CP Ti, Ti-5Al-2.5Sn, and Ti-3Al-2.5V examined in this dissertation and other materials previously studied in the literature in Chapter 5.

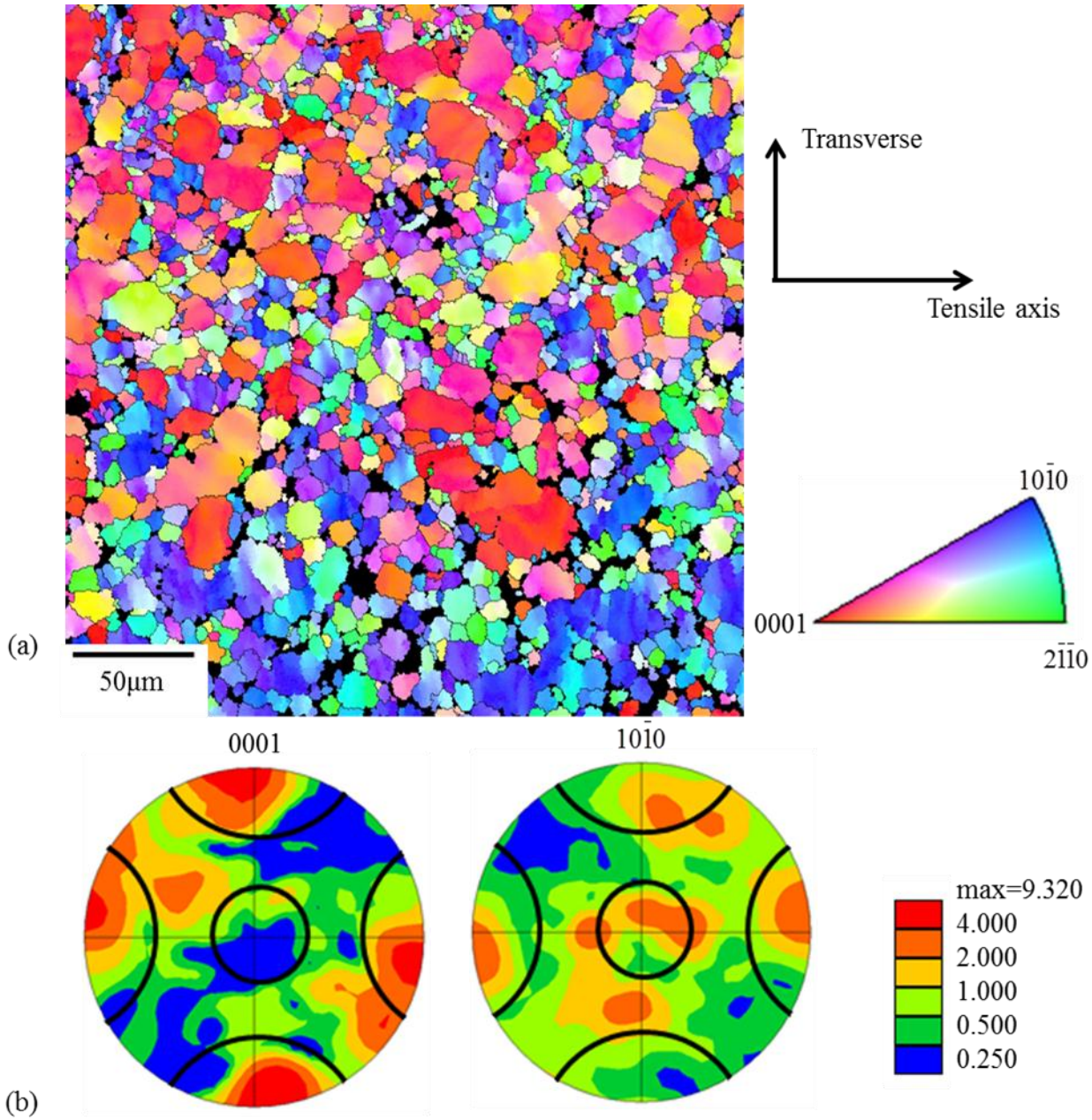

Figure 4.89 EBSD data of the Ti-6Al-4V 296K tensile-tested specimen B: (a) EBSD IPF map in the tensile direction of the α-phase Ti containing approximately 1480 α grains, (b) the {0001} and the $\{10\bar{1}0\}$ pole figures with 30 ° cones along the major axes. The loading direction was horizontal.

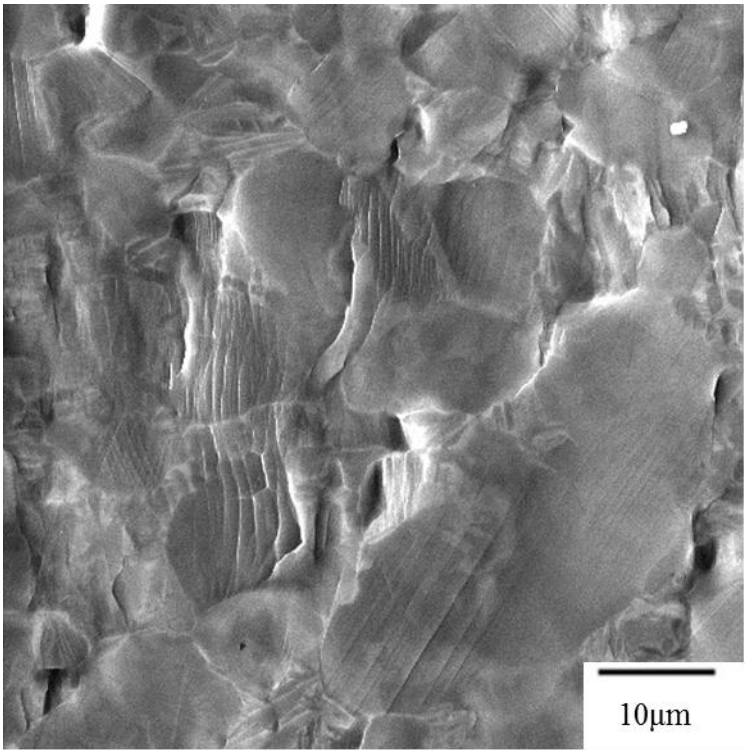

Figure 4.90 SE SEM image showing a tensile deformed microstructural patch of the Ti–6Al–4V specimen B at 296K after ~8.2% strain.

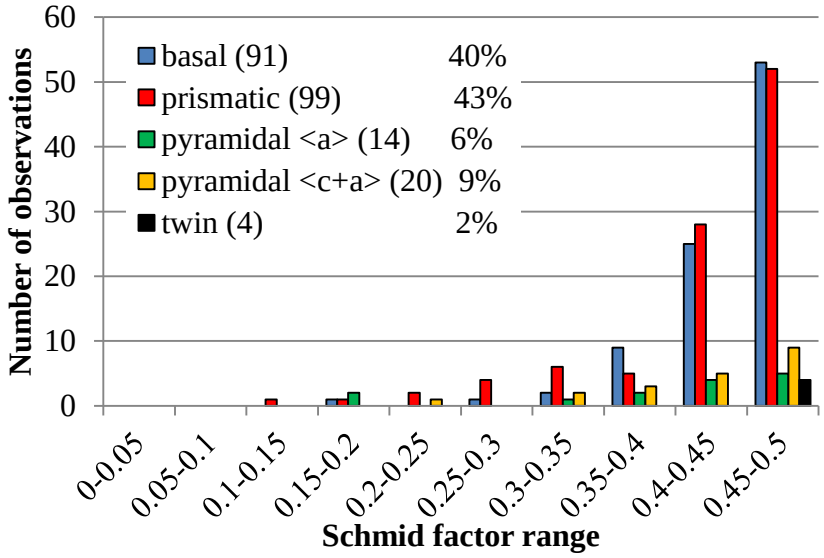

Figure 4.91 A histogram of the Schmid factor distribution of basal, prismatic, pyramidal <a>, and pyramidal <c+a> slip systems and T1 twinning systems for the Ti-6Al-4V 296K tensile specimen B after ~8.2 % strain.

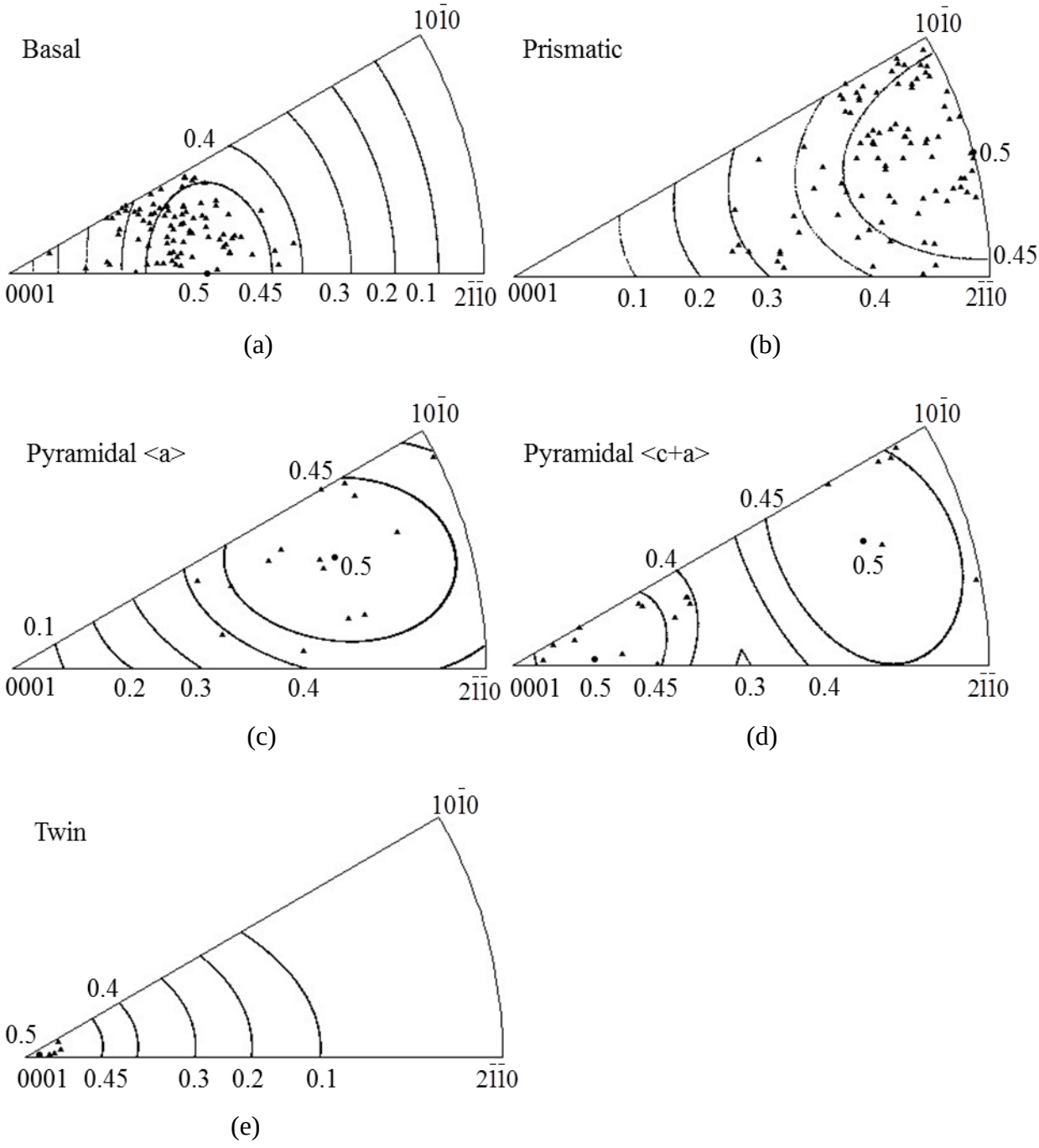

Figure 4.92 Unit triangle plots of grains which exhibited (a) basal, (b) prismatic, (c) pyramidal <a>, (d) pyramidal <c+a>, and (e) T1 twin deformation systems for the Ti-6Al-4V 296K tensile specimen B deformed to ~8.2% strain with Schmid factor contours overlaid.

4.4.3.2 728K tension

4.4.3.2.1 Specimen C

Figure 4.93 shows the EBSD IPF map in the tensile direction and the corresponding {0001} and $\{10\bar{1}0\}$ pole figures from a selected area of the gage section of the 728K tensile-tested specimen C for Ti-6Al-4V. In Figure 4.93, there were about 1600 α grains (including α_p grains and lamellas) and the maximum peak intensity of the pole figures was approximately 13 times random. Similar to the texture of the Ti-6Al-4V specimens A and B tensile tested at 296K, the texture of specimen C included both hard and soft orientations. The peak locations of the {0001} pole figure in Figure 4.93 were also similar to that observed for specimens A (Figure 4.85) and B (Figure 4.89).

Figure 4.94 shows the sequential SE SEM images of the same area acquired for the 728K tensile-tested specimen C. Three slip bands were first observed shortly after global yielding (~1.3% strain) and all of them were identified to be for basal slip (blue lines in Figure 4.94 (b)). The associated Schmid factors were 0.26, 0.26, and 0.43 respectively. The activation of basal slip systems with relatively low Schmid factors at an early stage of deformation suggests that the local stress state may vary from the global stress state and that basal slip may be easy to activate at 728K. At ~3.8% strain, four new basal slip, two new prismatic, and one new pyramidal <c+a> slip systems were identified for this microstructural patch (see Figure 4.94 (c)). Each of the newly activated slip systems were associated with Schmid factors greater than 0.4. After 10.2% strain, ~76% of the α_p grains in the observed region exhibited slip traces. Usually, only one deformation system was observed for each slipped grain. GBS was also observed. The extent of the GBS, as evidenced by the grain boundary ledge formation similar to that described in section

4.2 for Ti-5Al-2.5Sn, was more dramatic compared to 296K tensile-tested specimen B with a similar strain (see Figure 4.90).

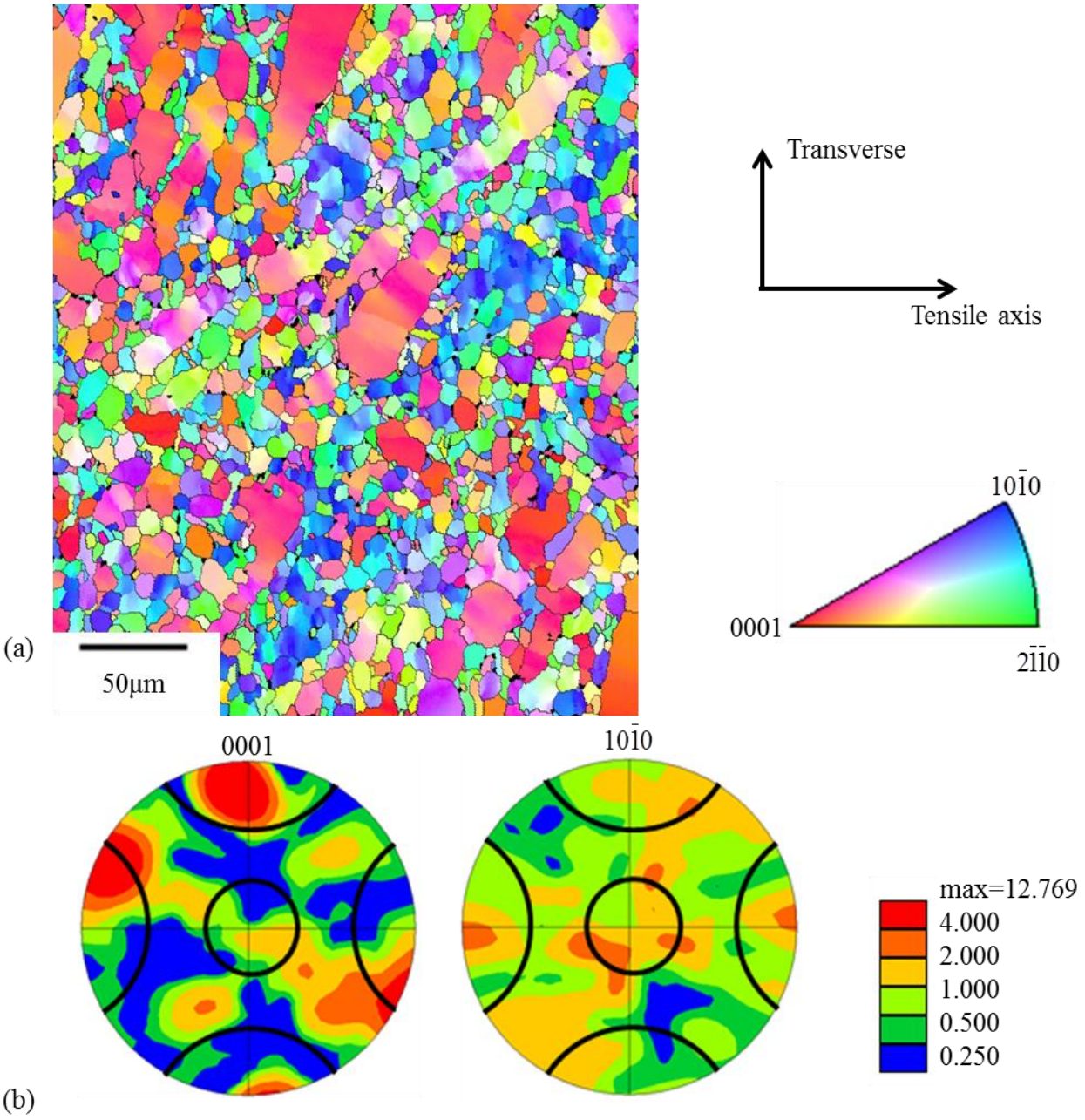

Figure 4.93 EBSD data of the Ti-6Al-4V 728K tensile-tested specimen C: (a) EBSD IPF map in the tensile direction of the α-phase Ti containing approximately 1600 α grains, (b) the {0001} and the $\{10\bar{1}0\}$ pole figures with 30° cones along the major axes. The loading direction was horizontal.

(a)

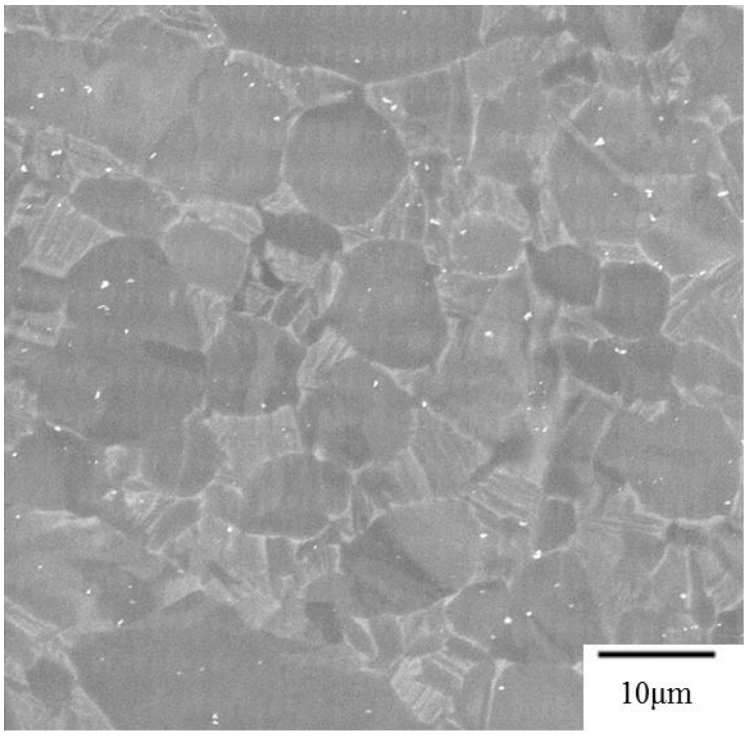

(b)

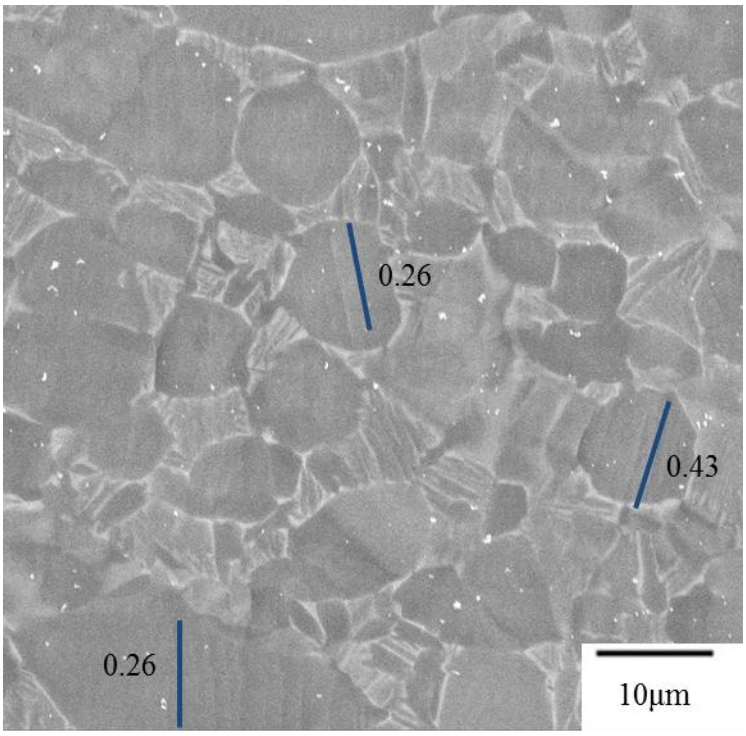

Figure 4.94 Sequential SE SEM images for Ti-6Al-4V specimen C tensile tested at 728K: (a) undeformed, (b) 463MPa (~1.3% strain, when slip bands were first observed), (c) 523MPa (~3.8% strain), and (d) 557MPa (~10.2% strain). In (b) and (c), planes traces are color coded for prismatic slip (red), basal slip (blue), and pyramidal <c+a> (orange). The loading direction was horizontal.

Figure 4.94 (cont'd)

(c)

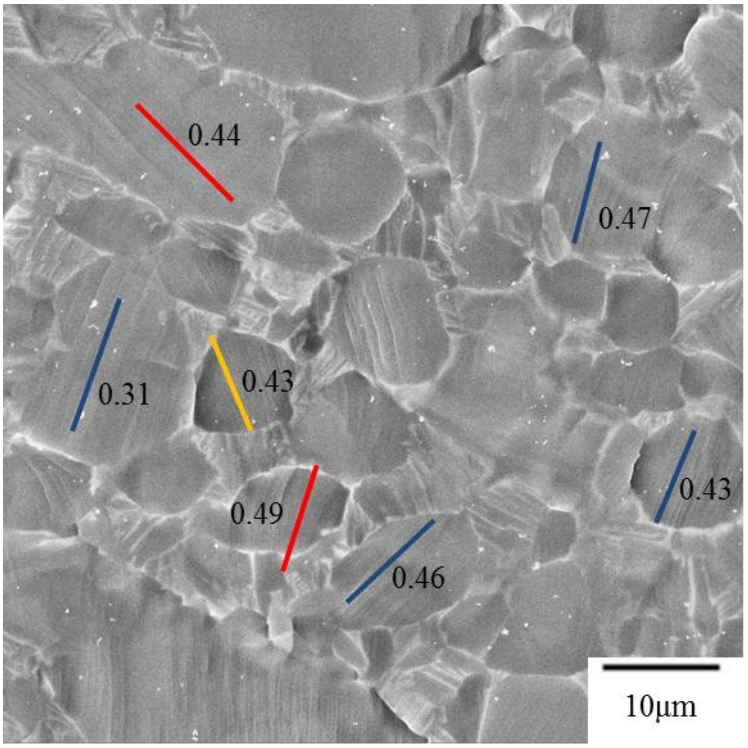

(d)

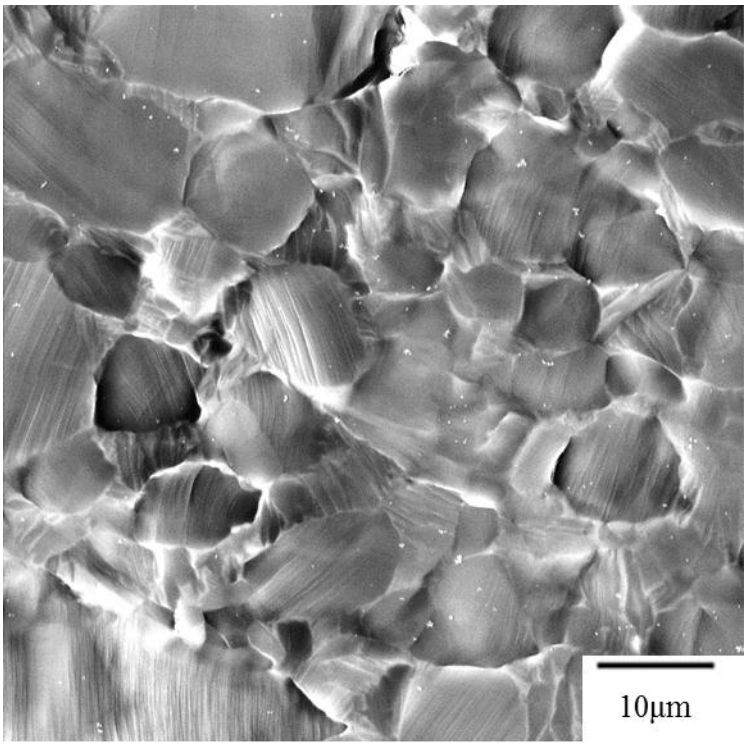

The slip-trace technique was used to identify a total of 185 active deformation systems in 179 α_p grains, as summarized in Figure 4.95. In the 179 grains analyzed, 99 basal slip systems were identified and comprised 54% of the total deformation systems. 57 prismatic slip systems were identified and comprised 31% of the total deformation systems. Note that the texture of this specimen favored the activation of prismatic slip over basal slip. Thus, the experimental observations suggest that basal slip was more likely to activate than prismatic slip in tension at 728K. The enhanced basal slip activity relative to prismatic slip at 728K in the current work is consistent with the work of Williams et al. [2002] who found that basal slip became more dominant during higher temperature deformation. 13 pyramidal <a> slip systems (13/185=5%) and 9 pyramidal <c+a> slip systems (9/185=5%) were observed. Twinning was also observed but to a much lesser extent; i.e. it made up only 4% of the total deformation systems.

Figure 4.96 shows the stereographic triangles with the grain orientations plotted for basal, prismatic, pyramidal <a>, pyramidal <c+a>, and T1 twinning deformation modes with the Schmid factor contours overlaid. Grains with prismatic slip, pyramidal <a> slip, pyramidal <c+a> slip, and T1 twin were confined to the high Schmid factor regions (>0.4). Grains which exhibited basal slip were distributed over a large part of the stereographic triangle. Some grains which exhibited basal slip were distributed in a region where the Schmid factor for basal slip was below 0.2.

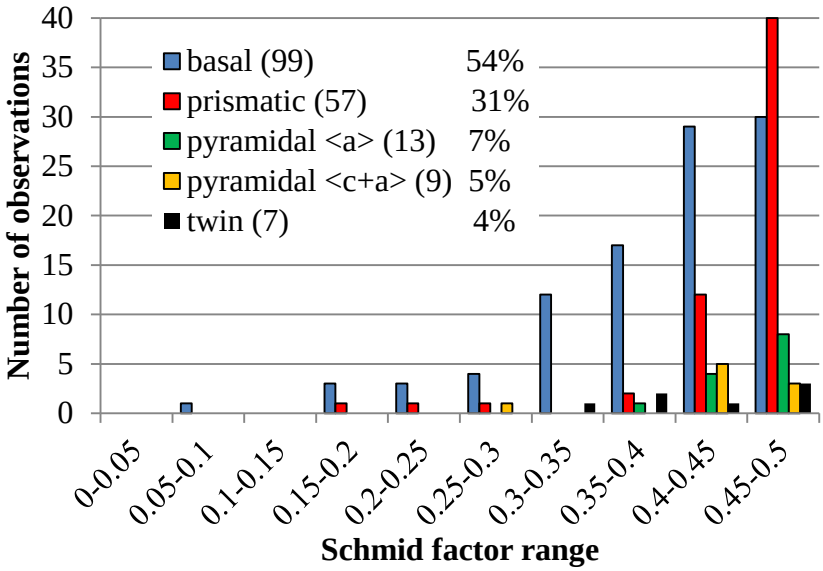

Figure 4.95 A histogram of the Schmid factor distribution of basal, prismatic, pyramidal <a>, and pyramidal <c+a> slip systems and T1 twinning systems for the Ti-6Al-4V 728K tensile specimen C after ~10.2 % strain.

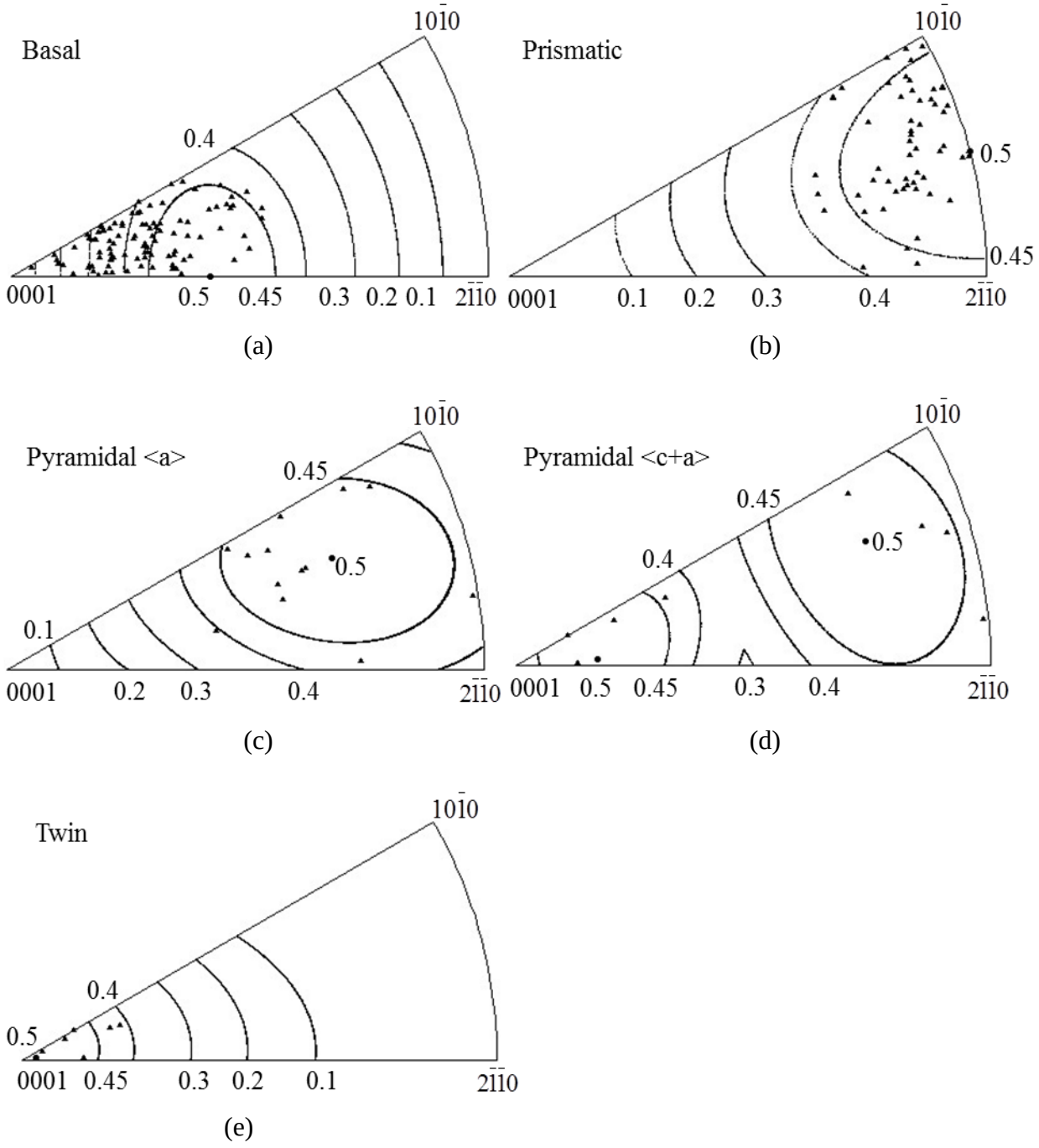

Figure 4.96 Unit triangle plots of grains which exhibited (a) basal, (b) prismatic, (c) pyramidal <a>, (d) pyramidal <c+a>, and (e) T1 twin deformation systems for the Ti-6Al-4V 728K tensile specimen C deformed to ~10.2% strain with Schmid factor contours overlaid.

4.4.3.2.2 Specimen D

A second 728K tensile test was performed on the Ti-6Al-4V specimen D. Figure 4.97 shows the EBSD IPF map in the tensile direction and the corresponding {0001} and $\{10\bar{1}0\}$ pole figures from the gage section of specimen D. There were approximately 980 grains and collectively they exhibited ~14 times random texture. In the {0001} pole figure, the locations with maximum peak intensities were on the 30° arc of the transverse direction. Unlike that for the tensile specimens A, B, and C, specimen D exhibited a texture dominated by purple grain orientations, where pyramidal <a> slip system had high Schmid factors, see Figure 4.97 (a).

A deformed microstructural patch from the 728K tensile-tested specimen D after ~11.6% strain is shown in Figure 4.98. Wavy slip lines indicated the development of cross slip. After ~11.6% strain, about 60% of α_p grains exhibited slip traces and grain boundary ledges, suggesting sliding, were observed for some grain boundaries. 70 slip systems were determined for a total of 63 α_p grains. The histogram illustrating the deformation modes with respect to the Schmid factor is provided in Figure 4.99. In the 63 grains analyzed, 26 basal slip, 19 prismatic slip, 21 pyramidal <a> slip, and 4 pyramidal <c+a> slip systems were identified, corresponding to 37%, 27%, 30%, and 6% of the total deformation systems, respectively. Twinning was not observed for this test. This is different from the 728K tensile test performed on specimen C, where T1 twins were observed in some grains. Similar to that for the 728K tensile-tested specimen C, most of the slip deformation systems exhibited Schmid factors greater than 0.4.

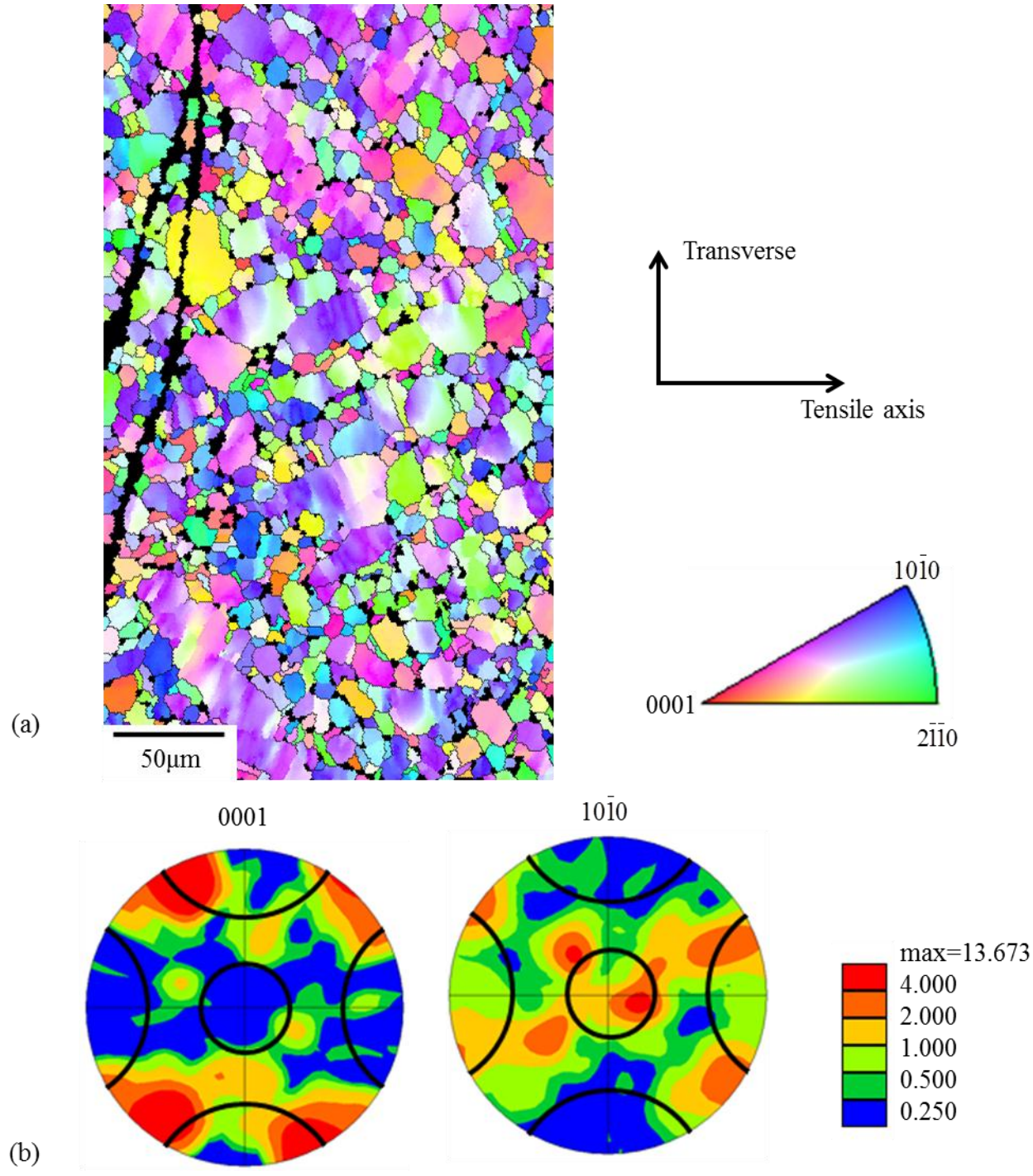

Figure 4.97 EBSD data of the Ti-6Al-4V 728K tensile-tested specimen D: (a) EBSD IPF map in the tensile direction of the α-phase Ti containing approximately 980 α grains, (b) the {0001} and the $\{10\bar{1}0\}$ pole figures with 30° cones along the major axes. The intentional scratch on the middle of the EBSD map was used as a fiducial marker. The loading direction was horizontal.

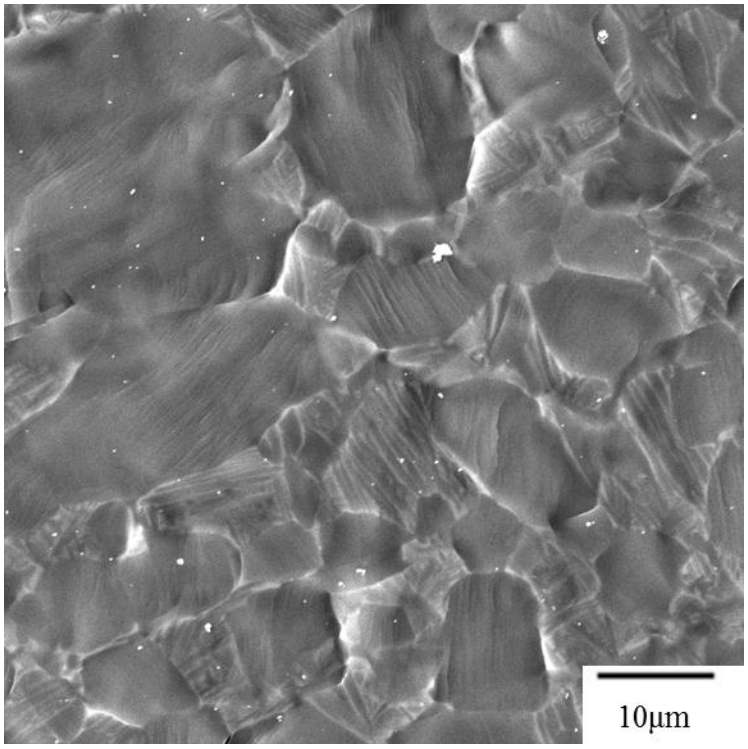

Figure 4.98 SE SEM image showing a tensile-deformed microstructural patch of Ti–6Al–4V specimen D at 728K after ~11.6% strain.

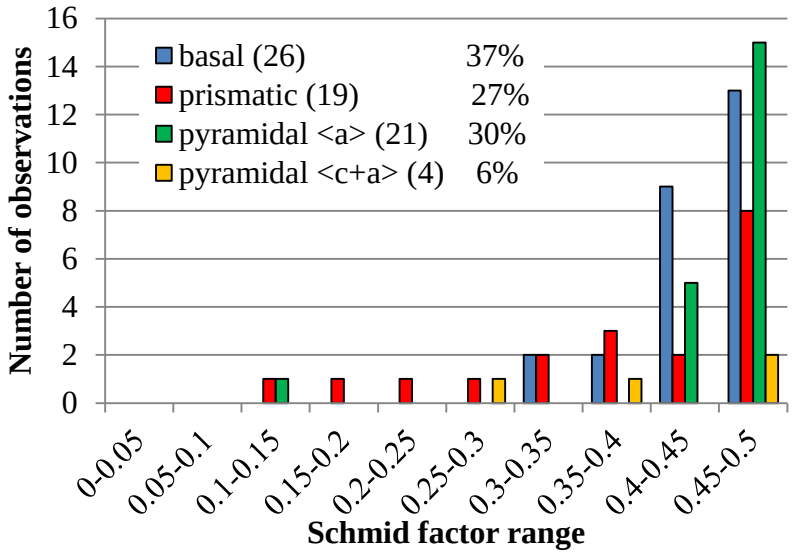

Figure 4.99 A histogram of the Schmid factor distribution of basal, prismatic, pyramidal <a>, and pyramidal <c+a> slip systems for the Ti-6Al-4V 728K tensile specimen D after ~11.6 % strain.

Figure 4.100 shows the stereographic triangles with the grain orientations plotted for basal, prismatic, pyramidal <a>, and pyramidal <c+a> slip with Schmid factor contours overlaid. The majority of the slip systems were activated in grains with high Schmid factors, which is similar to the observation made for the 728K tensile specimen C.

Overall, comparing specimen C and specimen D, it appeared that the texture had a strong effect on the active deformation modes. This will be discussed in Chapter 5.

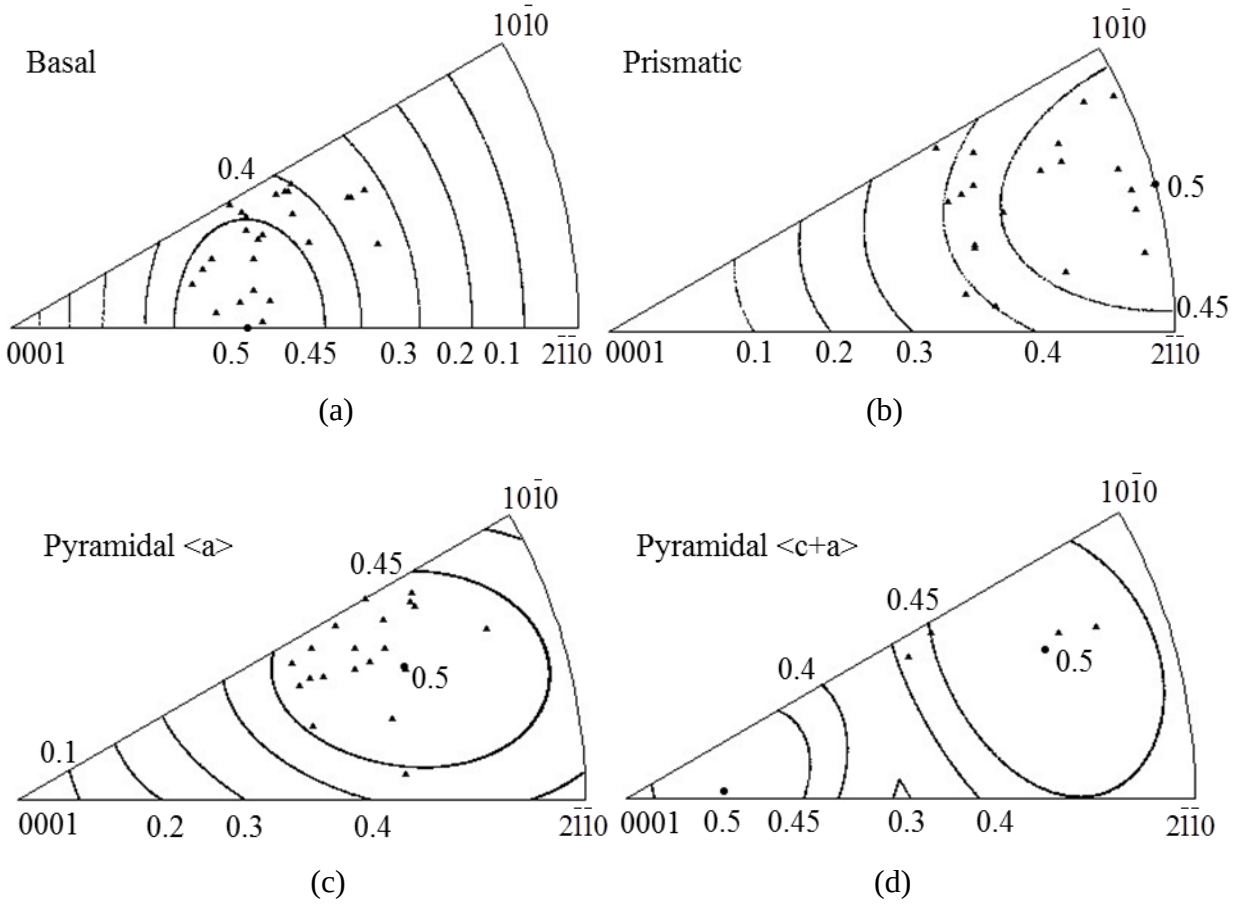

Figure 4.100 A histogram of the Schmid factor distribution of basal, prismatic, pyramidal <a>, and pyramidal <c+a> slip systems for the Ti-6Al-4V 728K tensile specimen D deformed to ~11.6% strain.

4.4.4 *In-situ* 728K-310MPa creep

One *in-situ* creep test was performed on Ti-6Al-4V at 728K with a constant stress of 310MPa, which was equivalent to 74% of the YS at 728K. Figure 4.101 shows the EBSD IPF map in the tensile direction and the corresponding {0001} and $\{10\bar{1}0\}$ pole figures acquired from the gage section of the 728K-310MPa creep-tested specimen. In Figure 4.101, there were approximately 1490 α grains which collectively exhibited an approximately 14 times random texture. The majority of the grains are soft orientations (blue orientations), indicating that this area was inside a macrozone dominated by soft orientations. The peak locations of the {0001} pole figure were within 30 ° of the transverse direction, where prismatic slip was favored for activation.

Figure 4.102 shows the sequential SE SEM images taken from the same area during the 728K-310MPa tensile-creep test. In Figure 4.102 (d), surface cracks were first observed at ~6.8% strain, prior to any noticeable surface slip trace formation. Grain boundary ledges, indicative of grain boundary sliding, were also apparent. No surface slip traces were observed after ~9.9% strain. The cross section of the creep-tested specimen was metallographically polished to investigate the subsurface cracking behavior. No cracks were observed in the interior of the sample (see Figure 4. 103), suggesting that the cracks observed in Figure 4.102 were localized at the specimen surface. Thus, the surface cracking phenomenon may have been related to the environment. This issue is expected to be addressed by future studies.

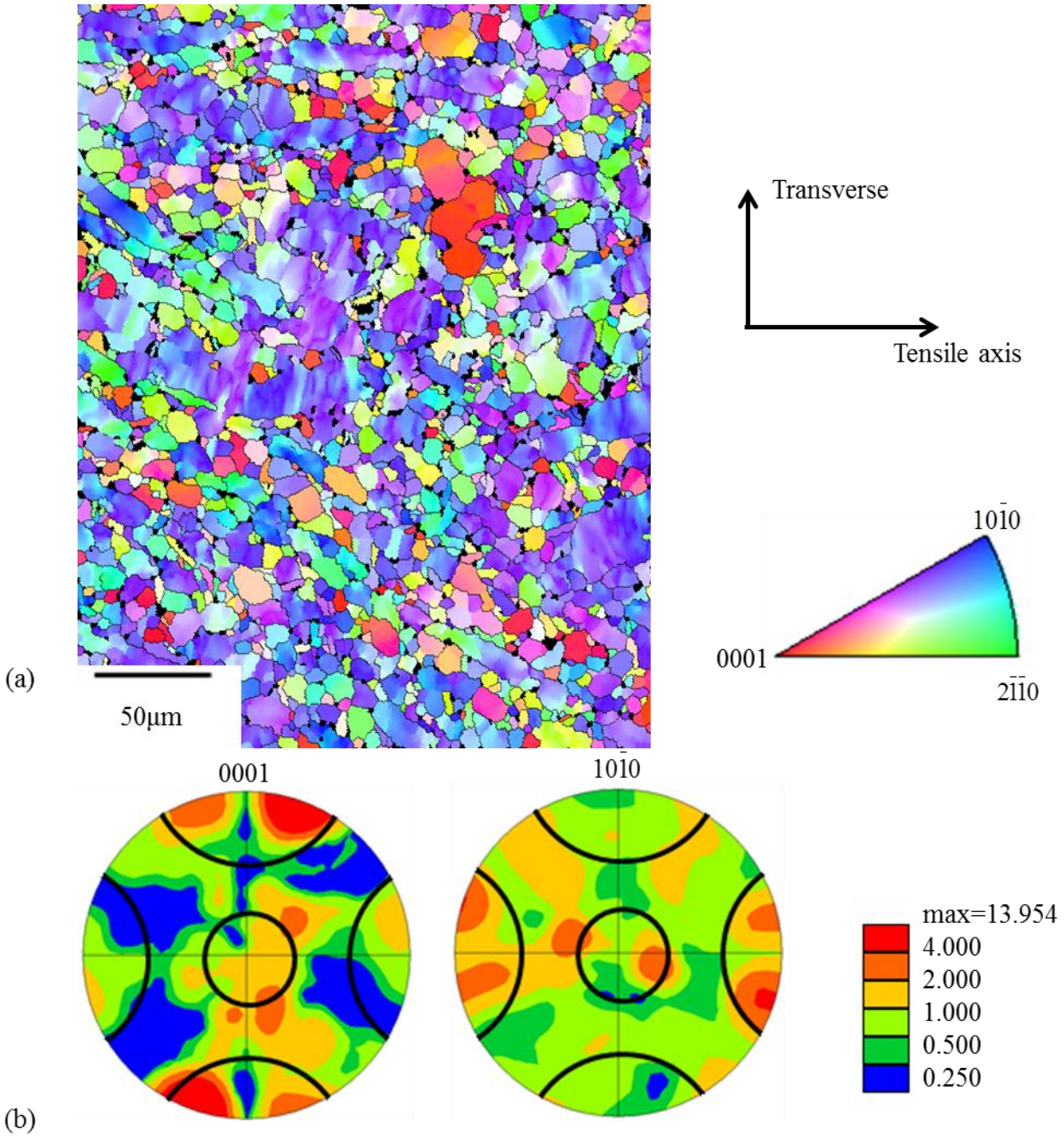

Figure 4.101 EBSD data of the Ti-6Al-4V 728K-310MPa tensile-creep tested specimen E: (a) EBSD IPF map in the tensile direction of the α-phase Ti containing approximately 1490 α grains, (b) the {0001} and the $\{10\bar{1}0\}$ pole figures with 30° cones along the major axes. The loading direction was horizontal.

(a)

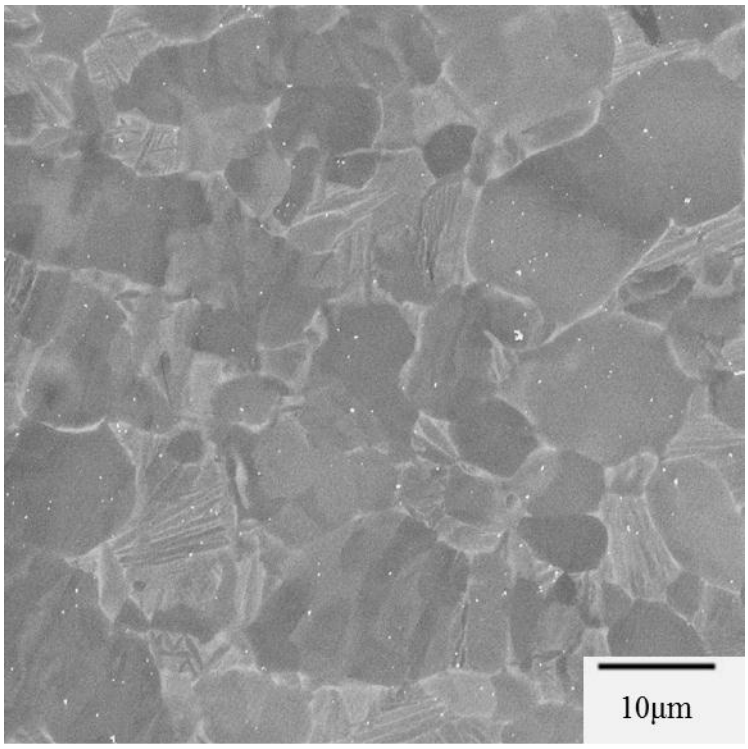

(b)

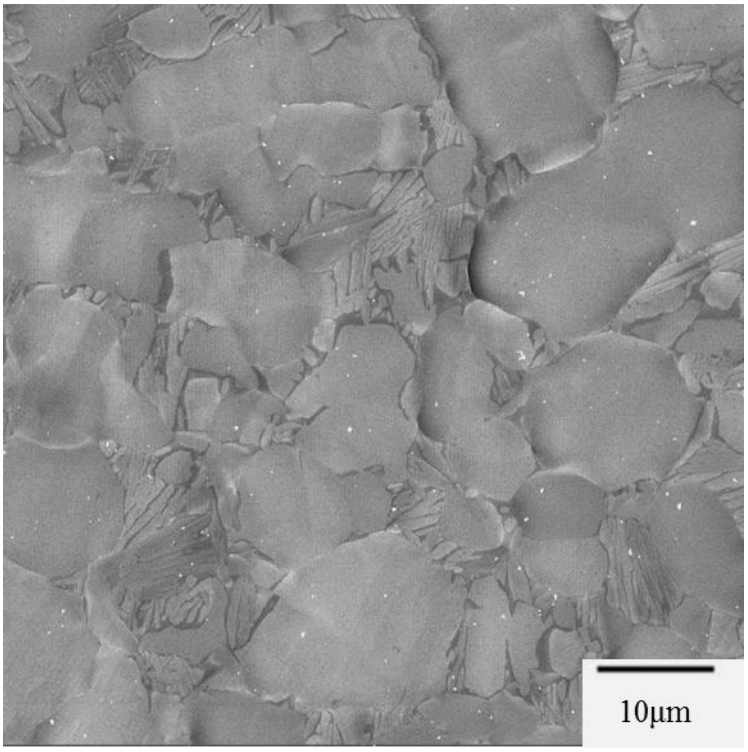

Figure 4.102 Sequential SE SEM images for Ti-6Al-4V tensile-creep tested at 763K-310MPa: (a) before loading; (b) ~3.2% strain, 16 h; (c) ~6.0% strain, 40 h; (d) ~6.8% strain, 64 h; (e) ~7.3% strain, 100 h; (f) ~9.9% strain, 148 h. The loading direction was horizontal.

Figure 4.102 (cont'd)

(c)

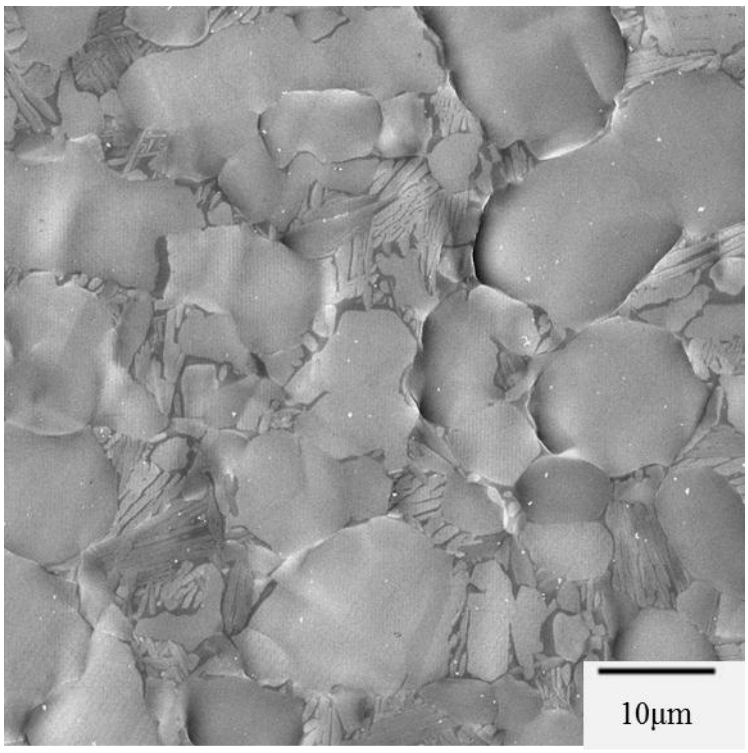

(d)

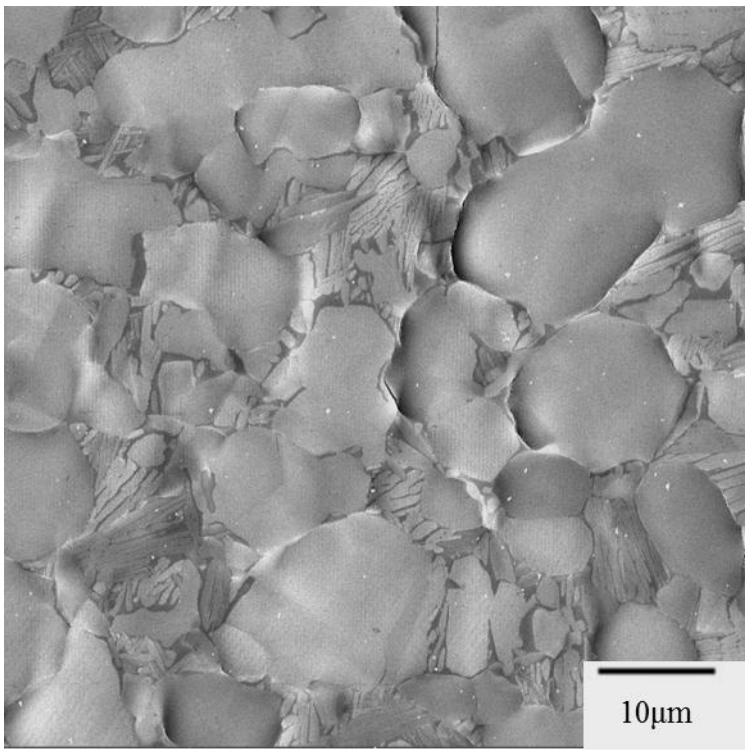

Figure 4.102 (cont'd)

(e)

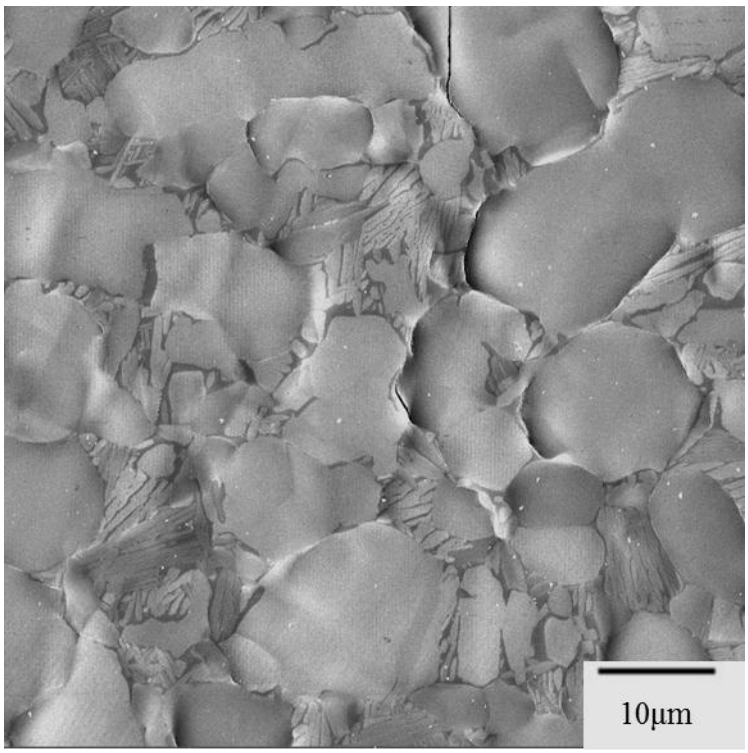

(f)

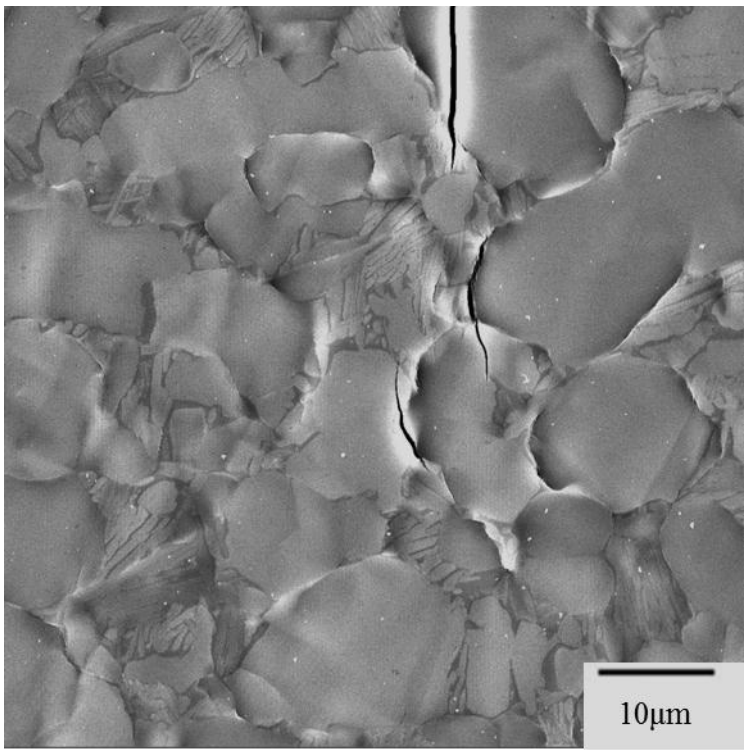

(a)

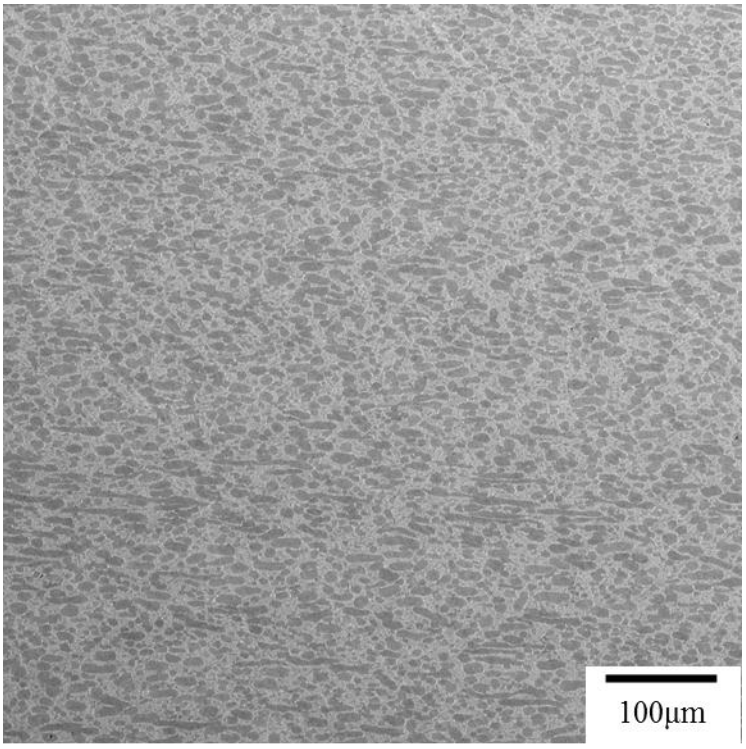

(b)

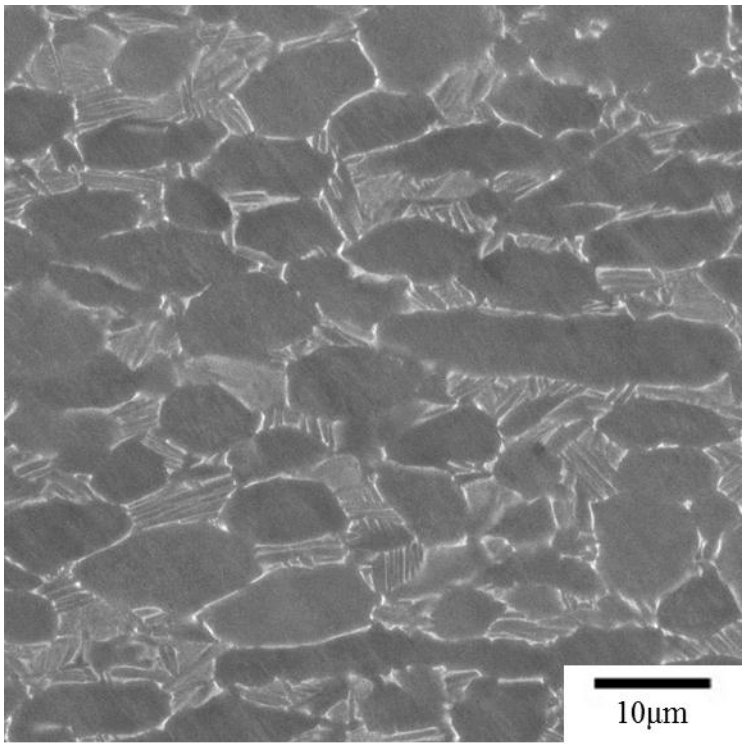

Figure 4.103 (a) Low- and (b) high-magnification BSE images of the polished cross section of the Ti-6Al-4V 728K-310MPa creep-tested specimen after ~9.9% strain.

CHAPTER 5

DISCUSSION

This chapter provides an analysis of the results presented in Chapter 4. This chapter also compares the deformation behavior of CP Ti, Ti-5Al-2.5Sn, Ti-3Al-2.5V, and Ti-6Al-4V. First the microstructure and texture of these four materials are compared. Then, the effect of temperature and alloying on the YS is discussed. Next the active deformation mechanisms for each material during tension and tensile-creep are discussed and compared. During the creep deformation of Ti-5Al-2.5Sn and Ti-6Al-4V, cracks were observed and the effect of local crystallographic orientations on the crack formation are discussed. Finally, for CP Ti and Ti-5Al-2.5Sn, a statistical analysis is carried out to assess the significance of the comparative activity of the different deformation systems under the tensile deformation conditions. Some content of this Chapter was published in two journal papers [Li H., Mason D.E., Yang Y., Bieler T.R., Crimp M.A., and Boehlert C.J., 2013, Comparison of the deformation behavior of commercially pure titanium and Ti–5Al–2.5Sn (wt.%) at 296 and 728 K, Philosophical Magazine, Vol.93, No.21, pp.2875-2895 and Li H., Boehlert C.J., Bieler T.R., and Crimp M.A., 2012, Analysis of slip activity and heterogeneous deformation in tension and tension-creep of Ti–5Al–2.5Sn (wt.%) using in-situ SEM experiments, Philosophical Magazine, Vol.92, No.23, pp.2923-2946.]. Therefore some content in Chapter 5 is similar to the published papers.

5.1 Microstructure

The phase volume percentages and grain sizes of the CP Ti, and the Ti-5Al-2.5Sn, Ti-3Al-2.5V, and Ti-6Al-4V alloys varied, see Table 5.1. The CP Ti and Ti-5Al-2.5Sn did not

contain any β-phase stabilizers. The CP Ti exhibited a fully-α microstructure and the Ti-5Al-2.5Sn exhibited a near-α microstructure with more than 99% α-phase. Figure 2.2 in Chapter 2 showed that an increase in the amount of β-phase stabilizers in Ti alloy leads to an increase in the β-phase volume fraction [Donachie 1988, Boyer 1996]. The β-phase volume percentages of Ti-3Al-2.5V and Ti-6Al-4V were 6.1%±1.1% and 18.2±3.2%, respectively. The morphology of the β phase also changed with composition. The β phase was globular in Ti-5Al-2.5Sn (see Figure 4.17 (c)), either striped or globular in Ti-3Al-2.5V (see Figure 4.57 (b)), and lamellar in Ti-6Al-4V (see Figure 4. 81 (b)). It is noted that different thermomechanical processes and heat treatments for Ti alloys can result in different phase volume percentages and morphologies [Donachie 1988, Boyer 1996]. For example, heat treatment of Ti-6Al-4V at 1228K for 1 hour followed by furnace cooling resulted in more than 80% primary α_p (with the remainder being β phase) without formation of lamellar microstructure [Semiatin et al. 2003]. This microstructure is different from the bimodal microstructure of the Ti-6Al-4V examined in the present work. Thus, the phase volume percentages and morphologies of the studied materials depend strongly on thermomechanical processing history.

Thermomechanical processing also affected the grain size. CP Ti (140.4±25.7μm) exhibited the largest grain size among all of the four materials examined. The grain size of Ti-5Al-2.5Sn was 39.5±10.0μm. Both Ti-3Al-2.5V and Ti-6Al-4V exhibited grain sizes less than 10μm. The grain sizes of Ti and Ti alloys can change due to thermomechanical processing history [Boyer 1996]. For example, by altering the cold-rolling reduction percentages and subsequent annealing temperatures and time, Ghaderi et al. [2011] obtained a variety of grain sizes, ranging from 6.6μm to 204μm, for CP Ti.

Table 5.1 Summary of the α and β phase volume percentages and grain sizes of the CP Ti, and the Ti-5Al-2.5Sn, Ti-3Al-2.5V, and Ti-6Al-4V alloys.

	CP Ti (fully α)	Ti-5Al-2.5Sn (near-α)	Ti-3Al-2.5V (near-α)	Ti-6Al-4V (α+β duplex)
α phase pct.	100%	>99%	93.9±1.1%	81.8%±3.2%
β phase pct.	0	<1%	6.1±1.1%	18.2±3.2%
Grain size	140.4±25.7μm	39.5±10.0μm	5.1±0.8μm	6.4 ±4.4μm

5.2 Yield Stress

The YS changed with alloy composition and testing temperature. At 296K, the YS of CP Ti was ~440MPa, the YS of Ti-5Al-2.5Sn was ~660MPa, the YS of Ti-3Al-2.5V was ~580MPa, and the YS of Ti-6Al-4V was ~820MPa. Compared to CP Ti, the increase in the YS of the alloys is mainly due to a combination of two factors. First, the Al, Sn, and V additions in the alloys increase the YS by solid-solution strengthening [Callister et al. 2009]. Second, compared to the grain size of CP Ti (140.4±25.7μm, see Table 5.1), the grain size of the alloys was much smaller, especially for Ti-3Al-2.5V (5.1±0.8μm) and Ti-6Al-4V (6.4 ±4.4μm). The grain size reduction can result in an increase in the YS [Callister et al. 2009]. With increasing temperature from 296K to 728K, the YSs of each of the materials decreased. At 728K, the YSs of CP Ti, Ti-5Al-2.5Sn, Ti-3Al-2.5V, and Ti-6Al-4V were ~62MPa, ~330MPa, ~250MPa, and ~420MPa, respectively. With increasing temperature, the YS of CP Ti decreased by a factor of ~7. However, the YSs of other materials only decreased by a factor of ~2. Overall, at both 296K and 728K, Ti-6Al-4V exhibited the highest YS among all the materials studied, which is consistent with previous data compiled for all these materials [Boyer et al. 1994].

5.3 Texture

The textures of the four materials examined in this work also varied. CP Ti exhibited a relatively weak fiber texture (at approximately 4 times random), see Figure 4.3, Figure 4.9, and Figure 4.13. Ti-5Al-2.5Sn also exhibited a weak texture (an approximately 4 times random) but lacked any symmetric texture characteristics (see Figure 4.20, Figure 4.25, Figure 4.30, Figure 4.38, Figure 4.43, and Figure 4.48). Unlike the weak textures of the CP Ti and the Ti-5Al-2.5Sn, the two Ti-3Al-2.5V plates examined in this work exhibited moderate textures (an approximately 5-6 times random). Ti-6Al-4V exhibited the strongest texture among all of the four materials studied (an approximately 10-14 times random).

To fully assess the deformation system activity as a function of testing condition, it is first necessary to understand the role of the underlying texture in biasing the activity of the different deformation systems. Since the majority of the active deformation systems were associated with Schmid factors greater than 0.4 in all the tensile and tensile-creep specimens, it is insightful to examine the potential number of each deformation system type exhibiting Schmid factors greater than 0.4 (resulting from texture) for each specimen and study how these potential number affected the deformation system activity. For each grain, there are 3 basal, 3 prismatic, 6 pyramidal <a>, 12 pyramidal <c+a>, and 6 T1 twinning systems (other twinning systems were not observed and therefore they were ignored in this analysis). The number of each of these deformation types with Schmid factors greater than 0.4 were determined for each grain in each of the microstructural patches examined. Note that since dislocation slip is bidirectional, this determination was based on the absolute values of the Schmid factors of the 24 dislocation slip systems, but because twinning is unidirectional, only those systems with positive Schmid factors were considered. Table 5.2 summarizes the ratio of the number of the deformation systems

exhibiting a Schmid factor of at least 0.4 for basal, prismatic, pyramidal <a>, pyramidal <c+a>, and T1 twins over the total number of deformation systems exhibiting a Schmid factor of at least 0.4 for all of the grains in the EBSD mapped areas for each individual specimens. For each row in Table 5.2, the ratios add up to 1.

For CP Ti, the ratios of the different deformation system types did not vary significantly from specimen to specimen (see Table 5.2). The ratios for basal and prismatic slip were similar (ratio of ~0.1) for all the tensile and tensile-creep specimens, indicating that both basal and prismatic slip systems were on average equally stressed in these specimens.

For Ti-5Al-2.5Sn, basal slip (~0.14) was slightly higher than prismatic slip (~0.08) and T1 twinning (~0.09) in tensile specimens. For the creep specimens, the ratios of basal slip, prismatic slip, and T1 twin were almost equivalent.

For Ti-3Al-2.5V, the ratios of the different deformation system types varied between plate 1 and plate 2, as shown in Table 5.2, indicative of the significant texture differences. For example, the prismatic slip ratios (0.16-0.18) for plate 1 were approximately twice the basal ratios (0.08), indicating that prismatic slip systems were on average more highly stressed in plate 1. However, in plate 2, the ratios for prismatic and basal slip were similar. The ratios for basal and T1 twinning also varied for different plates. In section 5.5.1, the effect of texture on the deformation system activation will be discussed.

For Ti-6Al-4V, both prismatic slip and T1 twin were more stressed than basal slip for the 296K tensile-tested specimens A and B. For the 728K tensile-tested specimen C, prismatic slip ratio was higher than basal slip. Compared to specimens A and B, the specimen C exhibited smaller ratio for T1 twin (0.18 for specimen A, 0.16 for specimen B, and 0.08 for specimen C). The 728K tensile-tested specimen D exhibited the same ratio for basal and prismatic slip (0.13)

but exhibited the smallest ratio for T1 twin (0.02) among all of the four tensile-tested specimens. Furthermore, specimen D exhibited the largest ratio (0.32) for pyramidal <a> slip among specimens A-D (see Table 5.2). These observations indicate that the texture of specimen D was distinct from specimens A, B, and C. This was also supported by Figure 5.1, where the IPFs of tensile direction for regions in which the slip trace analysis was performed for specimens A-D were plotted. As shown in Figure 5.1, the grain orientations of specimens A, B, and C were distributed near the <0001> and $<10\bar{1}0>$ corners. However, the grain orientations of specimen D were more concentrated in the middle of the IPF, where the Schmid factors of pyramidal <a> slip were high. Such texture differences should be taken into consideration when comparing the deformation modes of specimen D with the other tensile-tested specimens. In section 5.4.4, the results of specimens A, B, and C were chosen to compare the effect of temperature on the activation of the different deformation modes at 296K and 728K. The results of specimens C and D were chosen to compare the effect of texture on the activation of the different deformation modes.

Table 5.2 Ratio of deformation systems exhibiting a global Schmid factor of at least 0.4 for basal, prismatic, pyramidal <a>, pyramidal <c+a>, and T1 twins over the total number of deformation systems exhibiting a global Schmid factor of at least 0.4 for the undeformed microstructural patch characterized for each specimen.

Materials, testing conditions	basal	prismatic	pyramidal <a>	pyramidal <c+a>	T1 twin
CP Ti, 296K tension	0.08	0.10	0.20	0.44	0.18
CP Ti, 728K tension	0.12	0.11	0.19	0.46	0.13
CP Ti, 728K-45MPa creep	0.09	0.10	0.19	0.45	0.17
Ti-5Al-2.5Sn, 296K tension	0.14	0.08	0.18	0.49	0.10
Ti-5Al-2.5Sn, 728K tension	0.14	0.09	0.22	0.46	0.09
Ti-5Al-2.5Sn, 728K-250MPa creep	0.11	0.10	0.21	0.44	0.13
Ti-5Al-2.5Sn, 728K-300MPa creep	0.10	0.11	0.20	0.45	0.13
Ti-5Al-2.5Sn, 763K-200MPa creep	0.12	0.10	0.21	0.45	0.12
Ti-5Al-2.5Sn, 763K-250MPa creep	0.12	0.12	0.23	0.43	0.09
Ti-3Al-2.5V, 296K tension, plate 1	0.08	0.18	0.24	0.45	0.05
Ti-3Al-2.5V, 296K tension, plate 2	0.10	0.10	0.21	0.44	0.15
Ti-3Al-2.5V, 728K tension, plate 1	0.08	0.16	0.24	0.45	0.07
Ti-3Al-2.5V, 728K tension, plate 2	0.13	0.10	0.22	0.45	0.10
Ti-3Al-2.5V, 728K-180MPa creep, plate 1	0.09	0.17	0.24	0.45	0.05
Ti-6Al-4V, 296K tension, specimen A	0.06	0.11	0.18	0.47	0.18
Ti-6Al-4V, 296K tension, specimen B	0.07	0.12	0.20	0.45	0.16
Ti-6Al-4V, 728K tension, specimen C	0.10	0.14	0.23	0.45	0.08
Ti-6Al-4V, 728K tension, specimen D	0.13	0.13	0.32	0.40	0.02
Ti-6Al-4V, 728K-310MPa creep	0.06	0.14	0.29	0.42	0.08

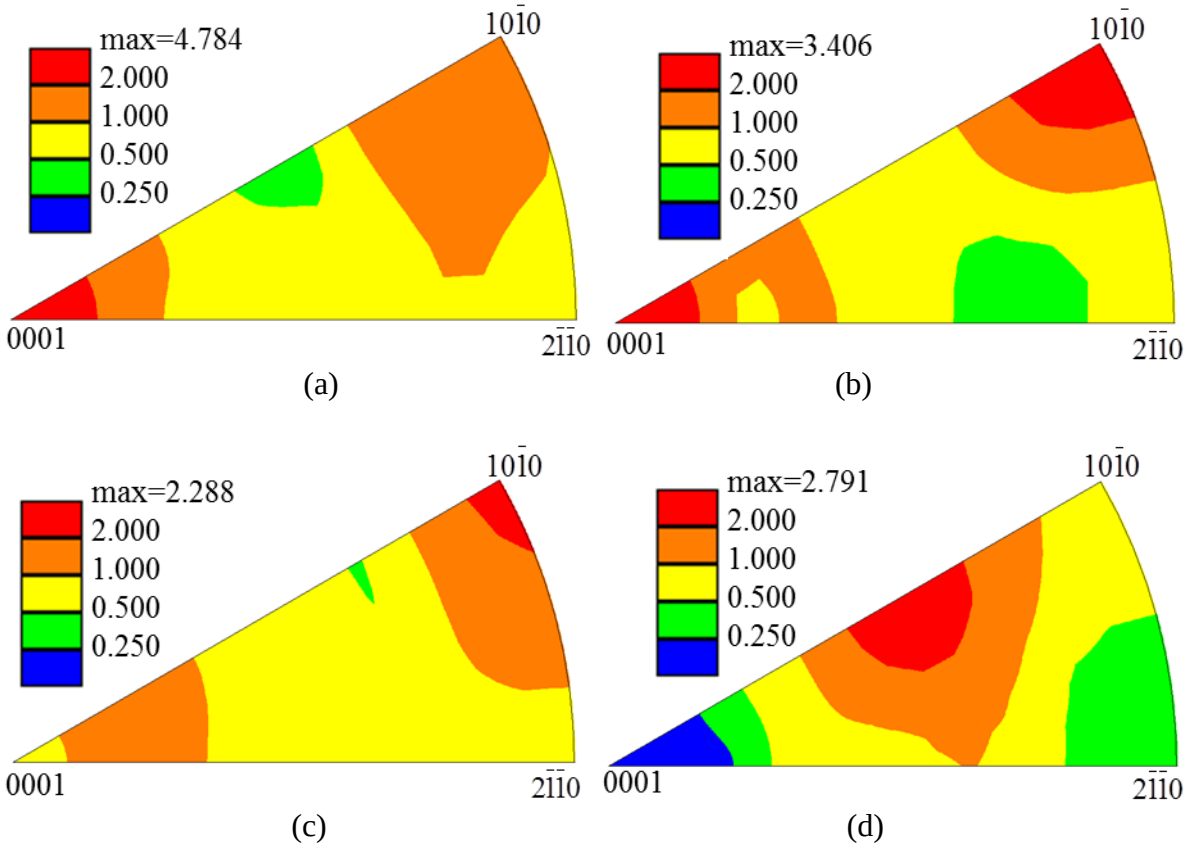

Figure 5.1 IPFs of tensile direction for regions in which slip the trace analysis was performed for Ti-6Al-4V (a) 296K tensile specimen A, (b) 296K tensile specimen B, (c) 728K tensile specimen C, and (d) 728K tensile specimen D.

5.4 Deformation mechanisms

In this section, the deformation mechanisms of the CP Ti, and the Ti-5Al-2.5Sn, Ti-3Al-2.5V, and Ti-6Al-4V alloys during tensile and tensile-creep experiments are discussed based on the results presented in Chapter 4. This section is divided into five subsections (i.e. 5.4.1 to 5.4.5). Subsections 5.4.1 to 5.4.4 represent the discussion for each of the above four materials. For each material, the dominant deformation mechanisms during the tensile and tensile-creep tests are discussed. In subsection 5.4.5, a comparison of the deformation mechanisms for all of the four materials investigated in this study is presented. The results of the current study are also compared with the literature in subsection 5.4.5.

5.4.1 CP Ti

Dislocation slip was the major deformation mechanism observed in both the tensile and tensile-creep tests. Table 5.3 lists the distribution of the deformation modes at 296K and 728K. During tension, at least 80% of grains exhibited slip traces and GBS was not prevalent. The percentage of observations for each deformation mode did not change significantly with increasing temperature, indicating that the relative activity of the deformation modes is not sensitive to temperature. This hypothesis is assessed statistically in section 5.5. Similar to that observed in the tension tests, extensive dislocation slip was observed during the creep test and GBS was not prevalent.

Prismatic slip was commonly observed in both the tensile and tensile-creep tests at both 296 and 728K (see Table 5.3, Figure 4.7, Figure 4.11, and Figure 4.15). More than 61% of the total deformation systems were identified to be prismatic slip for each specimen. This is consistent with previous studies which showed that prismatic slip is significantly easier to activate than other deformation modes in CP Ti [Yoo et al. 1981, Gong et al. 2009, Conrad 1981, Akhtar et al. 1975, Zaefferer 2003, Williams et al. 2002].

Prismatic slip was also activated over a large global Schmid factor range (0-0.05). The activation of prismatic slip systems with relatively low Schmid factor suggests that the local stress state can vary from the global stress tensor. If the global stress was realized in each grain, then all the same type of slip systems with equivalent Schmid factors would activate simultaneously at a given stress level. Analysis of the images where slip traces were first observed in each specimen (see Figure 4.4 (b) and Figure 4.10 (b)) indicates that this was not the case. The factor most likely responsible for this is the heterogeneity of the local stress tensor, which has been demonstrated in crystal plasticity computational simulations of microstructural

patches [Yang et al. 2011, Molinari et al. 1987, Prakash et al. 2009, Kanjarla et al. 2010, and Kalidindi et al. 2004]. In the heterogeneous deformation caused by differential deformation processes in adjacent grains, the variation in local strains affects the local stress tensor. While slip systems with high Schmid factors are observed more often, the presence of the observed slip systems with low global Schmid factors is an indirect indicator of the heterogeneous stress states and the ease of nucleation of deformation systems that can accommodate required geometric changes [Yang et al. 2011, Molinari et al. 1987, Prakash et al. 2009, Kanjarla et al. 2010, Kalidindi et al. 2004].

The relative activity of other deformation systems, such as pyramidal <a> and twinning, changed with the testing conditions. Comparing the 728K tension test with the 728K-45MPa tensile-creep test, there was a slight decrease in the relative extent of pyramidal <a> slip activity in the 728K-45MPa creep test, suggesting that the CRSS of pyramidal <a> slip may have increased as a result of the lower strain rate creep experiment condition. Twinning was frequently observed in the CP Ti tensile deformed at 296K and 728K. In contrast, the twinning activity during creep was much less than that in the high strain rate tensile test at 728K. This implies that strain rate plays an important role in the elevated temperature deformation behavior for CP Ti.

Table 5.3 Distribution of the observed deformation systems in CP Ti.

Test mode, Approx. strain	(%) of grains showing slip traces	Deformation mode					
		Dislocation slip					Grain boundary ledges/sliding
		Basal (%)	prismatic (%)	pyr<a> (%)	pyr <c+a> (%)	twin (%)	
296K tension ~8.4%	~80%	11	61	5	13	10	Not prevalent
728K tension ~11.2%	~90%	9	61	6	13	11	Not prevalent
728K-45MPa creep ~23.2%	~97%	9	64	14	10	3	Not prevalent

5.4.2 Ti-5Al-2.5Sn

For Ti-5Al-2.5Sn, dislocation slip and GBS were the two major deformation mechanisms observed in this study (see Table 5.4). At least 93% of the α grains exhibited slip traces in the 296K and 728K tension experiments, while the percentage of grains that displayed slip traces was much smaller in the elevated-temperature creep experiments. During the creep experiments, GBS was more active, as evidenced by the observed grain boundary ledges (see Figure 4.31, Figure 4.39, Figure 4.44, and Figure 4.49). The highest-stress creep experiment (728K-300MPa) appeared to be near the transition between these two processes (i.e. dislocation slip and GBS) as the percentage of grains which exhibited slip traces was similar to that observed in the tension experiments (i.e. 86% in the 728K-300MPa creep sample and ~94% in the 728K tension sample, see Table 5.4). The lower-stress creep experiments, for which a significantly lower fraction (10%-15%) of grains exhibited slip traces (see Table 5.4), revealed more extensive grain boundary ledge formation compared to the higher-stress creep experiments. This is consistent with the work of Lüthy et al. [1979] which indicated (using deformation mechanism maps) that GBS tended to be the dominant deformation mechanism, relative to dislocation glide and power law creep, at lower stresses.

In addition to the change in the dominant deformation mechanisms with applied stress and temperature, the relative activation of the different slip systems also changed with testing condition. During the tensile tests, the observed basal and prismatic slip systems were almost equal in number, but prismatic slip was activated within a larger Schmid factor range (see Figure 4.23 and Figure 4.27). This could be explained by the fact that the prismatic slip systems with low Schmid factors usually activated later in the deformation process and were found to be localized at the grain boundaries and triple points, suggesting these low Schmid factor systems were activated under local stress concentrations to accommodate the local strain. Nevertheless, the relative activation of basal and prismatic slip systems was affected by the applied stress level during the creep deformation. At the same creep temperature, as the stress level decreased, the overall amount of observed dislocation slip activity decreased, but the amount of basal slip system activation increased relative to the observation of prismatic slip.

Cracks were found at both grain boundaries and triple points in all of the four tensile-creep tested specimens. For cracks that formed at grain boundaries, most were observed in association with grain boundaries that had at least one of the two neighboring grains in a hard orientation, where the c-axis was within 30° of the loading direction, as shown in Figure 5.2 (a). Likewise, cracks that formed at triple points were also found to form in association with at least one grain having a c-axis oriented within 30˚ of the loading axis, as shown in Figure 5.2 (b). Because the hard-oriented grains were more difficult to deform than the surrounding grains, incompatibilities were expected to develop at the boundaries, leading to large local stress gradients and cracking. Grain boundary cracking associated with hard-oriented grains has also been observed in hot deformation of Ti-6Al-4V and analyzed using self-consistent models [Bieler et al. 2005a and 2005b].

Table 5.4 Distribution of the observed deformation systems in Ti-5Al-2.5Sn.

Test mode, Approx. strain	(%) of grains showing slip traces	Deformation mode					
		Dislocation slip					Grain boundary ledges/sliding
		Basal (%)	prismatic (%)	pyr<a> (%)	pyr <c+a> (%)	twin (%)	
296K tension ~3.5%	~93%	42	50	3	4	1	Not prevalent
728K tension ~9%	~97%	42	47	5	6	0	Not prevalent
728K-250MPa creep ~16.5%	~10%	78	16	2	4	0	Prevalent
728K-300MPa creep ~21.4%	~86%	45	49	4	3	0	Prevalent
763K-200MPa creep ~24.8%	~15%	74	24	2	0	0	Prevalent
763K-250MPa creep ~15.3%	~67%	55	39	5	2	0	Prevalent

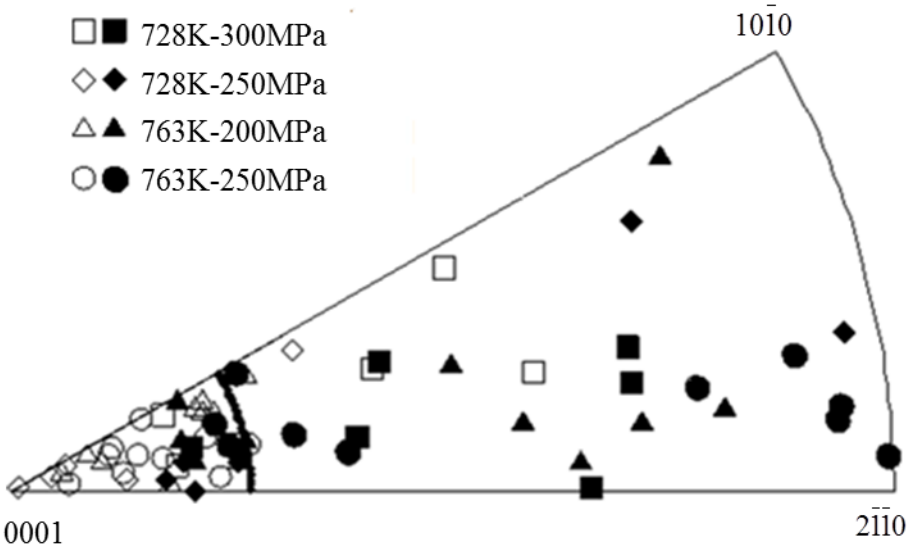

(a) Grain boundary crakcs

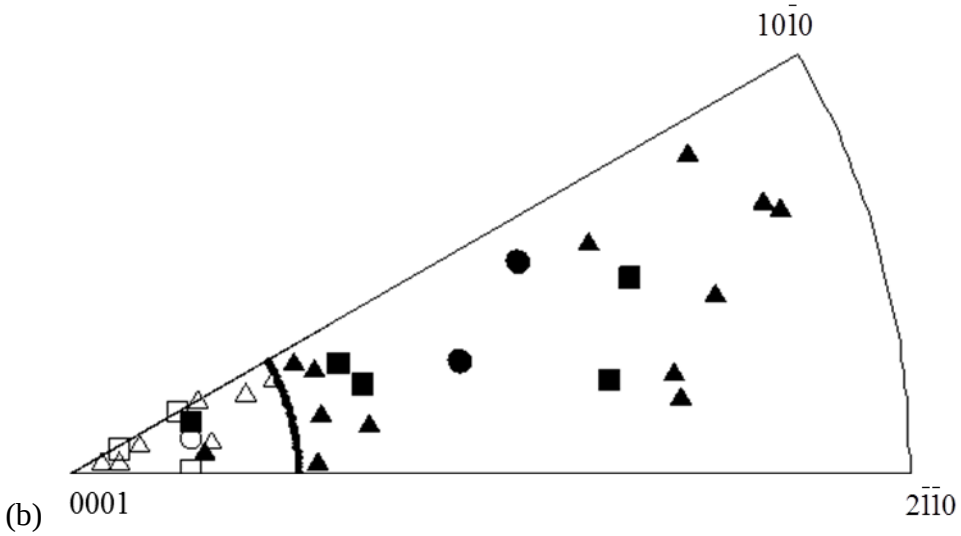

(b) Triple point cracks

Figure 5.2 Unit triangle plots of grain orientations associated with (a) grain boundary cracks and (b) triple point cracks in four Ti-5Al-2.5Sn creep specimens, open symbols represent relatively hard orientations and close symbols represent relatively soft orientations in a pairs of grains or a group of grains, arc represents the orientations which has its c-axis 30 degrees away from the loading direction.

5.4.3 Ti-3Al-2.5V

As shown in Table 5.2 in section 5.2 that there were significant texture variations between plate 1 and plate 2 of the Ti-3Al-2.5V alloy, these texture variations may affect the deformation system activation. In Table 5.2, the prismatic slip ratios (0.16-0.18) for plate 1 were approximately twice the basal ratios (0.08), indicating that prismatic slip systems were on average more highly stressed in plate 1. However, in plate 2, the ratios for prismatic and basal slip were similar. The differences between these prismatic and basal Schmid factor ratios in plates 1 and 2 explain the much higher percentages of prismatic slip activity observed at the 296K and 728K tensile tests for plate 1 compared to plate 2 under the same testing conditions. Moreover, the ratios for basal slip in plate 1 (0.08) were somewhat lower than the ratios in plate 2 (0.10-0.13), consistent with the decreased basal activity observed in plate 1 (2% at 296K, 6% at 728K) relative to plate 2 under the same testing conditions (8% at 296K, 14% at 728K). Likewise, the ratios for T1 twinning in plate 1 (0.05-0.07) were much lower than in plate 2 (0.10-0.15), consistent with the reduced twin activity in plate 1 (10% at 296K, 4% at 728K) in comparison to plate 2 tested under the same conditions (23% at 296K, 6% at 728K). Therefore, much of the differences of the deformation system activity observed in plate 1 and plate 2 were resulted from the significant texture variations.

Prismatic slip was the dominant deformation system observed in Ti-3Al-2.5V, accounting for at least 48% of the observed deformation systems, as summarized in Table 5.5. Prismatic slip was also the preferred deformation mode in CP Ti [Gong et al. 2009, Zaefferer 2003, Wang et al. 2011, Zeng et al, 2009, Farenc et al. 1993]. For Ti-3Al-2.5V, basal slip accounted for no more than 14% of the total deformation modes observed for all the specimens tested. As noted above, the texture of plate 1 favored the activation of prismatic slip while the texture of plate 2 almost equally stressed the basal and prismatic slip systems. For CP Ti, where basal and

prismatic slip were equally favored for activation based on the texture, basal activity only accounted for 10% of the deformation systems for the 296K and 728K tensile experiments. However, extensive basal activity has been observed in recent studies on Ti-5Al-2.5Sn [Li et al. 2013, Seal et al. 2012, Pilchak et al. 2010], Ti-6Al-4V [Bridier et al. 2005], and Ti-6Al [Neeraj et al. 2000]. It also has been shown that the basal slip activity increases with increasing Al content [Williams et al. 2002, Li et al. 2013]. Thus, the relatively low activity of basal slip observed in this study may be attributed to the lower Al content in Ti-3Al-2.5V compared with Ti-5Al-2.5Sn, Ti-6Al-4V, and Ti-6Al.

Twinning was an active deformation system during the 296K and 728K tension experiments in the Ti-3Al-2.5V alloy evaluated. The addition of Al has been shown to suppress twinning in single crystal Ti-Al alloys [Paton et al. 1976, Williams et al. 2002] and polycrystalline Ti alloys [Zeafferer 2003]. Therefore, it might be reasonable to expect less twinning activity in Ti-3Al-2.5V than in CP Ti. However, for CP Ti tensile deformed at 296K in this work, about 10% of the observed deformation systems were T1 twins, which is smaller than the 23% in the Ti-3Al-2.5V plate 2 tensile tested at 296K. Note that the ratio of twinning systems with Schmid factors greater than 0.4 out of the total number of deformation systems with Schmid factors greater than 0.4 was similar in the CP Ti (0.18) and the Ti-3Al-2.5V plate 2 tested at 296K (0.15). Zaefferer [2003] reported that Ti with 0.1 wt.% (1000ppm) O was found to exhibit larger twinning activity than that with 0.2 wt.% (2000ppm) O. Thus, the relatively high twinning activity observed in the Ti-3Al-2.5V alloy in the present study may be due to the low O content (0.085 wt.% for plate 1 and 0.092 wt.% for plate 2, see Table 3.1), compared to the CP Ti with 0.25 wt.% O.

Table 5.5 Distribution of the observed deformation systems in Ti-3Al-2.5V.

Test mode, Approx. strain Specimen	(%) of grains showing slip traces	Deformation mode					
		Dislocation slip					
		Basal (%)	prismatic (%)	pyr<a> (%)	pyr <c+a> (%)	twin (%)	surface relief
296K tension, ~6.5%, plate 1	~15%	2	80	7	2	9	heterogeneous
296K tension, ~10.5%, plate 2	~25%	8	48	15	6	23	heterogeneous
728K tension, ~9.7%, plate 1	~45%	6	67	17	6	4	heterogeneous
728K tension, ~16.2%, plate 2	~54%	14	49	25	6	6	heterogeneous
728K-180MPa creep ~11.7%, plate1	~3%	4	70	17	9	0	homogenous

During creep, grain boundary sliding appeared to be more active than dislocation slip. Using the calculated mechanistic creep parameters (i.e. the stress exponent and activation energy) of Ti-3Al-2.5V samples, Gollapudi et al. [2008] concluded that grain boundary sliding was an active deformation mechanism in an intermediate stress regime ($0.6\times10^{-3}\ \sigma/E \sim 3\times10^{-3}\ \sigma/E$) in the temperature range of 723K-873K. The normalized stress value in Gollapudi's work was estimated considering the dependence of Young's Modulus on temperature (°C) [Fisher et al. 1964]:

$$E\ (GPa) = 130.55 - 0.0777T \qquad (5.1)$$

Using this equation to normalize the creep stress, the testing condition in the present work ($\sim1.6\times10^{-3}\ \sigma/E$, 728K) was similar to that in the Gollapudi et al. [2008] study. The *in-situ* observations of grain boundary ledge formation combined with limited slip traces in the current study provided evidence that GBS is an important deformation mechanism in the intermediate stress regime of Ti-3Al-2.5V.

The surface relief from the grain boundary sliding evident during creep was different than the surface relief observed during the tension experiments (compare Figures 4.61, 4.66, 4.70, and 4.74, and 4.78). The surface relief observed during the tensile tests occurred for some cluster of grains and was more heterogeneous while the grain boundary sliding in the creep test was observed for almost all of the grains and occurred more homogenously throughout the sample gage length. The reason for this is that during the lower applied stress (i.e. lower $\dot{\varepsilon}$) creep experiment (~250hrs), more diffusion was allowed to occur, resulting in more homogenous grain boundary sliding, compared to the 2-hour tensile experiments.

5.4.4 Ti-6Al-4V

For Ti-6Al-4V, dislocation slip and GBS were the two major deformation mechanisms observed (see Table 5.6). During the 296K tension tests, at least 50% of the α_p grains exhibited slip traces and GBS was not prevalent. With increasing temperature from 296K to 728K, both dislocation slip and GBS were active, indicating that GBS became more active at elevated temperature. However, no slip traces were observed in the 728K-310MPa creep test. Instead, GBS was prevalent.

For specimens A, B, and C tensile tested at 296K and 728K, both basal and prismatic slip were the primary deformation modes as together they comprised at least 80% of the total deformation systems (see Table 5.6). For these three specimens, more than 95% of the basal and prismatic slip systems were activated with Schmid factors greater than 0.3. This suggests that the activation of these two deformation modes was highly influenced by the global stress state. Although both basal and prismatic slip were the primary deformation modes, the relative activity of these two slip systems changed with temperature. At 296K, the percentages of basal slip were

smaller than prismatic for both specimen A and B. With increasing temperature to 728K, the percentages of basal slip were found to be higher than prismatic slip, indicating that basal slip was easier to activate with increasing temperature (see Table 5.6). Note that for specimens A, B, and C, there were more prismatic slip systems favored for activation than basal slip based on the texture (see Table 5.1). The CRSS ratios of these two deformation systems will be assessed in Chapter 6. Pyramidal <a> and pyramidal <c+a> slip were also observed at both 296K and 728K in the tensile deformed specimens A, B, and C. The percentages of these two slip systems did not change significantly with increasing temperature.

Twinning was an active deformation mode during the 296K and 728K tensile tests of specimens A, B, and C for Ti-6Al-4V. This is consistent with previous studies on polycrystalline Ti-6Al-4V that twinning has been reported during deformation under very high strain rates of 1000 s^{-1} at RT [Johnson et al. 2003] and 1 s^{-1} at 1073K [Yapici et al. 2006] as well as for a low strain rate of 10^{-6} s^{-1} at RT [Prakash et al. 2010]. Note that the strain rate of the tensile tests in the current study was 10^{-3} s^{-1}. Twinning has also been reported for monotonic tensile deformation of Ti-6Al-4V at 20K (no strain rate value was given) [Di Iorio et al. 2004 and 2007]. However, the observation of twinning activity in Ti-6Al-4V is in contrast with previous studies on single crystals of Ti alloyed with 6 wt.% Al where twinning was not observed [Williams et al. 2002, Paton et al. 1976]. The grain size and lack of grain boundaries for single crystal materials may have contributed to this behavior.

Texture played an important role in the activation of the different deformation modes. For specimen C, where both soft and hard orientations were present and 7% of the deformation systems favored twinning activation based on the texture (see Table 5.1), 4% of the total active

deformation systems were identified to be twins after ~10.2% strain. For specimen D, where soft orientations dominated and only 2% of the deformation systems favored twinning activation based on the texture (see Table 5.1), twinning was not observed after ~11.6% strain. Therefore, the absence of twinning in specimen D was most likely due to the fact that the texture of specimen D did not favor twinning activation. Furthermore, because that pyramidal <a> slip systems were not strongly stressed for activation in specimen C compared with specimen D based on the texture (see Figure 5.1 and Table 5.1), much higher fraction of pyramidal <a> slip activity was observed in specimen D than specimen C.

Table 5.6 Distribution of the observed deformation systems in Ti-6Al-4V.

Test mode, Approx. strain	(%) of α_p grains showing slip traces	Deformation mode					
		Dislocation slip					Grain boundary ledges/sliding
		Basal (%)	prismatic (%)	pyr<a> (%)	pyr <c+a> (%)	T1twin (%)	
296K tension ~6.3%, specimen A	~50%	36	47	8	6	3	Not prevalent
296K tension ~8.2%, specimen B	~82%	40	43	6	9	2	Not prevalent
728K tension ~10.2%, specimen C	~76%	54	31	7	5	4	Somewhat prevalent
728K tension ~11.6%, specimen D	~60%	37	27	30	6	0	Somewhat prevalent
763K-310MPa creep, ~9.9%	~0%	-	-	-	-	-	Prevalent

It is noted that the majority of the deformation systems were observed in α_p grains, rather than the α+β lamellar colonies. This may be due to two reasons. First, although it is possible that the α/β phase boundaries in the lamellar colonies may act as nucleation sites for dislocations,

more dislocations may have been absorbed by the extra α/β phase boundaries inside the colonies, compared to the α_p grains, which did not contain interior phase boundaries. Second, due to continuity requirement of dislocation slip, the lamellar arrangement of the β phase and the α_s phase in Ti-6Al-4V may act as barriers to restrict the propagation of slip activity [Morrissey et al. 2001, Kim et al. 2004].

5.4.5 Comparison of the deformation mechanisms

5.4.5.1 Comparison of the tensile deformation mechanisms

Dislocation slip was the primary tensile deformation mechanism observed in the tensile tests for all of the four materials evaluated (i.e. CP Ti, Ti-5Al-2.5Sn, Ti-3Al-2.5V, and Ti-6Al-4V). However, the relative activity of the different deformation modes changed as a function of alloy composition and temperature. Prismatic slip was commonly observed for all of the four materials, and it comprised at least 61% of the total deformation systems for CP Ti, 47% for Ti-5Al-2.5Sn, 48% for Ti-3Al-2.5V, and 27% for Ti-6Al-4V, see Table 5.3, Table 5.4, Table 5.5, and Table 5.6. However, basal slip was more active in Ti-5Al-2.5Sn and Ti-6Al-4V. Extensive basal slip has also been observed in Ti–6Al–4V [Bridier et al. 2005] and Ti–6Al [Neeraj et al. 2000]. These observations, along with the current work, are consistent with prior work that showed that as the *c/a* ratio increases with increasing Al content [Teer et al. 1977, Buckley et al. 1966], the basal plane becomes more closely packed and thus more favorable for slip, while the prismatic planes become less closely packed and less favorable for slip. Higher Al content also results in a decrease in the stacking fault energy on the basal planes, and thus, dislocation movement is increasingly restricted to the basal planes [Zaefferer 2003].

The relative activity of pyramidal <a> and pyramidal <c+a> also changed with alloying. The pyramidal <a> slip system comprised less than 8% of the total deformation systems in CP Ti, Ti-5Al-2.5Sn, and Ti-6Al-4V (specimens A, B, and C) at both 296K and 728K. In contrast, for Ti-3Al-2.5V specimens from plate 2, pyramidal <a> slip comprised at least 15% of the total deformation systems. These observations suggest that the CRSS of pyramidal <a> in Ti-3Al-2.5V is the lowest among all the materials examined in this work. This is supported by the CRSS ratio calculation results of the different deformation modes for the four different materials in Table 6.10 in Chapter 6. Compared to the alloys, there was slightly more pyramidal <c+a> slip activity in CP Ti at both 296K and 728K, suggesting that the CRSS of pyramidal <c+a> slip may increase with alloying content. The relative CRSS ratios will be calculated to justify this statement in Table 6.10 in Chapter 6.

Alloying suppressed twin formation. Twins were only evident in a few grains for Ti–5Al–2.5Sn deformed at 296K (about 1%) and for Ti-6Al-4V deformed at both 296K and 728K (no more than 4%). However, twinning was more frequently observed in CP Ti and Ti-3Al-2.5V deformed at 296 and 728K and it comprised at least 9% of the total deformation systems. The observation of the lack of deformation twinning in polycrystalline Ti–5Al–2.5Sn and Ti-6Al-4V is therefore consistent with the observations of Williams et al. [2002], who showed that twinning was inhibited by the ordering of Al in the α phase. It is noteworthy that for the Ti-3Al-2.5V plate 2 tensile deformed at 296K, twinning comprised 23% of total deformation systems, which was significantly greater than that in CP Ti, where twinning only comprised 10% of the total deformation systems. As mentioned previously, the relatively high twinning activity in Ti-3Al-2.5V may be due to the low O, which is also known to enhance twinning [Zeafferer 2003]. The CP Ti in this work contained 0.25 wt.% O, which was significantly greater than the 0.092 wt.%

O of the Ti-3Al-2.5V plate 2. For Ti-6Al-4V, which contained 0.24 wt.% O, much less twinning activity was observed, compared to CP Ti and Ti-3Al-2.5V. This may be due to the high O and Al content present in this material.

In addition to the change of the relative activity of the different deformation modes of these four materials as a function of alloying, the relationship between the activation of these deformation systems and the associated global Schmid factors also varied. Although the local stress state can vary between individual grains and within grains due to stress concentrations, inhomogeneities, etc., the Schmid factor is an important parameter that is typically correlated with the activation of a particular deformation mode. For both Ti-3Al-2.5V and Ti-6Al-4V, only 2-9% of the activated deformation systems in the tension tests exhibited Schmid factors below 0.3, which is unlike that observed for the tension tests performed on Ti-5Al-2.5Sn (<1% β phase, 39.5±10.0μm α grain size) and CP Ti (140.4±25.7μm α grain size), where 13-21% of the activated deformation systems activated with Schmid factors smaller than 0.3. This suggests that local stress concentrations are less likely to build up in the Ti-3Al-2.5V alloy, compared to the CP Ti and Ti-5Al-2.5Sn. This may be due to two reasons. First, Ti-3Al-2.5V (6.1±1.1% β phase) and Ti-6Al-4V (18.2±3.2% β phase) exhibited a larger volume fraction of the soft β phase than CP Ti and Ti-5Al-2.5Sn (<1% β phase), and the soft β phase may act to mitigate stress concentrations during deformation. Indeed, observations have shown that the β phase, with a large number of slip systems, can readily accept slip transfer from the harder α phase [Seal et al. 2012]. Second, compared to CP Ti and Ti-5Al-2.5Sn, Ti-3Al-2.5V and Ti-6Al-4V exhibited a finer grain size (see Table 5.1), which is also effective in reducing stress concentrations [Lasalmonie et al. 1986]. More observations of slip system activation associated with high Schmid factors for Ti-6Al-4V in the present study are also consistent with previous work on Ti-

6Al-4V by F. Bridier et al. [2005]. Their alloy exhibited a grain size similar to that for the Ti-6Al-4V evaluated in this study and found that less than 95% of the basal and prismatic slip systems were activated with Schmid factors below 0.3.

5.4.5.2 Comparison of the tensile-creep deformation mechanisms

During the elevated-temperature tensile-creep tests, the relative activity of dislocation slip and GBS varied from material to material. During the 728K-250MPa creep deformation of Ti-5Al-2.5Sn, 728K-180MPa creep deformation of Ti-3Al-2.5V, and 728K-310MPa creep deformation of Ti-6Al-4V, GBS appeared to be the primary deformation mechanism rather than dislocation slip. Although the ratio of the applied creep stress to the YS was similar in CP Ti (0.73), Ti-5Al-2.5Sn (0.76) Ti-3Al-2.5V (0.72), and Ti-6Al-4V (0.74), dislocation slip, rather than GBS, was the dominant deformation mechanism in CP Ti creep. It has been reported that finer grain sizes enhance GBS [Zelin et al. 1992, Langdon 1970, and Chokshi 1990]. Thus, the deformation mechanism difference between the four materials during creep may be partially explained by the grain size difference between these four materials (see Table 5.1). In Table 5.1, CP Ti (140.4±25.7μm) exhibited the largest grain size among the four materials examined, followed by Ti-5Al-2.5Sn (39.5±10.0μm). Both Ti-6Al-4V (6.4 ±4.4μm) and Ti-3Al-2.5V (6.4 ±4.4μm) exhibited grain sizes less than 10μm.

The percentage of grains exhibiting slip traces out of the total number of grains and the preferred slip systems when slip occurred also varied from material to material. During the 728K-45MPa creep test of CP Ti, ~97% of the total grains exhibited slip traces and the prismatic slip dominated (64%) (see Table 5.3). Thus, in CP Ti, dislocation slip was the dominant deformation mechanism in the tensile-creep test of this material, and when slip occurred,

prismatic slip was preferred. In contrast, in the 728K-250MPa creep test of Ti-5Al-2.5Sn, only ~10% of the total grains exhibited slip traces, where 78% of deformation systems were for basal slip and prismatic slip only comprised 16% (see Table 5.4). Therefore, for Ti-5Al-2.5Sn, GBS was the primary deformation mechanism in the 728K-250MPa creep test and when slip occurred, basal slip was the preferred system. For the 728K-180MPa creep test of Ti-3Al-2.5V, only ~3% of the total grains exhibited slip traces, which was similar to the creep test of Ti-5Al-2.5Sn (see Table 5.5). Unlike Ti-5Al-2.5Sn, prismatic slip was the preferred system when slip occurred during creep of Ti-3Al-2.5V. Therefore, for Ti-3Al-2.5V, GBS was the primary deformation mechanism and when slip occurred, prismatic slip was preferred. Note that no slip traces were observed during the 728K-310MPa creep test of Ti-6Al-4V, and GBS was the major deformation mechanisms to accommodate plastic deformation.

5.5 Statistical analysis

The data presented in section 5.4 suggest a number of different trends in the activation of the different deformation systems as a function of the different testing conditions. The large number of observations allows a more robust parametric statistical analysis to be carried out, which is presented in this section. In particularly, the statistical analysis is carried out to assess the significance of the comparative activity of the different deformation systems under the variety of experimental conditions examined for both CP Ti and Ti-5Al-2.5Sn. Table 5.7 lists the distribution of the deformation modes in both materials at similar strain levels. All statistical analysis was performed using original code written in *Mathematica* by Professor Darren Mason of Albion College.

When comparing different deformation systems and their observed prevalence across all experiments, it is important to first test that any variation in the relative sample frequency was

the result of an underlying systemic difference and not simply data noise (i.e. test of homogeneity) [Miller 1998]. One-way analysis of variance (ANOVA) determined that, across all experiments, the data supported rejecting the hypothesis that all deformation systems were equally likely to be observed in a given material. These tests were conducted using both Tukey and Bonferroni methods at a 0.01 level of significance and yielded similar results.

Pairwise t-tests were then conducted to assess the significance of the observed differences in the prevalence of the different types of active deformation systems [Croarkin et al. 2012]. For a given pair of distinct experiments, each with five possible deformation systems, there were 25 possible comparisons. Since there are 9 data sets (each row in Table 5.7), there are 36 possible distinct data set pairs (${}_9C_2$ i.e. 9!/7!/2!). With five different deformation systems in each data set to be compared, a total of 900 possible comparisons of the relative activity of deformation systems can be considered. Moreover, with five deformation systems in each of the 9 data sets, 20 distinct comparisons within each data set could also be made (omitting self-comparison). This results in an additional 180 potential tests, leaving a total of 1080 pairwise comparisons of the relative deformation system activity. Of these 1080 possible comparisons, 225 cases related to the observations above were investigated.

As an example of one of the 36 possible data set comparisons, Table 5.8 provides a list of all the possible comparisons for the five types of deformation systems observed in CP Ti at 296K and ~4% strain with the same types of the deformation systems in Ti-5Al-2.5Sn at 296K and ~3.5% strain. The number corresponding to a given row/column combination represents the probability of an error in asserting that the deformation mechanism listed in a given *row* is more likely than that listed in the related *column*. Negative numbers are the result of reversing the role of the column and row in the comparison. For example, the assertion that prismatic slip is more

likely to be observed in CP Ti at ~4% strain and 296K (row 1 in Table 5.7) than prismatic slip in Ti-5Al-2.5Sn at 3.5% strain and 296K (row 6 in Table 5.7) has only a 1.29% chance of being incorrect (bold number in row 2 column 2 in Table 5.8). Similarly, the assertion that pyramidal <c+a> slip is more likely to be observed at 296K and ~4.3% strain in CP Ti than pyramidal <c+a> slip at 296K and ~3.5% strain in Ti-5Al-2.5Sn, has a 5.44% chance of being an incorrect conclusion. This type of analysis allows the qualitative assessment of the relatively likelihood of the slip activity discussed in sections 5.4.5 to be assigned a level of statistical confidence.

Thus, a number of statements can be supported by this statistical analysis. Note that in all of the conclusions below, the given *P-value* corresponds to the probability of making an error in rejecting the asserted hypothesis:

1. In tensile tests of CP Ti, the activation of different slip systems is unaffected by the change in temperature from 296K to 728K for similar strain level. Specifically, the probability of making an error in rejecting a hypothesis that temperature does affect the activity of different slip systems is at least 20% and can be as high as 50%, depending on which slip systems are being compared. ($0.20 \leq P \leq 0.50$).
2. In tensile tests of Ti-5Al-2.5Sn, activation of different slip systems is also unaffected by a change in temperature. However, the likelihood of making an error with an assertion that temperature *is* important in Ti-5Al-2.5Sn is markedly lower than in CP Ti, with the maximum error in Ti-5Al-2.5Sn no larger than 32.7% (pyramidal <a> slip) and as small as 12.4% (prismatic slip). The latter statistic indicates that prismatic slip is slightly favored at lower temperatures.

3. At similar strain levels (~4.0% strain), the basal slip activity in Ti-5Al-2.5Sn was significantly more likely than in CP Ti at both 296K ($P = 3.7 \cdot 10^{-11}$) and 728K ($P = 2.8 \cdot 10^{-7}$).
4. Twinning was more likely in CP Ti than in Ti-5Al-2.5Sn at similar strain levels (~ 4%) and at both 296K and 728K (in all cases, $P \leq 0.0015$).
5. Pyramidal <c+a> slip in CP Ti is more likely than pyramidal <c+a> slip in Ti-5Al-2.5Sn under similar strain and temperature conditions ($P \leq 0.054$).
6. In CP Ti, for each individual data set, prismatic slip is by far the most likely slip system to activate at all temperatures and strain levels. The largest chance of making an error with this assertion occurs at ~4.3% strain and 728K with $P = 1.2 \cdot 10^{-12}$.
7. For sufficiently high Schmid factors, the data support the assertion that basal slip is preferred to prismatic slip in Ti-5Al-2.5Sn. Indeed, when the Schmid factor exceeds 0.35, the likelihood of making an error with such an assertion is no larger than 1.2%. However, when data including all possible Schmid factors is considered, any assertion that either basal or prismatic slip is preferred over the other in Ti-5Al-2.5Sn is more likely to be wrong ($P \geq 0.178$).
8. In CP Ti at 728K, the relative likelihood of basal, prismatic, and pyramidal <c+a> slip systems being activated in tension at ~11.2% strain was indistinguishable from analogous activation likelihoods in creep at 45MPa deformed to ~23.2% strain ($P \geq 0.181$). On the other hand, pyramidal <a> slip was significantly more likely during creep at ~23.2% strain than in tension at ~11.2% strain ($P = 0.0132$), and twinning was significantly more likely in tension at ~11.2% strain than in creep at ~23.2% strain ($P = 0.0119$).

9. In Ti-5Al-2.5Sn at 728K, the relative likelihood of pyramidal <a> and pyramidal <c+a> slip being activated in tension at ~9% strain was indistinguishable from analogous activation likelihoods in creep at 250MPa with ~16.5% strain ($P \geq 0.179$). However, prismatic slip was significantly more likely in tension at ~9% strain than in creep at ~16.5% strain ($P = 1.27 \cdot 10^{-6}$). Further, basal slip in tension at ~9% strain is less prevalent than in creep at ~16.5% strain ($P = 6.2 \cdot 10^{-7}$).

10. When comparing the relative activity of slip systems in CP Ti at 728K undergoing creep at ~23.2% strain and Ti-5Al-2.5Sn undergoing creep at ~16.5% strain, prismatic ($P = 1.88 \cdot 10^{-12}$), pyramidal <a> ($P = 0.000633$), and pyramidal <c+a> slip ($P = 0.0807$) were all more likely in CP Ti than Ti-5Al-2.5Sn. On the other hand, basal slip was significantly more likely in Ti-5Al-2.5Sn than CP Ti during creep ($P = 7.5 \cdot 10^{-21}$).

Table 5.7 Distribution of the observed deformation systems in Ti-5Al-2.5Sn and CP Ti.

Percentage of observations showing Slip/twin system activity→ Materials, test mode (approx. strain)	Basal	Prism	Pyramidal <a>	Pyramidal <c+a>	Twin
CP Ti, 296K tension (~4%)	10%	63%	6%	10%	11%
CP Ti, 296K tension (~8.4%)	11%	61%	5%	13%	10%
CP Ti, 728K tension (~4.3%)	11%	59%	6%	14%	10%
CP Ti, 728K tension (~11.2%)	9%	61%	6%	13%	11%
CP Ti, 728K-45MPa creep (~23.2%)	9%	64%	14%	10%	3%
Ti-5Al-2.5Sn, 296K tension (~3.5%)	42%	50%	3%	4%	1%
Ti-5Al-2.5Sn, 728K tension (~4.4%)	48%	41%	5%	6%	0
Ti-5Al-2.5Sn, 728K tension (~9%)	42%	47%	5%	6%	0
Ti-5Al-2.5Sn, 728 K-250MPa creep (~16.5%)	78%	16%	2%	4%	0

Table 5.8 The *P value* associated with rejecting the hypothesis that the deformation system listed in a given row is *more likely* to be observed than that listed in the corresponding column. Negative numbers correspond to same probability of an error when a system in a given row is *less likely* to be observed than that in a given column. The bold numbers were discussed in the text of section 5.4.5.2 to show examples of comparison.

		Ti-5Al-2.5Sn at 296K and 3.5% Strain				
		Basal	Prismatic	Pyramidal <a>	Pyramidal <c+a>	Twin
CP Ti at 296K and 4% Strain	Basal	-3.7E-11	-1.2E-15	0.0275	0.0544	0.0028
	Prismatic	0.00024	**0.0129**	1.4E-25	1.25E-24	4.08E-28
	Pyramidal <a>	-3E-16	-7.6E-22	0.219	0.342	0.0347
	Pyramidal <c+a>	-3.7E-11	-1.2E-15	0.0275	**0.0544**	0.00284
	Twin	-3.3E-10	-1.8E-14	0.0157	0.0323	0.00149

CHAPTER 6

CRSS METHODOLOGY

A methodology for estimating the CRSS ratios for α-phase Ti is presented in this chapter. This methodology utilized a least squares optimization procedure to minimize the difference between the experimentally-observed deformation system distribution (from the slip trace analysis results) and the expected deformation system distribution (accounting for the texture) in all of the grains from a given microstructural patch. The CRSS ratios of the different deformation systems were determined so that the modified texture distribution can best mimic the experimental observations. The majority content of this Chapter was published in a journal paper [Li H., Mason D.E., Boehlert C.J., Bieler T.R., and Crimp M.A., 2013, Methodology for estimating the critical resolved shear stress ratios of α-phase Ti using EBSD based trace analysis, Acta Materialia, Vol. 61, No.20, pp.7555-7567]. Therefore the similarity between Chapter 6 and the paper in press is high.

6.1 Experimentally-observed deformation system activation distribution

For each of the experimental condition combinations of alloy composition and deformation temperature, the deformation system activity is recorded as a function of deformation system type (as identified by trace analysis) and the Schmid factor based on an assumption of a uni-axial global stress state. An example of this data distribution is shown in Table 6.1, which shows the number of observations of each of the five deformation system types (i.e. basal, prismatic, pyramidal<a>, pyramidal<c+a>, and T1 twinning) and the correlated global Schmid factor at ambient temperature. The number of observed deformation systems is binned

based on Schmid factor increments of 0.05, so there are 10 Schmid factor bins for each of the five deformation system types. This defines a matrix where the value for each pair (i, j) is denoted as N_{ij} ($i=1,\ldots,10$, $j=1,\ldots,5$). This table is entitled as the deformation system-Schmid factor distribution. This table is populated based on the number of instances that each combination of deformation system and Schmid factor is observed on a grain-by-grain basis. For example, if a given grain displays the activation of two prismatic slip systems and one pyramidal <c+a> slip system, this will result in three entries in the table. Examination of this table reveals that, as expected, as the global Schmid factor decreases, the number of observed deformation systems of a given type generally decreases. It also suggests that some deformation system types, such as basal slip, are more likely to be activated than others, such as pyramidal <c+a>. This is not a surprising observation since the CRSS is expected to be different for different deformation systems. Mitigating these apparent biases of one deformation system over another in assessing CRSSs is complicated by the fact that a given microstructural patch of grains also possesses an underlying texture. Consequently, some deformation systems will be oversampled in the deformation system-Schmid factor distribution if there are preferred orientations that have a particularly high Schmid factor for a given system.

It is the goal of the following section to develop an approach for removing these inherent biases and, as a result, deduce the underlying relative CRSS for the different deformation types. This is done by comparing the experimentally-developed deformation system-Schmid factor distribution tables to theoretically-developed tables based on the orientation distributions of the experimentally characterized microstructural patches.

6.2 Methodology for calculating the relative CRSS for the different slip system types

In this section a methodology for calculating the ratios of the CRSS for the various deformation system types is presented, based on the experimental observations of the activation of the different deformation system types. In section 6.2.1, the manner for determining the total number of possible deformation systems for all the grains in a given microstructural patch is developed. The relative activation of the different deformation system types is then determined by comparing the potentially-activated systems to the experimentally-observed systems. In section 6.2.2, an approach for taking into account the likelihood of deformation system activation as a function of the global Schmid factor is developed, incorporating the distribution of grain orientations in the microstructural region of interest. This results in prediction of the activation distribution of the different deformation system types for the given microstructural patch, under the assumption that all of the deformation system types have the same CRSS (which is clearly not the case). Finally, in section 6.2.3, the results of section 6.2.2 are compared to the experimentally-observed activation distribution, and through a least squares optimization procedure the approximate relative CRSSs of the different deformation system types are determined, so that the results of section 6.2.2 are modified to mimic the experimental observations.

6.2.1 Comparison between the experimentally-observed deformation system activation distribution and the texture distribution

The Ti-5Al-2.5Sn tested in tension at ambient temperature will continue to be used as an example to illustrate the method. Table 6.2 lists the number of possible slip systems of a given deformation type and Schmid factor bin for all of the 147 grains in the EBSD mapped region,

again based on a global uni-axial stress state, regardless of whether the deformation system was activated or not. For each HCP α grain, there are 24 possible slip systems, including 3 basal slip, 3 prismatic slip, 6 pyramidal <a>, and 12 pyramidal <c+a> slip systems. Since dislocation slip is bidirectional, for the 24 slip systems in each of the 147 grains, the absolute value of the Schmid factor was computed for each grain, yielding 3528 values. However, since T1 twinning is unidirectional, each of the 6 possible T1 twin systems in each grain was counted only if it had a positive Schmid factor, yielding an additional 534 values, or a total of 4062 potential deformation systems are distributed in Table 6.2, which we henceforth refer to as a potential deformation system-Schmid factor distribution. The data in Table 4 are binned in the same manner as described for Table 6.1, defined so that a particular Schmid factor range and deformation type can be uniquely denoted D_{ij}. In comparison, 204 deformation systems were actually observed, as seen in Table 6.1.

The experimentally-observed deformation system-Schmid factor distribution is compared with the potential deformation system-Schmid factor distribution by dividing each pair in Table 6.1 (N_{ij}) with the corresponding pair in Table 6.2 (D_{ij}) resulting in:

$$\omega_{ij}=N_{ij}/D_{ij} \tag{6.1}$$

This new Table 6.3 is call a deformation system-Schmid factor activation ratio distribution, with ω_{ij} representing the ratio of the number of observed deformation systems of type j with Schmid factor bin i, to the corresponding potential number. If all the deformation systems represented in Table 4 were actually activated in the experiment, the value of each pair ω_{ij} in Table 6.3 would

be 1, but this is clearly not the case. This deviation from a value of 1 in each Table 6.3 entry results from two reasons. First, because the activation of a particular deformation system depends on the resolved shear stress on the given deformation system, we expect that a deformation system with a small Schmid factor (i.e. small resolved shear stress) is less likely to be activated than one with a large Schmid factor. Therefore, it is no surprise that the ω_{ij} associated with low Schmid factors in Table 6.3 are much smaller than for high Schmid factors. Second, since we expect the CRSS values of the five deformation systems to be different, different deformation systems subjected to the same resolved shear stress should have different levels of activity. This feature in the data is observed by comparing pairs of ω_{ij} within the same row (same Schmid factor bin) of Table 6.3. For example, Table 6.3 suggests that the CRSS of basal slip is much smaller than pyramidal <c+a> slip for the Ti-5Al-2.5Sn ambient tension test. In section 6.2.3, a CRSS ratio optimization process will be developed so that the difference between the number of experimental observations of the five deformation system types and the modified number of deformation systems based on the EBSD data is minimized.

6.2.2 Prediction of deformation system activation assuming the CRSS is the same for all deformation systems

Table 6.2 categorizes the number of *potentially-activated* deformation systems of a given deformation system type and Schmid factor range in a given microstructural patch for the ambient tested Ti-5Al-2.5Sn sample. However, as stated in the analysis of Table 6.3 in section 6.2.1, it does not represent the number of *likely-activated* deformation systems, which varies based on Schmid factor and deformation type. Using Table 6.3 as a guide, we now reduce the values in Table 6.2 associated with low Schmid factors and convert Table 6.2 to a table that

reflects the relative importance of the Schmid factor on the deformation activity but still assumes that the CRSS is the same for all of the deformation system types. The results of Table 6.3 are plotted in Figure 6.1 showing the activation ratio of the different deformation system types as a function of the global Schmid factor, which can be fitted using a cubic weighting function:

$$W_{ij} = D_{ij} \times ((i-1)/9)^3 \tag{6.2}$$

resulting in Table 6.4, which will be referred to as a weighted deformation system-Schmid factor distribution. This weighting function will not change the relative potential activation of the deformation systems associated with the highest Schmid factor value 0.45-0.5 (in equation (6.2), when $i = 10$, $W_{ij}=D_{ij}$, and the values in the bottom row of Table 6.4 are unchanged from Table 6.2), but will strongly suppress the potential activation of the deformation systems with smaller Schmid factors (i.e. for i small, since only a very small number of deformation systems with low Schmid factors are expected to be activated, the values in the first row of Table 6.4 are zero – consistent with those in Table 6.3 and much lower than those in Table 6.2). It should be noted that different scaling functions of the form in equation (6.2) may be more applicable for different metals and/or different deformation systems. Nevertheless, in this study, a number of different polynomial functions were tested, including quadratic, cubic, and 4th order weighting functions, and there was no significant effect on the final results. In the present study, the cubic weighting function (equation (6.2)) is used.

Based on the weighted deformation system-Schmid factor distribution in Table 6.4, an approximate probability density function is generated using

$$p_{ij} = W_{ij} / \sum_{i,j} W_{ij} \tag{6.3}$$

which, as shown in Table 6.5, represents the approximate probability of having deformation *j* with Schmid factor bin *i* activated, again assuming the CRSS of all the deformation systems are the same. This approximate probability density function now allows the prediction of the *expected* number of observations of deformation system type *j* and Schmid factor bin *i*, denoted by P^0_{ij}, for any given total number of deformation systems *S* to be determined via

$$P^0_{ij} = p_{ij} S \tag{6.4}$$

For the Ti-5Al-2.5Sn ambient tension test, a total of 204 deformation systems were observed ($S = \sum_{i,j} N_{ij} = 204$). So in this case P^0_{ij} represents the expected number of observations of a given deformation type *j* and Schmid factor bin *i* based on the probability density function generated in equation (6.3) if the total number of deformation systems were 204, shown in Table 6.6. This table contains the expected number of activated deformation systems for the given texture of the microstructural patch assuming the CRSSs are the same for all the deformation system types. Note that the total number of observed deformation systems will vary for a given experimentally-characterized microstructural patch, testing condition, and material.

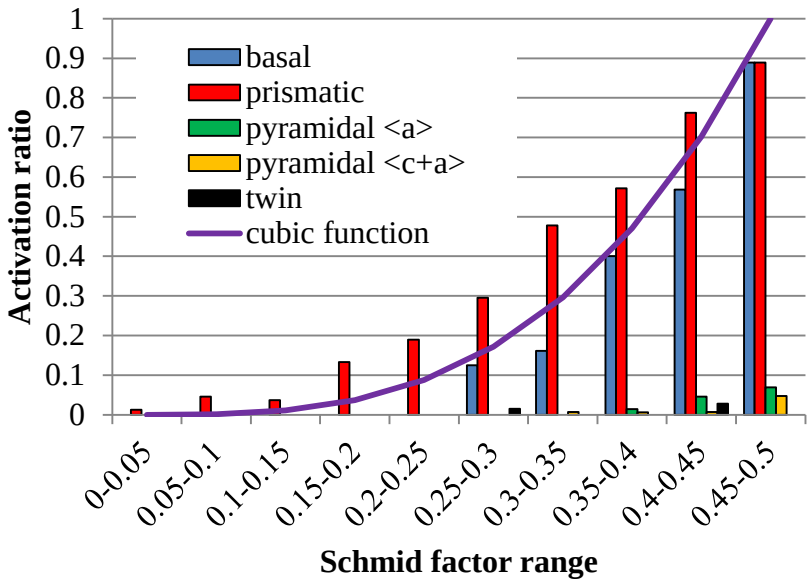

Figure 6.1 Activation fraction versus Schmid factor for the different deformation system types for Ti-5Al-2.5Sn tensile tested at ambient temperature, with the cubic parabola function overlaid.

6.2.3 Optimization of CRSS ratio

The procedures in section 6.2.2 do not consider the CRSS differences of the five deformation system types, so consequently the experimentally-observed deformation system-Schmid factor distribution (N_{ij}) in Table 6.1 is significantly different from the expected distribution (P^0_{ij}) in Table 6.6. The next step is to optimize the CRSS ratios of the five deformation system types so that the difference between the experimental observations and the expected values is minimized. In this section, a methodology for determining the CRSS ratio is presented. This methodology involves a modification of P^0_{ij} (in Table 6.5, assuming CRSS is the same) using hypothetical CRSS values and the least-square minimization to match the modified P^0_{ij} with the experimentally-observed deformation system-Schmid factor distribution (N_{ij}) in Table 6.1.

Let τ_j denote the true CRSS of deformation system type j and P_{ij} the number of observations of deformation system type j and Schmid factor bin i, where it is *not* assumed that the CRSS are identical. Then the expected number of observations of deformation system type j and Schmid factor bin i in Table 6.6, where it was assumed that the CRSS are identical, can be related to this modified number P_{ij} via

$$P_{ij} = \frac{c}{\tau_j} P^0{}_{ij} \tag{6.5}$$

where c is an unknown constant with units of MPa. If the CRSS for one slip system type has been experimentally measured, the constant c can be determined, allowing the actual CRSS to be determined for all of the other deformation system types. Nevertheless, this is not the case in the present analysis, so only the ratios of the CRSSs of the different deformation systems will be determined, and c was set to 1MPa. Note that if all of the CRSS are identical, i.e.

$$\tau_1=\tau_2=\tau_3=\tau_4=\tau_5=c \tag{6.6}$$

then the modified number of observations P_{ij} agree with the expected values given in Table 6.6. Alternatively, if $\tau_j > \tau_k$, then the modified number of observations P_{ij} for deformation system j is related to the analogous quantity P_{ik} for deformation system k by

$$\frac{P_{ik}}{P^0{}_{ik}} = \frac{\tau_j}{\tau_k} \frac{P_{ij}}{P^0{}_{ij}} \tag{6.7}$$

so that the modified number of observations (relative to the expected number if the CRSSs are identical) in deformation system *k* is *greater* than the same relative number in deformation system *j*. This is consistent with deformation system *k* having a smaller CRSS than deformation system *j*.

The squared difference *d* between the number of experimental observations of each pair N_{ij} in Table 6.1 and the corresponding modified predicted number of observations P_{ij} is given by

$$d(\tau_1,\tau_2,\tau_3,\tau_4,\tau_5;c)=\sqrt{\Sigma_{i,j=1}^{10,5}(P_{ij}-N_{ij})^2}=\sqrt{\Sigma_{i,j=1}^{10,5}(\frac{c}{\tau_j}P^0{}_{ij}-N_{ij})^2} \qquad (6.8)$$

The "optimal" values for the CRSS values are then computed by solving the first order derivative conditions for *d* with respect to τ_1, τ_2, τ_3, τ_4, and τ_5 (treating *c* as an unknown parameter) and using the result to minimize *d:*

$$\frac{\partial d}{\partial \tau_j}=0\rightarrow \tau^*{}_j=c\frac{\Sigma_{i=1}^{m}(P^0{}_{ij})^2}{\Sigma_{i=1}^{m}N_{ij}P^0{}_{ij}} \qquad (6.9)$$

$\tau^*{}_1$, $\tau^*{}_2$, $\tau^*{}_3$, $\tau^*{}_4$, and $\tau^*{}_5$ are the "optimal" CRSS values for basal, prismatic, pyramidal <a>, pyramidal <c+a>, and T1 twin deformation systems, respectively. In equation (6.9), although *c* is an unknown constant, the CRSS *ratio* of any two deformation systems will not depend on *c*. Thus, the CRSS ratios of the basal, prismatic, pyramidal <a>, pyramidal <c+a>, and T1 twin are given as:

$$\text{Basal: Prismatic: Pyramidal <a>: Pyramidal<c+a>: T1 twin}=\frac{\tau^*{}_1}{\tau^*{}_1}:\frac{\tau^*{}_2}{\tau^*{}_1}:\frac{\tau^*{}_3}{\tau^*{}_1}:\frac{\tau^*{}_4}{\tau^*{}_1}:\frac{\tau^*{}_5}{\tau^*{}_1} \qquad (6.10)$$

For the Ti-5Al-2.5Sn tested at 296K, the estimated ratios are 1: 0.79: 15.5: 30.1: 54.5 for basal: prismatic: pyramidal <a>: pyramidal<c+a>:T1 twin. Using the above CRSS ratios, the predicted number of observations for a given deformation type *j* and Schmid factor bin *i* (P_{ij}) in equation (6.5) is shown in Table 6.7. Comparison of this table with the experimental results in Table 6.1 shows good agreement.

The same methodology discussed in sections 6.1-6.2 was employed to calculate the CRSS ratios for the CP Ti, Ti-5Al-2.5Sn, Ti-3Al-2.5V, and Ti-6Al-4V tensile tested at 296K and 728K. The significance of these values will be discussed next.

Table 6.1 Experimentally-observed deformation system-Schmid factor distribution of the Ti-5Al-2.5Sn 296K tension test.

Schmid factor	basal	prism	pyra a	pyra c+a	twin
0-0.05	0	1	0	0	0
0.05-0.1	0	3	0	0	0
0.1-0.15	0	2	0	0	0
0.15-0.2	0	8	0	0	0
0.2-0.25	0	7	0	0	0
0.25-0.3	5	13	0	0	1
0.3-0.35	5	11	0	1	0
0.35-0.4	18	16	1	1	0
0.4-0.45	25	16	2	1	1
0.45-0.5	32	24	4	6	0

Table 6.2 Potential deformation system-Schmid factor distribution for all the grains in the EBSD mapped region of the Ti-5Al-2.5Sn 296K tension test.

Schmid factor	basal	prism	pyra a	pyra c+a	twin
0-0.05	57	81	178	264	64
0.05-0.1	54	66	106	244	55
0.1-0.15	56	54	103	195	62
0.15-0.2	38	60	87	164	52
0.2-0.25	40	37	92	180	59
0.25-0.3	40	44	82	137	66
0.3-0.35	31	23	61	148	59
0.35-0.4	45	28	71	154	58
0.4-0.45	44	21	44	151	36
0.45-0.5	36	27	58	127	23

Table 6.3 Deformation system-Schmid factor activation ratio distribution of the Ti-5Al-2.5Sn 296K tension test.

Schmid factor	basal	prism	pyra a	pyra c+a	twin
0-0.05	0	0	0	0	0
0.05-0.1	0	0.05	0	0	0
0.1-0.15	0	0.04	0	0	0
0.15-0.2	0	0.13	0	0	0
0.2-0.25	0	0.19	0	0	0
0.25-0.3	0.13	0.30	0	0	0.02
0.3-0.35	0.16	0.48	0	0.01	0
0.35-0.4	0.40	0.57	0.01	0.01	0
0.4-0.45	0.57	0.76	0.05	0.01	0.03
0.45-0.5	0.89	0.89	0.07	0.05	0

Table 6.4 Weighted potential deformation system-Schmid factor distribution for all the grains in the EBSD mapped region of the Ti-5Al-2.5Sn 296K tension test.

Schmid factor	basal	prism	pyra a	pyra c+a	twin
0-0.05	0	0	0	0	0
0.05-0.1	0.07	0.09	0.15	0.33	0.08
0.1-0.15	0.61	0.59	1.13	2.14	0.68
0.15-0.2	1.41	2.22	3.22	6.07	1.93
0.2-0.25	3.51	3.25	8.08	15.80	5.18
0.25-0.3	6.86	7.54	14.06	23.49	11.32
0.3-0.35	9.19	6.81	18.07	43.85	17.48
0.35-0.4	21.17	13.17	33.41	72.46	27.29
0.4-0.45	30.90	14.75	30.90	106.05	25.28
0.45-0.5	36	27	58	127	23

Table 6.5 Probability density function of the Ti-5Al-2.5Sn 296K tension test.

Schmid factor	basal	prism	pyra a	pyra c+a	twin
0-0.05	0	0	0	0	0
0.05-0.1	0.0001	0.0001	0.0002	0.0004	0.0001
0.1-0.15	0.0007	0.0007	0.0013	0.0025	0.0008
0.15-0.2	0.0016	0.0026	0.0037	0.0070	0.0022
0.2-0.25	0.0041	0.0038	0.0094	0.0183	0.0060
0.25-0.3	0.0080	0.0088	0.0163	0.0273	0.0131
0.3-0.35	0.0107	0.0079	0.0210	0.0509	0.0203
0.35-0.4	0.0246	0.0153	0.0388	0.0841	0.0317
0.4-0.45	0.0359	0.0171	0.0359	0.1231	0.0293
0.45-0.5	0.0418	0.0313	0.0673	0.1474	0.0267

Table 6.6 Expected activated deformation system-Schmid factor distribution of the Ti-5Al-2.5Sn 296K tension test with a total of 204 deformation systems assuming CRSSs are the same for all the deformation system types.

Schmid factor	basal	prism	pyra a	pyra c+a	twin
0-0.05	0	0	0	0	0
0.05-0.1	0.02	0.02	0.03	0.08	0.02
0.1-0.15	0.15	0.14	0.27	0.51	0.16
0.15-0.2	0.33	0.53	0.76	1.44	0.46
0.2-0.25	0.83	0.77	1.91	3.74	1.23
0.25-0.3	1.62	1.79	3.33	5.56	2.68
0.3-0.35	2.17	1.61	4.28	10.38	4.14
0.35-0.4	5.01	3.12	7.91	17.16	6.46
0.4-0.45	7.32	3.49	7.32	25.11	5.99
0.45-0.5	8.52	6.39	13.73	30.07	5.45

Table 6.7 Predicted activated deformation system-Schmid factor distribution of the Ti-5Al-2.5Sn 296K tension test with a total of 204 deformation systems using optimized CRSS ratios.

Schmid factor	basal	prism	pyra a	pyra c+a	twin
0-0.05	0	0	0	0	0
0.05-0.1	0.06	0.10	0.01	0.01	0.00
0.1-0.15	0.52	0.63	0.06	0.06	0.01
0.15-0.2	1.18	2.35	0.17	0.17	0.03
0.2-0.25	2.94	3.43	0.44	0.44	0.08
0.25-0.3	5.75	7.97	0.76	0.65	0.17
0.3-0.35	7.70	7.20	0.98	1.22	0.27
0.35-0.4	17.75	13.92	1.81	2.02	0.42
0.4-0.45	25.91	15.59	1.68	2.95	0.39
0.45-0.5	30.19	28.54	3.14	3.53	0.35

6.3 CRSS ratio results and discussion

One expects that if the same experiment was repeated numerous times on a patch of the same material (e.g. same texture, temperature, strain), the set of observed activated deformation systems would be slightly different than that given in Table 6.1 since each set of observations would represent a sample from the same population (and therefore with the same probability distribution). Therefore, the specific numbers computed using the observations in Table 6.1 and represented in equation (6.10) are only an estimate of the CRSS ratios, not the true CRSS ratios. Indeed, since the computed CRSS ratios depend on all of the data in Table 6.1, without further experiments it is not possible to explicitly compute additional estimates of the CRSS ratios. Despite this limitation however, the accuracy of the CRSS ratio estimates computed using the method of sections 6.1–6.2 and given in equation (6.10) can be assessed in two fundamental ways. First, the statistical resampling technique of bootstrapping allows the generation a large number of pseudo datasets and simulate the repetition of numerous deformation experiments, compute the optimal set of CRSS ratios for each dataset, and then determine the corresponding mean CRSS ratios from this collection [Effron et al. 1979 and 1981]. We can then use these averaged values as a more robust measure of true CRSS ratios, thereby facilitating discussion of the relationship between the mean CRSS ratios, the experimental data, and relevant values in the literature. Second, using the resampling distribution as an estimate of the true CRSS ratio distribution, we can compute rough confidence intervals for the CRSS ratios and analyze their corresponding significance.

6.3.1 Statistical analysis

For each of the tensile experiments considered in this work (CP Ti, Ti-5Al-2.5Sn, Ti-3Al-2.5V, and Ti-6Al-4V at 296K and 728K), the bootstrapping analysis described below was followed.

1. Treating each experimental observation of deformation as an independent and identically distributed random variable, the raw experimental data (e.g. Table 6.1) was used to construct a discrete probability distribution $f_{ij} = N_{ij}/N$ where N_{ij} is the number of observations of deformation with Schmid factor bin i and deformation type j and $N = \sum_{i,j=1}^{10,5} N_{ij}$ is the total number of deformation system observations for the experiment under consideration. Here f_{ij} represents an empirical probability distribution for all possible Schmid factor bins and deformation types, constructed by assigning a probability of $1/N$ to each experimental observation, regardless of Schmid factor bin or deformation type.
2. M pseudo data sets (each corresponding to a simulated experiment) were constructed by randomly sampling (with replacement) the observation sample space using the distribution f_{ij}, which represents the empirical probability that a given observation will lie in Schmid factor bin i and be of deformation type j. Each of the M data sets consisted of N "observations".
3. For each of the M pseudo data sets, the optimization problem from section 6.1-6.2 was solved to deduce CRSS ratio estimates of the form given in equation (6.10).
4. Each of the generated populations of CRSS ratios were analyzed statistically by computing the mean and confidence intervals using the resampling distribution.

Figure 6.2 depicts how this method was applied to the data in Table 6.1 for the Ti-5Al-2.5Sn strained to 3.5% at 296K. The resulting resampled CRSS ratio distributions are depicted in Figure 6.3. Corresponding mean values, standard errors, and confidence intervals were then computed from these simulated distributions [Carpenter et al. 2000]. The mean values of the CRSS ratios for all bootstrapped pseudo data sets are given in Tables 6.8, 6.9, and 6.10. Unless otherwise stated, the subsequent discussion refers to these mean values. The significance of the confidence intervals contained in Table 6.10 will be discussed in section 6.3.2.

It is noted that the CRSS ratios of the different deformation systems were not calculated for Ti-3Al-2.5V with approximately 4% strain at both 296K and 728K. Because for the Ti-3Al-2.5V alloy deformed to 4% strain, there were only very few grains (less than 10) exhibited slip traces and most of the strain were accommodated by GBS (see Figure 4.61, Figure 4.66, and Figure 4.74 for Ti-3Al-2.5V deformed to ~4% strain).

Table 6.8 Bootstrapped mean CRSS ratios of basal, prismatic, pyramidal<a>, pyramidal<c+a>, and T1 twin deformation systems for CP Ti and Ti-5Al-2.5Sn tested at ambient and 728K with approximately ~4% plastic deformation. * Twinning was not observed for Ti-5Al-2.5Sn tested at 728K.

Materials	Testing temperature	Strain	Basal	Prismatic	Pyramidal <a>	Pyramidal <c+a>	T1 twin
CP Ti	296K	4%	1	0.28	7.1	6.3	1.7
CP Ti	728K	4.3%	1	0.29	5.4	4.7	1.8
Ti-5Al-2.5Sn	296K	3.5%	1	0.81	19.1	35.5	74
Ti-5Al-2.5Sn	728K	4.4%	1	1.17	16.7	24.4	*
Ti-6Al-4V	296K	6.3%	1	1.2	13.2	38	27
Ti-6Al-4V	728K	3.8%	1	1.38	20.2	40.2	8.4

Table 6.9 Bootstrapped mean CRSS ratios of basal, prismatic, pyramidal<a>, pyramidal<c+a>, and T1 twin deformation systems for CP Ti at 296K and 728K, Ti-5Al-2.5Sn at 728K, Ti-3Al-2.5V plate 2 at 296K and 728K, and Ti-6Al-4V at 296K and 728K (specimens A, B, and C) with ~10% plastic deformation. Note that the 728K tension test of Ti-3Al-2.5V plate 2 exhibited a strain of 16.2%, which is significantly higher than for the other tests. * Twinning was not observed for Ti-5Al-2.5Sn tested at 728K.

Materials	Testing temperature	Strain	Basal	Prismatic	Pyramidal <a>	Pyramidal <c+a>	T1 twin
CP Ti	296K	4%	1	0.28	7.1	6.3	1.7
CP Ti	296K	8.4%	1	0.32	9.2	4.6	2.2
CP Ti	728K	4.3%	1	0.29	5.4	4.7	1.8
CP Ti	728K	11.2%	1	0.23	4.2	3.9	1.2
Ti-5Al-2.5Sn	728K	4.4%	1	1.17	16.7	24.4	*
Ti-5Al-2.5Sn	728K	9%	1	0.83	14.1	19.2	*
Ti-3Al-2.5V	296K	10.5%	1	0.16	0.81	5.72	0.37
Ti-3Al-2.5V	728K	16.2%	1	0.33	1.1	12.3	2.8
Ti-6Al-4V	296K	6.3%	1	1.2	13.2	38	27
Ti-6Al-4V	296K	8.2%	1	1.5	23.7	32.5	45.4
Ti-6Al-4V	728K	3.8%	1	1.38	20.2	40.2	8.4
Ti-6Al-4V	728K	10.2%	1	1.8	15.5	51.8	15.7

Table 6.10 Bootstrapped mean CRSS ratios and their associated 90% confidence intervals. For each of the strain levels, the bootstrapped mean is listed above the corresponding 90% confidence interval. * Mean CRSS ratios and confidence intervals were not computed for T1 twins in the Ti-5Al-2.5Sn at 728K and the Ti-6Al-4V specimen D at 728K due to a lack of observations.

Means & 90% Confidence Intervals

Materials	Testing temperature	Strain	Prismatic Basal	Pyramidal <a> Basal	Pyramidal <c+a> Basal	T1 Twin Basal
CP Ti	296K	4%	0.28	7.1	6.3	1.7
			(.12, .48)	(.81, 25.9)	(2.1, 13.1)	(.6, 3.5)
	728K	4.3%	0.29	4.9	4.7	1.8
			(.14, .49)	(1.5, 11.4)	(2, 9.1)	(.6, 3.8)
	296K	8.4%	0.32	9.2	2.3	1.3
			(.15, .53)	(2.4, 21.9)	(1.8, 8.5)	(.78, 4.4)
	728K	11.2%	0.23	4.1	3.9	1.2
			(.11, .38)	(1.2, 9)	(1.7, 7.4)	(.48, 2.3)
Ti-5Al-2.5Sn	296K	3.5%	0.81	19	35	74
			(.61, 1.05)	(8.7, 38.5)	(17.2, 65.2)	(21, 187)
	728K	4.4%	1.17	16.7	24.4	*
			(.68, 1.85)	(1.96, 46.1)	(7.3, 72.9)	*
	728K	9%	0.83	14.1	19.2	*
			(.6, 1.09)	(7, 26.3)	(10.7, 32.2)	*
Ti-3Al-2.5V (plate 1)	296K	6.5%	.05	1.1	11.9	.22
			(.01, 0.14)	(.23, 3.4)	(1.7, 33.6)	(.06, .5)
	728K	9.7%	.2	1.2	6.3	2.2
			(.07, .34)	(0.44, 2.3)	(1.8, 13.9)	(.54, 5.6)
Ti-3Al-2.5V (plate 2)	296K	10.5%	.16	.81	5.72	.37
			(.07, .25)	(.31, 1.5)	(1.77, 12.5)	(.14, .68)
	728K	16.2%	.33	1.1	12.3	2.8
			(.20, .5)	(.62, 1.7)	(4.9, 25.2)	(1.2, 5.6)
Ti-6Al-4V	296K (Spec. A)	6.3%	1.2	13.2	38	27
			(.95, 1.5)	(8.8, 19.4)	(24.2, 57.3)	(13, 49)
	296K (Spec. B)	8.2%	1.5	23.7	32.5	45.5
			(1.1, 1.9)	(13.4, 39.7)	(20.5, 49.7)	(15, 133)
	728K (Spec. C)	3.8%	1.38 (.77, 2.2)	20.2 (6, 55.7)	40.2 (12.1, 105)	8.4 (2.5, 22)
	728K (Spec. C)	10.2%	1.8	15.5	51.8	15.7
			(1.3, 2.4)	(9.1, 25.8)	(25.3, 93.7)	(7.1, 30)
	728K (Spec. D)	11.6%	2	2.5	35.9	*
			(1.1, 3.4)	(1.4, 3.9)	(10.5, 92.5)	*

6.3.2 Comparison of the analysis of mean CP Ti CRSS ratios at 296K with previous results

The calculated CRSS ratios of the CP Ti tested at 296K are consistent with the prior work, indicating the validity of this technique. In Table 6.8, the calculated prismatic/basal CRSS ratio is 0.28, which is close to the value of 0.2 reported by Wu et al. [2007]. This ratio has also been reported from other studies, with a wide range of 0.2-1.35 shown in Table 1.2. Pyramidal slip systems exhibited much higher mean CRSS values relative to basal (7.1 for pyramidal <a>, 6.3 for pyramidal <c+a>), which are similar to those reported in [Paton et al. 1973] and used in [Balasubramanian et al. 2002]. Furthermore, the CP Ti exhibits a moderate resistance to twinning (CRSS ratio = 1.7) among all of the deformation system types, which is larger than prismatic slip (0.28) but smaller than pyramidal <a> (7.1) and pyramidal <c+a> slip (6.3). This is also consistent with the prior observations that indicated that twinning is frequently observed for CP Ti and that the observed activity was less than that for prismatic and basal slip but more than that for pyramidal slip systems [Williams et al. 2002, Yang et al. 2011, and Wang et al. 2011].

6.3.3 Analysis of the effect of alloy composition and deformation temperature on the CRSS ratios at low strain

In this section, the relative activity of the different deformation systems changes with alloying composition and deformation temperature are compared at low strain. Examination of Table 6.8 allows several statements to be made. Comparisons of the mean prismatic/basal CRSS ratios determined for 296K shows while prismatic slip is strongly favored in CP Ti (0.28), prismatic slip becomes less favorable in the alloys (0.81 for Ti-5Al-2.5Sn and 1.2 for Ti-6Al-4V). The lower resistance of prismatic slip relative to basal slip is unaffected by temperature for CP Ti

(prismatic/basal CRSS ratios of 0.28 and 0.29 respectively). In contrast, for both the Ti-5Al-2.5Sn and Ti-6Al-4V alloys, similar analysis suggests that basal slip becomes more favorable with increasing deformation temperature (from 0.81 to 1.17 for Ti-5Al-2.5V, from 1.2 to 1.38 for Ti-6Al-4V). The CRSS of basal was even lower than prismatic slip for Ti-5Al-2.5Sn at 728K and for Ti-6Al-4V at both 296K and 728K. These trends agree with earlier observations indicating that prismatic slip is favored in unalloyed Ti and that basal activity increases with Al additions and temperature [Williams et al. 2002].

The activity of the other deformation systems relative to the activity of basal slip is also affected by alloying and temperature. With increasing temperature for CP Ti, the relative CRSS of pyramidal <a> and pyramidal <c+a> slip decreases slightly (7.1 and 6.3 at 296K, 5.4 and 4.7 at 728K, see Table 6.8). For Ti-5Al-2.5Sn, a similar decrease in the activity of pyramidal <a> and pyramidal <c+a> slip was also observed with increasing temperature. In contrast, for Ti-6Al-4V, with increasing temperature, the relative CRSS of pyramidal <a> and pyramidal <c+a> slip increases slightly (13.2 and 38 at 296K, 20.2 and 40.2 at 728K). Overall, the mean pyramidal/basal CRSS ratio in CP Ti (4.7-7.1) is much lower than for Ti-5Al-2.5Sn (16.7-35.5) and Ti-6Al-4V (13.2-40.2), see Table 6.8.

The relative activity of twinning also changes with alloying and temperature. For the CP Ti, twinning is an active deformation system at both 296K and 728K, and the relative activity of twinning is not significantly affected by temperature (1.7 at 296K, 1.8 at 728K, see Table 6.8). However, Ti-5Al-2.5Sn exhibits a very high resistance to twinning (74, see Table 6.8) compared with other deformation systems at 296K. Furthermore, as twinning was not observed in the Ti-5Al-2.5Sn at elevated temperature, no CRSS ratio value was calculated. Twinning was observed in a few grains in Ti-6Al-4V, but the relative CRSS of twinning to basal slip in Ti-6Al-4V was

still much higher than that for CP Ti at both 296K and 728K. This low twinning activity in both Ti-5Al-2.5Sn and Ti-6Al-4V is consistent with the observations of Williams et al. [2002] where it was reported that twinning can be restricted by the ordering of Al in the α phase and that twinning can be further suppressed with increasing temperature for Ti-Al alloys.

The present work ignores any influences that the β phase may have on the mechanical response of the microstructure and how such influences may affect the deformation response of the α phase. As the β phase makes up less than 1% of the microstructure of the Ti-5Al-2.5Sn alloy, it may be reasonable to assume that the β phase of the Ti-5Al-2.5Sn alloy does not significantly affect the relationship between the activation of deformation in the α phase and the associated CRSSs. This is confirmed by recent CPFE modeling of a Ti-5Al-2.5Sn microstructural patch, which shows that the small amount of β at the grain boundaries does not alter the local stress state significantly when compared to the same microstructural patch simulated without the grain boundary phase [Zhang et al. to be submitted, 2013]. Another justification to ignore the β phase is that the statistical approach used in the present work does not consider the geometry of the microstructure. That is, the orientations and mechanical responses of neighboring grains are not taken in to account when identifying the activated deformation systems in a given grain. This lack of dependence on the local grain environment leads to the potential to use the method outlined here to assess the CRSS ratios of different phases in complex multiphase materials, if the effects of microstructural details average out with a sufficiently large population.

6.3.4 Analysis of the effect of strain on the CRSS ratios

As noted previously [Li et al. 2013], with increasing strain more deformation systems were observed. For the CP Ti, and the Ti-3Al-2.5Sn and Ti-6Al-4V alloys tested at 296K and 728K and the Ti-5Al-2.5Sn alloy tested at 728K, the activated deformation system data sets were collected at ~10% plastic strain. Using the same methodology described in section 6.3.1, the mean CRSS ratios were determined and are shown in Table 6.9. Some variation in the calculated ratios for a given set of alloy/temperature conditions as a function of strain is observed. For example, when deformed at high temperatures, both the CP Ti and the Ti-5Al-2.5Sn show a decrease in the CRSS ratios for basal to prismatic slip from their ambient temperature values, decreasing from 0.29 to 0.23 and 1.17 to 0.83 respectively. However, Ti-6Al-4V exhibits an increase in the CRSS ratios of basal to prismatic slip (from 1.38 at 296K to 1.8 at 728K). Since no data was collected at low strain for Ti-3Al-2.5V, the effect of strain on the CRSS ratios was not clear for this alloy.

In addition to statistical uncertainty discussed in the sections 6.3.1 and 6.3.5, there may be other reasons to expect the ratios to change as a function of strain. First, it is expected that as the polycrystalline samples deform, the individual grains will rotate. The resulting change in texture with deformation has not been accounted for in this methodology, with the texture corrections being based only on the texture in the undeformed state. Second, as the strain increases, some of the lower activity systems may become more evident and contribute to the deformation system-Schmid factor distributions (representing actual experimentally-observed deformation events first detailed in Table 6.1). As deformation continues, additional deformation on the systems initially observed in the deformation system-Schmid factor distribution is not quantified as a change in the table, but activation of additional deformation

systems will be reflected in the deformation system-Schmid factor distribution. Third, while the current analysis assesses the Schmid factors relative to the global state of stress, the local state of stress varies to some degree due to the constraints of polycrystalline deformation [Molinari et al. 1987, Prakash et al. 2009, Kanjarla et al. 2010, Kalidindi et al. 1992 and 2004]. These variations should average out with large data sets. Nevertheless, the biases associated with local deviations from the global state of stress are complex, and will evolve as the rate of deformation in neighboring grains varies. Finally, it is possible that the changes in the observed CRSS ratios with strain reflect a real change in materials behavior in that the work hardening for the different deformation system types is expected to be different [Salem et al. 2005, Zambaldia et al. 2012, Wang et al. 2011, Kalidindi et al. 1994 and 2004], and consequently, the stress necessary to activate these different systems will vary with strain. If this is in fact the case, the method developed here has the potential to allow assessment of these differences in work hardening behavior, allowing access to evolving work hardening parameters critical to CPFE models used for anisotropic deformation studies.

6.3.5 Statistical confidence and data resampling

The uncertainty inherent in the CRSS ratios computed in sections 6.2-6.3 is influenced by both non-systematic errors resulting from the choice of microstructural patch and sample sizes, as well as from systematic errors such as those that may result from the inability to identify certain deformation systems [Li et al. 2012 and 2013]. Although application of the bootstrap method discussed in section 6.3.1 to the raw experimental data provides a robust way to estimate the mean CRSS ratios for various deformation system pairs in the CP Ti and the Ti-5Al-2.5Sn, Ti-3Al-2.5V, and Ti-6Al-4V alloys, it cannot completely remove uncertainty in the original

observations. Nevertheless, such uncertainty can be quantified using confidence intervals computed form the sampling distributions computed and displayed in Figure 6.2 (d) and Figure 6.3. Using the percentile method discussed in [Carpenter et al. 2000], $100(1-\alpha)\%$ confidence intervals of the form $(l_{\alpha/2}, r_{\alpha/2})$ were computed for the mean CRSS ratios. The endpoints $l_{\alpha/2}$ and $r_{\alpha/2}$ were deduced so that $(-\infty, l_{\alpha/2})$ contained the lowest $\alpha/2\%$ of the resampled data from the bootstrapping simulation and $(r_{\alpha/2}, \infty)$ contained the largest $(1-\alpha/2)\%$ of the resampled data. Note that such intervals are typically not symmetric about the distribution mean. Intervals of 90% confidence ($\alpha = 0.1$) and their corresponding means are given in Table 6.10. Based on this, a number of comparisons of the different pairs of CRSS ratios across experiments and deformation systems can be made, all with at least 90% confidence:

1. Under all conditions in CP Ti, the CRSS of prismatic slip is no more than 53% of the CRSS of basal slip. At 296K and 4% strain the CRSS of pyramidal <a> slip is at least 81% of the CRSS of basal slip, but under all other conditions the CRSS of pyramidal <a> slip is at least 120% of the CRSS of basal slip.
2. In CP Ti, changes in deformation temperature and strain do not significantly alter the prismatic-to-basal CRSS ratio.
3. While the mean prismatic-to-basal CRSS ratio in the Ti-5Al-2.5Sn alloy is 0.81 at low strain and 296K, it is 1.17 at 728K, suggesting that the prismatic-to-basal CRSS ratio changes from favoring prismatic slip to favoring basal slip with increasing temperature. Although the confidence intervals do not support such a definitive statement, visual comparison of the resampling distributions in Figure 6.4 does suggest that the mean

prismatic-to-basal CRSS ratio at low temperature is significantly lower than at high temperature.

4. Increasing temperature also resulted in an increase in the mean prismatic-to-basal CRSS ratio in the two Ti-3Al-2.5V plates and the Ti-6Al-4V alloy at ~10% strain. For Ti-3Al-2.5V, the mean prismatic-to-basal CRSS ratio increased from 0.05 at 296K to 0.2 at 728K for plate 1 and increased from 0.16 at 296K to 0.33 at 728K for plate 2. For Ti-6Al-4V, the mean prismatic-to-basal CRSS ratio increased from 1.5 at 296K with 8.2% strain to 1.8 at 728K with 10.2% strain.
5. In Ti-5Al-2.5Sn at 296K and 3.5% strain, the mean pyramidal <a>-to-basal CRSS ratio (19) is considerably less than the mean pyramidal <c+a>-to-basal CRSS ratio (35). Moreover, despite inconclusive confidence intervals, the resampled population distributions shown in Figure 6.5 indicate a clear separation of the populations, supporting the hypothesis that pyramidal <c+a> slip is significantly more difficult to activate than pyramidal <a> slip in Ti-5Al-2.5Sn.
6. Under all conditions in Ti-3Al-2.5V, both the mean pyramidal <a>-to-basal CRSS ratio (0.81-1.2) and the mean T1 twin-to-basal CRSS ratio (0.22-2.8) are significantly smaller than the mean pyramidal <c+a> to basal CRSS ratio (6.3-12.3).
7. Under all conditions in CP Ti and Ti-3Al-2.5V, the CRSS of prismatic slip is no more than 53% and 50% of the CRSS of basal slip respectively, while in Ti-5Al-2.5Sn and Ti-6Al-4V the CRSS of prismatic slip is at least 60% and 77% of the CRSS of basal slip respectively. This suggests that basal slip is more likely to activate in alloys containing high Al content.

(a)

Ti5Al2.5Sn 296K tension experimental observations					
SF	Basal	Prism	Pyr <A>	Pyr <C+A>	T1 Twin
0-0.05	0	1	0	0	0
0.05-0.1	0	3	0	0	0
0.1-0.15	0	2	0	0	0
0.15-0.2	0	8	0	0	0
0.2-0.25	0	7	0	0	0
0.25-0.3	5	13	0	0	1
0.3-0.35	5	11	0	1	0
0.35-0.4	18	16	1	1	0
0.4-0.45	25	16	2	1	1
0.45-0.5	32	24	4	6	0

Construct PDF

Resample Data $M = 2000$ Times

(b)

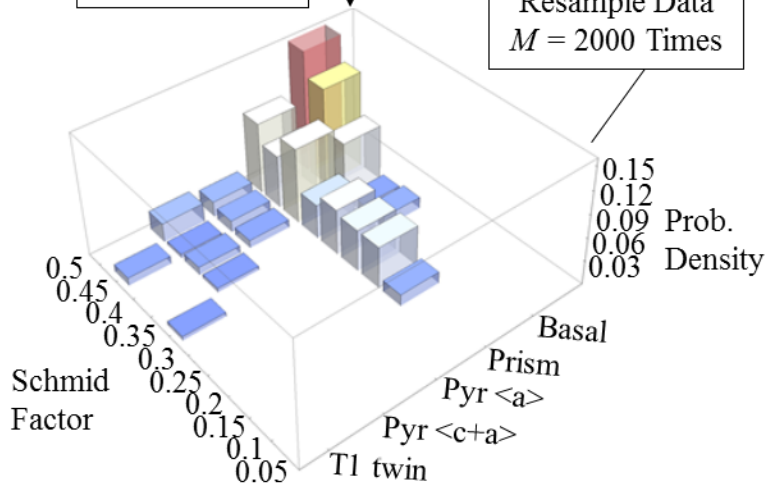

(c)

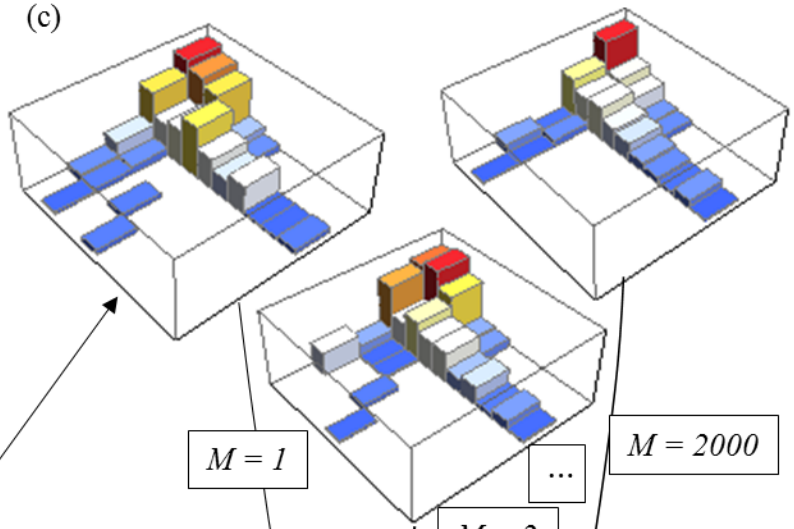

Solve Optimization Problem $M = 2000$ Times

(d)

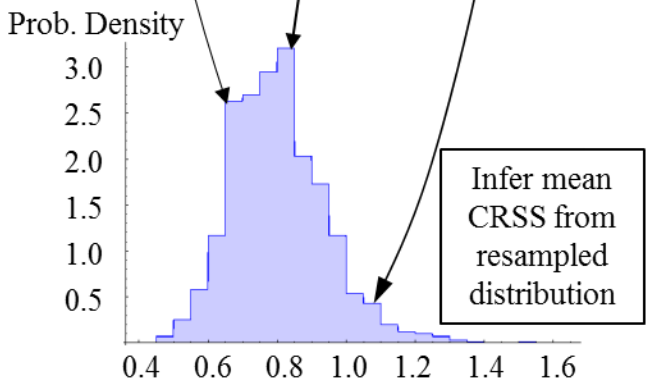

Figure 6.2 The bootstrap method applied to computing CRSS ratios for Ti-5Al-2.5Sn tensile tested at 296K to 3.5% strain. (a): Original experimental observations. (b): Probability density function (PDF) constructed directly from observations. (c): Exemplar pseudo dataset resulting from one possible sample of the PDF given in (b). (d): Probability density function constructed from of the optimal Prismatic/Basal CRSS ratios that result from 2000 resamples of the original dataset in (a).

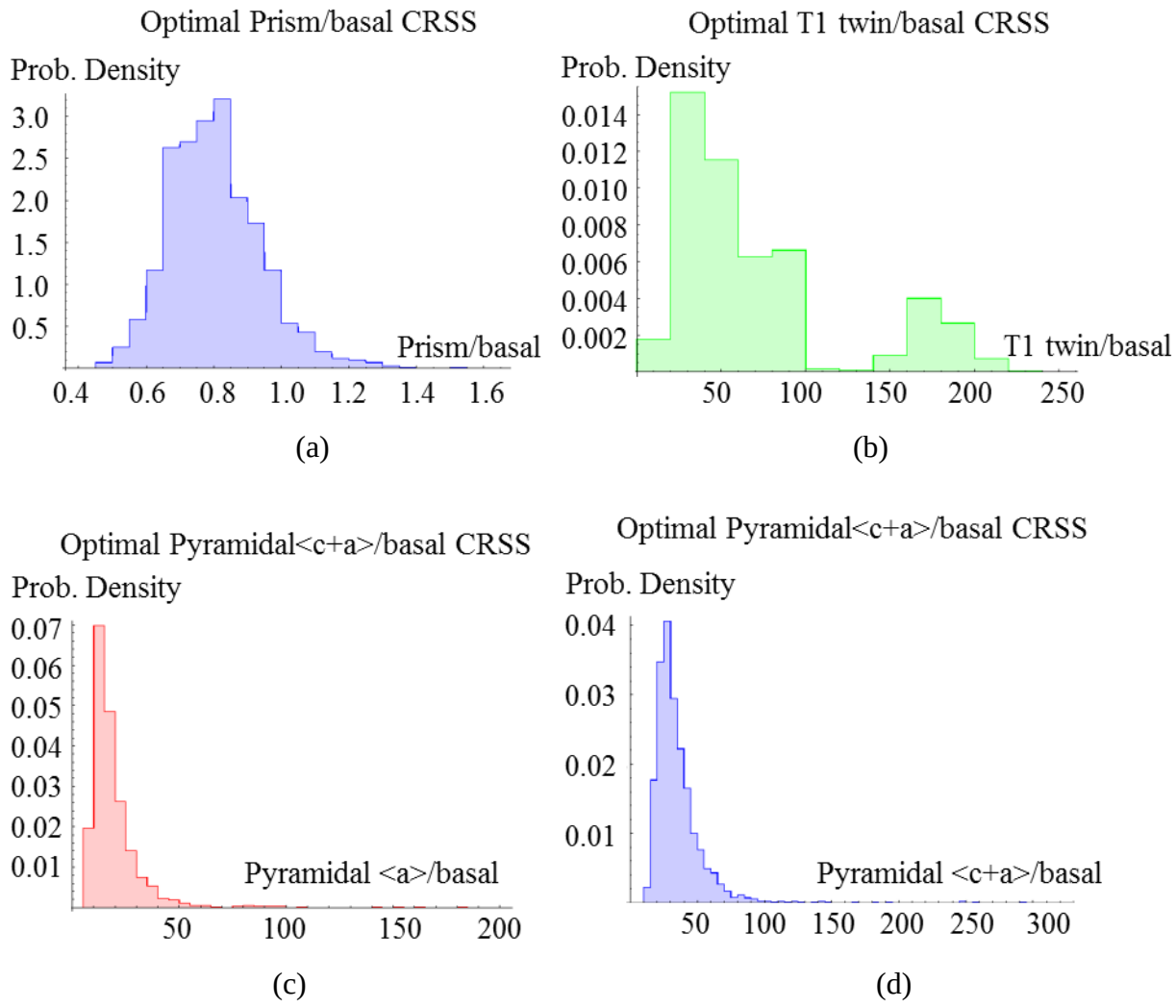

Figure 6.3 Resampling probability density functions for Ti-5Al-2.5Sn tensile tested at 296K and 3.5% strain. The second low peak in the T1 Twin / Basal CRSS ratio is due to the existence of only two T1 Twin observations with different Schmid factors. Although the Pyramidal <a>/Basal and Pyramidal <c+a> / Basal CRSS ratio distributions exhibit overlap, the populations also are nevertheless visually distinct.

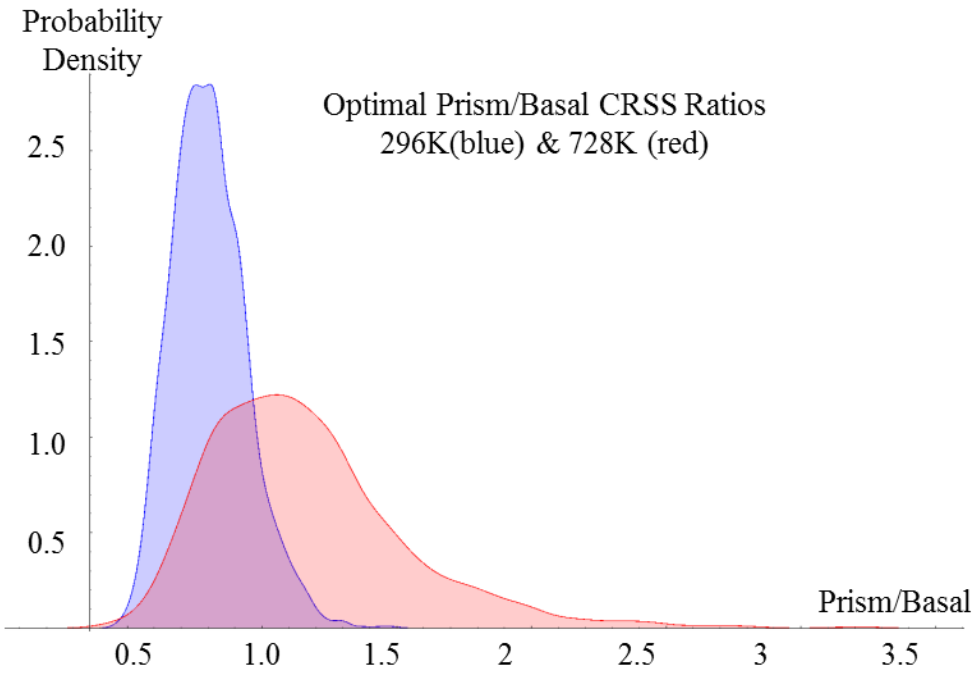

Figure 6.4 Smoothed resampling probability density functions for Ti-5Al-2.5Sn tensile tested at both 296K and 3.5% strain (Blue), and at 728K and 4.4% strain (red). Although spread in the densities prohibit a definitive statistical statement about the relative sizes of these ratios (see Table 6.9), a clear visual distinction between the two populations exists.

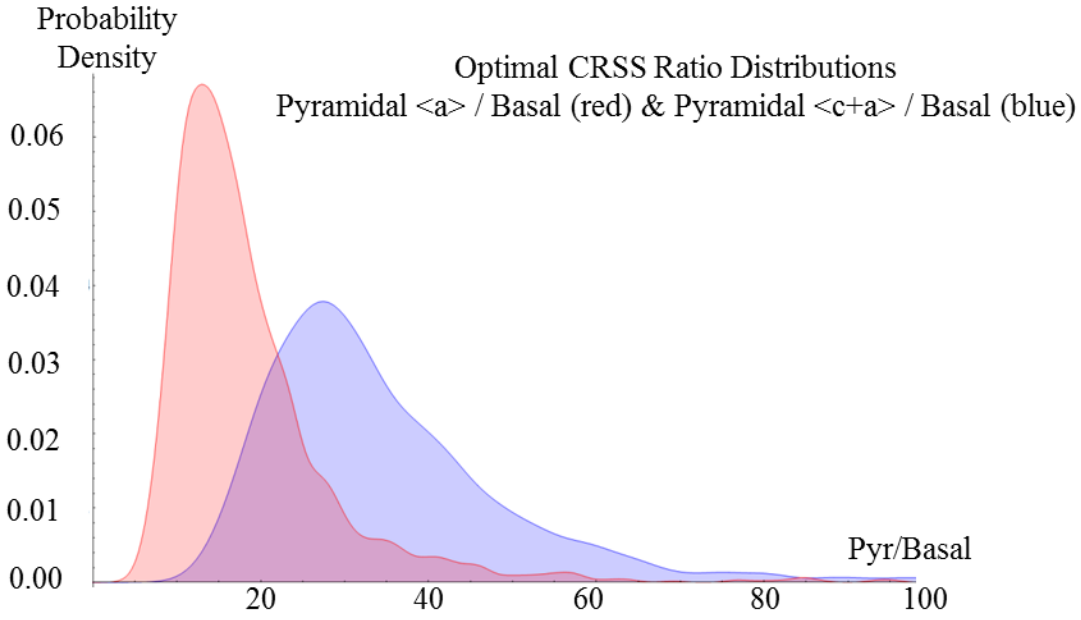

Figure 6.5 Smoothed resampling probability density functions for the pyramidal <a> / basal CRSS ratios (red) and the pyramidal <c+a> CRSS ratios (blue) in Ti-5Al-2.5Sn tensile tested at 296K and 3.5% strain. The densities suggest that the CRSS ratio for pyramidal <a>/basal is significantly less than the pyramidal <c+a>/basal CRSS ratio.

6.4 Broader Implications

Overall, the novel approach outlined here provides a flexible manner to assess the CRSS for a variety of deformation systems, and it has the potential to be applied to a wide range of materials and crystal systems. The CRSS ratio values can be obtained within one week using this methodology, including the time for performing the in-situ test and analyzing slip traces to generate experimentally-observed deformation system-Schmid factor distribution. When combined with the knowledge of specific CRSSs that are more easily obtained using more conventional methods, such as for the CRSS of prismatic slip in Ti, the absolute values of the CRSSs of slip systems with higher slip resistance can be determined. This technique allows these values to be determined over a wide range of temperatures, as long as the tests do not inhibit the observation of slip lines. Furthermore, this technique should be viable for determining CRSS ratios in multiphase materials, where most traditional approaches cannot be used. To date, the approach has also been shown to work well for the CRSS ratio estimation of Mg-RE alloys tested over a range of temperatures [Ying et al., to be submitted, 2013]. Access to these parameters has the potential to allow for more advanced modeling and understanding of materials behavior in the future.

It is important to note that the methodology presented in this work only identifies slip activity indirectly through the observation of surface slip traces. This approach has the potential to miss the activation of some deformation systems. First, slip systems with Burgers vectors parallel to the sample surface will not develop observable slip traces. Likewise, diffuse slip will not lead to well-defined slip bands. Furthermore, the deformation systems observed at the surface may not reflect the subsurface activity, as the nature of the constraint will change, which may affect the activation of the various deformation systems. It would be instructive to combine

the methodology outlined here with subsurface characterization techniques, such as transmission electron microscopy (TEM) or XRD methods to determine if the surface observations accurately reflect the subsurface activity. These approaches could be used as a check for specific grain observations, but it would be difficult to carry out enough observations to have the statistical robustness of the methodology presented here.

CHAPTER 7

SUMMARY AND CONCLUSIONS

7.1 Summary

This dissertation describes a systematic study of the deformation behavior of the CP Ti, Ti-5Al-2.5Sn, Ti-3Al-2.5V, and Ti-6Al-4V alloys. The effect of temperature on the active deformation modes was investigated for each of the four above mentioned materials. For Ti-3Al-2.5V and Ti-6Al-4V, the effect of texture on the active deformation modes was also investigated. In addition, the effect of alloy composition on the microstructure, YS, and deformation modes was investigated and compared for these four materials. Finally, a novel methodology of calculating the mean CRSS ratios of the different deformation systems was developed. This methodology has been successfully employed to calculate the mean CRSS ratios for each of the deformation systems in each of the materials tensile deformed in this work. The insights gained from these studies have a broad impact on understanding the heterogeneous deformation processes in Ti and Ti alloys and also on development of CPFE modeling.

7.2 Conclusions

7.2.1 Deformation behavior of CP Ti

(1) With increasing temperature, the YS of CP Ti decreased from ~440MPa to ~62MPa, which represents a decrease by a factor of ~7.

(2) Prismatic slip was the most likely slip system to activate during tension at both 296K and 728K. Basal slip and twinning were not as active as prismatic slip.

(3) The relative CRSS of prismatic slip and twinning to basal slip was not significantly affected with increasing temperature from 296K to 728K, while the relative CRSS of pyramidal <a> and pyramidal <c+a> slip decreased slightly.

(4) At ~4% strain, the mean CRSS ratios of basal, prismatic, pyramidal <a>, pyramidal <c+a>, and T1 twin were 1: 0.28: 7.1: 6.3: 1.7, respectively, for the 296K tensile deformation and 1: 0.29: 5.4: 4.7: 1.8, respectively, for the 728K tensile deformation.

(5) Dislocation slip was the primary deformation mechanism during 728K-45MPa creep deformation of CP Ti. During creep, prismatic remained the most active deformation system.

7.2.2 Deformation behavior of Ti-5Al-2.5Sn

(1) With increasing temperature, the YS of Ti-5Al-2.5Sn decreased from ~660MPa to ~330MPa, which represents a decrease factor of 2.

(2) Basal and prismatic slip systems were dominant for the 296K and 728K tension experiments. With increased temperature, basal slip systems became easier to activate, implying that the CRSS for basal slip decreases with increasing temperature. Twinning was almost completely suppressed in Ti-5Al-2.5Sn.

(3) At ~4% strain, the mean CRSS ratios of basal, prismatic, pyramidal <a>, pyramidal <c+a>, and T1 twin were 1: 0.81: 19.1: 35.5: 74, respectively, for the 296K tensile deformation and the mean CRSS ratios of basal, prismatic, pyramidal <a>, and pyramidal <c+a> were 1: 1.17: 16.7: 24.4, respectively, for the 728K tensile deformation.

(4) During creep, slip was observed to a significantly lesser extent than for the higher-stress tension experiments. Instead GBS was dominant. With decreasing temperature, GBS activity increased. Grain boundaries with larger misorientations and orientations nearly perpendicular to the loading axis tended to form ledges earlier in the deformation process during

creep. Most of the grain boundary cracks formed in association with grains displaying hard orientations, where the c-axis was nearly perpendicular to the tensile direction.

(5) The transition from GBS to dislocation slip during creep appeared to be around an applied creep stress close to the YS, based on the observation of a significantly increased fraction of grains which exhibited slip traces in the highest-stress creep experiment at 728K, compared to the 728K tensile test.

(6) During creep, prismatic slip was much less active than basal slip. However, the prismatic slip activity was increased by both increased creep stress and temperature.

7.2.3 Deformation behavior of Ti-3Al-2.5V

(1) With increasing temperature from 296K to 728K, the YS of Ti-3Al-2.5V decreased from ~580MPa to ~250MPa, which represents a decrease by a factor of ~2.

(2) Prismatic slip was the dominant slip mode in all the specimens tested. Specimens from plate 1, where the texture favored the activation of prismatic slip, showed significantly greater percentages of prismatic slip than specimens from plate 2, which exhibited textures that were less favorably orientated for prismatic slip.

(3) Twinning was an active deformation mode in both 296K and 728K tension experiments. Compared to plate 1, there were higher fractions of T1 twinning activity in plate 2, which was more favorably orientated for activating T1 twinning systems, at both 296K and 728K tension. Less twinning activity was observed at 728K, compared with 296K, suggesting that increasing temperature suppresses twinning in Ti-3Al-2.5V.

(4) More dislocation slip and grain boundary relief were observed during the 728K tension test compared with the 296K tension tests, due to the elevated temperature condition.

(5) For plate 2, the mean CRSS ratios of basal, prismatic, pyramidal <a>, pyramidal <c+a>, and T1 twin were 1: 0.05: 1.1: 11.9: 0.22, respectively, for the 296K tensile deformation after 6.5% strain and were 1: 0.2: 1.2: 6.3: 2.2, respectively, for the 728K tensile deformation after 9.7% strain.

(6) During creep, GBS appeared to be more active than dislocation slip.

7.2.4 Deformation behavior of Ti-6Al-4V

(1) With increasing temperature from 296K to 728K, the YS of Ti-6Al-4V decreased from ~810MPa to ~420MPa, which represents a decrease by a factor of ~2.

(2) Both basal and prismatic slip systems were the primary deformation systems observed during the 296K and 728K tensile tests. CRSS analysis indicated that the CRSS of basal slip was the lowest in all the deformation modes for all of the tensile tests, while the CRSS of prismatic slip was slightly higher. This is different from both CP Ti and Ti-3Al-2.5V, where the CRSS of prismatic slip was significantly lower than that for basal slip.

(3) Similar to Ti-5Al-2.5Sn, twinning was observed to a much lesser extent in Ti-6Al-4V than CP Ti and Ti-3Al-2.5Sn. This is explained by the presence of relatively high Al content which suppresses twinning formation.

(4) Compared with other materials, Ti-6Al-4V exhibited the highest YS at both 296K and 728K. This is mainly because of the solid-solution strengthening and grain boundary strengthening (relative fine grain size compared to CP Ti and Ti-5Al-2.5Sn).

(5) The mean CRSS ratios of basal, prismatic, pyramidal <a>, pyramidal <c+a>, and T1 twin were 1: 1.2: 13.2: 38: 27, respectively, for the 296K tensile deformation after 6.3% strain and were 1: 1.38: 20.2: 40.2: 8.4, respectively, for the 728K tensile deformation after 3.8% strain.

(6) During creep, GBS was the dominant deformation mechanisms and no surface slip traces were observed.

7.2.5 Summary of new insight and understanding that came from this work

This thesis provides a comprehensive study of the deformation behavior of polycrystalline CP Ti, Ti-5Al-2.5Sn, Ti-3Al-2.5V, and Ti-6Al-4V alloys under various testing conditions. In the literature, there has been no systematic study that has compared the relative CRSS values of the different deformation systems change as a function of alloy composition and temperature, as typically there are comparisons between two conditions or two alloys. This research provides a broad comparison of these relationships over the relevant range of alloy compositions. There are three important findings came from this work, which provided new insight and understanding about the deformation mechanisms of polycrystalline Ti alloys. First, similar to the work of Williams et al. [2002] on single crystals, high Al content in polycrystalline Ti alloys significantly promotes basal slip relative to prismatic slip, resulting in enhanced basal slip activity in the alloys with high Al content (i.e. Ti-5Al-2.5Sn and Ti-6Al-4V). Increasing temperature also results in an increase in basal slip activity in polycrystalline Ti alloys (except for CP Ti, where the prismatic/basal CRSS ratio did not change with temperature). Therefore, the fact that basal slip activity increases with increasing Al and testing temperature is unaffected by the polycrystalline microstructure, as compared to single crystals. Second, O may be a more important factor influencing the twinning activity than Al at low temperature but a less important factor at elevated temperature. High Al and high O are generally believed to suppress twinning activation [Paton et al. 1976, Williams et al. 2002, and Zeafferer 2003]. Which factor is more influential in twinning formation is unclear in the literature. The twinning activity observed in

the Ti-3Al-2.5V plate 2 296K tensile test (23%) was more than twice the activity observed in the CP Ti at 296K (10%) and the twinning systems with Schmid factors greater than 0.4 were similar in the textures of these two specimens (see Table 5.2). It is important to note that twins are more likely to occur in large grains [Conrad 1981], suggesting that the CP Ti with a large grain size of 140μm should favor the activation of twins more than the Ti-3Al-2.5V with a small grain size of 5.1μm. Therefore, the unexpected high twinning activity observed in the Ti-3Al-2.5V alloy in the present study is very likely due to the low O content (0.092 wt.% for plate 2, see Table 3.1), compared to the 0.25 wt.% O of CP Ti. Ti-6Al-4V with 0.24 wt.% O (high Al and high O) exhibited much less twinning activity than CP Ti and Ti-3Al-2.5V at 296K. However, at elevated temperature, there was much less twinning activity in Ti-3Al-2.5V and Ti-6Al-4V, compared to CP Ti, indicating that high Al may be a more influential factor in suppressing twinning formation than high O at elevated temperature. Third, texture is a very important factor influencing the relative activity of the different deformation systems. Different slip/twin activities were observed for the two Ti-3Al-2.5V plates with different textures at both 296K and 728K as well as for the two Ti-6Al-4V 728K tensile-tested specimens with different textures (i.e. different microzones). Using the CRSS methodology developed in this dissertation, the effect of texture on the relative activation of the different deformation systems was considered to have a linear relationship with Schmid factors. However, this relationship is complicated by the dislocation interaction and local deformation accommodation requirements imposed by neighboring grains that lead to heterogeneous deformation. Therefore, a texture with a variety of grain orientations (i.e. weak texture) is beneficial to understand the relative activity of the different deformation systems.

7.3 Recommendations for future work

(1) To gain a deeper understanding of the deformation mechanisms in polycrystalline Ti alloys as a function of alloying composition, future work can focus on studying other Ti alloys with different compositions to compare the deformation system activation with the results found in this dissertation work. For example, the present work indicates that higher Al content suppresses twining formation but whether this trends is still valid for alloys with Al content more than 6 wt.% is unknown.

(2) To gain a larger statistical data set, multiple areas (e.g. 4) could be imaged during *in-situ* tests at various strain levels, especially for the early stage of the deformation process. More images at the early stage of the deformation process would help build a better statistical understanding of the deformation system distribution just before and just after global yielding.

(3) To gain a better understanding of the heterogeneous deformation, future *in-situ* tests can be incorporated with *in-situ* EBSD mapping. The combination of grain orientation and surface deformation evolution can be used to promote a better understanding of the deformation behavior, especially at the early stages of the deformation process, where most of the damage nucleation occurs.

(4) To gain a better understanding of the dislocation activity beneath specimen surface, future work may use other methods to study the subsurface dislocation activity, such as TEM and XRD. All the results and conclusions made on the deformation system activity in this dissertation are based on the surface slip-trace analysis technique. It is still unknown how well the results based on this technique can reflect the subsurface deformation activity. Thus, studying the subsurface dislocation activity may be a target for future work.

(5) To gain a better understanding of the surface cracking phenomenon observed during the *in-situ* creep deformation of Ti-6Al-4V, future work can study the effect of environment on the surface deformation behavior, especially at elevated temperature.

APPENDIX

APPENDIX

The following Matlab code provides a visualization of the calculated plane traces for all the deformation systems as well as a calculation of the Schmid factors for all the deformation systems for a given orientation. The input orientation of a particular grain is three Euler angles ($\phi 1$, Φ, $\phi 2$), given by the EDAX EBSD software. In this example, $\phi 1=323.096$, $\Phi=51.790$, $\phi 2=12.66$. The variable "ssa" contains the 24 common slip systems in Ti, where the slip plane normal directions and slip directions are stored in 24 cells of this variable. In particularly, basal slip systems are stored in cells No.1-3. Prismatic slip systems are stored in cells No.4-6. Pyramidal <a> slip systems are stored in cells No.7-12. Pyramidal <c+a> slip systems are stored in cells No.13-24. In the EBSD coordinate system, x-axis is pointing down and y-axis is pointing right. Therefore, the stress tensor is defined to be [0,0,0;0,1,0;0,0,0]. However, in the lab coordinate system, x-axis is pointing right and y-axis is pointing up. In order to compare the calculated slip traces based on the EBSD coordinate with the SE/BSE images based on the lab coordinate, additional 90° degree counterclockwise rotation need to be performed on the calculated slip traces, which is outputted by the Matlab™ code as a figure.

```
% code wrote by Hongmei Li in year 2010
clc;
clear;
close
%  basal <a>-glide
ssa(:,:,1) = [0 0 0 1; 2 -1 -1 0];
ssa(:,:,2) = [0 0 0 1; -1 2 -1 0];
ssa(:,:,3) = [0 0 0 1; -1 -1 2 0];
%  prism <a>-glide
ssa(:,:,4) = [0 1 -1 0; 2 -1 -1 0];
ssa(:,:,5) = [1 0 -1 0; -1 2 -1 0];
ssa(:,:,6) = [-1 1 0 0; -1 -1 2 0];
```

```
%  pyramidal <a>-glide
ssa(:,:,7) = [0 1 -1 1; 2 -1 -1 0];
ssa(:,:,8) = [1 0 -1 1; -1 2 -1 0];
ssa(:,:,9) = [-1 1 0 1; -1 -1 2 0];
ssa(:,:,10) = [0 -1 1 1; 2 -1 -1 0];
ssa(:,:,11) = [-1 0 1 1; -1 2 -1 0];
ssa(:,:,12) = [1 -1 0 1; -1 -1 2 0];
%  pyramidal <c+a>-glide
ssa(:,:,13) = [1 0 -1 1; 2 -1 -1 -3];
ssa(:,:,14) = [1 0 -1 1; 1 1 -2 -3];
ssa(:,:,15) = [0 1 -1 1; 1 1 -2 -3];
ssa(:,:,16) = [0 1 -1 1; -1 2 -1 -3];
ssa(:,:,17) = [-1 1 0 1; -1 2 -1 -3];
ssa(:,:,18) = [-1 1 0 1; -2 1 1 -3];
ssa(:,:,19) = [-1 0 1 1; -2 1 1 -3];
ssa(:,:,20) = [-1 0 1 1; -1 -1 2 -3];
ssa(:,:,21) = [0 -1 1 1; -1 -1 2 -3];
ssa(:,:,22) = [0 -1 1 1; 1 -2 1 -3];
ssa(:,:,23) = [1 -1 0 1; 1 -2 1 -3];
ssa(:,:,24) = [1 -1 0 1; 2 -1 -1 -3];
euler=[ 323.096   51.790   12.66 ]; % input three Euler angles here
sliptrace=[0,0,0]; % define the calculated sliptrace to be a 1×3 Zero vector
phi1=euler(1,1);
PHI=euler(1,2);
phi2=euler(1,3);
g11=cosd(phi1)*cosd(phi2)-sind(phi1)*sind(phi2)*cosd(PHI);
g12=sind(phi1)*cosd(phi2)+cosd(phi1)*sind(phi2)*cosd(PHI);
g13=sind(phi2)*sind(PHI);
g21=-cosd(phi1)*sind(phi2)-sind(phi1)*cosd(phi2)*cosd(PHI);
g22=-sind(phi1)*sind(phi2)+cosd(phi1)*cosd(phi2)*cosd(PHI);
g23=cosd(phi2)*sind(PHI);
g31=sind(phi1)*sind(PHI);
g32=-cosd(phi1)*sind(PHI);
g33=cosd(PHI);
g=[g11,g12,g13;g21,g22,g23;g31,g32,g33]; %define the rotation matrix
sigma=[0,0,0;0,1,0;0,0,0]; %define the global stress state tensor
c_a=1.59; %define the c/a ratio of Ti

for i=1:1:24            % Change n & m to unit vector
   n=[ssa(1,1,i)  (ssa(1,2,i)*2+ssa(1,1,i))/3^.5  ssa(1,4,i)/c_a]; % Plane normal of a slip system
   m=[ssa(2,1,i)*1.5  3^.5/2*(ssa(2,2,i)*2+ssa(2,1,i))  ssa(2,4,i)*c_a]; % Slip direction of a slip
system
   ss(1,:,i) = n/norm(n);  % normalization of the slip plane normal direction
   ss(2,:,i) = m/norm(m);  % normalization of the slip direction
end
```

```
for j=1:1:24 %This loop includes the calculation of plane traces and plotting the plane traces in the coordinate system where x-axis pointing down and y-axis pointing right
plane=ss(1,:,j);
plane=plane';
rot_plane=g'*plane; % rotate slip plane normal direction from the crystal coordinate to lab coordinate
z=[0,0,1];
sliptrace(:,:,j)=cross(rot_plane',z); % perform cross product of the rotated slip plane normal direction and the [001] direction in the lab coordinate
x=sliptrace(1,1,j);
y=sliptrace(1,2,j);
X=[0,x];
Y=[0,y];
axis([-1.2 1.2 -1.2 1.2])
axis square  % The figure plotted here need to be counterclockwise rotated by 90 degrees to match the lab coordinate where x-axis is pointing right and y-axis is point up.

if j<4 %This part is to get a prorate number to calculate the space between the slip system labels
    k=j;
elseif j<=6
    k=j-4;
elseif j<=9;
    k=j-5;
elseif j<=12;
    k=j-7.5;
elseif j<=15;
    k=j-12;
elseif j<=18;
    k=j-15;
elseif j<21;
    k=j-18;
else
    k=j-21;
end

if j>=7 % use black color to plot the calculated plane traces and label the slip system numbers
plot(X,Y,'k'); text(x-0.09*k,y,num2str(j));
else
   plot(X,Y,'k'); text(x-0.08*k,y,num2str(j));
end
hold on
end;

for i=1:1:24 % Schmid factor calculation
a=ss(1,:,i);
b=ss(2,:,i);
```

```
schmidfactor(i)=a*sigma*b';
end
rot_c=g'*[0 0 1]'; % This part is to calculate the angle between c-axis of a particular orientation and the tensile direction
angle_C=acosd([0 1 0]*rot_c);
if angle_C>90
   angle_C=180-angle_C
else
```

BIBLIOGRAPHY

BIBLIOGRAPHY

ASTM, 2004, E112-96 standard test methods for determining average grain size.

Ashby M.F., 1972, A first report on deformation-mechanism maps, Acta Metallurgica, Vol. 20, No. 7, pp. 887-897.

Ayensu A. and Langdon T.G., 1996, The inter-relationship between grain boundary sliding and cavitation during creep of polycrystalline copper, Metallurgical and Materials Transactions A, Vol. 27, No. 4, pp. 901-907.

Le Biavant R., Pommier S., and Prioup C., 2002, Local texture and fatigue crack initiation in a Ti-6Al-4V titanium alloy, Fatigue and Fracture of Engineering Materials & Structures, Vol. 25, No. 6, pp. 527-454.

Bache M.R., 2003, A review of dwell sensitive fatigue in titanium alloys: the role of microstructure, texture and operating conditions, International Journal of Fatigue, Vol. 25, No. 9-11, pp. 1079-1087.

Balasubramanian S. and Anand L., 2002, Plasticity of initially textured hexagonal polycrystals at high homologous temperatures: application to titanium, Acta Matererilia, Vol. 50, No. 1, pp. 133-148.

Barnett M.R., Nave, M.D., and Bettles, C.J., 2004, Deformation microstructure and textures of some cold rolled Mg alloys, Matererials Science and Engineering. A, Vol. 386, No. 1-2, pp. 205-211.

Barnett M. R., Ghaderi, A., Sabirov, I. and Hutchinson, B., 2009, Role of Grain Boundary Sliding in the Anisotropy of Magnesium Alloys, Scripta Materialia, Vol. 61, No. 3, pp. 277-280.

Bevis M. and Crocker A. G., 1968, Twinning shears in lattices, Proceedings of the Royal Society A, Vol. 304, No. 1476, pp. 123-134.

Beyerlein I.J., Capolungo L., Marshall P.E., McCabe R.J., and Tome C.N., 2010, Statistical analyses of deformation twinning in magnesium, Philosophical Magazine, Vol. 90, No. 16, pp. 2161–2190.

Bieler T.R and Semiatin S.L., 2002, The origins of heterogeneous deformation during primary hot working of Ti–6Al–4V, International Journal of Plasticity, Vol. 18, No. 9, pp. 1165-1189.

Bieler T.R., Nicolaou P.D, and Semiatin S.L., 2005a, An experimental and theoretical investigation of the effect of local colony orientations and misorientation on cavitation during hot working of Ti-6Al-4V, Metallurgical and Materials Transactions A, Vol. 36A, No. 1, pp. 129-140.

Bieler T.R., Goetz R.L., and Semiatin S.L, 2005b, Anisotropic plasticity and cavity growth during upset forging of Ti–6Al–4V, Materials Science and Engineering A, Vol. 405, No. 1-2, pp. 201-213.

Bieler T.R., Wang L., Beaudoin A.J., Kenesei P., and Lienert U., 2013, In situ characterization of twin nucleation in pure Ti using 3D-XRD, Metallurgical and Materials Transactions A, in press.

Bingert J.F., Mason T.A., Kaschner G.C., Maudlin P.J., and Gray G.T., 2002. Deformation twinning in polycrystalline Zr: Insights from electron backscattered diffraction characterization. Metallurgical and Materials Transactions A, Vol. 33, No. 3, pp. 955-963.

Boehlert C.J., Chen Z., Gutiérrez-Urrutia I., Llorca J., and Pérez-Prado M.T, 2012, In situ analysis of the tensile and tensile-creep deformation mechanisms in rolled AZ31, Acta Materialia, Vol. 60, No. 4, pp. 1889–1904.

Boyer R., 1996, An overview on the use of titanium in the aerospace industry, Materials Science and Engineering A, Vol. 213, No. 1-2, pp. 103-114.

Boyer R., Welsch G., and Collings E.W., editors. Materials Properties Handbook: Titanium Alloys. Materials Park, OH: ASM International, 1994.

Bridier F., Villechaise P., and Mendez J., 2005, Analysis of the different slip systems activated by tension in a α/β titanium alloy in relation with local crystallographic orientation, Acta Materialia, Vol. 53, No. 3, pp. 555-567.

Bridier F., Villechaise P., and Mendez J., 2008, Slip and fatigue crack formation processes in a α/β titanium alloy in relation to crystallographic texture on different scales, Acta Materialia, Vol. 56, No. 15, pp. 3951-3962.

Buckley D. and Johnson R., NASA Tech. Note, 1966, TN-D-3235.

Burgers W.G., 1934, On the process of transition of the cubic-body-centered modification into the hexagonal-close-packed modification of zirconium, Physica, Vol. 1, No. 7-12, pp. 561-586.

Callister W. D. and Jr. Rethwisch D.G., Materials Science and Engineering: An Introduction, 8th ed., Wiley, New York 2009

Cannon W.R. and Nix W.D., 1973, Models for grain rearrangement resulting from grain boundary sliding, Philosophical Magazine, Vol. 27, No. 1, pp. 9-16.

Chan K.S., 2004, A micromechanical analysis of the yielding behavior of individual widmanstätten colonies of an α+ β titanium alloy, Metallurgical and Materials Transactions A, Vol. 35, No. 11, pp. 3409-3422.

Chokshi A.H., 1990, An evaluation of the grain-boundary sliding contribution to creep deformation in polycrystalline alumina, Journal of Materials Science, Vol. 25, No. 7, pp. 3221-3228.

Christian J.W. and Mahajan S., 1995, Deformation twinning, Progress in Materials Science, Vol. 1995, No.1-2, pp.1-157.

Churchman A.T., 1954, The slip modes of titanium and the effect of purity on their occurrence during tensile deformation of single crystals, Proceedings of the Royal Society A, Vol. 226, No. 1165, pp. 216-226.

Clarisse L., Bataille A., Pennec Y., Crampon J., and Duclos R., 1999, Investigation of grain boundary sliding during superplastic deformation of a fine-grained alumina by atomic force microscopy, Ceramics International, Vol. 25, No. 4, pp. 389–394.

Clementi E., Raimondi D.L, and Reinhardt W.P., 1963, Atomic screening constants from SCF functions, The Journal of Chemical Physics, Vol. 38, No. 11, pp. 2686-2689.

Conrad H., 1981, Effect of interstitial solutes on the strength and ductility of titanium, Progress in Materials Science, Vol. 26, pp. 123-403.

Crossman F. W. and Ashby M. F., 1975, The non-uniform flow of polycrystals by grain-boundary sliding accommodated by power-law creep, Acta Metallurgica, Vol. 23, No. 4, pp. 425-440.

Croarkin C., Tobias P., NIST/SEMATECH e-Handbook of Statistical Methods, http://www.itl.nist.gov/div898/handbook/index.htm, April 2012.

Dick T. and Cailletaud G., 2006, Fretting modelling with a crystal plasticity model of Ti6Al4V, Computational Materials Science, Vol. 38, No.1, pp. 113-125.

Dieter G. E. Mechanical Metallurgy, 3rd ed., New York: McGraw-Hill, 1986.

Di Iorio S., Briottet L., Cayron C., Rauch E.F., and Guichard D., 2004, Damage Mechanisms at a Microscopic Scale of PM Ti-6Al-4V at 20 K, Journal of Materials Science & Technology, Vol. 20, pp. 15–18.

Di Iorio S., Briottet L., Cayron C., Rauch E.F., and Guichard D., 2007, Plastic deformation, damage and rupture of PM Ti–6Al–4V at 20K under monotonic loading , Acta Materialia, Vol. 55, No. 1, pp. 105–118.

Dunst D. and Mecking H., 1996, Analysis of experimental and theoretical rolling textures of two-phase titanium alloys, Z. Metallkde, Vol. 87, pp. 498.

Donachie M.J., Titanium — A Technical Guide (Second Edition) ASM International, OH, USA, 1988.

Evans W.J. and Bache M.R., 1994, Dwell-sensitive fatigue under biaxial loads in the near-alpha titanium alloy IMI685, International Journal of Fatigue, Vol. 16, No. 7, pp. 443-452.

Feaugas X., Pilvin P., and Clavel M., 1997, Cyclic deformation behaviour of an α/β titanium alloy—II. Internal stresses and micromechanic modelling, Acta Materialia, Vol. 45, No. 7, pp. 2703-2714.

Fisher E.S. and Renken C.J., 1964, Single-crystal elastic moduli and the hcp→bcc transformation in Ti, Zr, and Hf, Phys Rev 2A, Vol. 135, No. 2A, pp. 482-494.

Flegler S.L., Heckman J.W.Jr., and Klomparens K.L., Scanning and Transmission Electron Micrscopy: An Introduction, W.H.Freeman, New York, 1993.

Frost H.J. and Ashby M.F., Deformation-Mechanism Maps, The Plasticity and Creep of Metals and Ceramics, Pergamon Press, New York, 1982.

Germain L., Gey N., Humbert M., Bocher P., and Jahazi M., 2005, Analysis of sharp microtexture heterogeneities in a bimodal IMI 834 billet, Acta Materialia, Vol. 53, No. 13, pp. 3535-3543.

Germain L., Gey N., Humbert M., Vo P., Jahazi M., and Bocher P., 2008, Texture heterogeneities induced by subtransus processing of near α titanium alloys, Acta Materialia, Vol. 56, No. 16, pp. 4298-4308.

Gey N., Bocher P., Uta E., Germain L., and Humbert M., 2012, Texture and microtexture variations in a near-α titanium forged disk of bimodal microstructure, Acta Materialia, Vol. 60, No. 6-7, pp. 2647-2655.

Ghaderi A. and Barnett M.R., 2011, Sensitivity of deformation twinning to grain size in titanium and magnesium, Acta Materilia, Vol. 59, No. 20, pp. 7824-7839.

Gifkins R.C., 1976, Grain-boundary sliding and its accommodation during creep and superplasticity, Metallurgical Transaction A, Vol. 7, No. 8, pp. 1225-1232.

Gifkins R.C., 1994, Grain-boundary participation in high-temperature deformation: An historical review, Materials Characterization, Vol. 32, No. 2, pp. 59-77.

Glavicic M.G., Kobryn P.A., Bieler T.R., and Seminatin S.L., 2003 a, An automated method to determine the orientation of the high-temperature beta phase from measured EBSD data for the low-temperature alpha-phase in Ti–6Al–4V, Materials Science and Engineering A, Vol. 351, No.1-2, pp.258-264.

Glavicic M.G., Kobryn P.A., Bieler T.R., and Seminatin S.L., 2003 b, A method to determine the orientation of the high-temperature beta phase from measured EBSD data for the low-temperature alpha phase in Ti-6Al-4V, Materials Science and Engineering A, Vol. 346, pp.50-59.

Gollapudi S., Charit I., and Murty K.L., 2008, Creep mechanisms in Ti–3Al–2.5 V alloy tubing deformed under closed-end internal gas pressurization, Acta Materialia, Vol. 56, No. 10, pp. 2406-2419.

Gong J. and Wikinson A.J., 2009, Anisotropy in the plastic flow properties of single-crystal α titanium determined from micro-cantilever beams, Acta Materialia, Vol. 57, No. 19, pp. 5693-5705.

Guo Z., Miodownik A.P., Saunders N., and Schillé J-Ph, 2006, Influence of stacking-fault energy on high temperature creep of alpha titanium alloys, Scripta Materialia, Vol. 54, No. 12, pp. 2175-2178.

Ishiday Y. and Henderson-Brown M., 1967, Dislocations in grain boundaries and grain boundary sliding, Acta Metallurgica, Vol. 15, No. 5, pp. 857-860.

Johnson A.J.W., Bull C.W., Kumar K.S., and Briant C.L., 2003, The influence of microstructure and strain rate on the compressive deformation behavior of Ti-6Al-4V, Metallurgical and Materials Transactions A, Vol. 34, No. 2, pp. 295–306.

Joshi V. A., Titanium alloys: An Atlas of Structure and Fracture Features, Taylor & Francis Group, 2006.

Kalidindi S.R., Bhattacharyya A., and Doherty R.D., 2004, Detailed analyses of grain–scale plastic deformation in columnar polycrystalline aluminum using orientation image mapping and crystal plasticity models, Proceedings of the Royal Society A, Vol. 49, No. 2047, pp. 1935-1956.

Kalidindi S.R., Bronkhorst C.A., and Anand L., 1992, Crystallographic texture evolution in bulk deformation processing of FCC metals, Journal of the Mechanics and Physics of Solids, Vol. 40, No. 3, pp. 537-569.

Kanjarla A.K., Houtte P.V., and Delannay L., 2010, Assessment of plastic heterogeneity in grain interaction models using crystal plasticity finite element method, International Journal of Plasticity, Vol. 26, No. 8, pp. 1220-1233.

Kim S.M., Kin J., Shin D.H., Ko Y.G., Lee C.S., and Semiatin S.L., 2004, Microstructure development and segment formation during ECA pressing of Ti–6Al–4V alloy, Scripta Materialia, Vol. 50, No. 7, pp. 927-930.

Koike J., Ohyama R., Kobayashi T., Suzuki M., and Maruyama K., 2003, Grain-boundary sliding in AZ31 magnesium alloys at room temperature to 523 K, Materials Transaction, 2003, vol. 44, No. 4, pp. 445-451.

Langdon T.G., 1970, Grain boundary sliding as a deformation mechanism during creep, Philosophical Magazine, Vol. 22, No. 178, pp. 689-700.

Langdon T.G., 2006, Grain boundary sliding revisited: Developments in sliding over four decades, Journal of Materials Science, Vol. 41, No. 3, pp. 597-609.

Larson B.C., Yang W., Ice G.E., Budai J.D., and Tischler J.Z., 2002, Three-dimensional X-ray structural microscopy with submicrometre resolution, Nature, Vol. 415, pp. 887-90.

Lasalmonie A. and Strudel J.L., 1986, Influence of grain size on the mechanical behaviour of some high strength materials, Journal of Materials Science, Vol. 21, No. 6, pp. 1837-1852.

Lebensohn R.A. and Canova G.R., 1997, A self-consistent approach for modelling texture development of two-phase polycrystals: application to titanium alloys, Acta Materialia, Vol. 45, No. 9, pp. 3687-3694.

Leyens C. and Peters M., Titanium and Titanium Alloys, Fundamentals and Applications, Wiley–VCH GmbH & Co. KGaA , 2003.

Li H., Boehlert C.J., Bieler T.R., and Crimp M.A., 2012, Analysis of slip activity and heterogeneous deformation in tension and tension-creep of Ti–5Al–2.5Sn (wt%) using in-situ SEM experiments, Philosophical Magazine, Vol. 92, No. 23, pp. 2923-2946.

Li H., Mason D.E., Yang Y., Bieler T.R., Crimp M.A., and Boehlert C.J., 2013a, Comparison of the deformation behaviour of commercially pure titanium and Ti–5Al–2.5Sn (wt.%) at 296 and 728 K, Philosophical Magazine, Vol. 93, No. 21, pp. 2875-2895.

Li H., Mason D.E., Bieler T.R., Boehlert C.J., and Crimp M.A., 2013b, Methodology for estimating the critical resolved shear stress ratios of α-phase Ti using EBSD-based trace analysis, Acta Materialia, in press.

Lifshitzi M., 1963, On the theory of diffusion-viscous flow of polycrystalline bodies, Soviet Physics JETP, Vol. 17, pp. 909.

Liu W., Ice G. E., Larson B. C., Yang W., Tischler J. Z., and Budai J. D., 2004, The three-dimensional X-ray crystal microscope: A new tool for materials characterization, Metallurgical and Materials Transactions A, Vol. 35, No. 7, pp. 1963-1967.

Lüthy H., White R.A., and Sherby O.D., 1979, Grain boundary sliding and deformation mechanism maps, Materials Science and Engineering, Vol. 39, No. 2, pp. 211-216.

Lütjering G. and Williams J.C., Titanium, Springer-Verlag, Berlin, 2003.

Massalski T.B., Okamoto H., and Subramanian P.R., Binary alloy phase diagrams, Vol. 1-3, Materials Park, Ohio, ASM International, 1990.

Meyers M. and Chawla K., Mechanical Behaviors of Materials, 2nd edition, Cambridge University Press, 2009.

Mises R. von, 1913, Mechanik der Festen Korper im plastisch deformablen, Math-Phys., Vol. 1, pp. 582-592.

Miller Jr. RG., Beyond ANOVA: basics of applied statistics, New York (NY): Chapman & Hall/CRC; 1998.

Mohamed F.A. and Langdon T.G., 1974, Deformation mechanism maps based on grain size, Metallurgical Transactions, 1974, vol. 5, No. 11, pp. 2339-2345.

Molinari A., Canova G.R., and Ahzi S., 1987, A self consistent approach of the large deformation polycrystal viscoplasticity, Acta Materialia, Vol. 35, No. 12, pp. 2983-2994.

Morrissey R.J., McDowell D.L., and Nicholas T., 2001, Microplasticity in HCF of Ti–6Al–4V, International Journal of Fatigue, Vol. 23, pp. 55-64.

Murray J.L., The Sn-Ti (Tin-Titanium) System, Phase Diagrams of Binary Titanium Alloys, ASM International, Metals Park, OH, 1987.

Murray J.L. and Wriedt H.A., 1987, The O− Ti (Oxygen-Titanium) system, Journal of Phase Equilibria, Vol. 8, No. 2, pp.148-165.

Neeraj T., Hou D.H., Daehn G.S., and Mills M.J., 2000, Phenomenological and microstructural analysis of room temperature creep in titanium alloys, Acta Materialia, Vol. 48, No. 6, pp. 1225-1238.

Ottaviani G., Nava F., Quierolo G., Iannuzzi G., De Santi G., and Tu K.N., 1987, Low temperature oxygen dissolution in titanium, Thin Solid Films, Vol. 146, No. 2, pp. 201-207.

Okamoto H., Desk Handbook: phase diagram for binary alloys, ASM International, Materials Park Press, 2000.

Paton N.E., Williams J.C., and Rauscher G.P., 1973. Titanium science and technology. In: Jaffee RI, Burte HM, editors. In: Proceedings of the second international conference. New York: Plenum Press;

Paton N.E., Baggerly R.G., and Williams J.C., 1976, Deformation and Solid Solution Strengthening of Titanium-Aluminum Single Crystals, DTIC Document.

Peters M., Kumpfert J., Ward C.H., and Leyens, C., 2003, Titanium alloys for aerospace applications, Advanced Engineering Materials, Vol. 5, No. 6, pp. 419-427.

Philippe M.J., Serghat M., Vanhoutte P., and Esling C., 1995, Modelling of texture evolution for materials of hexagonal symmetry—II. Application to zirconium and titanium α or near α alloys, Acta Metallurgica et Materialia, Vol. 43, No. 4, pp. 1619–1630.

Pilchak A.L. and Williams J.C., 2010, Crystallography of fluted fracture in near-α titanium alloys, Metallurgical and Materials Transactions A, Vol. 41, No. 1, pp. 22-25.

Poty A., Raulot J.M., Xu H., Bai J., and Schuman C., 2011, Classification of the critical resolved shear stress in the hexagonal-close-packed materials by atomic simulation: Application to α-zirconium and α-titanium, Journal of Applied Physics, Vol. 110, No. 1, pp. 014905-014905-15.

Prakash A. and Lebensohn R.A., 2009, Simulation of micromechanical behavior of polycrystals: finite elements versus fast Fourier transforms, Modeling and Simulation in Materials Science and Engineering, Vol. 17, No. 17, pp .064010.

Prakash D.G., Ding R., Moat R.J., Jones I., Withers P.J., Quinta da Fonseca J., and Preuss M., 2010, Deformation twinning in Ti-6Al-4V during low strain rate deformation to moderate strains at room temperature, Materials Science and Engineering A, Vol. 527, No. 21–22, pp. 5734–5744.

Prakash D.G., Honniball P., Rugg D., Withers P.J., Quinta da Fonseca J., and Preuss M., 2013, The effect of β phase on microstructure and texture evolution during thermomechanical processing of α+ β Ti alloy, Acta Materialia, Vol. 61, No. 9, pp. 3200-3213.

Rachinger W.A., 1952, Relative grain translations in the plastic flow of aluminium, Journal of the Institute of Metals, Vol. 81, pp. 33-41.

Salem A.A., Glavicic M.G., and Semiatin S.L., 2008, A coupled EBSD/EDS method to determine the primary-and secondary-alpha textures in titanium alloys with duplex microstructures, Materials Science and Engineering A, Vol. 494, No. 1-2, pp. 350-359.

Salem A.A., Kalidindi S.R., and Semiatin S.L., 2005, Strain hardening due to deformation twinning in α-titanium: Constitutive relations and crystal-plasticity modeling, Acta Materialia, Vol. 53, No. 12, pp. 3495-3502.

Seal J.R., Crimp M.A., Bieler T.R., and Boehlert C.J., 2012, Analysis of slip transfer and deformation behavior across the α/β interface in Ti–5Al–2.5Sn (wt.%) with an equiaxed microstructure, Materials Science and Engineering A, 2012, Vol. 552, pp. 61-68.

Sector 34-ID-E: http://www.aps.anl.gov/Sectors/33_34/microdiff/downloads/

Semiatin S.L., Knisley S.L., Fagin P.N., Barker D.R., and Zhang F., 2003, Microstructure evolution during alpha-beta heat treatment of Ti-6Al-4V, Metallurgical and Materials Transactions A, Vol. 34, No. 10, pp. 2377-2386.

Sinha V., Mills M.J., and Williams J.C., 2004, Understanding the contributions of normal-fatigue and static loading to the dwell fatigue in a near-alpha titanium alloy, Metallurgical and Materials Transactions A, Vol. 35, No. 10, pp. 3141-3148.

Sinha V., Spowart J.E., Mills M.J., and Williams J.C., 2006, Observations on the faceted initiation site in the dwell-fatigue tested Ti-6242 alloy: crystallographic orientation and size effects, Metallurgical and Materials Transactions A, Vol. 37, No. 5, pp. 1507-1518.

Song S.G. and Gray G.T., 1995. Structural interpretation of the nucleation and growth of deformation twins in Zr and Ti. Part 1. Application of the coincidence site lattice (CSL) theory to twinning problems in hcp structures. Acta Metallurgica et Materialia. Vol. 43, No. 6, pp. 2325-2337.

Stanford N., Carlson U., and Barnett M.R., 2008, Deformation twinning and the Hall-Petch relation in commercial purity Ti, Metallurgical and Materials Transactions A, Vol. 39, No. 4, pp. 934-944.

Suri S., Viswanathan G.B., Neeraj T., Hou D.H., and Mills M. J., 1999, Room temperature deformation and mechanisms of slip transmission in oriented single-colony crystals of an α/β titanium alloy, Acta Materialia, Vol. 47, No. 3, pp. 1019-1034.

Suri S., Neeraj T., Daehn G.S., Hou D.H., Scott J.M., Hayes R.W., and Mills M.J., 1997, Mechanisms of primary creep in α/β titanium alloys at lower temperatures, Materials Science and Engineering A, Vol. 234-236, pp. 996-999.

Szczepanski C.J., Jha. S.K., Larsen. J.M., and Jones J.W., 2008, Microstructural influences on very-high-cycle fatigue-crack initiation in Ti-6246, Metallurgical and Materials Transaction A, Vol. 39, No. 12, pp. 2841-2851.

Teer D.G. and Salem F.B., 1977, The formation of low friction wear-resistant surfaces on titanium by ion plating, Thin Solid Films, Vol. 45, No. 3, pp. 583-589.

Venkatesan V., Sarma D.S., and Murty K.L., 1991, On the origin of creep anisotropy in a Ti-3Al-2.5 V alloy, Journal of Materials Science Letters, Vol. 10, No. 16, pp. 984-986.

Wang L., Eisenlohr P., Yang Y., Bieler T.R., and Crimp M.A., 2010a, Nucleation of paired twins at grain boundaries in titanium, Scripta Materialia, Vol. 63, No. 8, pp. 827-830.

Wang L., Yang Y., Eisenlohr P., Bieler T.R, Crimp M.A., and Mason D.E. 2010b, Twin nucleation by slip transfer across grain boundaries in CP titanium, Metallurgical and Materials Transaction A, Vol. 41, No. 2, pp. 421-30.

Wasz M.L., Brotzen, F.R., McLellan R.B., and Griffin Jr A.J., 1996, Effect of oxygen and hydrogen on mechanical properties of commercial purity titanium, International Materials Reviews, Vol. 41, No. 1, pp. 1-12.

Wilkinson A.J., 1996, Measurement of elastic strains and small lattice rotations using electron back scatter diffraction, Ultramicroscopy, Vol. 62, No.4, pp.237-242.

Williams J.C., Baggerly R.G., and Paton N.E., 2002, Deformation behavior of HCP Ti-Al alloy single crystals, Metallurgical and Materials Transaction A, Vol. 33, No. 13, pp. 837-850.

Wang J., Beyerlein I.J., and Tome C.N., 2010, An atomic and probabilistic perspective on twin nucleation in Mg, Scripta Materialia, Vol. 63, No. 7, pp. 741–746.

Wang J., Beyerlein I.J., and Hirth J.P., 2012, Nucleation of elementary {-1 0 1 1} and {-1 0 1 3} twinning dislocations at a twin boundary in hexagonal close-packed crystals, Modelling and Simulation in Materials Science and Engineering, Vol. 20, No. 2, pp. 024001.

Wu X., Kalidindi S.R., Necker C., and Salem A.A., 2007, Prediction of crystallographic texture evolution and anisotropic stress–strain curves during large plastic strains in high purity α-titanium using a Taylor-type crystal plasticity model, Acta Materialia, Vol. 55, No. 2, pp. 423-432.

Yang Y., Wang L., Bieler T.R, Eisenlohr P., and Crimp M.A., 2011, Quantitative atomic force microscopy characterization and crystal plasticity finite element modeling of heterogeneous deformation in commercial purity titanium, Metallurgical and Materials Transactions A, Vol. 42, No. 3, pp. 636-644.

Yapici G.G., Karaman I., and Luo Z.P., 2006, Mechanical twinning and texture evolution in severely deformed Ti–6Al–4V at high temperatures, Acta Materialia, Vol. 54, No. 14, pp. 3755–3771.

Ying D.D., Wang Q.D., Boehlert C.J., Chen Z., Li H., Mishra R.K., Chakkedath A., and Sachdev A.K., 2013, to be submitted.

Yoo M.H., Morris J.R., Ho K.M., and Agnew S.R., 2002, Nonbasal deformation modes of HCP metals and alloys: Role of dislocation source and mobility, Metallurgical and Materials Transactions A, Vol. 33, No. 3, pp. 813-822.

Zaefferer S., 2003, A study of active deformation systems in titanium alloys: dependence on alloy composition and correlation with deformation texture, Materials Science and Engineering A, Vol. 344, No. 1-2, pp. 20-30.

Zelin M.G., Yang H.S., Valiev R.Z., and Mukherjee A.K., 1992, Interaction of high-temperature deformation mechanisms, Metallurgical Transactions A, Vol. 23, No. 11, pp. 3135-3140.

Zhang C., Li H., Eisenlohr P., Liu W., Boehlert C.J., Crimp M.A., and Bieler T.R., 2013, Effect of Realistic 3D Microstructure in Crystal Plasticity Finite Element Analysis of Polycrystalline Ti-5Al-2.5Sn, to be submitted.